Conference Proceedings of the Society for Experimental Mechanics Series

Antonio Baldi · John M. Considine · Simon Quinn
Xavier Balandraud *Editors*

Residual Stress, Thermomechanics & Infrared Imaging, Hybrid Techniques and Inverse Problems, Volume 8

Proceedings of the 2017 Annual Conference on Experimental and Applied Mechanics

SEM

Springer

Conference Proceedings of the Society for Experimental Mechanics Series

Series Editor

Kristin B. Zimmerman, Ph.D.
Society for Experimental Mechanics, Inc.,
Bethel, CT, USA

More information about this series at http://www.springer.com/series/8922

Antonio Baldi • John M. Considine • Simon Quinn • Xavier Balandraud
Editors

Residual Stress, Thermomechanics & Infrared Imaging, Hybrid Techniques and Inverse Problems, Volume 8

Proceedings of the 2017 Annual Conference on Experimental and Applied Mechanics

Springer

Editors
Antonio Baldi
Department of Mechanical Engineering,
Chemical and Materials Engineering
University of Cagliari
Cagliari, Italy

Simon Quinn
Research Institute for Industry
Faculty of Engineering and Environment
University of Southampton
Southampton, UK

John M. Considine
Materials Research Engineer
U.S. Forest Service, Forest Products
Laboratory
Madison, WI, USA

Xavier Balandraud
Université Clermont-Auvergne
Clermont-Ferrand, France

ISSN 2191-5644 ISSN 2191-5652 (electronic)
Conference Proceedings of the Society for Experimental Mechanics Series
ISBN 978-3-319-62898-1 ISBN 978-3-319-62899-8 (eBook)
DOI 10.1007/978-3-319-62899-8

Library of Congress Control Number: 2016949067

© The Society for Experimental Mechanics, Inc. 2018
This work is subject to copyright. All rights are reserved by the Publisher, whether the whole or part of the material is concerned, specifically the rights of translation, reprinting, reuse of illustrations, recitation, broadcasting, reproduction on microfilms or in any other physical way, and transmission or information storage and retrieval, electronic adaptation, computer software, or by similar or dissimilar methodology now known or hereafter developed.
The use of general descriptive names, registered names, trademarks, service marks, etc. in this publication does not imply, even in the absence of a specific statement, that such names are exempt from the relevant protective laws and regulations and therefore free for general use.
The publisher, the authors and the editors are safe to assume that the advice and information in this book are believed to be true and accurate at the date of publication. Neither the publisher nor the authors or the editors give a warranty, express or implied, with respect to the material contained herein or for any errors or omissions that may have been made. The publisher remains neutral with regard to jurisdictional claims in published maps and institutional affiliations.

Printed on acid-free paper

This Springer imprint is published by Springer Nature
The registered company is Springer International Publishing AG
The registered company address is: Gewerbestrasse 11, 6330 Cham, Switzerland

Preface

Residual Stress, Thermomechanics & Infrared Imaging, Hybrid Techniques and Inverse Problems represents one of nine volumes of technical papers presented at the 2017 SEM Annual Conference & Exposition on Experimental and Applied Mechanics organized by the Society for Experimental Mechanics and held in Indianapolis, IN, June 12–15, 2017. The complete Proceedings also includes volumes on: *Dynamic Behavior of Materials; Challenges In Mechanics of Time-Dependent Materials; Advancement of Optical Methods in Experimental Mechanics; Mechanics of Biological Systems, Materials and other topics in Experimental and Applied Mechanics; Micro-and Nanomechanics; Mechanics of Composite, Hybrid & Multifunctional Materials; Fracture, Fatigue, Failure and Damage Evolution; and Mechanics of Additive and Advanced Manufacturing.*

Each collection presents early findings from experimental and computational investigations on an important area within Experimental Mechanics; Residual Stress, Thermomechanics & Infrared Imaging, Hybrid Techniques and Inverse Problems being three of these areas.

Residual stresses are self-balanced stress fields induced during most materials processing procedures, for example, welding/joining, casting, thermal conditioning, and forming. Their hidden character often causes them to be underrated or overlooked. However, they profoundly influence structural design and substantially affect strength, fatigue life, and dimensional stability. Thus, they must be taken seriously and included in practical applications.

In recent years the applications of infrared imaging techniques to the mechanics of materials and structures has grown considerably. The expansion is marked by the increased spatial and temporal resolution of the infrared detectors, faster processing times and much greater temperature resolution. The improved sensitivity and more reliable temperature calibrations of the devices have meant that more accurate data can be obtained than were previously available.

Advances in inverse identification have been coupled with optical methods that provide surface deformation measurements and volumetric measurements of materials. In particular, inverse methodology was developed to more fully use the dense spatial data provided by optical methods to identify mechanical constitutive parameters of materials. Since its beginnings during the 1980s, creativity in inverse methods has led to applications in a wide range of materials, with many different constitutive relationships, across material heterogeneous interfaces. Complex test fixtures have been implemented to produce the necessary strain fields for identification. Force reconstruction has been developed for high strain rate testing. As developments in optical methods improve for both very large and very small length scales, applications of inverse identification have expanded to include geological and atomistic events. Researchers have used in-situ 3D imaging to examine microscale expansion and contraction and used inverse methodologies to quantify constitutive property changes in biological materials.

Sardinia, Italy	Antonio Baldi
Madison, WI, USA	John M. Considine
Southampton, UK	Simon Quinn
Sigma Clermont, France	Xavier Balandraud

Contents

Chapter 1
Residual Stresses in Bovine Femurs

Yongbo Zhang and Drew Nelson

Abstract The slitting method has become well-established for determining residual stresses in engineering materials. This study develops and applies a version of that method using a small slot to find residual stresses vs. depth in layers near the surface of bovine femurs. Results are obtained for the central region (diaphysis) of hydrated femurs from both mature and young cows. The magnitude of residual stresses was found to be greatest in thin layers near the surface, typically 100–200 μm deep. Residual stresses in those layers were compressive in mature femurs at the circumferential location tested, but tensile in hydrated young femurs.

Keywords Residual stress • Bone • Femur • Slitting method • X-ray diffraction

1.1 Introduction

The presence of residual stresses in components made of engineering materials is well known. Residual stresses and strains also exist in arteries [1–6], the esophagus [7–10], intestines [11, 12], brain [13], skin [14], etc. and may play an important role in the mechanical behavior of biological structures. For instance, at the inner diameter of arteries, compressive circumferential residual strains are believed to significantly reduce tensile stresses from blood pressure [4, 15–17] and enhance resistance to failure [18]. (The distinction between residual stresses and strains is made here because residual strains can have a different influence on the nonlinear stress-strain behavior of soft tissue than residual stresses).

The existence and possible role of residual stresses in bone does not appear to be well-understood. X-ray diffraction (XRD) has been widely applied to find residual stresses in engineering materials with crystalline structures [19]. More recently, it has been applied to bone, a major constituent of which is the mineral hydroxyapatite (HAP) [20]. In the following summary, residual stresses refer to values determined by XRD with HAP crystals serving as "miniature strain sensors." Residual stresses have been measured in specimens taken mainly from bovine femurs [21, 22–29], but also from canine fibula [30, 31] and the extremities of rabbits [32, 33]. The size and condition of specimens prior to and during experiments has varied considerably from study-to-study. A number of studies [21, 23–27] have used sizeable specimens removed from the central portion (diaphysis) of bovine femurs as depicted in Fig. 1.1 and measured residual stresses at the surface or at various depths. All but one of those studies used air dried specimens, and reported longitudinal tensile stresses, in some cases exceeding 100 MPa at the surface, with smaller values of compressive stress (≈ -10 MPa) at depths of 1 mm. Residual stresses were found to vary considerably with position around the circumference of specimens. Other studies used much smaller specimens (dimensions on the order a few mm) of bovine femurs [22, 28, 29] or canine fibula [31] that were kept hydrated. Compressive residual stresses and strains were measured through the thickness with synchrotron X-rays, with values as large as -150 MPa and -2500 με, respectively. For perspective on the magnitude of residual stress and strain values mentioned above, the longitudinal tensile yield stress of bovine femurs is approximately 100–130 MPa [20, 34]. The yield strain is estimated to be about 6500 με [35].

The interpretation of results from the XRD studies can be complicated by the following factors. Using $1 \times 1 \times 10$ mm specimens taken from bovine femurs, Tung et al. [29] found that initial compressive residual stresses (exceeding -100 MPa) became tensile after about 20 min without hydration, climbing to approximately $+75$ MPa after an hour. Measured values of residual stresses may thus be altered if dehydration occurs during XRD experiments, although the extent of that influence

---

Y. Zhang
Institute of Solid Mechanics, Beihang University, Beijing 100191, China

D. Nelson (✉)
Mechanical Engineering Department, Stanford University, Stanford, CA 94305, USA
e-mail: dnelson@stanford.edu

A. Baldi et al. (eds.), *Residual Stress, Thermomechanics & Infrared Imaging, Hybrid Techniques and Inverse Problems, Volume 8*,
Conference Proceedings of the Society for Experimental Mechanics Series, DOI 10.1007/978-3-319-62899-8_1

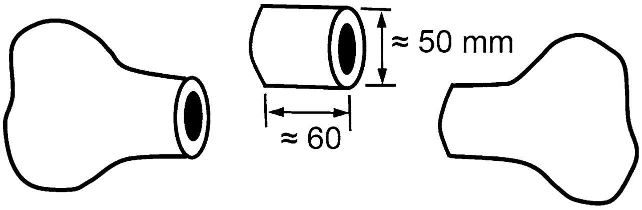

Fig. 1.1 Schematic of a specimen cut from the central portion (diaphysis) of a bovine femur

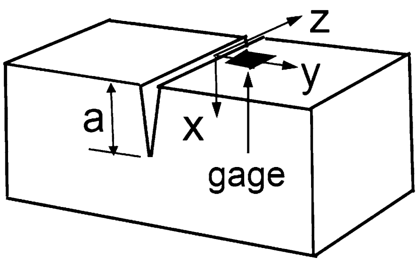

Fig. 1.2 Slitting geometry

is unknown for larger specimens. Dissecting a bone into successively smaller pieces changed values of residual stresses measured by XRD [32]. Recent studies [22, 29] have also found that compressive residual stresses in small specimens, as measured via HAP crystals, dropped significantly with radiation dose. Doses are not reported in most of the XRD studies of bone and may or may not have influenced results.

Residual stresses can also be measured in objects by releasing residual stresses, measuring resulting strains or deflections, and then using a computational model that relates the strains or deflections to the residual stresses. Stanwyck et al. [36] applied a strain gage in the longitudinal direction of a bovine metatarsal bone and sawed a 2 mm deep cut in the transverse direction of the bone, near the gage. A compressive strain of −180 με was reported. When the cut was deepened to 3 mm, the strain increased to −280 με. The area surrounding the cut was irrigated with saline solution during the sawing. This experiment could be considered an early form of the slitting method for residual stress determination. Residual stresses were not computed from the measured strains, which is understandable since the methodology to do so was in its infancy when the experiment was conducted in the early 1980s. This paper will explore a version of the slitting method adapted to find residual stress vs. depth in bovine femurs, using a refined experimental approach and a finite element model.

1.2 Slitting Method

As background, key features of the slitting method will be summarized. Suppose that a slit is introduced incrementally in depth into an object containing residual stresses σ normal to the slit and varying in an unknown manner with depth x, as depicted in Fig. 1.2. The slit releases residual stresses, causing the surface to develop strains ε normal to the slit, which are typically measured with a strain gage near the slit location (and/or on the opposite side of the object if desired). Measured strain vs. depth data can be used with a computational model to determine the variation of σ with depth [37–39]. Assuming that residual stresses are constant in the z-direction, residual stresses σ can be related to strains by [40]:

$$\epsilon\left(a_i\right) = \int_0^{a_i} G\left(x, a_i\right) \sigma\left(x\right) dx \tag{1.1}$$

where $\epsilon(a_i)$ is the measured strain when a slit is at depth a_i. The function $G(\mathrm{x}, a_i)$ gives the strain response from a unit stress at depth x for a slit of depth a_i.

Residual stresses vs. depth can approximated by

$$\sigma(x) = \sum\nolimits_{j=1}^{n} A_j\, U_j(x) \tag{1.2}$$

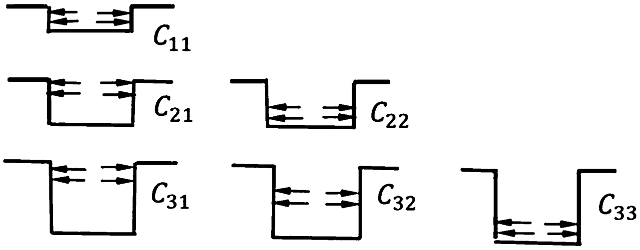

Fig. 1.3 Illustration of unit stresses applied to different increments of depth to find compliance matrix C_{ij}.

where A_j are coefficients to be found and $U_j\,(x)$ are unit pulses with $U_j\,(x) = 1$ for a depth increment $a_{j-1} \leq x \leq a_j$ and zero for $x \leq a_{j-1}, x \geq a_j$. Substituting Eq. 1.2 into Eq. 1.1 gives

$$\epsilon\,(a_i) = \sum\nolimits_{j=1}^{n} A_j C_{ij} \tag{1.3}$$

with a compliance matrix given by

$$C_{ij} = \frac{1}{E}\int_{a_j}^{a_{j-1}} G\,(x, a_i)\,U_j(x)dx \tag{1.4}$$

and $E =$ modulus of elasticity.

From Eqs. 1.1 and 1.4, the matrix elements C_{ij} represent strains at the surface from unit stresses applied to various increments of depth $a_{j-1} \leq x \leq a_j$. Values of C_{ij} can be found by a creating a finite element model of a slit and applying stresses as in Fig. 1.3.

Expressing Eq. 1.3 as $\{\epsilon\} = [\mathrm{C}]\,\{A\}$ leads to a solution for the coefficients A_j in Eq. 1.2 in terms of measured strains:

$$\{A\} = \left([C]^T\,[C]\right)^{-1}\,[C]^T\,\{\varepsilon_{\mathrm{meas}}\} \tag{1.5}$$

The determination of residual stresses vs. depth using the “unit pulse” method can be improved by Tikhonov regularization [41] to reduce effects of experimental uncertainties.

1.3 Slotting Model

The slitting method was adapted for application to the central portion of femurs by the use of a small slot as depicted in Fig. 1.4 at regions that were flat over the length of a slot. Prior to performing experiments on bone, a finite element model was developed to determine compliance coefficients *Cij* for incremental slotting. The finite element code ABAQUS was with the model shown in Fig. 1.5, which employed eight-node linear brick elements. The nodes on the bottom of the model were fixed. The slot length D was 2.6 mm and the width 2R was 0.8 mm. The width of the slit was based on the smallest diameter end mill that would not break when making a slot. The slot was extended to a depth of 0.61 mm in ten steps. Each of the first six steps was 0.051 mm, followed by four steps of 0.076 mm each. Compliance *Cij* values were computed by applying a unit stress step-by-step as illustrated in Fig. 1.3. Slot extension in depth was simulated by deleting elements. Displacement data were used to compute strains using the method in Ref. 42. Orthotropic material behavior was used in the model, with longitudinal and transverse (tangential) moduli of elasticity $\mathrm{E_L}$ and $\mathrm{E_T}$ values as described shortly, plus values for Poisson’s ratios and shear moduli available for bovine femur [43]. As might be anticipated, the value of $\mathrm{E_L}$ governed strains from slotting. Experiments utilized hydrated femurs from mature (20–24 months old) and young (3–4 months old) cows. Rather than assuming that published values of $\mathrm{E_L}$ and $\mathrm{E_T}$ for bovine femurs would be applicable over the depth of slotting used here, tests were performed to find $\mathrm{E_L}$, $\mathrm{E_T}$ values relevant to that depth. Specimens with a length of 9.0 mm and a rectangular cross-section with a 1.0 mm width and 0.4–0.5 mm thickness were carefully milled from surface layers of different femurs and stored in PBS at room temperature. The specimens were tested in a miniature three point bending fixture with a span of 8.0 mm. The mid-point deflection of each specimen was monitored using a 100 power microscope. Modulus of elasticity

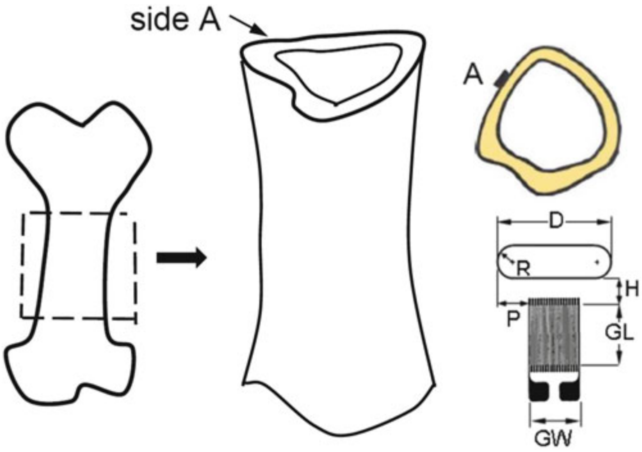

Fig. 1.4 Schematic of femur, typical specimen and a slot with adjacent strain gage (D = 2.6, R = 0.4, H = 1.0, P = 0.55, GL = 3.0, GW = 1.5 mm)

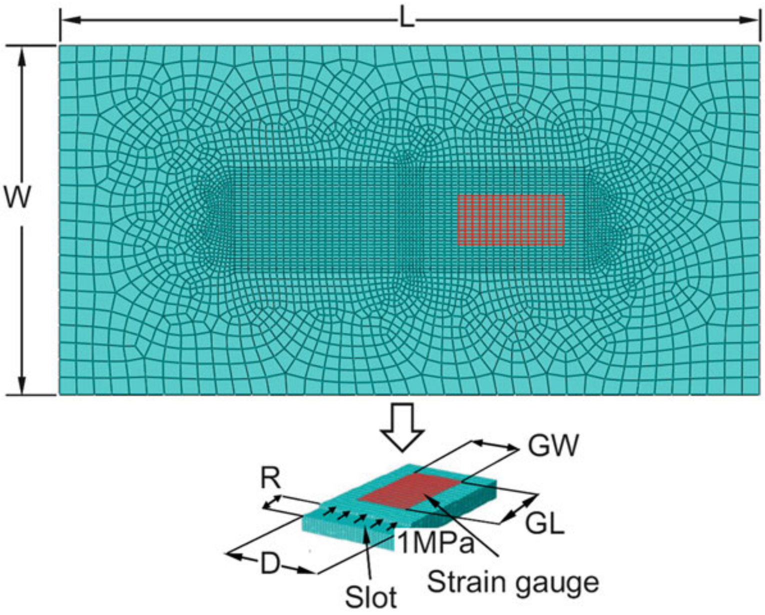

Fig. 1.5 Finite element model to simulate slotting with unit stresses applied along the straight portion of the slot

was computed from a relation between mid-point deflection and bending moment. For tests of femurs from two mature cows, average E_L and E_T were 22.0 and 9.1 GPa, respectively. The range of E_L for specimens from previous studies [34, 43–45], which used specimens roughly an order of magnitude larger than those here, was 19.3–22.6 GPa, and 12.4 to 14.6 GPa for E_T. Tests using specimens from two young cows gave average E_L and E_T of 14.6 and 8.5 GPa. Values of E_L and E_T of 6.6 and 5.3 GPa have been reported in a recent study involving young bovine femurs [45].

1.4 Slotting Experiments with Bone Specimens

Each refrigerated bovine femur (with ends removed as illustrated in Fig. 1.4) was obtained from a butcher within 24 h of slaughter. Soft tissue was removed and the resulting specimen placed in phosphate buffered saline (PBS) for 48 h. Specimens were 125–150 mm long, with cross sectional widths between 50 and 75 mm. Next, each specimen was placed in a fixture that held it steady for slotting and enabled fine adjustments of tilt in two directions. A specimen and its holding fixture were then submerged in a water tank at room temperature, and a slotting setup illustrated in Fig. 1.6 installed over the specimen.

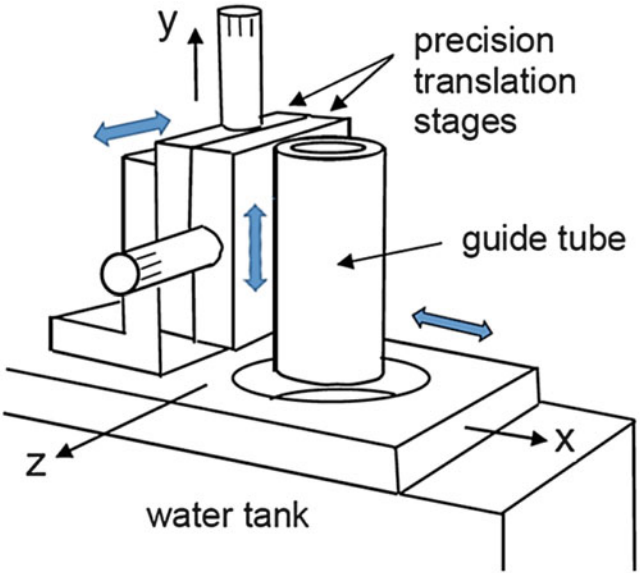

Fig. 1.6 Schematic of setup used to perform slotting experiments, adjustable in x,y,z directions

The setup enabled translation in x,y and z directions. Next, a displacement probe was slid into the guide tube and used to map the flatness of the region. Through adjustment of the location and tilt of a specimen, it was possible to identify surface regions that were on average flat to within 0.013 mm (0.0005 in.) over a prospective slot length. Those regions were marked with waterproof ink. With a specimen temporarily removed from the water tank, a strain gage was attached to the surface adjacent to a prospective slot using cyanoacrylate adhesive, which cures well in the presence of moisture. Care was taken to ensure that no adhesive extended into the region of a prospective slot. A strain gage and its terminal pad were covered with a polyurethane coating for protection from water, with the slot area masked temporarily to prevent it from being covered. After allowing 20 min for the coating to dry, a specimen was returned to the water tank and the orientation of an intended slot adjusted to ensure it was horizontal. The specimen was submerged in the water tank for 24 h for additional hydration and to allow the temperature of the specimen to equilibrate with that of the water surrounding it. Prior to making a slot, the thermal stability of strain readings was checked. Strains did not fluctuate by more than 2 $\mu\varepsilon$ over the anticipated duration of an experiment.

Slotting was performed by sliding a boring bar with an end mill into the tubular guide in Fig. 1.6. Slot depth was set using a precision translation stage (y-direction). Each slot was made by manually rotating the boring bar and gradually translating the end mill in the z direction using a second translation stage. Powered drilling has been found to damage bone tissue by heating [46] and thus gentle manual rotation (less than 10 RPM) was used in an effort to avoid such damage and its unknown effect on results of the experiments. After each slotting step, actual depth was measured at four locations along the length of a slot, and the average of those values used in expressing strain vs. depth. The actual depth after each step during slotting experiments was not exactly the same as in the finite element model. Depths were measured after each step to a resolution of 0.0025 mm (0.0001 in.). Values of strain corresponding to the depths used in the finite element model were found by interpolation from the measured strains vs. depth. Each specimen, including slot and strain gage, was submerged during the entirety of a slotting experiment. Final slot depths were close to 0.61 mm.

1.5 Initial Results

Residual stresses vs. depth as determined by slotting are shown in Fig. 1.7. Magnitudes are most significant in thin layers just beneath the surface. Compressive residual stresses near the surface were found for femurs from mature cows, while those from young cows had tensile residual stresses. The magnitudes of residual stresses found by slotting may seem insignificant at first glance. However, the magnitudes may be of more significance when noting again that the tensile yield stress of mature bovine femurs is on the order 100–130 MPa [20, 34] (and perhaps somewhat lower for young femurs). Experiments to provide residual stress data for other circumferential locations on young and mature femurs are planned.

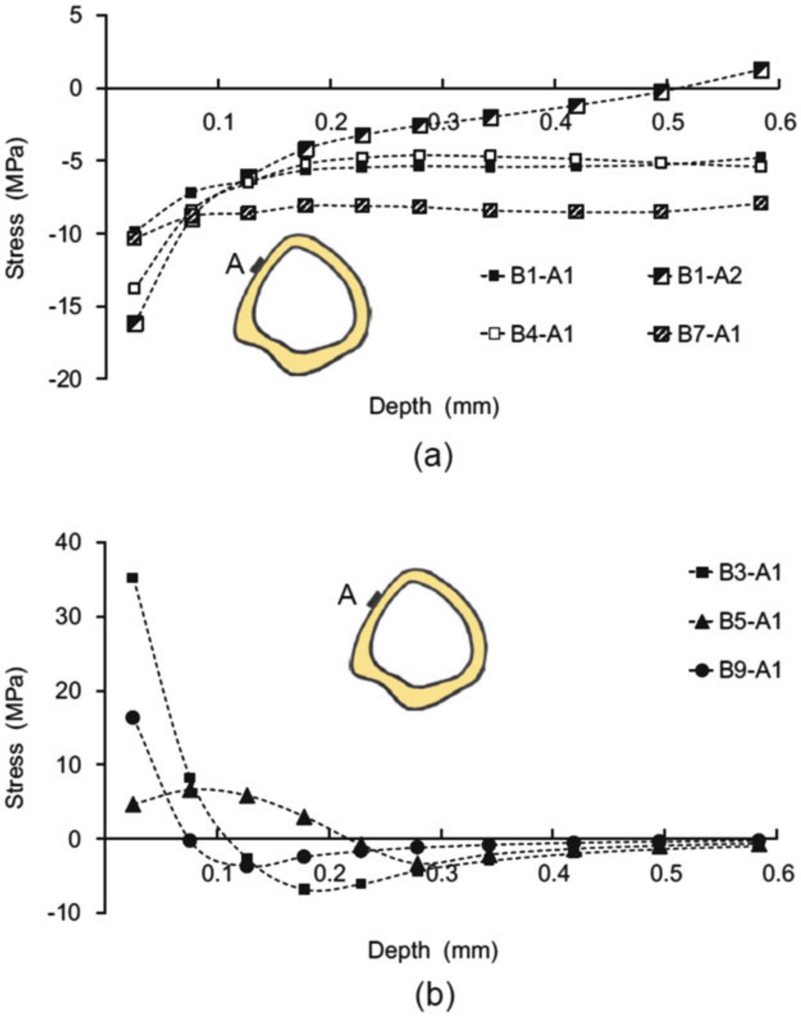

Fig. 1.7 Residual stresses vs. depth for (**a**) mature and (**b**) young femurs at location A

1.6 Discussion

Determination of residual stresses in layers near the surface may be of interest since fracture [47], fatigue [48, 49] and bone growth [50] mechanisms are prominent there.

The observation in this study of tensile residual stresses in surface layers of hydrated young femurs was not anticipated. An XRD study of young but air dried femurs [25] found minimal residual stresses at the surface (between about 0 and −10 MPa) and stresses that alternated between tension and compression (approx. +10 to −10 MPa depending on circumferential location) at depths between 0.5 and 3 mm. The unknown effect of air drying makes comparison with results observed here difficult. Maintaining hydration of larger bone specimens during XRD experiments can be challenging.

Bone is a microstructurally complex material [20]. An example is shown in Fig. 1.8, where the outer layers of a bovine femur have a lamellar structure like layers of bricks, while deeper layers have cylindrical osteons (Haversian structure). Residual stresses in this study represent values averaged over the volume of material removed by each step of slotting and may differ from values of residual stresses in smaller volumes.

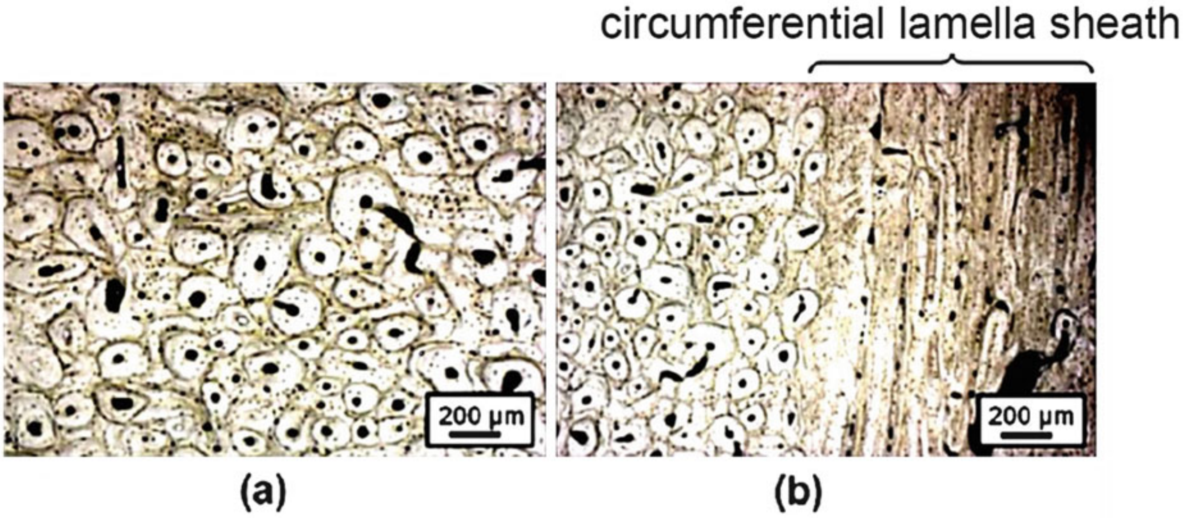

Fig. 1.8 Example showing (**a**) Haversian (osteons) and (**b**) lamellar microstructures (in circumferential sheath) of bovine femur, with micrographs from [44]

1.7 Conclusions

1. Development and application of a slotting method to find longitudinal residual stresses vs. depth in specimens of bone is feasible.
2. In hydrated bovine femurs from both mature and young animals, residual stresses were found to be greatest in thin layers near the surface, typically 100–200 μm deep.
3. In those layers, residual stresses in hydrated mature femurs were compressive at the circumferential location tested, but tensile in young femurs.

References

1. Fung, Y.: Biodynamics: Circulation, pp. 54–60. Springer, New York (1984)
2. Vishnav, R., Vossoughi, J.: Estimation of residual strains in aortic segments. In: Hall, C (ed.) Biomedical Engineering II, Recent Developments, pp 330–333. Pergamon Press, Elmsford, New York (1983)
3. Choung, C., Fung, Y.: On residual stresses in arteries. J. Biomech. Eng. **108**, 189–192 (1986)
4. Rachev, A., Greenwald, S.: Residual strains in conduit arteries. J. Biomech. **36**, 661–670 (2003)
5. Humphrey, J.: Cardiovascular Solid Mechanics: Cells, Tissues and Organs. Springer, New York (2002)
6. Holzapfel, G., et al.: Layer-specific 3D residual deformation of human aortas with non-atherosclerotic intimal thickening. Ann. Biomed. Eng. **35**, 530–545 (2007)
7. Gregersen, H., Lee, T., Chien, S., Skalak, R., Fung, Y.: Strain distribution in the layered wall of the esophagus. J. Biomech. Eng. **121**, 442–448 (1999)
8. Laio, F.Y., Zeng, G., Gregersen, H.: Stress distribution in the layered wall of the rat oesophagus. Med. Eng. Phys. **25**, 731–738 (2003)
9. Zhao, J., et al.: Opening angle and residual strain in a three-layered model of pig oesophagus. J. Biomech. **40**, 3187–3192 (2007)
10. Sokolis, D.: Strain-energy function and three-dimensional stress distribution in esophageal biomechanics. J. Biomech. **43**, 2753–2764 (2010)
11. Gao, C., Gregersen, H.: Biomechanical and morphological properties in rat large intestine. J. Biomech. **33**, 1089–1097 (2000)
12. Dou, Y., et al.: Longitudinal residual strain and stress-strain relationship in rat small intestine. Biomed. Eng. Online. **5**, 37 (2006). doi:10.1186/1475-925-5-37
13. Xu, G., Bayly, P., Taber, L.: Residual stress in the adult mouse brain. Biomech. Model. Mechanobiol. **8**, 253–262 (2009)

14. Matsumoto, T., Ikuta, N., Mori, M., Nagayam, K.: Mechanics of wrinkle formation: micromechanical analysis of skin deformation during wrinkle formation in ultraviolet-irradiated mice. Skin. Res. Tech. **16**, 179–189 (2010)
15. Fung, Y.: What are the residual stresses doing in our blood vessels? Ann. Biomed. Eng. **19**, 237–249 (1991)
16. Destrade, M., Liu, Y., Murphy, J., Kassab, G.: Uniform transmural strain in pre-stresses arteries occurs at physiological pressure. J. Theo. Biol. **303**, 93–97 (2012)
17. Delfino, A., Stergiopulos, N., Moore, J., Meister, J.: Residual strain effects on the stress field in a thick wall finite element model of the human carotid bifurcation. J. Biomech. **30**, 777–786 (1997)
18. Volokh, K.: Prediction of arterial failure based on microstructural bi-layer fiber-matrix model with softening. J. Biomech. **41**, 447–453 (2008)
19. Noyan, I., Cohen, J.: Residual Stress: Measurement by Diffraction and Interpretation. Springer, New York (1987)
20. Currey, J.: Bones: Structure and Mechanics. Princeton University Press, Princeton (2006)
21. Todoh, M., Tadano, S., Shibano, J., Ukai, T.: Polychromatic X-ray measurements of anisotropic residual stress in bone femoral bone. JSME Int. J. C. Mech. Sy. **43**, 795–801 (2000)
22. Singhal, A., Deymier-Black, A., Almer, J., Dunand, D.: Effect of high-energy X-ray doses on bone elastic properties and residual strains. J. Mech. Behav. Biomed. Mater. **4**, 1774–1786 (2011)
23. Yamada, S., Tadano, S.: Residual stress around the cortical surface in bovine femoral diaphysis. J. Biomech. Eng. **132**, 044503-1–044503-4 (2010)
24. Yamada, S., Tadano, S., Todoh, M., Fujisaki, K.: Residual stress distribution in the bovine femoral diaphysis measured by synchrotron. J. Biomech. Sci. Engr. **6**, 114–124 (2011)
25. Yamada, S., Tadano, S.: Effects of growth on residual stress distribution along the radial depth of cortical cylinders from bovine femurs. J. Biomech. **46**, 2130–2136 (2013)
26. Yamada, S., Tadano, S., Onuma, M.: X-ray diffraction technique with imaging plate for detecting surface distribution of residual stress in diaphysis of bovine femurs. Exp. Mech. **54**, 633–640 (2014)
27. Onuma, M., Yamada, S., Tadano, S.: Age-related residual stresses at diaphyseal surface of bovine femur measured by XRD-IP system. 15th Int. Conf. Biomed Eng, IFMBE Proc. **43**, 743–744 (2014)
28. Hoo, P., Fratrzl, P., Daniels, J., Dunlop, J., Honkimaki, V., Hoffman, M.: Cooperation of length scales and orientations in the deformation of bovine bone. Acta Biomater. **7**, 2943–2951 (2011)
29. Tung, P., Mudie, S., Daniels, J.: Hydration and radiation effects on the residual stress state of cortical bone. Acta Biomater. **9**, 9503–9507 (2013)
30. Almer, J., Stock, S.: Internal strains and stresses measured in cortical bone via high-energy X-ray diffraction. J. Struc. Biol. **152**, 14–27 (2005)
31. Almer, J., Stock, S.: Micromechanical response of mineral and collagen phases in bone. J. Struc. Biol. **157**, 365–370 (2007)
32. Tadano, S., Okoshi, T.: Residual stress in bone structure and tissue of rabbit's tibiofibula. Biomed. Mater. Eng. **16**, 11–21 (2006)
33. Yamada, S., Tadano, S., Fujisaki, K.: Residual stress distribution in rabbit limb bones. J. Biomech. **44**, 1285–1290 (2011)
34. Kotha, S., Guzelsu, N.: Effect of bone mineral content on the tensile properties of cortical bone: experiments and theory. J. Biomech. Eng. **125**, 785–793 (2003)
35. Currey, J.: What determines the bending strength of compact bone? J. Exp. Biol. **202**, 2495–2502 (1999)
36. Stanwyck, T., Fischer, R., Pope, M., Seligson, D.: Studies on prestress in bone. Biorheology. **19**, 301–306 (1982)
37. Prime, M.: Residual stress measurement by successive extension of a slot: the crack compliance method. Appl. Mech. Rev. **52**, 75–96 (1999)
38. Cheng, F., Finnie, I.: Residual Stress Measurement and the Slitting Method. Springer, New York (2007)
39. Hill, M.: Slitting (chap. 4). In: Schajer, G. (ed.) Practical Residual Stress Measurement Methods, pp. 89–108. Wiley, Chichester (2013)
40. Shokrieh, M., Akbari, A.: Measuring residual stress in composite materials, chap.5. In: Shokrieh, M. (ed.) Residual Stresses in Composite Materials. Woodhead Publishing, Cambridge, UK (2014)
41. Schajer, G., Prime, M.: Use of inverse solutions for residual stress measurements. J. Eng. Mater. Technol. **128**, 375–382 (2006)
42. Schajer, G.: Use of displacement data to calculate strain gauge response in non-uniform strain fields. Strain. **29**, 9–13 (1993)
43. Van Buskirk, W., Cowin, S., Ward, R.: Ultrasonic measurement of orthotropic elastic constants of bovine femoral bone. J. Biomech. Eng. **103**, 67–72 (1981)
44. Novitskaya, E., Chen, P., Lee, S., Castro-Cesena, A., Hiarta, G., Lubarda, V., McKittrick, J.: Anisotropy in the compressive mechanical properties of bovine cortical bone and the mineral and protein constituents. Acta Biomater. **7**, 3170–3177 (2011)
45. Manilay, Z., Novitskaya, E., Sadovnikov, E., McKittrick, J.: A comparative study of young and mature bovine cortical bone. Acta Biomater. **9**, 5280–5288 (2013)
46. Augustin, G., Zigman, T., Davila, S., Udilljak, T., Staroveski, T., Brezak, D., Babic, S.: Cortical bone drilling and thermal necrosis. Clin. Biomech. **27**, 313–325 (2012)
47. Gupta, H., Zioupos, P.: Fracture of bone tissue: the 'hows' and the 'whys'. Med. Eng. Phys. **30**, 1209–1226 (2008)
48. Kruzic, J., Ritchie, R.: Fatigue of mineralized tissues: cortical bone and dentin. J. Mech. Behav. Biomed. Mater. **1**, 3–17 (2008)
49. Yeni, Y., Fyhrie, D.: Fatigue damage-fracture mechanics interaction in cortical bone. Bone. **30**, 509–514 (2002)
50. Henderson, J., Carter, D.: Mechanical induction in limb morphogenesis: the role of growth-generated strains and prestress. Bone. **31**, 645–653 (2002)

Chapter 2
Experimental Stress Analysis of Unsymmetrical, Irregularly-Shaped Structure Containing an Arbitrarily-Shaped Hole

B. Kalayciogli, A. Alshaya, and R. Rowlands

Abstract This paper describes the ability to process load induced temperature information with an Airy stress function in real polar coordinates and some local known boundary conditions to determine the stresses experimentally in an isotropic linear elastic finite arbitrarily-shaped structure containing an irregularly-shaped hole. The proposed method simultaneously smooths the measured data, separates the stress components, and evaluates the individual stress components full-field, including at the boundary of the hole (location of highest tensile stress).

Keywords Thermoelastic stress analysis • Irregularly-shaped holes • Stress concertation • Airy stress function • Hybrid method

2.1 Introduction

References [1–3] treat non-circular cutouts using complex variables and conformal mapping but are restricted to infinitely large members having relatively simple and known external boundary conditions. References [4–16] combine thermoelastic stress data with a series solution of Airy stress function in either real or complex variables along with imposed traction-free boundary conditions on the edge of a hole to determine full-field individual components of stress, strain and displacements. Unlike with Fig. 2.1, all previous situations enjoyed a simple eternal shape, symmetry and/or necessitated imposing the boundary condition only on the internal boundary. Although a few cases imposed the internal boundary conditions discretely, most enabled imposing them analytically. The predominance of asymmetrically-loaded arbitrarily-shaped mechanical structures having irregularly-shaped holes necessitates the present technical extension.

Thermoelastic stress analysis (TSA) is a non-contacting, nondestructive experimental method for determining the full-field stresses in loaded members [17]. The technique enables the stress analysis of actual structures in their operating environment with a sensitivity comparable to that of strain gages. No surface preparation is required other than perhaps a flat black paint to provide an enhanced and uniform emissivity. For proportional loading under adiabatic, reversible elastic conditions, the stress- induce temperature information, S^*, is proportional to the changes in the sum of the normal stresses, S,

$$S^* = K\Delta S = K\Delta\left(\sigma_1 + \sigma_2\right) = K\Delta\left(\sigma_{xx} + \sigma_{yy}\right) = K\Delta\left(\sigma_{rr} + \sigma_{\theta\theta}\right) = K\Delta\left(\sigma_{\xi\xi} + \sigma_{\eta\eta}\right) \tag{2.1}$$

where K is experimentally-determined thermoelastic material coefficient, and σ_1, σ_2, σ_{rr}, $\sigma_{\theta\theta}$, σ_{xx}, σ_{yy}, $\sigma_{\xi\xi}$, and $\sigma_{\eta\eta}$ are the normal stress components in the principal, polar, Cartesian rectangular coordinates, and normal and tangent to the edges of the structure, respectively. Combining experimental information with analytical and numerical tools enables one to separate stress components. The plate was sinusoidally compressed at 1334.46 ± 667.23 N at a rate of 20 Hz in a 20 kips capacity MTS hydraulic testing machine. The corresponding load-induced TSA data were recorded using a DeltaTherm model DT1410 system (Stress Photonics, Madison, WI) having a sensor array of 256 horizontal by 256 vertical pixels. The camera is cooled with liquid nitrogen to maintain the sensor at a very low temperature necessary for the accurate readings. The thermoelastic

---

B. Kalayciogli
Kirikkale University, Kirikkale, Turkey

A. Alshaya
Kuwait University, Kuwait, Kuwait

R. Rowlands (✉)
University of Wisconsin-Madison, Madison, WI, USA
e-mail: rowlands@engr.wisc.edu

A. Baldi et al. (eds.), *Residual Stress, Thermomechanics & Infrared Imaging, Hybrid Techniques and Inverse Problems, Volume 8*,
Conference Proceedings of the Society for Experimental Mechanics Series, DOI 10.1007/978-3-319-62899-8_2

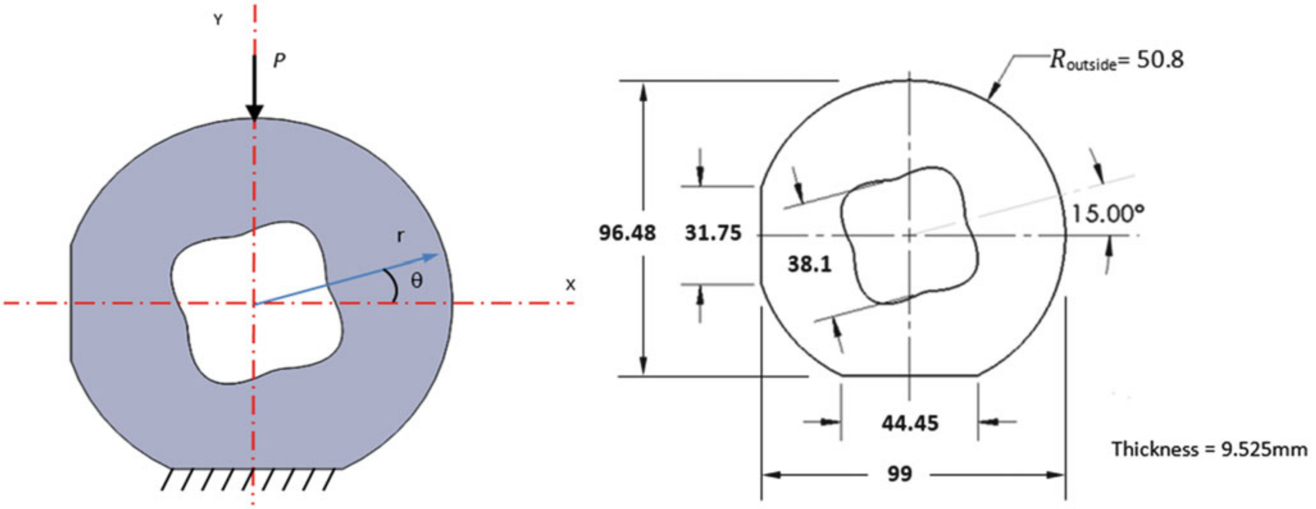

Fig. 2.1 CAD model of finite plate with arbitrary-shaped aluminum plate containing irregularly-shaped hole

signal, S^*, was recorded by the data acquisition system which is equipped with Delta Vision Software and TSA images were captured and averaged over two minute durations. Since TSA data typically are unreliable on and near an edge, no recorded TSA information was used within at least two pixel positions (0.92 mm) of the boundary.

2.2 Relevant Equations

For elasto-static plane isotropic problems in the absence of the body forces, the Airy stress function, Φ, satisfying stress equilibrium and strain compatibility conditions gives the biharmonic equation $\nabla^4\Phi = 0$ where ∇^2 is the Laplacian operator and $\nabla^2 = \frac{\partial}{\partial r^2} + \frac{1}{r}\frac{\partial}{\partial r} + \frac{1}{r^2}\frac{\partial}{\partial \theta^2}$. The general solution to $\nabla^4\Phi = 0$ in polar coordinates for the plate in Fig. 2.1 is [18]

$$\begin{aligned}\Phi = {} & a_0 + b_0 \ln r + c_0 r^2 + A_0\theta + \left(a_1 r + \tfrac{c_1}{r} + d_1 r^3\right)\sin\theta + \left(a_1^{'} r + \tfrac{c_1^{'}}{r} + d_1^{'} r^3\right)\cos\theta \\ & + \textstyle\sum_{n=2,3,..}^{\infty}\left(a_n r^n + b_n r^{n+2} + c_n r^{-n} + d_n r^{-(n-2)}\right)\sin n\theta \\ & + \textstyle\sum_{n=2,3,..}^{\infty}\left(a_n^{'} r^n + b_n^{'} r^{n+2} + c_n^{'} r^{-n} + d_n^{'} r^{-(n-2)}\right)\cos n\theta\end{aligned} \tag{2.2}$$

where r is the radial coordinate measured from the center of the notch, θ is measured counter-clockwise from the horizontal x-axis as shown in Fig. 2.1, and N is the terminating index of the series which is any positive integer. The individual components of stresses in polar coordinate can be evaluated from

$$\sigma_{rr} = \frac{1}{r}\frac{\partial\Phi}{\partial r} + \frac{1}{r^2}\frac{\partial^2\Phi}{\partial\theta^2},\quad \sigma_{\theta\theta} = \frac{\partial^2\Phi}{\partial r^2},\quad \sigma_{r\theta} = -\frac{\partial}{\partial r}\left(\frac{1}{r}\frac{\partial\Phi}{\partial\theta}\right) \tag{2.3}$$

Determination of individual stresses, strains, or displacements necessitates evaluating the unknown Airy coefficients of Eq. 2.2. To help evaluate all of the Airy coefficients, boundary conditions in terms of stresses as shown in Fig. 2.2 were imposed discretely at multiple locations on the interior and exterior boundaries of the structure.

2.3 Results

From the $m = 8564$ recorded thermoelastic values, and, $h = 2 \times 1192 = 2384$ and $t = 2 \times (2731 + 250) = 5962$ boundary conditions on the internal and external boundaries, the Airy coefficients can be solved by forming a linear system of equation represented in matrix form as $[A]_{(m+h+t)\times k}\{c\}_{k\times 1} = \{d\}_{(m+h+t)\times 1}$. The number of equations, $m + h + t = 16{,}910$ will exceed the number of coefficients, k. The resulting overdetermined system of equations with which to evaluate the unknown

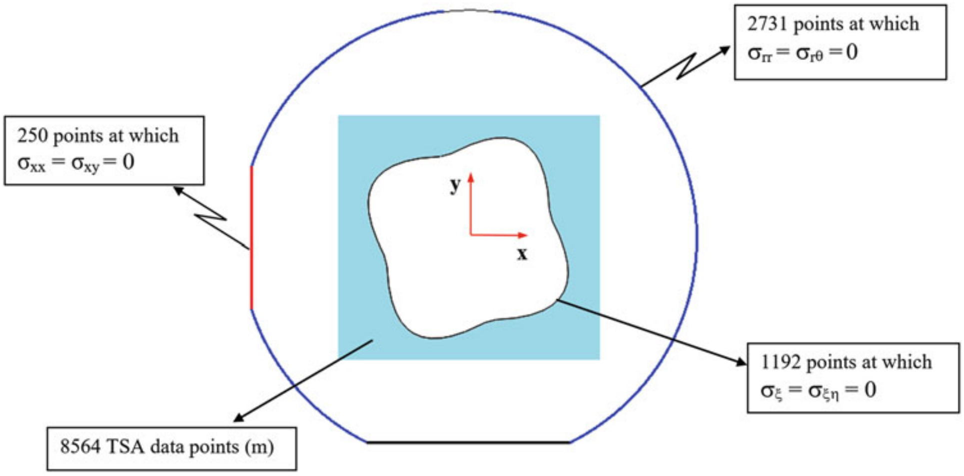

Fig. 2.2 Locations of TSA data and imposed traction-free boundary conditions

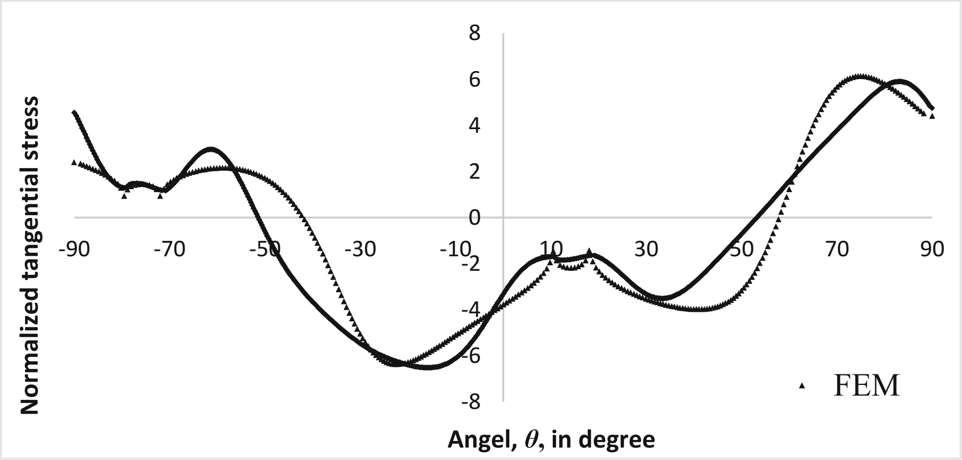

Fig. 2.3 Variations of tangential stress, $\sigma_{\eta\eta}$, on the edge of the irregularly-shaped hole from FEA and hybrid-TSA ($k = 103$ and $m + h + t = 16{,}910$)

Table 2.1 Strains $E_{\eta\eta}$ at locations on the internal boundary by each of hybrid-TSA, FEA (ANSYS), and strain gages for a static load of 1,334.46 N on structure of Fig. 2.1

Location on the inner surface of the hole	Strain value ($\mu\varepsilon$)	Average strain value ($\mu\varepsilon$)	Hybrid-TSA method	FEA (ANSYS)
$\theta = 58^{\circ}$	890	910	890	870
$\theta = 232^{\circ}$	930			
$\theta = 158^{\circ}$	−420	−410	−480	−440
$\theta = 338^{\circ}$	−400			

coefficients was solved using least-squares. The number of Airy coefficients to retain, $k = 103$, was assessed by monitoring the condition number of the respective Airy matrix, computing the Root Mean Square (RMS) for a series of different number of Airy coefficients and by comparing the reconstructed thermoelastic data with the actual measured thermoelastic signals.

With $\sigma_{\xi\xi}$ and $\sigma_{\xi\eta}$ in the $\xi\eta$-coordinate system (tangential-normal) being numerically zero as dictated by imposing the traction-free conditions on the edge of the of the irregularly-shaped hole, the normalized tangential stress, $\sigma_{\eta\eta}/\sigma_0$, along the edge from FEA and hybrid-TSA is shown in Fig. 2.3. The results of this hybrid experiment based on discrete input values of S^* agree with ANSYS, including along edges where no input values were employed. The stresses are normalized with respect to a far-field stress $\sigma_0 = 1334.46/99 \times 9.53 = 1.415$ MPa.

Table 2.1 compares the strains from hybrid-TSA, FEA, and the strain gages. The good agreement between the current hybrid-TSA results and those from FEA and the strain gages provides strong confidence in the presently developed ability to obtain reliable stresses from recorded thermal information.

2.4 Summary, Discussion and Conclusions

A major contribution of this paper is the demonstrated ability to combine experimental (TSA), numerical (least-squares) and analytical (Airy stress) techniques for the full-field determination of the separate components of stresses at and in the neighborhood of the irregularly-shaped hole in a loaded finite arbitrarily-shaped structure, Fig. 2.1, and to do so without having to model the situation, know the external loading or constitutive properties, or differentiate the recorded data. This paper deals with an irregularly-shaped internal boundary and arbitrarily-shaped external boundary. The authors are unaware of prior utilization of Airy stress function to evaluate experimentally the stresses for such complex geometry of the plate in Fig. 2.1 using recorded load-induced thermal information.

References

1. Muskhelishvili, N.: Some basic problems of the mathematical theory of elasticity. Springer, Leyden (1977)
2. Lekhnitskii, S.G.: Anisotropic plates. Gordon & Breach Scientific Publishers, New York (1968)
3. Timoshenko, S., Goodier, J.: Theory of elasticity. McGraw-Hill Publishing Company, New York (1970)
4. Foust, B.E., Rowlands, R.E.: Thermoelastic determination of individual stresses in a diametrally loaded disk. Strain. **47**(2), 146–153 (2011)
5. Lin, S.-J., Matthys, D.R., Rowlands, R.E.: Separating stresses thermoelastically in a central circularly perforated plate using an airy stress function. Strain. **45**(6), 516–526 (2009)
6. Samad, W.A., Rowlands, R.E.: Full-field thermoelastic stress analysis of a finite structure containing an irregularly-shaped hole. Exp. Mech. **54**(3), 457–469 (2014)
7. Samad, W.A., Khaja, A.A., Kaliyanda, A.R., Rowlands, R.E.: Hybrid thermoelastic stress analysis of a pinned joint. Exp. Mech. **54**(4), 515–525 (2014)
8. Lin, S.-J., Quinn, S., Matthys, D.R., New, A.M., Kincaid, I.M., Boyce, B.R., Khaja, A.A., Rowlands, R.E.: Thermoelastic determination of individual stresses in vicinity of a near-edge hole beneath a concentrated load. Exp. Mech. **51**(6), 797–814 (2011)
9. Lin, S.J., Matthys, D.R., Samad, W.A., Khaja, A.A., Boyce, B.R., Rowlands, R.E.: Infrared stress analysis of unsymmetrically-loaded perforated member, ISEM-ACEM-SEM-7th ISEM'12, Taipei (2012)
10. Samad, W.A., Rowlands, R.E.: Hybrid thermoelastic analysis of an unsymmetrically-loaded structure containing an arbitrarily-shaped cutout. In: Residual stress, thermomechanics & infrared imaging, hybrid techniques and inverse problems, vol 8, pp. 51–57. Springer (2014)
11. Abdel Samad, W.: Hybrid full-field stress analysis of structures containing irregularly-shaped cutouts, PhD Thesis, University of Wisconsin-Madison (2013)
12. Lin, S.J., Matthys, D.R., Quinn, S., Davidson, J.P., Boyce, B.R., Khaja, A.A., Rowlands, R.E.: Stresses at and in the neighborhood of a near-edge hole in a plate subjected to an offset load from measured temperatures. Eur. J. Mech. A Solids. **39**, 209–217 (2013)
13. Kurunthottikkal Philip, S.: Stress analysis of a finite structure containing an asymmetrical, arbitrarily-shaped cutout based on recorded temperature data, Master Thesis, University of Wisconsin – Madison (2015)
14. Lin, S.T., Rowlands, R.E.: Thermoelastic stress analysis of orthotropic composites. Exp. Mech. **35**(3), 257–265 (1995)
15. Alshaya, A., Shuai, X., Rowlands, R.: Thermoelastic stress analysis of a finite orthotropic composite containing an elliptical hole. Exp. Mech. **56**(8), 1373–1384 (2016)
16. Alshaya, A.A.: Experimental, analytical and numerical analyses of orthotropic materials and biomechanics application, PhD Thesis, University of Wisconsin-Madison (2017)
17. Greene, R., Patterson, E., Rowlands, R.: Thermoelastic stress analysis. In: Sharpe, J., William, N. (eds.) Springer handbook of experimental solid mechanics, pp. 743–768. Springer, New York (2008)
18. Soutas-Little, R.W.: Elasticity. Dover Publications, Mineola (1999)

Chapter 3
Quantitative Calorimetry and TSA in Case of Low Thermal Signal and Strong Spatial Gradients: Application to Glass Materials

Guillaume Corvec, Eric Robin, Jean-Benoît Le Cam, Pierre Lucas, Jean-Christophe Sangleboeuf, and Frédéric Canevet

Abstract In the present paper, the thermo-mechanical characterization of a holed glass sample under cyclic loading is carried out. Due to the low thermoelastic response obtained for such a material, the thermal movie has been preliminary filtered. The experimental stress field obtained from the Thermoelastic Stress Analysis (TSA) is well correlated to the finite element model. It validates both the use of this experimental technique to study the thermoelastic response of brittle materials and the filtering methodology. Finally, the corresponding calorimetric response has been determined by using a simplified formulation of the heat diffusion equation. This permits to quantify heat sources and to carry out energy balances.

Keywords Infrared thermography • Denoising methodology • Inorganic oxide glass • Thermoelastic stress analysis • Quantitative calorimetry

3.1 Introduction

The Thermoelastic Stress Analysis (TSA) [1, 2] and the quantitative calorimetry are non-contact techniques, which have experienced an impressive expansion since the 1980s with the development of thermal cameras. They are used to access to the thermoelastic and the calorimetric effects accompanying the deformation of materials in order to better understand and model their mechanical behavior. Most materials have already benefited from these techniques including smart memory alloys [3], aluminum alloys [4], polymers [5], composites [6–10] and elastomers [11, 12]. These materials exhibit temperature variations in the range of one degree or more. In these conditions the experimental noise does not extensively affect the measurement and basic filters can be used to detect and to quantify temperature variations.

Concerning inorganic glasses, although these materials are used in a wide range of applications due to their transparency, heat resistance, pressure resistance, and chemical resistance, their fragility and low fracture toughness prevent them from use in most mechanical components. To understand or improve their mechanical behavior, most of the studies have been carried out on the crack tip movement [13], the mechanical properties [14] or fracture [15, 16], but rarely on their thermo-mechanical properties. A possible cause of this state is that the low strain level supported by glasses, combined with their low thermal conductivity, lead to very low temperature variations during the deformation process. Hence, to the best of authors knowledge, only two studies have been dedicated to the thermal and thermo-mechanical response of inorganic glasses [17, 18].

The aim of this paper is to present strong thermal gradients measurement at the surface of a holed disc in case of low temperature variation conditions, without altering the spatial resolution of the infrared images after the filtering process. The stress fields obtained by TSA are compared to a Finite Element Method model. As the mechanical behavior is well known under such tests conditions, this allows us to validate the presented denoising methodology. Then, quantitative calorimetry analysis is carried out by computing heat sources produced and absorbed from the temperature field measured at thespecimen

---

G. Corvec (✉) • E. Robin • J.-B. Le Cam • J.-C. Sangleboeuf
Universitée de Rennes 1, Institut de Physique UMR 6251, CNRS/Université de Rennes 1, Campus de Beaulieu, Bât. 10B, 35042 Rennes Cedex, France
e-mail: guillaume.corvec@gmail.com

P. Lucas
Arizona Materials Laboratory, 4715 East Fort Lowell Rd, Tucson, AZ 85712, USA

F. Canevet
Cooper Standard France, 194 route de Lorient, 35043 Rennes, France

A. Baldi et al. (eds.), *Residual Stress, Thermomechanics & Infrared Imaging, Hybrid Techniques and Inverse Problems, Volume 8*,
Conference Proceedings of the Society for Experimental Mechanics Series, DOI 10.1007/978-3-319-62899-8_3

surface. The methodology to identify intrinsic dissipation is given. The validation of this methodology at ambient temperature is a first step towards the use of thermal field measurements on glassy materials at temperatures close to glass temperature transition.

3.2 Experimental Setup

3.2.1 Specimen Geometry and Testing Conditions

The material considered here is a soda lime glass. The sample, presented in Fig. 3.1 corresponds to a disc of 2.1 mm in thickness and 29.7 mm in diameter with three elliptical holes. The major and minor axis lengths are respectively 6 and 3 mm. The holes are oriented in relation to each other according to the major axis with an angle of 120°. The centre of the holes are 6 mm far from the disc center. The holes were cut with a water jet cutting machine. During the mechanical test, one of the holes was oriented with an angle of 27.91° according to its major axis and the loading axis.

The disc was submitted to cyclic compressive loading by means of a 5543 Instron testing machine. An overview of the experimental setup is given in Fig. 3.1. The test was conducted under a prescribed periodic triangular signal. The minimum and maximum values of the compression force are 5 N and 520 N, respectively. The sample was submitted to ten cycles at a frequency of 2.9 Hz.

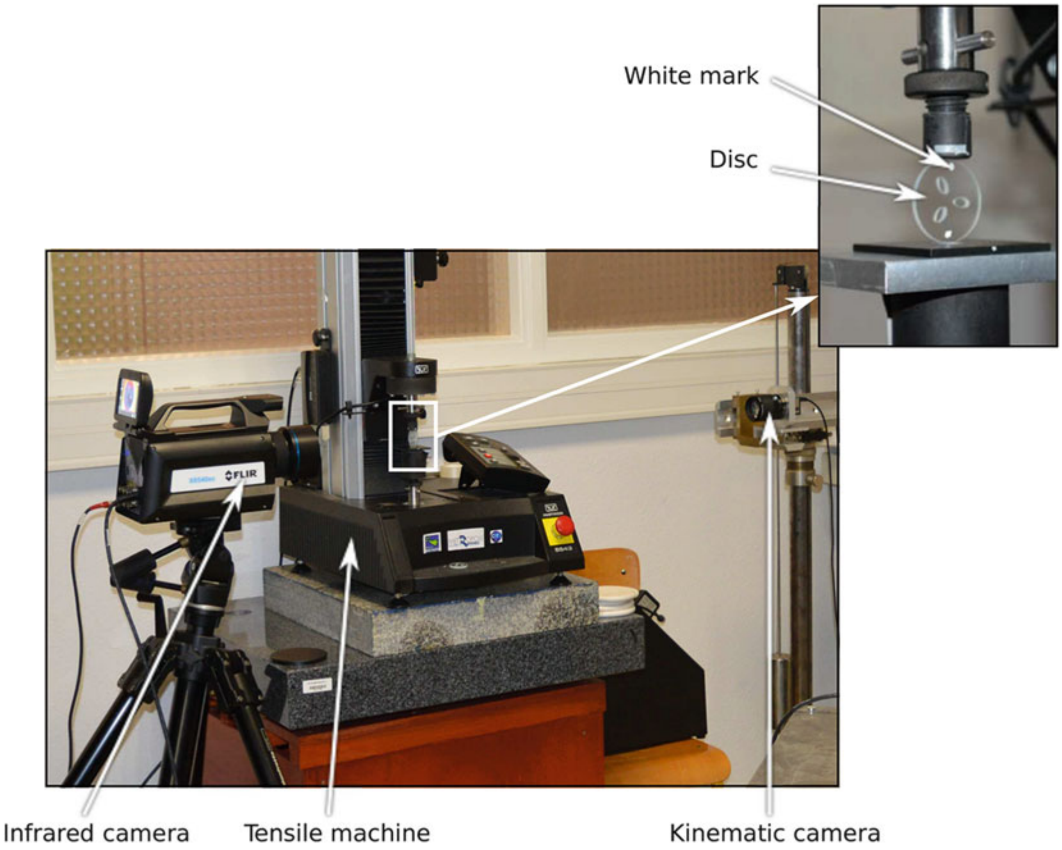

Fig. 3.1 Overview of the experimental setup

3.2.2 *Thermal Measurement*

Temperature measurements were performed at ambient temperature using a X6540sc FLIR infrared camera. It features a focal plane array of 640 × 512 pixels and detectors with a wavelength in the range of 1.5–5.1 m. The integration time was equal to 1,000 s and the acquisition frequency was set at 100 fps. The manufacturer's protocol was used to perform the Non Uniformity Correction (NUC) of the camera. The resolution of the thermal measurement is equal to 20 mK at 25 °C. The thermal emissivity of the material is close to 1 (>0.84 for soda lime glass). By adding a converter, the spatial resolution of the thermal measurement was such that the size of the pixel was equal to 63 μm. The mechanical loading was applied after the specimen temperature stabilization and the start of the temperature measurement.

3.3 Image Processing and Theoretical Background

3.3.1 *Image Processing*

Thermal expansion coefficient and the brittleness of glasses are such that their thermal activity at ambient temperature when submitted to a mechanical loading remains low. This leads to noisy thermal signals. Therefore, filtering infrared images is required. To preserve the spatial resolution (i.e. no smoothing) when denoising the infrared images, a filtering methodology has been recently developed. The idea is to reduce the thermal movie spatio-temporal filter to a purely temporal approach, considering all the pixels independent from one another. From a general point of view, this method requires to track each material point to measure its temperature. However, in the case of inorganic glasses submitted to a mechanical loading, the deformation is sufficiently low to assume that the temperature measurements are not affected by the displacement of the material points observed by the camera at the sample surface. In the present study, this assumption was validated with the help of a mark tracking method. The results showed that the displacements of a tracked mark painted at the sample surface, in a zone where they are supposed to be the highest, were lower than the spatial resolution of the thermal camera. As the material elasticity is linear and that temperature variations are proportional to stress variations, temperature variation and displacement evolve in the same way. As displacement measurement is less noisy than temperature variation measurement, the characteristics of the denoising filter applied to the temperature variation field are defined from the spectral analysis of the displacement signal. The temperature variation field was filtered with a short time fast Fourier transform (STFFT) by selecting the background and the first two harmonics of the displacement signal. The residual offset of each pixel was then identified and removed by using physically motivated considerations. Further details are provided in [19].

3.3.2 *Thermoelastic Stress Analysis (TSA)*

The TSA approach permits to link temperature and stress variations. Stress variation corresponds to change in the sum of principal Cauchy stresses $tr(\sigma)$, which corresponds to three times the hydrostatic stress. The thermomechanical framework of the TSA is described following the formalism introduced in [20]. Considering the heat diffusion equation in the case of a flat thin inorganic glass sample, the following assumptions can be made:

- The Fourier's law is used to model the heat conduction,
- The heat conduction is isotropic,
- The external heat sources, the density and the heat capacity are constant over the duration of the test,
- The intrinsic dissipation due to irreversibilities such as internal friction or damage are negligible.

These hypotheses lead to the fallowing equation:

$$\Delta\theta = -Atr\,(\sigma) \tag{3.1}$$

where θ $(=T-T_{ref})$ and $tr(\sigma)$ are respectively the temperature variation and the sum of principal Cauchy stresses. The variables range is represented by the Δ symbol. A is the so-called thermoelastic coefficient and is equal to $\alpha T_0/\rho C_{\mathrm{E,V_k}}$ where α is the thermal expansion coefficient, T_0 is the mean temperature of the specimen, ρ is the density and $C_{\mathrm{E,V_k}}$ the specific heat at constant E and V_k. E and V_k are respectively the strain tensor and other internal variables. TSA gives rise to numerous applications in the field of thermoelastic stress analysis. The reader can refer to [2, 21] for further information. For the material considered in this study, parameter A is equal to 1.341 10^{-3} *K/MPa* at 25 °C.

3.3.3 *Simplified Heat Diffusion Equation*

- Let us now assuming that no thermal conductivity occurs through the sample thickness,
- The loading frequency is sufficiently high to ensure quasi-adiabatic conditions, so that both conduction and convection can be neglected,
- The thermal diffusion length is lower than the spatial variations of stress in the disc,
- The ambient temperature remains constant during the test.

In such conditions, the heat diffusion equation is given by:

$$\rho \mathrm{C}_{\mathrm{E,V_k}} \left(\dot{\theta} + \frac{\theta}{\tau} \right) = \mathrm{s} \tag{3.2}$$

where τ is a time constant estimated by measuring the return to the thermal equilibrium of the material. To estimate heat sources s produced by the material, the procedure consists in calculating the left-hand side of Eq. 3.2 by processing the temperature variation fields. It should be noted that intrinsic dissipation (d_I) should be produced by the material. In this case the right hand side of Eq. 3.2 writes: $s + d_I$.

3.4 Results and Discussion

3.4.1 *Stress Field*

To determine the stress field from the temperature variation field, a short-time fast Fourier transform was used. The change of the sum of principal stresses was then calculated with the help of Eq. 3.1 applied at each pixel. It is signed using the following equation:

$$\Delta tr(\sigma)_{signed} = \Delta tr\,(\sigma) \times \left(-\frac{|\theta|}{\theta} \right) \tag{3.3}$$

A finite element model of the holed disc has been performed with Abaqus software. 38,277 finite elements C3D8R (52,084 nodes) have been used. The thickness of the disc has been discretized with 3 finite elements. The elastic parameters, Young modulus and Poisson coefficient, were set at 70 GPa and 0.2, respectively. A 520 N compressive loading was applied on the disc by the circular analytical surfaces. The numerical and experimental results are compared in Figs. 3.2 and 3.3. Figure 3.2 depicts the hydrostatic pressure field while Fig. 3.3 presents the value of the hydrostatic pressure along a section between the contact zones.

These results highlight the very good correlation between experimental and numerical approaches, both from spatial and quantitative point of view. Since the elastic mechanical behavior of materials is well known this validates the present experimental approach. This means that this denoising methodology could be used to characterize the non-predictable mechanical state at the surface of glasses under complex loading conditions, especially for temperature close to glass transition.

3.4.2 *Heat Source Field Reconstruction*

The heat source field has been reconstructed from temperature variation field and the simplified heat diffusion equation (see Eq. 3.2). Figure 3.4 presents the heat source map obtained for an image corresponding to a time when the heat sources reach a maximum.

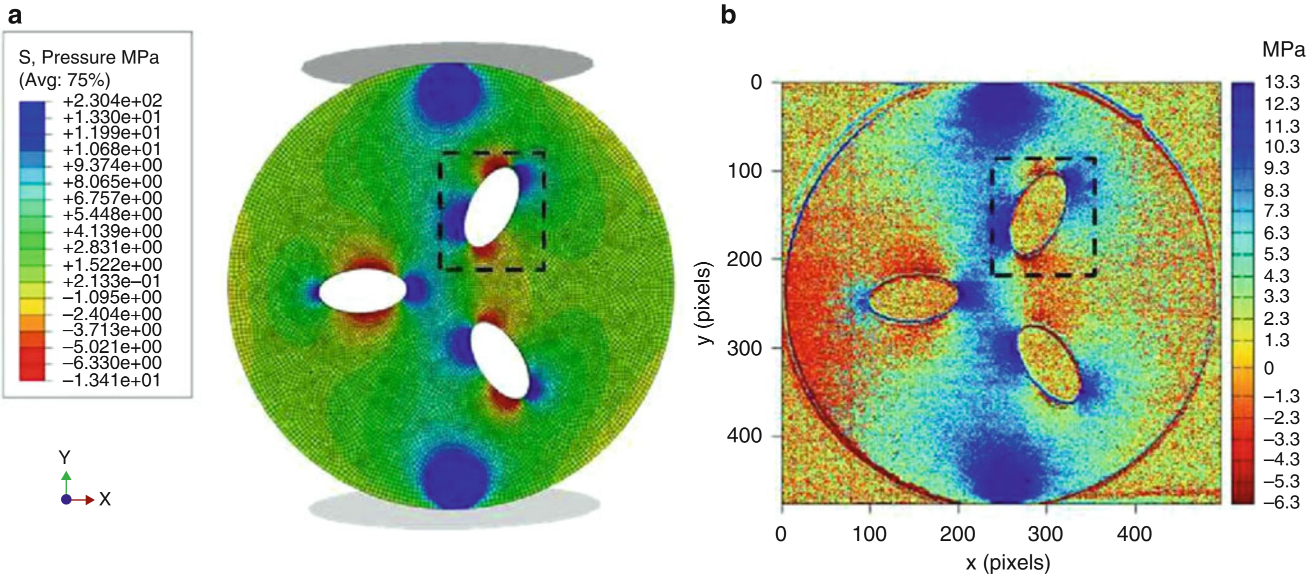

Fig. 3.2 Numerical (**a**) and experimental (**b**) fields of hydrostatic pressure

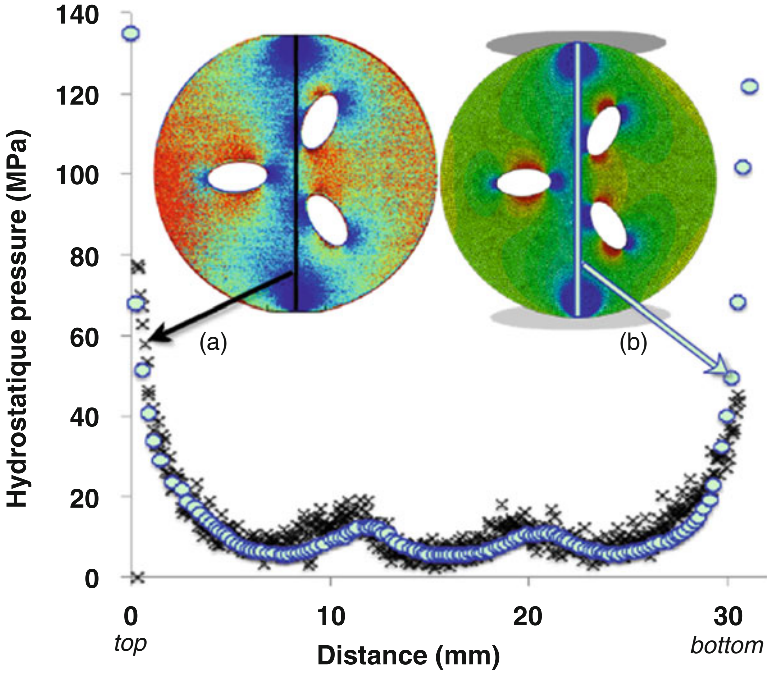

Fig. 3.3 Experimental (**a**) and numerical (**b**) value of the hydrostatic pressure along a profile defined between the contact zones

Figure 3.5a, b show the heat source variation at points A, B, C and D reported in Fig. 3.4. For each of them, heat sources oscillate around zero, meaning that no mechanical dissipation occurs. This is consistent with the fact that glass behaves as thermoelastic material at ambient temperature. The maximum value of the heat source is obtained at point A (>1.5 °C/s), located in the contact zone. Point D, located at the disc centre, far from the geometrical singularities induced by elliptical holes, exhibits very low heat source variations (<0.25 °C/s). In the vicinity of one of the elliptical holes, at point B and C, the heat sources oscillate in phase but with opposite signs.

Results obtained in terms of heat source variation enable us to calculate the mechanical dissipation by subtracting the heat absorbed to the heat produced over one mechanical cycle. An average over several cycles can be done to increase the resolution of the calculation. Obviously in the present case, the mechanical dissipation was found to be nul, but the final aim is to apply this methodology to characterize the occurrence of mechanical dissipation when the ambient temperature is increased.

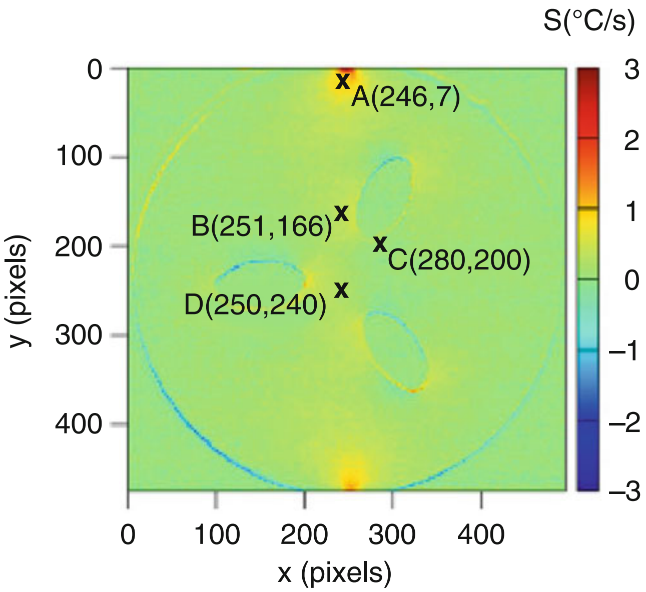

Fig. 3.4 Heat source field at a given time

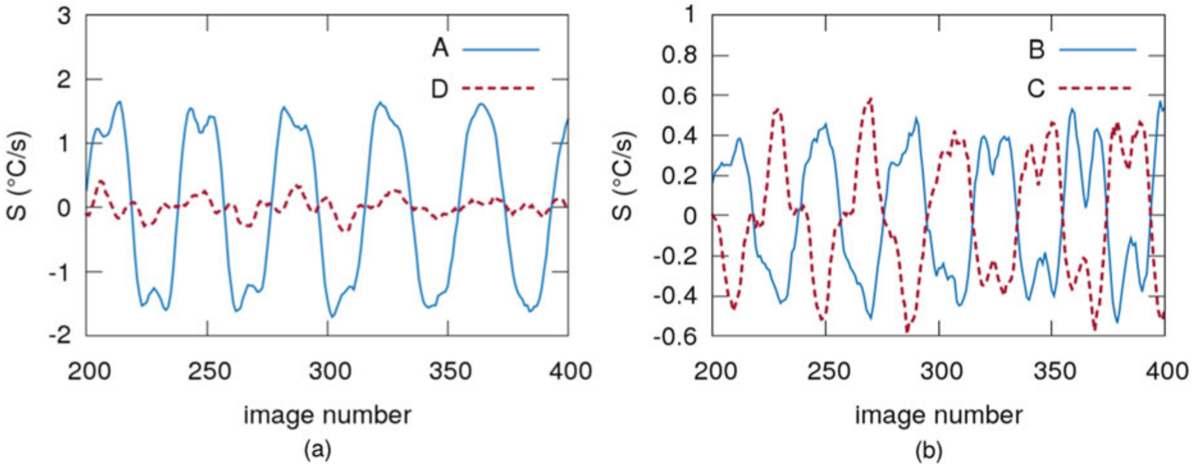

Fig. 3.5 Heat source variation (**a**) at points A and D (**b**) at points B and C

3.5 Conclusions

Thermomechanical characterization of a brittle material has been performed in the case of thermal signals of low amplitude and stress concentrations due to geometrical singularities. A disc of glass containing three elliptical holes has been submitted to a cyclic compressive load to investigate stress and strain concentration. Full thermal field measurement has been performed by using infrared thermography during cyclic loading. The temperature variation images stored during the test were denoised by using a methodology that permits to keep the spatial resolution equal to 1. The framework of the TSA was applied to map the stress field at the surface of the specimen. Experimental results were quantitatively compared with numerical simulation issued from a finite element analysis, which serves as validation of the experimental methodology to process stresses from temperature measurements. Finally, the calorific response of the material has been determined from the heat diffusion equation and the temperature variation field. Its spatial resolution was also equal to 1 pixel. This method should permit to identify mechanical dissipation in case of complex loading conditions, i.e. for which no prediction is possible, as those encountered when the temperature is increased close to the glass transition temperature and the mechanical field is heterogeneous.

Acknowledgements This work has received the financial support of AIS Scientific Grant from Rennes Métropole (2012), Mission of Resources and Skills Technology (MRCT) Grant from French National Center for Scientific Research (2012), Mission for Interdisciplinary(MI) Grant from French National Center for Scientific Research (2013), the Doctoral Politic Grant from Rennes 1 University.

References

1. Baker, L.R., Webber, J.M.B.: Thermoelastic stress analysis. Opt. Acta: Int. J. Opt. **29**(4), 555–563 (1982)
2. Dulieu-Barton, J.M., Stanley, P.: Development and application of thermoelastic stress analysis. journal of strain analysisfor engineering design. J. Strain Anal. Eng. Des. **33**, 93–104 (1998)
3. Chrysochoos, A., Licht, C., Peyroux, R.: Une modlisationthermomcanique unidimensionnelle de lapropagation d'un front de changement de phase dans un monocristal d'AMF. C. R. Mcanique. **331**, 25–32 (2003)
4. Delpueyo, D., Balandraud, X., Grédiac, M.: Calorimetric signature of the Portevin-Le Chatelier effect in an aluminumalloy from infrared thermography measurements and heat source reconstruction. Mater. Sci. Eng: Struct. Mater. Prop. Microstruct. Process. **651**, 135–145 (2016)
5. Chrysochoos, A.: Thermomechanical analysis of the cyclic behavior of materials. Procedia IUTAM. **4**, 15–26 (2012)
6. Dulieu-Barton, J.M., Fruehmann, R.K., Quinn, S.: A full-field stress based damage assessment approach for in-situ inspection of composite structures. Key Eng. Mater. **569–570**, 3–10 (2013)
7. Emery, T.R., Dulieu-Barton, J.M.: Thermoelastic stress analysis of damage mechanisms in composite materials. Compos. Pt. A-Appl. Sci. Manuf. **41**, 1729–1742 (2010)
8. Fruehmann, R.K., Wang, W., Dulieu-Barton, J.M., Quinn, S.: The application of thermoelastic stress analysis to evaluate debond damage in composite sandwich structures. In: Advances in experimental mechanics Viii, vol. 70, pp. 470–475. Applied Mechanics and Material, Trans Tech Publications, Switzerland (2011)
9. Wang, W., Martakos, G., Dulieu-Barton, J.M., Andreasen, J.H., Thomsen, O.T.: Fracture behaviour at tri-materialjunctions of crack stoppers in sandwich structures. Compos. Struct. **133**, 818–833 (2015)
10. Waugh, R.C., Dulieu-Barton, J.M., Quinn, S.: Modelling and evaluation of pulsed and pulse phase thermographythrough application of composite and metallic case studies. Ndt& E Int. **66**, 52–66 (2014)
11. Samaca Martinez, J.R., Le Cam, J.-B., Balandraud, X., Toussaint, E., Caillard, J.: Thermal and calorimetric effectsaccompanying the deformation of natural rubber. part 2: quantitative calorimetric analysis. Polymer. **54**, 2727–2736 (2013)
12. Samaca Martinez, J.R., Le Cam, J.-B., Balandraud, X., Toussaint, E., Caillard, J.: Thermal and calorimetric effectsaccompanying the deformation of natural rubber. part 1: thermal characterization. Polymer. **54**, 2717–2726 (2013)
13. Weichert, R., Schönert, K.: Heat generation at the crack tip of a moving crack. J. Mech. Phys. Solids. **26**, 151–161 (1978)
14. Pouvreau, C., Drissi-Habti, M., Michel, K., Bureau, B., Sangleboeuf, J.-C., Boussard-Pledel, C., Rouxel, T., Adam, J.-L.: Mechanical properties of a tasfiber: a preliminary study. J. Non-Cryst. Solids. **316**(1), 131–137 (2003)
15. Swain, M.V., Metras, J.C., Guillemet, C.G.: A deformation and fracture mechanics approach to the scoring and breaking of glass. J. Non-Cryst. Solids. **38–39**(Part 1), 445–450 (1980)
16. Guin, J.-P., Wiederhorn, S.M.: Crack growth threshold in soda lime silicate glass: role of hold-time. J. Non-Cryst. Solids. **316**(1), 12–20 (2003)
17. Le Cam, J.-B., Robin, E., Balandraud, X., Toussaint, E.: A new experimental route in thermomechanics of inorganic glasses using infrared thermography. J. Non-Cryst. Solids. **366**, 64–69 (2013)
18. Robin, E., Le Cam, J.-B., Balandraud, X., Toussaint, E., Brilland, L.: First steps towards thethermomechanical characterization of chalcogenide glass using quantitative infrared thermography. J. NonCryst. Solids. **391**, 101–105 (2014)
19. Corvec, G., Robin, E., Le Cam, J.-B., Sangleboeuf, J.-C., Lucas, P.: Improving spatio-temporal resolution of infraredimages to detect thermal activity of defect at the surface of inorganic glass. Infrared Phys. Technol. **77**, 193–202 (2016)
20. Nguyen, Q.S., Germain, P., Suquet, P.: Continuum thermodynamics. J. Appl. Sci. **50**, 1010–1020 (1983)
21. Sathon, N., Dulieu-Barton, J.M.: Evaluation of sub-surface stresses using thermoelastic stress analysis. Appl. Mech. Mater. **7/8**, 153–158 (2007)

Chapter 4
A New Denoising Methodology to Keep the Spatial Resolution of IR Images Equal to 1 Pixel

Guillaume Corvec, Eric Robin, Jean-Benoît Le Cam, Jean-Christophe Sangleboeuf, and Pierre Lucas

Abstract This paper proposes a noise suppression methodology to improve the spatio-temporal resolution of infrared images. The methodology is divided in two steps. The first one consists in removing the noise from the temporal signal at each pixel. In the second step, the residual offset is identified by considering thermal images for which no mechanical loading is applied. In this case, the temperature variation field is homogeneous and the value of temperature variation at each pixel is theoretically equal to zero. The method is first tested on numerical images. The results demonstrate that this approach permits to keep the spatial resolution of infrared images equal to 1 pixel. The methodology is then applied to characterize thermal activity of a defect at the surface of inorganic glass submitted to cyclic mechanical loading.

Keywords Infrared thermography • Denoising • Experimental mechanics • Soda lime glass • Indentation

4.1 Introduction

Thermal and calorimetric effects accompanying the deformation of materials are widely studied in literature to investigate thermomechanical couplings, fatigue and failure, non-exhaustively. Infrared thermography has proved to be a relevant technique for studying engineering materials such as steel, aluminum and composites. Experiments in this field consist in applying a mechanical loading and in measuring the temperature field induced at the material surface using an infrared camera. Temperature variation field is generally processed from temperature field to determine hydrostatic stress field by using thermoelastic stress analysis (TSA) [1], to investigate calorimetric response of materials or to access mechanical dissipation [2]. The results obtained provide information of importance for the understanding of deformation and damage mechanisms such as Luder's bands [3], fatigue [4, 5] strain localization [6] or strain-induced crystallization [7, 8]. In such conditions noise pollution does not alter significantly the measured temperature variation field and can be removed with the help of non-uniformity [9] correction of the infrared detector combined with a spatio-temporal filtering process. If the signal-to-noise ratio of infrared images in terms of temperature variation becomes low, processing infrared images is more complicated. Recent work has been carried out on this topic to characterize temperature variation gradients induced during a cyclic three points bending test applied to soda lime glass [10] and during cyclic compression test applied to a chalcogenide glass disk with a hole [11]. It is all the more complicated if higher gradients are induced during the mechanical loading. For example in the imprint zone after identation process [12], the use of an average filter in these conditions can smooth or remove the thermal activity. The present study aims at proposing a methodology to significantly improve the spatio-temporal resolution of thermal images in challenging conditions.

G. Corvec • E. Robin (✉) • J.-B. Le Cam • J.-C. Sangleboeuf
Université de Rennes 1, Institut de Physique UMR 6251, CNRS/Université de Rennes 1, Campus de Beaulieu,
Bât. 10B, 35042, Rennes Cedex, France
e-mail: eric.robin@univ-rennes1.fr

P. Lucas
Arizona Materials Laboratory, 4715 East Fort Lowell Rd, Tucson, AZ 85712, USA

A. Baldi et al. (eds.), *Residual Stress, Thermomechanics & Infrared Imaging, Hybrid Techniques and Inverse Problems, Volume 8*,
Conference Proceedings of the Society for Experimental Mechanics Series, DOI 10.1007/978-3-319-62899-8_4

4.2 Image Processing Methodology

After performing the Non Uniformity Correction [13, 14] and once the mechanical tests starts and infrared images are stored, image denoising algorithms consist classically in applying a spatio-temporal filtering: one dimension in time, two dimensions in space. In this case, the spatial resolution cannot be a priori equal to 1 pixel. This is why we propose to perform image processing in two steps. At first, images are filtered only temporally (at this step1 the user can use any type of filter) and the second step consists in spatial treatment of images. We propose to use one way of investigation based on the thermodynamic principle that if no mechanical loading is applied, no temperature variation can be observed. Typically, for images stored just before starting the mechanical test, the temperature variation field must be homogeneous and equal to zero. Therefore, residual offsets can be identified from these images, and removed for each thermal pixel. In practice the process leading to residual offset removing was performed by applying the following processing scheme with Matlab software:

$$M_s\left(x,y\right) = I_{step1}\left(x,y,t=t_0\right) - I_{step1}\left(x=x_0,y=y_0,t=t_0\right) \tag{4.1}$$

where $M_S(x, y)$ is the matrix of background shifting. Its components give the difference between the value at the reference pixel in reference image $I_{step1}(x, x, t = t0)$, which coordinates are i0 and j0, and the value at all the other ones. t0 is the time corresponding to the first image of the infrared movie. At t0, the value of temperature variation must be equal to zero at any pixel, since no mechanical loading is applied. Istep1 denotes the infrared image at step 1, meaning after the temporal filtering.

4.3 Numerical Evaluation of the Proposed Methodolgy

4.3.1 Noised Numerical Image Construction

The procedure consists in comparing anoriginal numerical noised image and its denoised version. However we must generate representative synthetic noise. In the case of infrared thermography, noise is due to two phenomena. The first one corresponds to photoelectric conversion and interference of signal processing circuits [15]. The second one is induced by experimental conditions, typically convection, radiations and image background. To avoid the development of models taking into account such phenomena, the noise was extracted experimentally from a repeatability test. This repeatability test was then performed at ambient temperature with a black body. The repeatability test consists in measuring the stabilized and homogeneous temperature field at the surface of a black body. Each infrared detector of the camera therefore provides a value of temperature that oscillates around the temperature of the black body. Consequently, extracting the noise means subtracting the average value of the corrupted signal to itself for each pixel. This enabled us to obtain the temporal evolution of the noise generated by the infrared camera considered in this study. The extracted experimental noise was then added to synthetic images. As the goal of this study is to keep 1 pixel spatial resolution after noise suppression, synthetic images without noise simulate local thermal activity of patterns “X”, “O” and “+” with a width set to 1 pixel (Fig. 4.1).

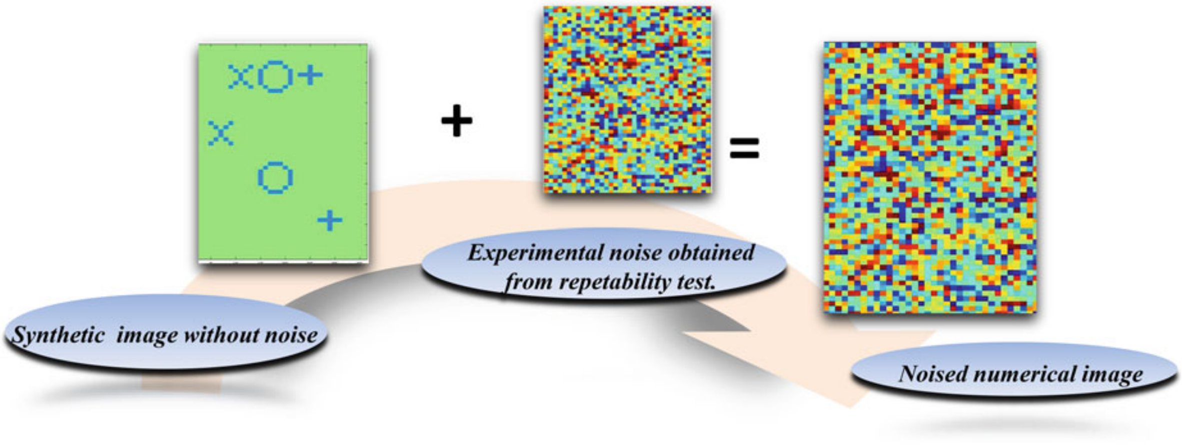

Fig. 4.1 Generation of numerical images

The thermal activity of these patterns, denoted T_{swn} evolved sinusoidally according to the following equation:

$$T_{swn}(x, y, t) = A\cos\left(\frac{2\pi}{p}(t - t_0)\right) + B \tag{4.2}$$

where A, B and p are amplitude modulation, offset and signal period, respectively. Such signal enables us to simulate thermal response of material under cyclic loading conditions. The signal amplitude modulation A was chosen to be equal to 0.05, i.e. close to temperature variation amplitude found experimentally in a previous study dealing with inorganic glass [10]. t corresponds to the image number and t_0 corresponds to the value chosen at the beginning of thermal activity. The period p corresponded to 200 frames and is related in practice to the loading frequency.

4.3.2 Denoising of Numerical Noised Images with the Proposed Method

Figure 4.2 presents result obtained with a spatio-temporal approach. More precisely a 3 × 3 × 41 average filter.

This filter is the smallest spatial one. It should be noted that this type of filter has previously been used for the detection of thermal activity in soda lime glasses [10]. It appears clearly that patterns are smoothed: crosses and diagonal lines are not distinguishable anymore. The spatial resolution is significantly altered by such a filter. Results clearly show that this type of basic filtering is not suitable to process low temperature variations combined with high temperature variation gradients. The objective is to show that even with basic temporal filters used during the first step, our methodology provides promising results in terms of spatial resolution. Denoising methodology was evaluated with these three filters:

- Average filter: In our case, a preliminary observation of thermal signal was carried out to determine a suitable kernel size which has to be lower than a quarter of the signal period. This kernel size leads to a filtered signal with sufficient modulation amplitude. Here, the kernel size was set at 41 images.
- Fitting with a polynomial form: Here, to avoid any oscillation due to noise, polynomial degree was set to 3 and the kernel size was chosen with respect to the period size, typically one-quarter of the signal period. Here, the kernel size was set at 61 images.
- Short time Fourier Transform: For each temporal signal, i.e. at each pixel, the maximum STFFT magnitude is determined. The cut-off value corresponds to the higher value of maximum STFFT magnitude field. Here, it is equal to 0.019 and the kernel size was set at 201 images.

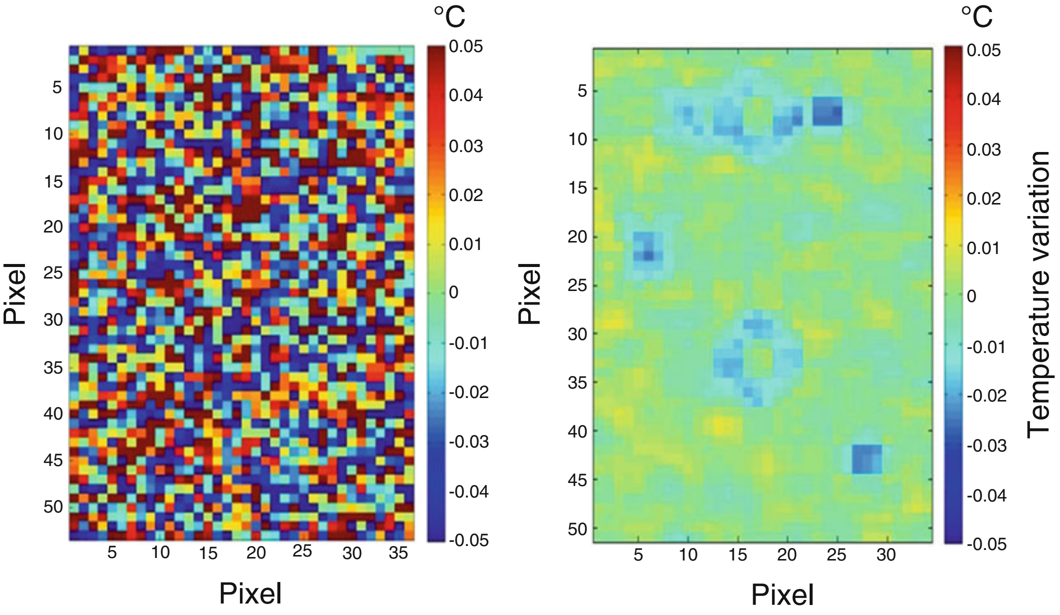

Fig. 4.2 Result obtained with a spatio_temporal approach (3×3×41)

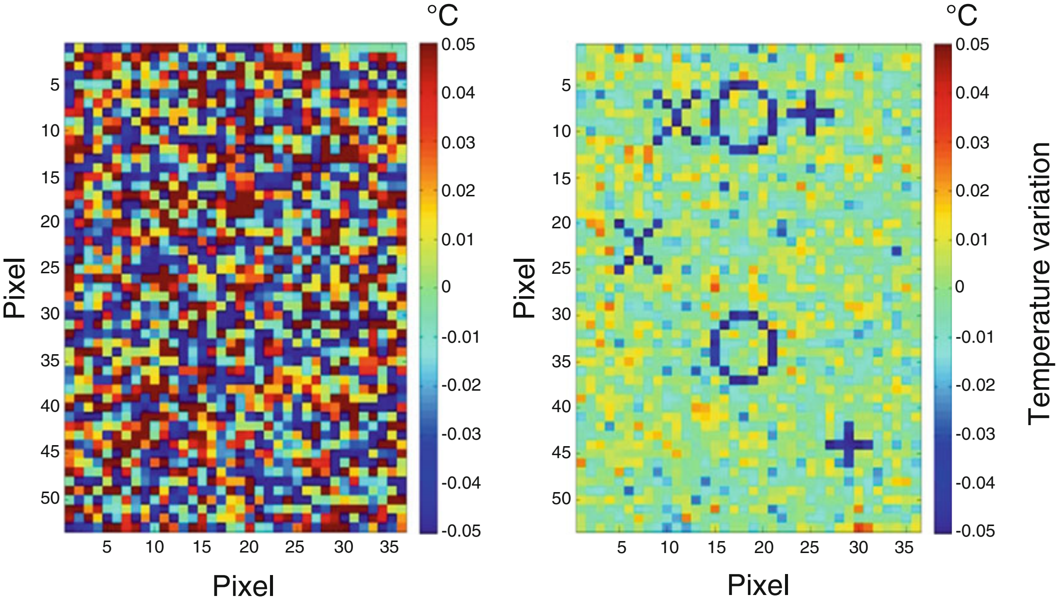

Fig. 4.3 Result obtained with an average filter during first step

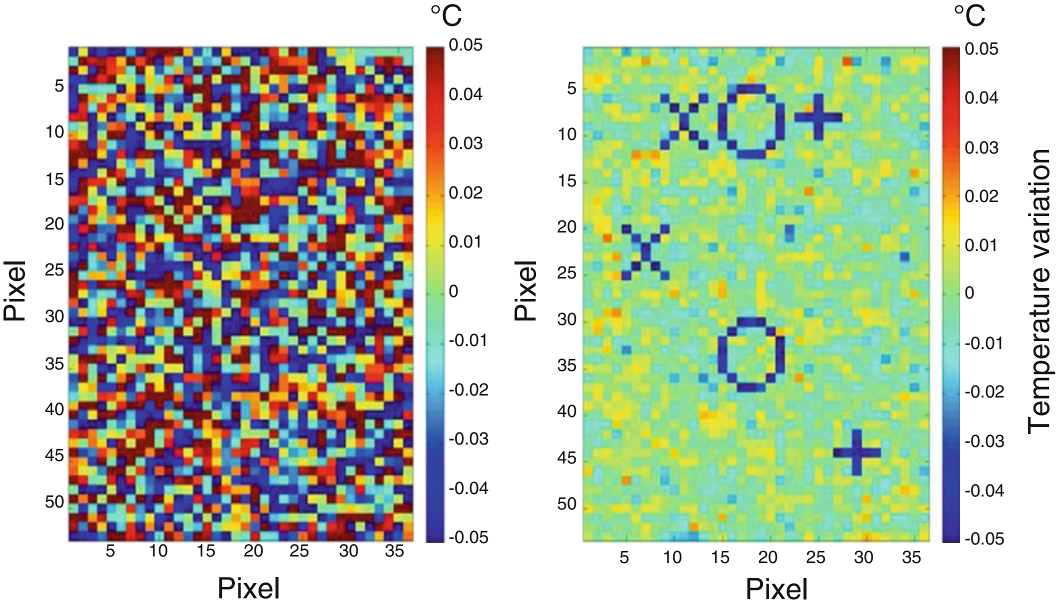

Fig. 4.4 Result obtained with a fit filter during first step

Figures 4.3, 4.4, and 4.5 gives results obtained by applying the background shifting after average, fit and STFFT temporal filtering, respectively. The pattern shape (“X”, “O” and “+”) is clearly retrieved. This demonstrates that this filtering methodology preserves the full spatial resolution of infrared images even with basic temporal filters. Nevertheless, even with the background shifting, thermal images still appear noisy after the fit filter (Figs. 4.2 and 4.3). It is due to oscillations induced by fit and average filters. In this paper, temporal filters used are basic ones. It should be noted that if the temporal filter used is more efficient and leads to very low oscillation amplitudes, the background shifting is the equivalent of removing fixed-pattern noise (FPN) [16]. The difference lies in the fact that classically FPN has a spatial structure [17–23], which is not the case here.

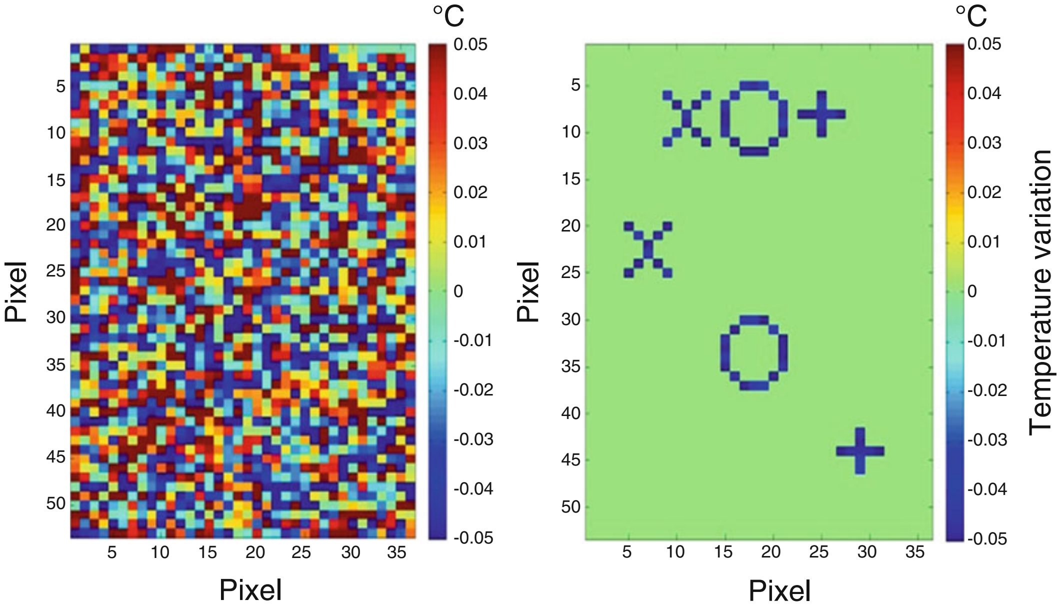

Fig. 4.5 Result obtained with a STFFT filter during first step

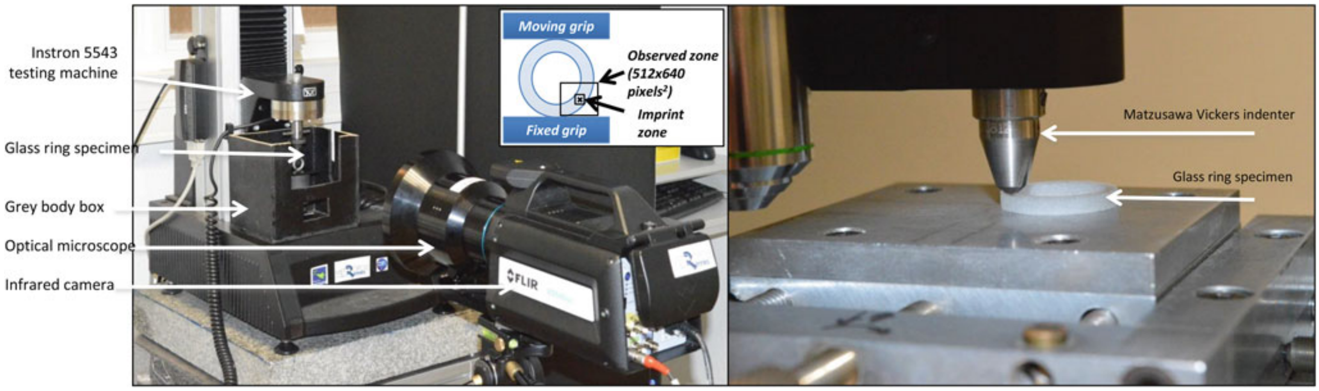

Fig. 4.6 Experimental setup

4.4 Experimental Validation: Detection of Thermal Activity Along the Chips Border After Indentation

4.4.1 Experimental Set-Up

The mechanical tests performed were based on the Brasilian test. In the case of the Brazilian test the specimen geometry is a disk while it is a ring in the present study. It is submitted to cyclic compression loading by means of a 5543 Instron testing machine. An overview of the experimental setup is given in Fig. 4.6.

The signal shape was sinusoidal. The minimum and the maximum values of the force were −7 N and −70 N, respectively. This corresponded to a displacement of 0.07 mm. The sample was submitted to fifteen cycles at a frequency equal to 3.6 Hz. Specimen geometry corresponded to a ring of soda lime glass. The specimen was 20 mm in external diameter, 13 mm in internal diameter and 2.8 mm in thickness. The ring was cut with a water jet cutting machine. An imprint was made at its surface with the help of a Matzusawa Vickers indenter. This is illustrated in Fig. 4.6. The indentation load was set to 50 N. The resulting surface defect was observed with a VHX Keyence microscope. Temperature measurements were performed at ambient temperature using the same X6540sc FLIR camera than that used for extracting the noise (section B). It features a focal plane array of 640 × 512 pixels and detectors with a wavelength range of 1.5–5.1 μm. The integration time was equal to 1,000 μs and the acquisition frequency was set at 200 fps. The resolution is equal to 20 mK at 25 °C, which is approximately

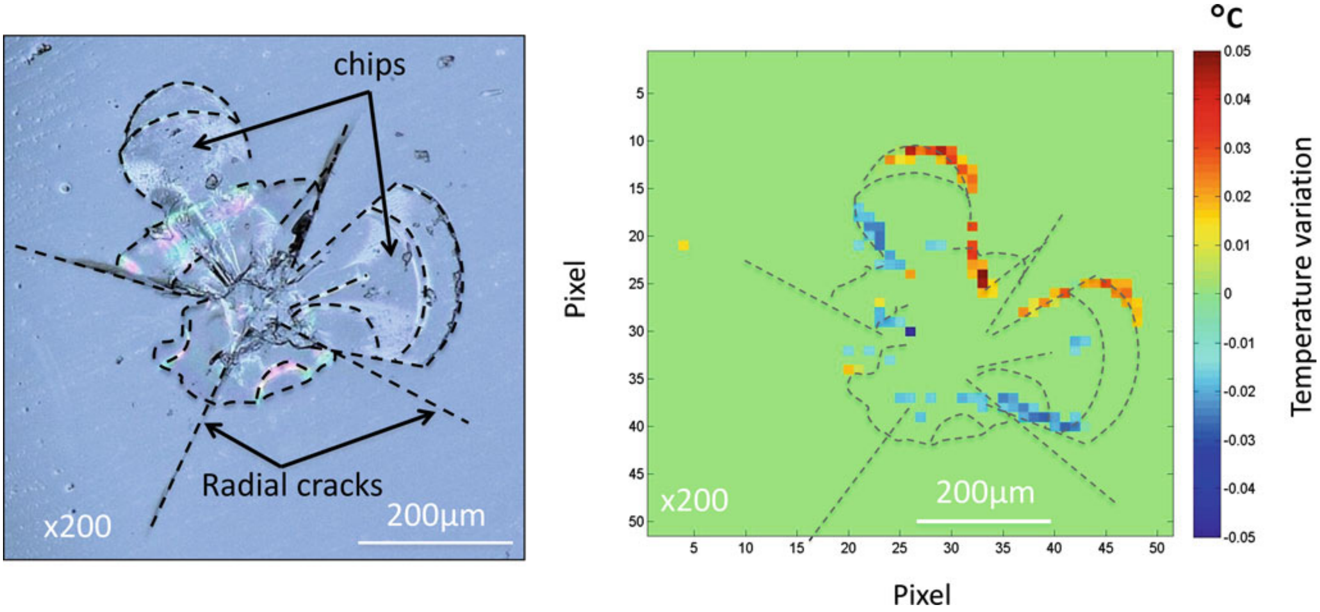

Fig. 4.7 Detection of thermal activity of imprint during a Brasilian test

equal to room temperature during the test. The thermal emissivity of the material is close to 1 (>0.84 for soda lime glass). The spatial resolution was such that the size of the pixel was equal to 0.015 mm, which is the size of the IR detectors. In order to ensure that the internal temperature of the camera was stabilized before performing the measurements, it was switched on 4 h before the experiment. Then, the Non Uniformity Correction (NUC) was performed by using the manufacturer's protocole. Once the temperature field at the specimen surface was stabilized, the temperature measurement was started.

4.4.2 Experimental Results

Figure 4.7 presents the superposition of temperature variation field obtained for the maximum of the cyclic force applied to the ring with the STFFT filter during first step.

Thermal activity was detected along the chips border, not at the tip of the radial cracks. The fact that no thermal activity was detected at the tip of the radial cracks does not mean that no stress variation occurred in these areas. Indeed, temperature variations are due to the variations of the sum of the principal Cauchy stresses, this is the basis of TSA (thermoelastic stress analysis [1]). So, if the mechanical loading induces a variation in the sum of the principal Cauchy stresses at the tip of the radial cracks, temperature variation will be detected. If the Cauchy stress tensor is mainly composed by a deviatoric part, a stress variation exists but does not induce temperature variation. In the present case, the only conclusion is that there is a variation in the sum of the principal Cauchy stresses at the chip's borders, not at the tip of the radial cracks.

4.5 Conclusion

In this study, a denoising methodology has been proposed to improve the spatial resolution of infrared images. The methodology is composed of two steps which consist first in removing the noise of the temporal signal at each pixel and second in shifting the residual offset value, which is different from one pixel to another. Results show that the approach is effective at preserving the spatial resolution of infrared images equal to 1 pixel, contrarily to the traditional spatio-temporal approach. By applying this denoising methodology to an imprint zone at the surface of a soda lime glass submitted to mechanical loading, results showed that thermal activity was detected in the chip zones. Negative and positive temperature variations were measured simultaneously, meaning that at a given time during the mechanical test, chips are submitted to very different loading conditions. The results obtained with this denoising methodology are promising and opennew ways of investigation to determine temperature variation fields in case of low signal-to-noise ratio. This is particularly valuable for understanding the thermomechanics of glassy materials, since stresses and heat sources in an imprint zone can henceforth be determined from accurate temperature field measurements.

Funding Information This work has received the financial support of AIS Scientific Grant from Rennes Métropole (2012), Mission of Resources and Skills Technology (MRCT) Grant from French National Center for Scientific Research (2012), Mission for Interdisciplinary (MI) Grant from French National Center for Scientific Research (2013), “Politiquedoctorale” Grant from Rennes 1 University (2013).

Acknowledgments The authors thank Dr. Laurent Calvez and Dr. Jean-Pierre Guin for fruitful discussions.

References

1. Dulieu-Barton, J., Stanley, P.: Development and application of thermoelastic stress analysis. journal of strain analysis for engineering design. J. Strain Anal. Eng. Des. **33**, 93–104 (1998)
2. Chrysochoos, A., Maisonneuve, O., Martin, G., Caumon, H., Chezeau, J.O.: Plastic and dissipated work and stored energy. Nucl. Eng. Des. **114**, 323–333 (1989)
3. Chrysochoos, A., Louche, H.: Thermal and dissipative effects accompanying luders band propagation. Mat Sci Eng A-struct. **307**, 15–22 (2001)
4. Berthel, B., Wattrisse, B., Chrysochoos, A., Galtier, A.: Thermoelastic analysis of fatigue dissipation properties of steel sheets. Strain. **43**, 273–279 (2007)
5. Pastor, M.L., Balandraud, X., Grédiac, M., Robert, J.L.: Applying infrared thermography to study the heating of 2024-t3 aluminium specimens under fatigue loading. Infrared Phys. Technol. **51**(6), 505–515 (2008)
6. Wattrisse, B., Chrysochoos, A., Muracciole, J., Nmoz-Gaillard, M.: Analysis of strain localization during tensile tests by digital image correlation. Exp. Mech. **41**, 2939 (2001)
7. Samaca Martinez, J.R., Le Cam, J.-B., Balandraud, X., Toussaint, E., Caillard, J.: Thermal and calorimetric effects accompanying the deformation of natural rubber. Part 1: thermal characterization. Polymer. **54**, 2717–2726 (2013)
8. Samaca Martinez, J.R., Le Cam, J.-B., Balandraud, X., Toussaint, E., Caillard, J.: Thermal and calorimetric effects accompanying the deformation of natural rubber. Part 2: quantitative calorimetric analysis. Polymer. **54**, 2727–2736 (2013)
9. Harris, J., Chiang, Y.-M.: Nonuniformity correction of infrared image sequences using the constant-statistics constraint. IEEE Trans. Image Process. **8**, 1148–1151 (1999)
10. Le Cam, J.-B., Robin, E., Balandraud, X., Toussaint, E.: A new experimental route in thermomechanics of inorganic glasses using infrared thermography. J. Non-Cryst. Solids. **366**, 64–69 (2013)
11. Robin, E., Le Cam, J.-B., Balandraud, X., Toussaint, E., Brilland, L.: First steps towards the thermomechanical characterization of chalcogenide glass using quantitative infrared thermography. J. Non-Cryst. Solids. **391**, 101–105 (2014)
12. Cook, R.F., Pharr, G.M.: Direct observation and analysis of indentation cracking in glasses and ceramics. J. Am. Ceram. Soc. **73**, 787–817 (1990)
13. Honorat V.: Analyse thermomcanique par mesure de champs des élastomères, Ph. D. thesis, Sciences et techniques du Languedoc. Montpellier, Universit Montpellier 2 (2006)
14. Poncelet M.: Multiaxiality, material and stress heterogeneities of self heating tests and high cycle fatigue tests, Ph. D. thesis, Ecolenormale-sup’erieure de Cachan -ENS Cachan (2007)
15. Scribner, D., Kruer, M., Gridley, C., Sarkady, K.: Measurement, characterization, and modeling of noise in staring infrared focal plane arrays. In: Technical Symposium Southeast, International Society for Optics and Photonics, pp. 147–160. SPIE 0782, Orlando (1987)
16. Perez, F., Pezoa, J.E., Figueroa, M., Torres, S.N.: Empirical frequency do-main model for fixed-pattern noise in infrared focal plane arrays. Infrared Phys. Technol. **67**, 413–426 (2014)
17. Schulz, M., Caldwell, L.: Nonuniformity correction and correctability of infrared focal plane arrays. Infrared Phys. Technol. **36**(4), 763–777
18. El Gamal, A., Fowler, B.A., Min, H., Liu, X.: Modeling and Estimation of fpn Components in cmos Image Sensors. International Congress Proceeding, pp. 168–177. SPIE 3301, San Jose (1998)
19. López-Alonso, J.M., Alda, J., Bernabeu, E.: Principal-component characterization of noise for infrared images. Appl. Opt. **41**(2), 320–331 (2002)
20. Zhao W., Zhang C.: Efficient scene-based non-uniformity correction and enhancement. In: Image processing, 2006 IEEE International Conference on, pp 2873–2876 (2006)
21. Zhao, W., Zhang, C.: Scene-based non-uniformity correction and enhancement: pixel statistics and subpixel motion. J. Opt. Soc. Am. A. **25**(7), 1668–1681 (2008)
22. Guadagnoli E., Giunti C., Mariani P., Olivieri M., Porta A., Sozzi B. Zatti S.: Thermal imager non-uniformity sources modeling. In: Proc. SPIE, 8014, 80140A-80140A-12 (2011)
23. Medina O.J., Pezoa J.E., Torres S.N.: A frequency domain model for the spatial fixed-pattern noise in infrared focal plane arrays. In: Proc. SPIE, 8155, 81550H-81550H-9 (2011)

Chapter 5
Calorific Signature of PLC Bands Under Biaxial Loading Conditions in Al-Mg Alloys

Jean-Benoît Le Cam, Eric Robin, Lionel Leotoing, and Dominique Guines

Abstract This paper investigates the thermomechanical behavior of Al-Mg alloys submitted to biaxial loading until fracture. The study aims to characterize calorimetric signature accompanying the formation and propagation of Portevin-Le Chatelier (PLC) bands induced by such a loading condition. Full kinematic and thermal fields on the specimen surface were characterized by using Digital Image Correlation (DIC) and infrared thermography (IRT). Heat source field was reconstructed from the temperature field and the heat diffusion equation. The heat source map enables us to visualize spatio-temporal gradients in the calorimetric response of the material and to investigate the kinematics of PLC bands induced by equibiaxial tensile loading. Under certain conditions, heat source maps can be seen as mechanical dissipation maps. At the specimen centre, the heat source exhibits jumps that fit with jumps of temperature and equivalent deformation rate.

Keywords Portevin-Le Chatelier effect • Aluminum alloy • Equibiaxial tension test • Infrared thermography • Heat source reconstruction

5.1 Introduction

Plastic instabilities take place in numerous materials, reduce material ductility and induce surface roughness, which are parameters of crucial significance in the field of sheet metal forming. The Portevin-Le Chatelier (PLC) effect is such a plastic instability and is one of the macroscopic manifestations of dynamic strain aging (DSA) [1, 2]. From a mechanical point of view, it corresponds to an irregular plastic flow and propagation of high-strain bands in the material [3, 4]. Generally, PLC effects are investigated under uniaxial tension. Very few studies focus on the occurrence of PLC under another monotonic strain path (compression [5] or simple shear [6]). Concerning the type of material used, Al-Mg alloys are some of the most studied systems [7–11], typically the AA5000 series. To our knowledge, no study has been reported in the literature on PLC effects in Al-Mg alloys under equibiaxial tension, while most metal forming operations are carried out under these loading conditions. Furthermore, plastic deformation in metals leads to the dissipation of the main part of the mechanical energy into heat. This intrinsic dissipation results in an increase of the material temperature. It is therefore relevant to investigate PLC effects in a complementary manner by measuring temperature variation at the surface of the material. Several studies in this field have been reported in the literature [6, 12–15]. In most studies, infrared cameras are used to measure the temperature field at the surface of the specimen. Nevertheless, numerous studies previously carried out by Chrysochoos et al. have shown that heat sources produced by the material itself are more relevant than temperatures for analyzing such phenomena [16–19]. The main reason is that the temperature field is influenced by heat conduction as well as heat exchanges with the ambient air and the grips of the testing machine. To our best knowledge, only studies [20, 21] provide heat source distributions induced by PLC effects in a metallic material, but under uniaxial tensile loading conditions.

The present paper investigates the PLC effects in Al-Mg alloy sheet under equibiaxial loading conditions by means of IR thermography measurements. Heat sources produced or absorbed by the material itself during deformation are deducted from temperature field measurements by using the heat diffusion equation. The heat source map enables us to visualize spatio-temporal gradients in the calorimetric response and to investigate the kinematics of PLC bands induced by equibiaxial tensile loading. In certain cases precisely detailed in the paper, the heat source map gives the mechanical dissipation field.

J.-B. Le Cam (✉) • E. Robin
Université de Rennes 1, Institut de Physique UMR 6251 CNRS/Université de Rennes 1, Campus de Beaulieu,
Bât. 10B, 35042, Rennes Cedex, France
e-mail: jean-benoit.lecam@univ-rennes1.fr

L. Leotoing • D. Guines
LGCGM, INSA, 20 avenue des Buttes de Coesmes, 35708, Rennes Cedex, France

A. Baldi et al. (eds.), *Residual Stress, Thermomechanics & Infrared Imaging, Hybrid Techniques and Inverse Problems, Volume 8*,
Conference Proceedings of the Society for Experimental Mechanics Series, DOI 10.1007/978-3-319-62899-8_5

5.2 Specimen Preparation and Testing Conditions

The material reviewed here is the aluminium alloy AA5086-H111. It is an Al-Mg alloy with an average magnesium weight ratio of 4 %. In order to reach high strain levels in the central zone of the specimen, a dedicated cruciform shape has been designed from finite element simulations (see Fig. 5.1a) and submitted by the present authors [22]. A progressive thickness reduction in the central zone is adopted. The central region of the specimen is manufactured by using a computer numerical control (CNC) lathe. The experimental device is a servo-hydraulic testing machine provided with four independent dynamic actuators, permitting biaxial tensile tests on cruciform specimens along two perpendicular axes. The overview of the experimental set-up is given in Fig. 5.1b. The strain path during the test can be directly controlled by the actuator motion. The results presented in this work are obtained under an equibiaxial strain state, with the same velocity of 1 mm/s for both axes.

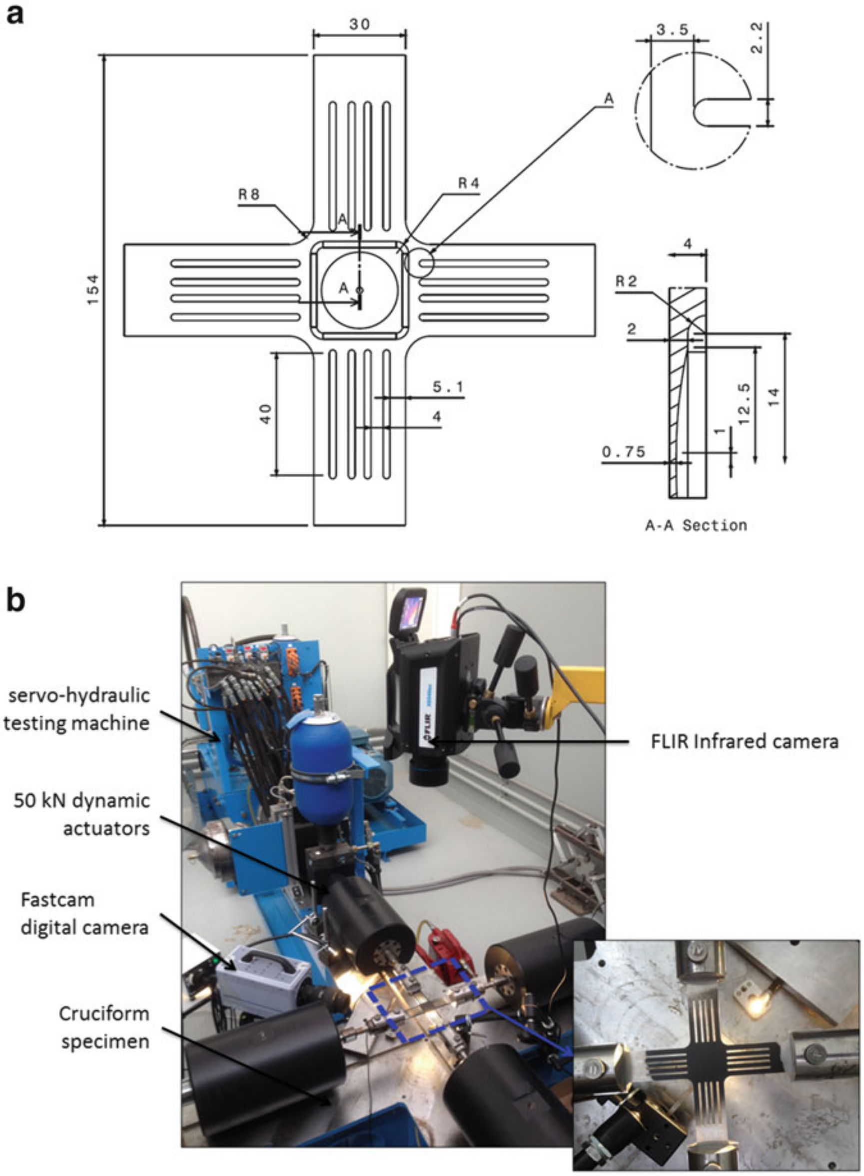

Fig. 5.1 Specimen geometry (**a**) and experimental set-up (**b**)

5.3 Full Field Measurements

5.3.1 Kinematic Field Measurement

Images of the gauge area of the cruciform specimen were recorded with a Fastcam Ultima APX-RS digital camera. As shown in Fig. 5.1b, the camera is placed perpendicularly to the surface observed. Images are obtained by using an optical mirror. The acquisition frequency is set at 250 frames per second. The spatial resolution is 0.054 mm/pixel. The DIC software CORRELA 2D was used to compute the in-plane strain field. Major and minor strains are calculated on a square area (approximately 16 × 16 mm). Equivalent strain is calculated as follows:

$$\overline{\varepsilon} = \sqrt{\frac{2}{3}\sum_{i,j}\varepsilon_{ij}^{2}}$$

where ε_{ij} are the components of the strain tensor.

5.3.2 Temperature Field Measurement

Temperature field measurements were performed using a FLIR X6540sc infrared camera, which features a focal plane array of 640 × 512 pixels and detectors with a wavelength range of 1.5–5.1 µm. Integration time was equal to 1,000 µs. The acquisition frequency was set at 250 frames per second. The NETD was equal to 20 mK at 25 °C. The camera detector calibration was performed with a black body using a Non-Uniformity Correction (NUC) procedure. Temperature variation fields were obtained by subtracting the initial temperature field (before applying mechanical loading) from the current one. The spatial resolution, corresponding to the pixel size on the measurement plane, was equal to 0.206 mm/pixel. A thin, opaque and uniform black paint was sprayed on the specimen surface to obtain a thermal emissivity close to one.

5.4 Bi-Dimensional Heat Source Reconstruction from Temperature Field Measurement

Considering the first and second principles of thermodynamics, assuming that Fourier's law is used to model heat conduction and that the heat conduction is isotropic, the 2D formulation of the heat diffusion equation writes [23]:

$$\rho C_{E,V_K}\left(\dot{\theta} + \frac{\theta + T_0 - T_{amb}}{\tau}\right) - k\Delta_{2D}\theta = s$$

where Δ_{2D} is the two-dimensional Laplace operator in the (x, y) plane. τ is the time constant, which is considered as a time constant characterizing the heat exchange with ambient air. ρ is the density, C_{E,V_K} is the specific heat at constant strain E and internal variables V_K and θ is the temperature variation.

5.5 Typical Results and Discussion

5.5.1 Mechanical Response

Figure 5.2a shows the evolution of forces during the test, along the two perpendicular directions. The first part of the curves (t ∈ [1.75; 2.2]) corresponds to the elastic deformation of the cruciform specimen and the two curves are quasi-superimposed. This means that the test was conducted under quasi-perfect equibiaxial loading conditions. In the second part of the curve (t > 2.2 s), plastic deformation starts at a corresponding force approximately equal to 2,400 N. In the plastic domain, the zoom in on the curves shows that force profiles exhibit slight fluctuations. Under tensile loading conditions, such fluctuations are the signature of type A PLC bands [4]. The gap between the values of the two forces is due to anisotropy.

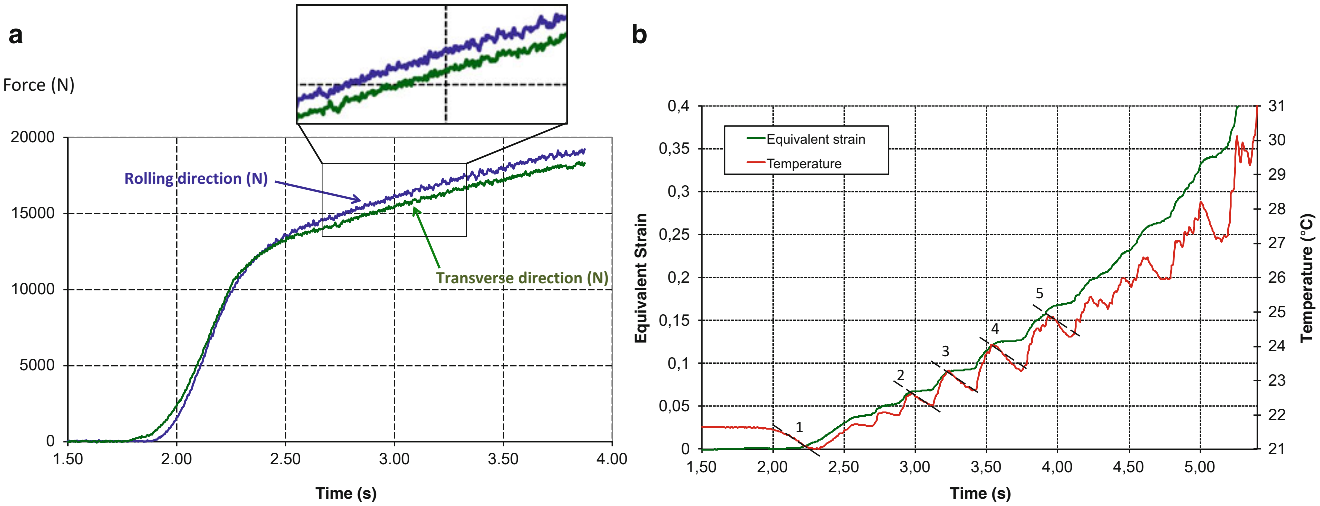

Fig. 5.2 (**a**) Mechanical response (**b**) temperature and equivalent strain evolution at the specimen centre

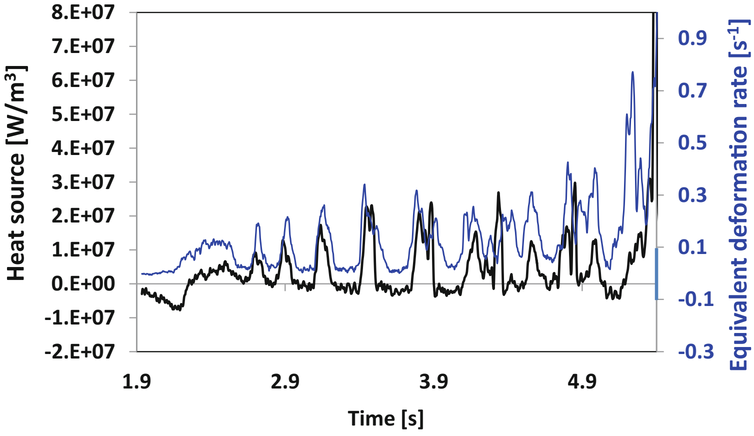

Fig. 5.3 Heat source and equivalent strain rate evolution at the specimen centre

5.5.2 *Thermal Response at the Specimen Centre*

Figure 5.2b gives the temperature variations and equivalent strain at the centre of the cruciform specimen versus time. At the very beginning of the test, strain increase leads to temperature decrease. This is typically observed in purely thermoelastic response of materials such as metallic ones. From $t = 2.3$ s on, temperature increases. Mechanical dissipation due to plasticity is produced and is of a first order compared to the thermoelastic coupling. In Fig. 5.3, equivalent strain rate alternates between low (but always positive) and high values, which forms steps in the plastic domain for the equivalent strain. When equivalent strain rate value is high, temperature strongly increases. This is the signature of PLC bands formation and propagation.

5.5.3 *Calorimetric Response at the Specimen Centre*

At the very beginning of the test, the material absorbs heat (heat source is negative). From $t = 2.2$ s on, the material continues absorbing heat but at a lower rate, since mechanical dissipation due to plasticity occurs. From $t = 2.3$ s on, heat produced due to plasticity is superior to heat absorbed due to thermoelasticity, and the heat source becomes positive. As a consequence, the temperature starts to increase. Subsequently, each jump in the equivalent strain induces a strong heat production and a jump in temperature. In terms of heat sources, the maximum value reached during the jumps increases monotonically from 5.10^6 to $3.10^7\mathrm{W/m}^3$ and more before failure. Between two strain jumps, equivalent strain rate is lower (but always positive) and corresponding average heat sources mostly negative. This proves that after PLC band passage, the material mainly deforms elastically, which mainly explains why temperature decrease after each jump. Heat diffusion also occurs but its contribution to the temperature decrease is less than 1 % of the total heat source. These results prove that temperature drops after PLC band passage are mainly due to thermoelasticity.

5.5.4 Bidimensional Heat Source Reconstruction

The kinematics of PLC bands is usually investigated under uniaxial loading conditions by using full field kinematic measurements. It is also investigated using quantitative calorimetry obtained by temperature field measurement, since these bands have a specific calorimetric signature [21]. To our knowledge, this is the first study of PLC band kinematics under equibiaxial loading condition by means of quantitative calorimetry.

Figure 5.4 presents heat source maps obtained for different jumps in terms of heat source, which corresponds to the formation and propagation of PLC bands. For each jump considered, a set of three heat source maps is given. The three maps correspond, from the bottom to the top, to the beginning, the middle and maximum value of heat source during the jump. In order to distinguish the calorimetric signature of PLC bands, the maps given are anamorphosed, i.e. the scale is given in maximum and minimum values in the considered image. Here, PLC band kinematics is studied qualitatively, this is why no bar scale is shown. Several results can be derived from these maps:

- PLC bands are highly dissipative: they clearly appear in red color in the heat source field.
- PLC bands form a cross that propagates from the specimen centre to the borders of the square zone. The cross is formed in a zone under equibiaxial loading, and branches propagate in zones of different loading condition, i.e. from equibiaxial to quasi-uniaxial strain states. Further investigations of the effects of strain path on PLC kinematics are currently carried out in our laboratory.

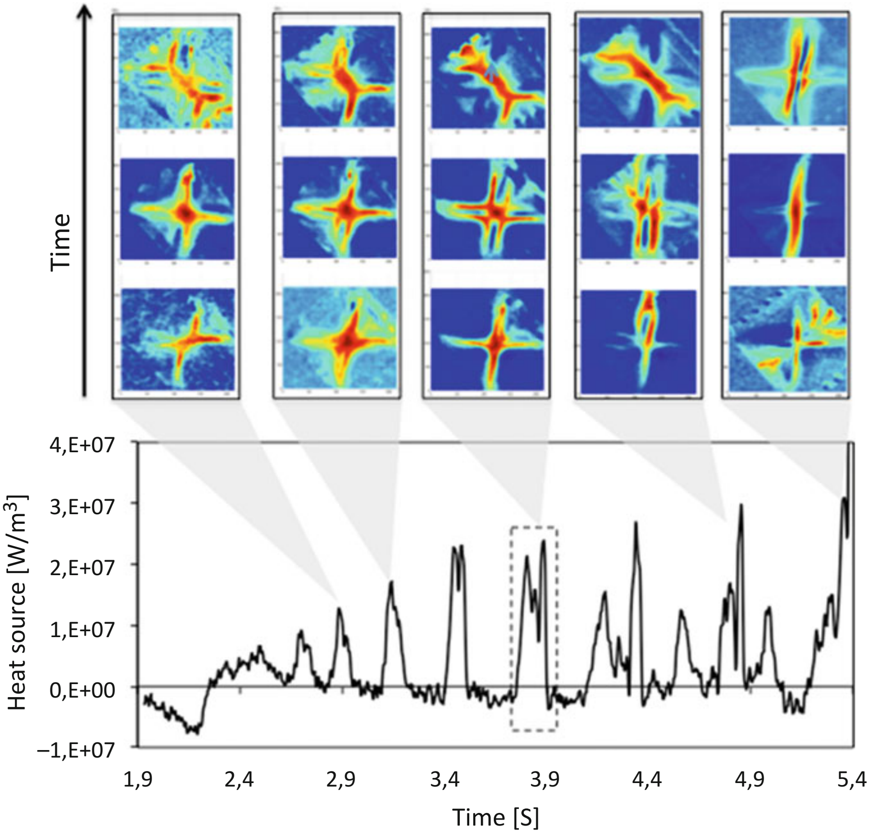

Fig. 5.4 Heat source map during different jumps

- PLC band kinematics is highly repeatable from one heat source jump to another: the same shape of PLC bands and the same angles of the formed cross are observed.
- As thermoelasticity leads to low heat absorption compared to the heat produced by PLC bands, these maps can be assumed to give mechanical dissipation field. This assumption is classically used to neglect the effect of thermoelastic coupling [16, 21]. Therefore, heat source maps can be considered as mechanical dissipation maps.

Further analyses on the PLC band kinematics have been carried out and four steps have been identified. They are precisely presented and detailed in [24].

5.6 Conclusion

This paper provides the first study on spatio-temporal distribution of heat produced by PLC bands formed under equibiaxial tensile loading. Equibiaxial tensile testing has been carried out at an ambient temperature with an Al-Mg alloy. The temperature field was measured during the test and corresponding heat sources were reconstructed by means of the bidimensional formulation of the heat diffusion equation. The heat source map enables us to visualize spatio-temporal gradients in the calorific response of the material and to investigate the kinematics of PLC bands induced by equibiaxial tensile loading, which forms dissipative waves. At the specimen centre, the heat source exhibits jumps that fit well with jumps in the equivalent deformation rate and the temperature. The results are a promising alternative of inquiry into the effects of complex loading conditions as those encountered during sheet metal forming processes on occurrence and kinematics of PLC bands. Additionally, the present study provides additional data for the development and validation of PLC band kinematic models.

Funding Information This work has received the financial support of the AIS Scientific Grant from Rennes Métropole (2012), the Mission of Resources and Skills Technology (MRCT) Grant from the French National Center for Scientific Research (2012), the Interdisciplinary Mission (MI) Grant from the French National Center for Scientific Research (2013).

References

1. Van Den Beukel, A.: Theory of the effect of dynamic strain aging on mechanical properties. Phys. Status Solidi. **30**, 197 (1975)
2. Kubin, L.P., Estrin, Y.: Acta Metall. **33**, 397 (1985)
3. Estrin, Y., Kubin, L.P., Aifantis, E.C.: Introductory remarks to the viewpoint set on propagative plastic instabilities. Scr. Metall. Mater. **29**(9), 1147–1150 (1993)
4. Jiang, H., Zhang, Q., Chen, X., Chen, Z., Jiang, Z., Wu, X., Fan, J.: Three types of Portevin-Le Chatelier effects: experiment and modelling. Acta Mater. **55**(7), 2219–2228 (2007)
5. Lebedkina, T.A., Lebyodkin, M.A.: Effect of deformation geometry on the intermittent plastic flow associated with the Portevin-Le Chatelier effect. Acta Mater. **56**(19), 5567–5574 (2008)
6. Coër, J., Manach, P.Y., Laurent, H., Oliveira, M.C., Menezes, L.F.: Piobert-Lüders plateau and Portevin-Le Chatelier effect in an al-mg alloy in simple shear. Mech. Res. Commun. **48**, 1–7 (2013)
7. Balik, J., Lukac, P.: Portevin-Le Chatelier instabilities in Al-3 Mg conditioned by strain rate and strain. Acta Metall. Mater. **41**(5), 1447–1454 (1993)
8. Fujita, H., Tabata, T.: The effect of grain size and deformation sub-structure on mechanical properties of polycrystalline aluminum. Acta Metall. **21**(4), 355–365 (1973)
9. Korbel, A., Dybiec, H.: The problem of the negative strain-rate sensitivity of metals under the Portevin-Le Chatelier deformation conditions. Acta Metall. **29**(1), 89–93 (1981)
10. Thomas, A.T.: The tensile deformation behaviour of an aluminium-magnesium alloy. Acta Metall. **14**(10), 1363–1374 (1966)
11. Li, M., Lege, D.J.: Serrated flow and surface markings in aluminum alloys. J. Eng. Mater. Technol. **120**, 48–56 (1998)
12. Coër, J., Bernard, C., Laurent, H., Andrade-Campos, A., Thuillier, S.: The effect of temperature on anisotropy properties of an aluminium alloy. Exp. Mech. **51**(7), 1185–1195 (2010)
13. Hu, Q., Zhang, Q., Cao, P., Fu, S.: Thermal analyses and simulations of the type a and type b Portevin-Le Chatelier effects in an al-mg alloy. Acta Mater. **60**(4), 1647–1657 (2012)
14. Ait-Amokhtar, H., Fressengeas, C., Boudrahem, S.: The dynamics of Portevin-Le Chatelier bands in an al-mg alloy from infrared thermography. Mater. Sci. Eng. A. **488**, 540–546 (2008)
15. Bernard, C., Coër, J., Laurent, H., Chauvelon, P., Manach, P.Y.: Relationship between local strain jumps and temperature bursts due to the Portevin-Le Chatelier effect in an al-mg alloy. Exp. Mech. **53**(6), 1025–1032 (2013)
16. Chrysochoos, A., Louche, H.: Thermal and dissipative effects accompanying luders band propagation. Mat. Sci. Eng. A Struct. **307**, 15–22 (2001)

17. Berthel, B., Wattrisse, B., Chrysochoos, A., Galtier, A.: Thermographic analysis of fatigue dissipation properties of steel sheets. Strain. **43**, 273–279 (2007)
18. Wattrisse, B., Chrysochoos, A., Muracciole, J.-M., Némoz-Gaillard, M.: Analysis of strain localization during tensile tests by digital image correlation. Exp. Mech. **41**, 29–39 (2001)
19. Chrysochoos, A., Huon, V., Jourdan, F., Muracciole, J.-M., Peyroux, R., Wattrisse, B.: Use of full-field digital image correlation and infrared thermography measurements for the thermomechanical analysis of material behaviour. Strain. **46**, 117–130 (2010)
20. Louche, H., Vacher, P., Arrieux, R.: Thermal observations associated with the Portevin-Le Chatelier effect in an al-mg alloy. Mater. Sci. Eng. A. **404**, 188–196 (2005)
21. Delpueyo, D., Balandraud, X., Grediac, M.: Calorimetric signature of the Portevin-Le Chatelier effect in an aluminum alloy from infrared thermography measurements and heat source reconstruction. Mater. Sci. Eng. A. **651**, 135–145 (2016)
22. Zidane, I., Guines, D., Leotoing, L., Ragneau, E.: Development of an in-plane biaxial test for forming limit curve (FLC) characterization of metallic sheets. Meas. Sci. Technol. **21**(5), 055701 (2010)
23. Chrysochoos, A., Louche, H.: An infrared image processing to analyse the calorific effects accompanying strain localisation. Int. J. Eng. Sci. **38**, 1759–1788 (2000)
24. Le Cam, J.-B., Robin, E., Leotoing, L., Guines, D.: Calorimetric analysis of Portevin-Le Chatelier bands under equibiaxial loading conditions in Al–Mg alloys: Kinematics and mechanical dissipation. Mech. Mater. **105**, 80–88 (2017)

Chapter 6
How Does Cristallizable Rubber Use Mechanical Energy to Deform?

Jean-Benoît Le Cam

Abstract Strain-induced crystallization (SIC) is responsible for the hysteresis loop observed in the mechanical response of Natural Rubber (NR). The present paper aims at determining the physical origin of such mechanical energy dissipation. For that purpose, temperature variations are measured by using infrared thermography during cyclic uniaxial tensile tests at ambient temperature. Heat sources (heat power densities) produced or absorbed by the material due to deformation processes are deduced from temperature fields by using the heat diffusion equation. Energy balance performed for each deformation cycle shows that crystallization/melting process does not produce intrinsic dissipation. The crystallization/melting process dissipates mechanical energy without converting it into heat. Hence, the whole dissipated mechanical energy corresponds to energy used by the material to change its microstructure. The demonstration that NR is able to dissipate mechanical energy without converting it into heat explains its ability to resist the crack growth and the fatigue loading.

Keywords Infrared thermography • Heat sources • Natural rubber • Strain-induced crystallization

6.1 Introduction

Mechanical properties of natural rubber (NR) are mainly related to Strain-Induced Crystallization (SIC) [1]. Especially, SIC enables NR to better resist the crack growth [2, 3] and the fatigue [4–7]. Clark et al. were the first to suggest experimentally that the mechanical hysteresis is closely related to SIC [8]. Up to date, the idea that mechanical hysteresis is due to the difference between the kinetics of crystallization and crystallite melting has been widely disseminated, but no further information on the origin of this mechanical dissipation has been provided. Indeed, the formation of a mechanical hysteresis is a complicated process and better understand the energetic nature of the hysteresis loop could provide information of importance on the reinforcement of NR. This paper aims at carrying out energy balances in order to identify and to evaluate the contribution of the different phenomena involved in the formation of the mechanical hysteresis in NR. For that purpose infrared thermography is used to measure the temperature evolution of specimens under quasi-static uniaxial loading at ambient temperature. Heat sources produced or absorbed by the material due to deformation processes are deduced from the temperature variations by using the heat diffusion equation. Energy balances performed at each cycle and at any time during each cycle are finally analyzed to determine the physical origin of the mechanical energy dissipation in NR.

6.2 Specimen Preparation and Testing Conditions

The material studied is an unfilled natural rubber (NR) supplied by the “Manufacture Française des pneumatiques Michelin”. It is composed of antioxidant (1.9 phr), stearic acid (2 phr), zinc oxide (2.5 phr), accelerator (1.6 phr) and sulphur (1.6 phr). The compound was cured for 22 min at 150 °C. In unfilled NR, SIC is observed in uniaxial tension starting from a stretch λ_c of about 4. During unloading, crystallite melting is complete at a lower stretch λ_m of about 3 [9–11]. The specimen geometry is 5 mm in width, 10 mm in height and 1.4 mm in thickness. Mechanical tests performed were those reported in the work by

---

J.-B. Le Cam (✉)
Université de Rennes 1, Institut de Physique UMR 6251 CNRS/Université de Rennes 1, Campus de Beaulieu,
Bât. 10B, 35042, Rennes Cedex, France
e-mail: jean-benoit.lecam@univ-rennes1.fr

A. Baldi et al. (eds.), *Residual Stress, Thermomechanics & Infrared Imaging, Hybrid Techniques and Inverse Problems, Volume 8*,
Conference Proceedings of the Society for Experimental Mechanics Series, DOI 10.1007/978-3-319-62899-8_6

Samaca Martinez, who investigated the thermal and caloric signature of the main phenomena involved in rubber deformation [12–16]. Mechanical loading was applied using a 50 N Instron 5,543 testing machine. It corresponds to four sets of three cycles, for four increasing maximum stretch ratios: $\lambda_1 = 2$, $\lambda_2 = 5$, $\lambda_3 = 6$ and $\lambda_4 = 7.5$. λ_1 was chosen inferior to λ_c, λ_2 was superior but close to λ_c, λ_3 and λ_4 are superior to λ_c. The signal shape chosen was triangular, to ensure a constant strain rate during loading and unloading. Tests were performed at a loading rate equal to ±100 mm/min and ±300 mm/min. The temperature was measured by using a Cedip Jade III-MWIR infrared camera (320×240 pixels, 3.5–5 μm).

6.3 Heat Source Calculation from Temperature Field Measurement

Considering the first and second principles of thermodynamics, assuming that Fourier's law is used to model heat conduction and that the heat conduction is isotropic, the 0D formulation of the heat diffusion equation writes [17]:

$$\rho C_{E,V_K}\left(\dot{\theta} + \frac{\theta}{\tau}\right) = s$$

where τ is considered as a time constant characterizing the heat exchange with ambient air. ρ is the density, C_{E,V_K} is the specific heat at constant strain E and internal variables V_K and θ is the temperature variation. This equation is used to process IR images and to calculate homogeneous heat source.

6.4 Typical Results and Discussion

6.4.1 Mechanical Response

Figure 6.1 presents the mechanical response obtained in terms of the nominal stress versus the stretch. The whole mechanical response is presented in the centre of the figure. The response obtained for each maximum stretch applied is given separately. First of all, whatever the maximum stretch applied, the mechanical cycles have no significant effect on the mechanical response, in the sense that no stress softening is observed. Several comments can be drawn with respect to the maximum stretches λ_i applied:

- For cycles at $\lambda_1 = 2$, a very small hysteresis loop is observed. The corresponding power density $P_{\text{inelastic}}$ is equal to 1.6 10^3 W/m^3. The energy contained in the hysteresis loop can be due to intrinsic dissipation and/or thermal dissipation and/or energy used by the material for microstructure changes,
- For cycles at $\lambda_2 = 5$ (the area of the hysteresis loop increases ($P_{\text{inelastic}} = 4.810^3$ W/m^3). The maximum stretch applied exceeds that at which crystallization starts ($\lambda_c = 4$). Again, both intrinsic dissipation and/or thermal dissipation and/or dissipation due to microstructure changes could contribute to this hysteresis loop. These results are in good agreement with those reported in the literature for unfilled natural rubber studied with X-ray diffraction: a significant hysteresis loop forms if SIC takes place in the material. Classically, the hysteresis loop is explained by the difference in the kinetics of crystallization and crystallite melting [9–11],
- For cycles at $\lambda_3 = 6$, the hysteresis loop is higher than for the previous stretches,
- For cycles at $\lambda_4 = 7.5$, a plateau is observed from $\lambda_3 = 6$ on, followed by a high stress increase. The hysteresis loop is much higher that for the stretch applied just before (4.5 10^4 W/m^3 versus 1.3 10^4 W/m^3 for the corresponding power density). As assumed by Flory [18] and highlighted by Toki et al. [9] and Trabelsi et al. [10], once crystallization occurs, relaxation is induced in the amorphous phase. The plateau observed is a manifestation of this relaxation. For higher stretches, crystallites act as fillers and strongly reinforce the material stiffness, which explains the high increase in the nominal stress. It should be noted that tensile test performed at the higher loading rate does not change the hysteresis area, meaning that thermal dissipation is negligible.

To summarize, the hysteresis loop can be due to intrinsic dissipation and/or microstructure changes only. Distinguishing these two types of energy dissipation is a main topic. The former is the signature of damage, the latter not, which is of paramount importance to explain the cyclic behaviour of NR. The next step is dedicated to the determination of the intrinsic dissipation over each cycle, i.e. the part of the mechanical energy converted into heat.

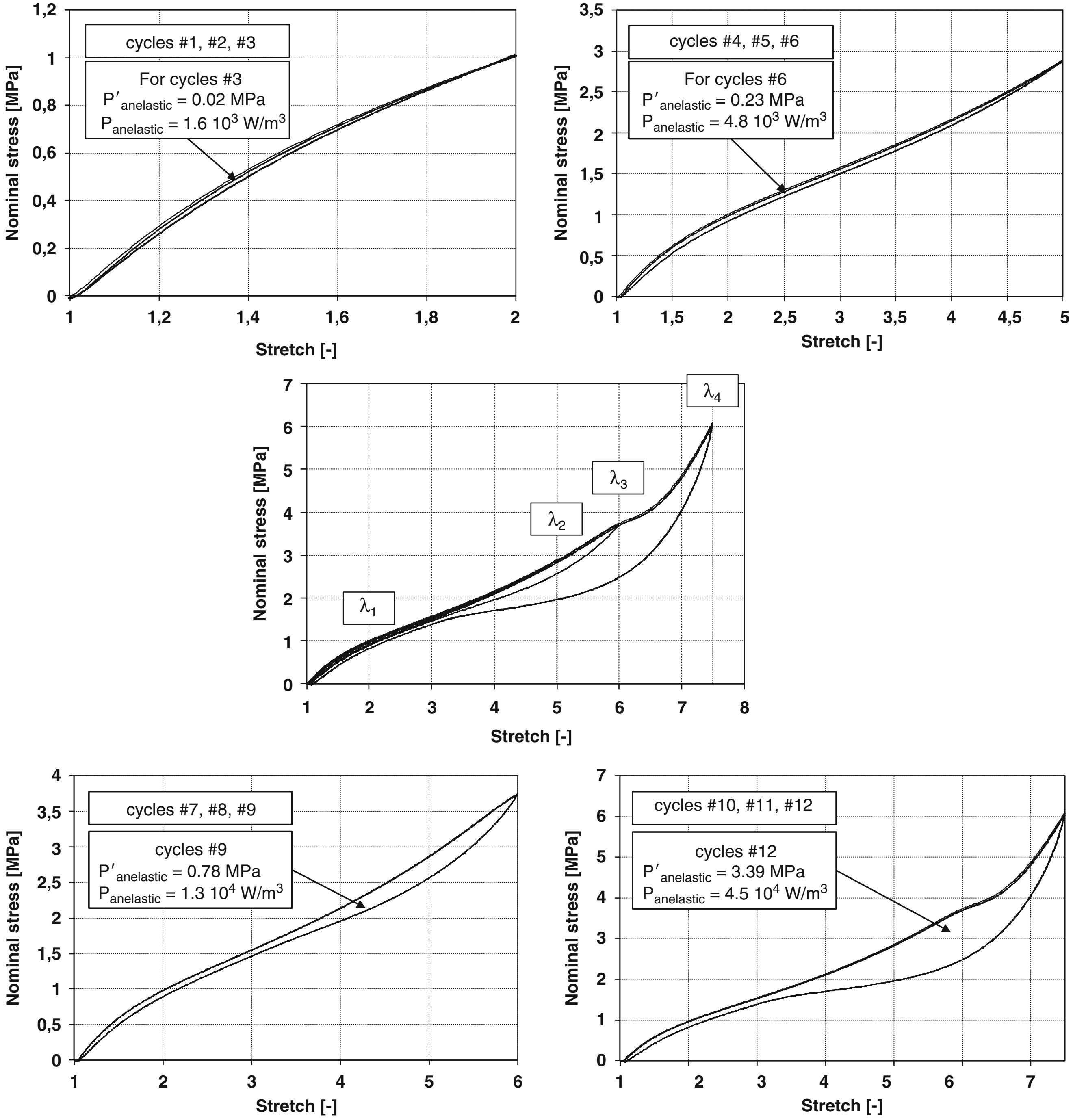

Fig. 6.1 Mechanical response

6.4.2 Calorimetric Response and Intrinsic Dissipation

Calorimetric response of NR has been established by using the simplified formulation of the heat diffusion. It should be noted that parameter τ was identified from natural return at ambient temperature for different stretches. Its expression was $\tau(\lambda) = 40.48–3.25\lambda$. Figure 6.2 gives the heat source as a function of the stretch during the cycles of each set of maximum stretch, for a loading rate equal to ± 100 mm/min. Integrating the heat source over one cycle provides the energy corresponding to the intrinsic dissipation $W_{\text{intrinsic}}$. The intrinsic dissipation d_1 is obtained by dividing $W_{\text{intrinsic}}$ by the

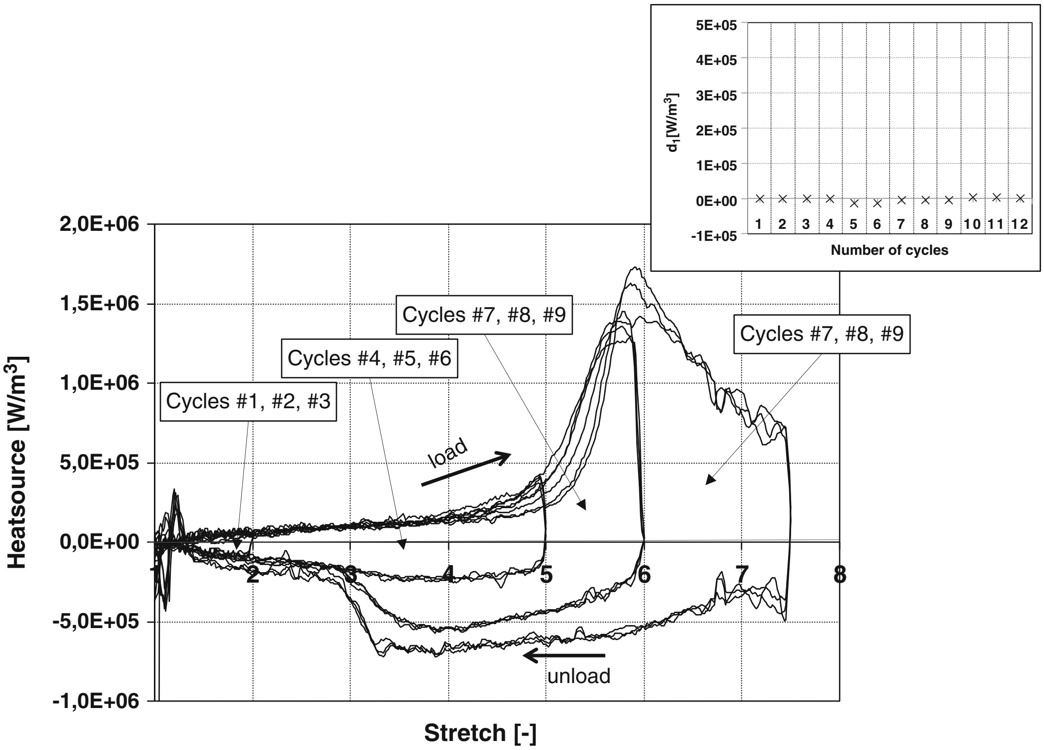

Fig. 6.2 Heat sources

considered cycle duration. Typically in polymers, d_1 is the calorimetric signature of viscosity or damage (see the calorimetric characterization of viscosity and stress softening induced by carbon black fillers in SBR [13]).

Several comments can be drawn from this figure, with respect to the maximum stretch applied:

- For cycles at $\lambda_1 = 2$, the heat source is positive during loading and increases with the stretch. During unloading, the heat source is negative. This is due to entropic elasticity that is preponderant in the thermal response of the stretched material. The load-unload evolution is symmetrical, meaning that the heat produced during loading phase is equal to the heat source absorbed during unloading phase. Therefore, no intrinsic dissipation is detected,
- For cycles at $\lambda_2 = 5$, the heat source evolutions for loading and unloading are not symmetrical anymore. This cannot be explained by entropic elasticity. During loading, the heat source evolves in a quasi-linear manner until reaching a stretch close to 4. This evolution can be explained by entropic coupling. The dissymmetry takes place for stretches higher than 4, the stretch level at which SIC starts. Moreover, the areas under the curves during loading and unloading are equal, meaning that no intrinsic dissipation is produced (see the diagram at the top, on the right side). Consequently, the only explanation for the dissymmetry is the occurrence of crystallization during loading, and a difference in the kinetics of crystallization and crystallite melting. This is in a good agreement with studies reported in the literature [9–11]. Concerning the stress-strain curve, a hysteresis loop larger than for $\lambda_1 = 2$ is observed. If thermal dissipation and intrinsic dissipation are negligible, this means that the area of the hysteresis loop corresponds to mechanical energy used by the material for crystallization and crystallite melting,
- For cycles at $\lambda_3 = 6$, the heat source first increases with the same slope as before, and then strongly increases starting from a stretch close to 4. The loading-unloading dissymmetry level of the heat source curves increases. Again, the heat produced is equal to the heat absorbed, meaning that no mechanical dissipation is detected,
- For cycles at $\lambda_4 = 7.5$, the phenomena are similar to those observed above, except for the evolution of the heat source for stretch ratios superior to 6. Indeed, during the loading phase, instead of increasing continuously, the heat source decreases from $\lambda_3 = 6$. This means that heat due to crystallization could continue to be produced (it remains positive), but at a lower rate, and/or that larger energetic effects take place.

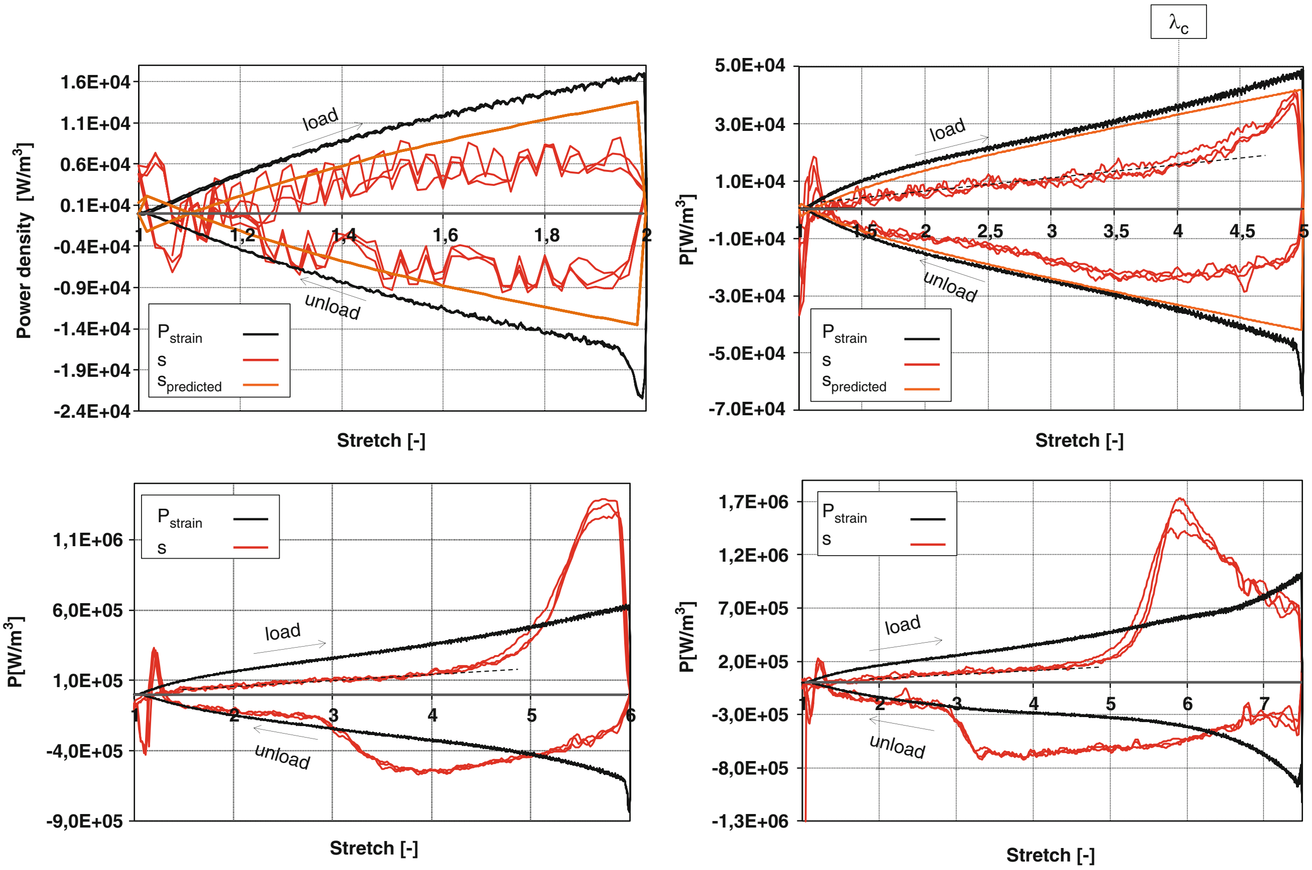

Fig. 6.3 Strain power density and heat sources for the different sets at increasing maximum stretches

6.4.3 Mechanical Energy Is Used for Structure Changes

Energy balance performed over each cycle highlights that NR deformation does not induce detectable intrinsic dissipation during mechanical cycles. The hysteresis area corresponds therefore to the energy used by the material to change its microstructure. It does not involve heat. Hence, the question is to define why the material needs this energy and if the energy dissipated is the same during loading and unloading. To answer this question, the energy balance is carried out at any time during the deformation cycle, by comparing the strain power density P_{strain} and the heat power density (heat source) s. Fig. 6.3 presents the evolution of P_{strain} (in *black* color) and s (in *red* color) for each set of maximum stretch.

For $\lambda_1 = 2 < \lambda_c$, these powers are not equal ($P_{strain} > s$). This means that NR does not behave as a purely entropic material. Internal energy also changes [19], which contributes to the calorific response. In this figure, the prediction of heat sources due to both entropy and internal energy is plotted in orange color (for the first two maximum stretch levels applied). Results show that the model fits well the level of thermoelastic inversion and the heat sources until to reach a stretch of about 1.6. This means first that the calorific response is strongly influenced by energetic elasticity, even though entropic elasticity is preponderant. Second, from a stretch equal to 1.6 on, the experimental heat sources are lower than the prediction. This means that the corresponding energy is used by the material to change its microstructure. This also explains which a hysteresis loop is observed for maximum stretches inferior to that at which SIC starts. Note that the model used to predict the heat source is not suitable at large deformations and when crystallization occurs, but it gives a realistic tendency before crystallization starts. For $\lambda_3 = 6 > \lambda_c$, a strong increase in the heat source is observed from $\lambda_2 = 5$ on, and $P_{strain} < s$, with $d_1 = 0$ W/m^3. Hence, the whole additional heat source is due to the crystallization. For $\lambda_4 = 7.5$, the same analysis can be drawn except for the change in the heat source curve slope from $\lambda_3 = 6$ on, which has already been discussed previously.

6.5 Conclusion

Strain-induced crystallization (SIC) is responsible for the hysteresis loop observed in the mechanical response NR. The inelastic energy contained in the mechanical hysteresis corresponds neither to intrinsic dissipation nor thermal dissipation. This energy is used by the material to change its microstructure. Calorimetric analyses have shown that crystallization/melting process does not produce intrinsic dissipation, i.e. crystallite melting absorbs the entire heat produced by SIC. As thermal dissipation was negligible, the crystallization/melting process does not convert mechanical energy into heat, neither through intrinsic nor thermal dissipation. The mechanical energy brought to the material is therefore used to change microstructure. The demonstration that NR is able to dissipate mechanical energy without converting it into heat explains its ability to resist the crack growth and the fatigue loading.

Funding Information Author acknowledges the “Manufacture Française des pneumatiques Michelin” for supporting this study. Author thanks J.R. Samaca Martinez, most of the results presented in the paper were obtained during his PhD Thesis. X. Balandraud, E. Toussaint, J. Caillard and D. Berghezan are acknowledged for the fruitful discussions.

References

1. Huneau, B.: Rubber Chem. Technol. **84**, 425–452 (2011)
2. Lee, D.J., Donovan, J.A.: Rubber Chem. Technol. **60**, 910–923 (1987)
3. Lake, G.J.: Rubber Chem. Technol. **68**, 435–460 (1995)
4. Cadwell, S.M., Merril, R.A., Sloman, C.M., Yost, F.L.: Ind. Eng. Chem.. (reprinted in Rubber Chem. and Tech. 1940;13:304–315). **12**, 19–23 (1940)
5. Beatty, J.R.: Rubber Chem. Technol. **37**, 1341–1364 (1964)
6. Saintier, N.: Prévisions de la durée de vie en fatigue du NR, sous chargement multiaxial. Thèse de doctorat, École Nationale Supérieure des Mines de Paris (2000)
7. Le Cam, J.-B., Huneau, B., Verron, E.: Int. J. Fatigue. **52**, 82–94 (2013)
8. Clark, G.L., Kabler, M., Blaker, E., Ball, J.M.: Hysteresis in crystallization of stretched vulcanized rubber from x-ray data. Ind. Eng. Chem. **32**, 1474–1477 (1940)
9. Toki, S., Fujimaki, T., Okuyama, M.: Strain-induced crystallization of natural rubber as detected real-time by wide-angle x-ray diffraction technique. Polymer. **41**, 5423–5429 (2000)
10. Trabelsi, S., Albouy, P.-A., Rault, J.: Crystallization and melting processes in vulcanized stretched natural rubber. Macromolecules. **36**, 7624–7639 (2003)
11. Le Cam, J.-B., Toussaint, E.: Macromolecules. **41**, 7579–7583 (2008)
12. Samaca Martinez, J.R., Le Cam, J.-B., Balandraud, X., Toussaint, E., Caillard, J.: Thermal and calorimetric effects accompanying the deformation of natural rubber. Part 1: thermal characterization. Polymer. **54**, 2717–2726 (2013)
13. Samaca Martinez, J.R., Le Cam, J.-B., Balandraud, X., Toussaint, E., Caillard, J.: Polym. Test. **32**, 835–841 (2013)
14. Samaca Martinez, J.R., Le Cam, J.-B., Balandraud, X., Toussaint, E., Caillard, J.: Thermal and calorimetric effects accompanying the deformation of natural rubber. Part 2: quantitative calorimetric analysis. Polymer. **54**, 2727–2736 (2013)
15. Samaca Martinez, J.R., Le Cam, J.-B., Balandraud, X., Toussaint, E., Caillard, J.: J. Eur. Polym. J. **55**, 98–107 (2014)
16. Le Cam, J.-B., Samaca Martinez, J.R., Balandraud, X., Toussaint, E., Caillard, J.: Exp. Mech. **55**, 771–782 (2015)
17. Chrysochoos, A., Louche, H.: Thermal and dissipative effects accompanying luders band propagation. Mat. Sci. Eng. A. **307**, 15–22 (2001)
18. Flory, P.J.: Thermodynamics of crystallization in high polymers. I. Crystallization induced by stretching. J. Chem. Phys. **15**, 397–408 (1947)
19. Treloar, L.R.G.: The elasticity and related properties of rubbers. Rep. Prog. Phys. **36**, 755 (1973)

Chapter 7
Use of Bulge Test Geometry for Material Property Identification

John M. Considine and X. Tang

Abstract The bulge test geometry, sometimes called blister or burst test, has a long history of use for material property identification. Paper materials are thin with relatively low stiffness; in a bulge test paper materials will exhibit a combination of membrane and plate behavior. We have developed a VFM examination to identify the in-plane stiffnesses of this type of material by incorporating both membrane and plate internal work.

Keywords VFM • Stiffness • Paperboard • Membrane • Plate

7.1 Introduction

This work describes the next stage in a larger research program to develop and use techniques to examine stiffness heterogeneity in thin materials. The authors have previously examined heterogeneity in uniaxial tensile tests [1]. With the understanding that identification of stiffness heterogeneity requires activation of all strains over a region much greater than the local heterogeneous region, different specimen and loading geometries have been investigated. One of the authors used a similar geometry to examine anisotropy in paperboard, a thin web material [2]. That geometry was capable of examining global anisotropy even though the center portion of the specimen experienced small strains and, therefore, was unsuitable for global heterogeneity investigations. This work performs a preliminary analysis to examine the ability of the bulge geometry and VFM to identify stiffnesses of an homogeneous, isotropic, linear elastic material.

The bulge geometry has many attractive features. The experimental fixture is relatively simple to construct; depending on the material investigated, specimen preparation is not challenging; external loading (pressure) is easy to apply and control; boundary conditions are comprehensible and can be mathematically modelled. Because of these features, the bulge test has become a standard technique to identify mechanical properties of thin films [3, 4], bilayer films [5], wafer materials [6, 7], MEMS [8], and biological tissues [9–12]. Because the bulge test is so prevalent, only a few examples are provided.

The most common procedure for mechanical property identification using the bulge test involves creating a pressure versus center deflection plot, whose slope is related to E, the elastic modulus, assuming only membrane behavior. Therefore, the greatest efforts for improving the bulge test have engaged in accurate measurement of the center deflection. Measurement of center deflection has been accomplished with calibrated displacement techniques [13], shadow moiré [14], moiré deflectometry [15], 3D-DIC [10–12, 16], Twyman-Green interferometry [17], laser interferometry [4, 18], position sensitive detectors using laser beams [19–21]. Some of these techniques do measure full field displacements, but a large portion of the data is discarded for property identification.

The approach presented here uses the entirety of lateral displacement information to identify E and ν by employing the Virtual Fields Method (VFM). The new development is the incorporation of both bending and membrane information, considering that even with large deflections some of the specimens may have more bending, or membrane, information than another.

J.M. Considine (✉)
Materials Research Engineer, U.S. Forest Service, Forest Products Laboratory, One Gifford Pinchot Drive, Madison, WI 53726, USA
e-mail: jonsidine@wisc.edu

X. Tang
Engineering Technician, U.S. Forest Service, Forest Products Laboratory, One Gifford Pinchot Drive, Madison, WI 53726, USA

A. Baldi et al. (eds.), *Residual Stress, Thermomechanics & Infrared Imaging, Hybrid Techniques and Inverse Problems, Volume 8*,
Conference Proceedings of the Society for Experimental Mechanics Series, DOI 10.1007/978-3-319-62899-8_7

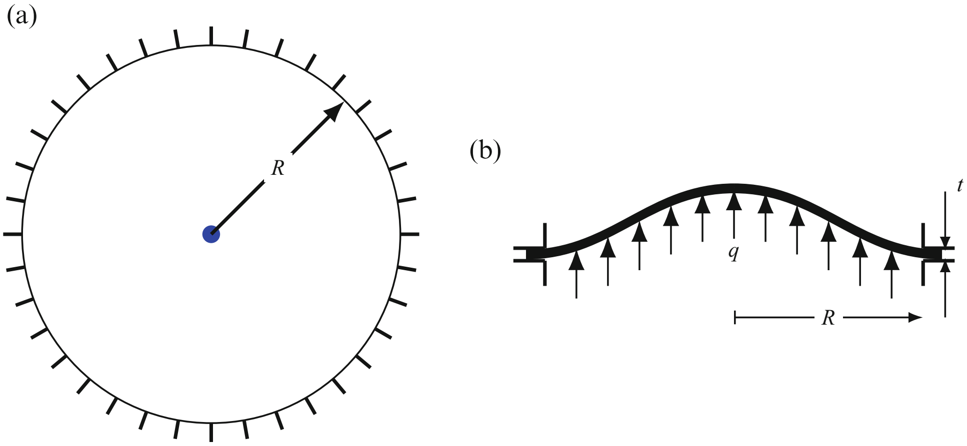

Fig. 7.1 Schematic of bulge test geometry. Specimen of thickness, *t*, was clamped (all DOF = 0) at radius *R* and loaded by lateral uniform pressure *q*. (**a**) Top view of bulge geometry. (**b**) Side view of bulge geometry

7.2 Test Geometry

The bulge test geometry examined here is shown in Fig. 7.1. Lateral uniform pressure, *q*, is shown perpendicular to original, undeformed surface. Central deflection is much greater than membrane thickness, *t*.

7.3 Virtual Fields Method

A more detailed development of VFM is found in Ref. [22]. VFM is based upon the Principle of Virtual Work (PVW) and its most basic form is

$$V^* = W^* \tag{7.1}$$

where V^* is the virtual work done by internal forces, and W^* is the virtual work done by external forces. For convenience, we can write

$$V^* = V^*_{bending} + V^*_{membrane} \tag{7.2}$$

For the bulge geometry, in the absence of body and intertial forces, the external work is entirely done by the uniform pressure. The external virtual work is

$$W^* = \int_S w^* q dS \tag{7.3}$$

where q is the uniform pressure applied to the lateral surface of the membrane, S is the area of the membrane, and w^* is the virtual out-of-plane displacement field of the membrane.

The virtual internal work due to membrane forces for a homogeneous, isotropic, linear elastic membrane can be written as

$$\begin{aligned} V^*_{membrane} &= t\int_S \left(\sigma_x \varepsilon^*_x + \sigma_y \varepsilon^*_y + \sigma_s \varepsilon^*_s\right) dS \\ &= Qt\int_S \left(\varepsilon_x \varepsilon^*_x + \varepsilon_y \varepsilon^*_y + \frac{1}{2}\varepsilon_s \varepsilon^*_s\right) dS + \nu Qt\int_S \left(\varepsilon_x \varepsilon^*_y + \varepsilon_y \varepsilon^*_x - \frac{1}{2}\varepsilon_s \varepsilon^*_s\right) dS \\ &= Qt\int_S \left(\varepsilon_x \varepsilon^*_x + \varepsilon_y \varepsilon^*_y\right) dS + \nu Qt\int_S \left(\varepsilon_x \varepsilon^*_y + \varepsilon_y \varepsilon^*_x\right) dS \end{aligned} \tag{7.4}$$

where t is the membrane thickness, Q is the in-plane stiffness from $\boldsymbol{\sigma} = \boldsymbol{Q\varepsilon}$, and ν is Poisson's ratio. The simplification in Eq. 7.4 is unique for this geometry because all shear components are 0.

Similarly, for the virtual work for bending

$$\begin{aligned} V^*_{bending} &= \int_V \left(\sigma_x \varepsilon^*_x + \sigma_y \varepsilon^*_y + \sigma_s \varepsilon^*_s\right) dV \\ &= D \int_S \left(k_x k^*_x + k_y k^*_y + \frac{1}{2} k_s k^*_s\right) dS + \nu D \int_S \left(k_x k^*_y + k_y k^*_x - \frac{1}{2} k_s k^*_s\right) dS \\ &= D \int_S \left(k_x k^*_x + k_y k^*_y\right) dS + \nu D \int_S \left(k_x k^*_y + k_y k^*_x\right) dS \\ &= \frac{1}{12} Q t^3 \int_S \left(k_x k^*_x + k_y k^*_y\right) dS + \frac{1}{12} \nu Q t^3 \int_S \left(k_x k^*_y + k_y k^*_x\right) dS \end{aligned} \tag{7.5}$$

where k_i are the component curvatures and D is the bending stiffness, that is $D = Qt^3/12$.

Final implementation of PVW requires strain-displacement relations which are

$$\varepsilon_x = \frac{\partial u}{\partial x} \tag{7.6}$$

$$\varepsilon_y = \frac{\partial v}{\partial y} \tag{7.7}$$

$$k_x = -\frac{\partial^2 w}{\partial x^2} \tag{7.8}$$

$$k_y = -\frac{\partial^2 w}{\partial y^2} \tag{7.9}$$

where u, v are the displacements in the x, y directions, respectively. Substituting virtual displacements in Eqs. 7.6, 7.7, 7.8, and 7.9 gives the relations for the virtual strains and curvatures.

7.4 Discussion and Conclusion

Use of the formulation in the previous section presents some experimental challenges. The curvatures, k_i, are assumed to be uniform through the material thickness. The in-plane strains, ε_i, are those at the thickness mid-point. Surface strain measurement is a combination of bending and membrane strains, which need to be separated for use in PVW. An obvious, but not trivial, experimental solution is to measure the strains on both the front and back surfaces of the membrane. A point-by-point average of front and back surface strain will be the membrane strain. Recognizing that $k_6 = 0$, the curvatures are related to the surface strains by

$$k_i = \frac{1}{t}\left(\varepsilon_i^{front} - \varepsilon_i^{back}\right) \tag{7.10}$$

Full field displacements are required for this analysis, including w, the out-of-plane displacement. Most full field displacement techniques require a reference image, including DIC, however capturing a reference image is problematic. If the specimen is exhibiting membrane-like behavior then a flat reference image is difficult to produce. Use of a reference image with very low magnitude q must be used with care because the problem is nonlinear, e.g. increasing the pressure magnitude to $2q$ does not increase the central deflection to $2w$.

The presentation will include a FEA simulation and experimental results demonstrating the use of VFM with the bulge geometry to identify material behavior.

References

1. Considine, J.M., Pierron, F., Turner, K.T., Lava, P., Tang, X.: Smoothly varying stiffness heterogeneity evaluated under uniaxial tensile stress. Strain (2017). doi:10.1111/str.12237
2. Considine, J.M., Pierron, F., Turner, K.T., Vahey, D.W.: General anisotropy identification of paperboard with virtual fields method. Exp. Mech. **54**(8), 1395–1410 (2014)
3. Small, M.K., Nix, W.D.: Analysis of the accuracy of the bulge test in determining the mechanical properties of thin films. J. Mater. Res. **7**(06), 1553–1563 (1992)
4. Vlassak, J.J., Nix, W.D.: A new bulge test technique for the determination of Young's modulus and Poisson's ratio of thin films. J. Mater. Res. **7**(12), 3242–3249 (1992)
5. Small, M.K., Daniels, B.J., Clemens, B.M., Nix, W.D.: The elastic biaxial modulus of Ag–Pd multilayered thin films measured using the bulge test. J. Mater. Res. **9**(01), 25–30 (1994)
6. Mitchell, J.S., Zorman, C.A., Kicher, T., Roy, S., Mehregany, M.: Examination of bulge test for determining residual stress, Youngs modulus, and Poissons ratio of 3C–SiC thin films. J. Aerospace Eng. **16**(2), 46–54 (2003)
7. Edwards, R.L., Coles, G., Sharpe, W.N.: Comparison of tensile and bulge tests for thin-film silicon nitride. Exp. Mech. **44**(1), 49–54 (2004)
8. Youssef, H., Ferrand, A., Calmon, P., Pons, P., Plana, R.: Methods to improve reliability of bulge test technique to extract mechanical properties of thin films. Microelectron. Reliab. **50**(9), 1888–1893 (2010)
9. Lu, J., Zhou, X., Raghavan, M.L.: Inverse method of stress analysis for cerebral aneurysms. Biomech. Model. Mechanobiol. **7**(6), 477–486 (2007)
10. Tonge, T.K., Atlan, L.S., Voo, L.M., Nguyen, T.D.: Full-field bulge test for planar anisotropic tissues: part I–experimental methods applied to human skin tissue. Acta Biomater. **9**(4), 5913–5925 (2013)
11. Davis, F.M., Luo, Y., Avril, S., Duprey, A., Lu, J.: Pointwise characterization of the elastic properties of planar soft tissues: application to ascending thoracic aneurysms. Biomech. Model. Mechanobiol. **14**(5), 967–978 (2015)
12. Davis, F.M., Luo, Y., Avril, S., Duprey, A., Lu, J.: Local mechanical properties of human ascending thoracic aneurysms. J. Mech. Behav. Biomed. Mater. **61**, 235–249 (2016)
13. Allen, M.G., Mehregany, M., Howe, R.T., Senturia, S.D.: Microfabricated structures for the in situ measurement of residual stress, Youngs modulus, and ultimate strain of thin films. Appl. Phys. Lett. **51**(4), 241–243 (1987)
14. Xu, D., Liechti, K.M., de Lumley-Woodyear, T.H.: Closed form nonlinear analysis of the peninsula blister test. J. Adhes. **82**(8), 831–866 (2006)
15. Xu, D., Liechti, K.M.: Bulge testing transparent thin films with moiré deflectometry. Exp. Mech. **50**(2), 217–225 (2010)
16. Machado, G., Favier, D., Chagnon, G.: Membrane curvatures and stress-strain full fields of axisymmetric bulge tests from 3D-DIC measurements. Theory and validation on virtual and experimental results. Exp. Mech. **52**(7), 865–880 (2012)
17. Hsu, J.-S., Wen, B.-J., Chen, P.-Y.: Full-field deflection measurement of the flexible transparent sheets. Polym. Test. **31**(8), 1105–1114 (2012)
18. Zheng, D.W., Xu, Y.H., Tsai, Y.P., Tu, K.N., Patterson, P., Zhao, Q.-Z., Liu, B., Brongo, M.: Mechanical property measurement of thin polymeric-low dielectric-constant films using bulge testing method. Appl. Phys. Lett. **76**(15), 2008–2010 (2000)
19. Kalkman, A.J., Verbruggen, A.H., Janssen, G.C.A.M., Groen, F.H.: A novel bulge-testing setup for rectangular free-standing thin films. Rev. Sci. Instrum. **70**(10), 4026–4031 (1999)
20. Kalkman, A.J., Verbruggen, A.H., Janssen, G.C.A.M.: High-temperature bulge-test setup for mechanical testing of free-standing thin films. Rev. Sci. Instrum. **74**(3), 1383–1385 (2003)
21. Schweitzer, E.W., Göken, M.: In situ bulge testing in an atomic force microscope: microdeformation experiments of thin film membranes. J. Mater. Res. **22**(10), 2902–2911 (2007)
22. Pierron, F., Grédiac, M.: The Virtual Fields Method: Extracting Constitutive Mechanical Parameters from Full-Field Deformation Measurements. Springer, New York (2012)

Chapter 8
Crystal Plasticity Parameter Identification by Integrated DIC on Microscopic Topographies

J. P. M. Hoefnagels, M. Bertin, C. Du, and F. Hild

Abstract The present study unravels details of the micromechanical behavior of a micro-specimen made of IF-steel. A triangular prism is machined via focused ion beam (FIB) and contains two ferritic grains. Four experimental tools are integrated to identify the material's crystal parameters: (i) an optical confocal microscope captures height profile images, (ii) an in-situ tensile stage prescribes the loading history to the macro-specimen, (iii) a global Digital Image Correlation (DIC) algorithm measures the 3D surface displacement fields, and iv) an extension of Integrated-DIC for 3D displacement fields is implemented to assess the micromechanical behavior. It is demonstrated that with this methodology the identification of the boundary conditions and crystal plasticity parameters is successfully achieved.

Keywords Digital image correlation • Crystal plasticity • Parameter identification • In-Situ testing • Digital height correlation • Integrated digital image correlation

8.1 Introduction

The mechanical properties of materials often originate from physical and multi-scale phenomena that are due to complex and heterogeneous microstructures. One of the first methods to consider heterogeneous media for computing macro-mechanical responses is based on homogenization. In order to solve this problem micromechanical frameworks have been developed for elastic materials and in elasto-plasticity. Due to complex behaviors and the difficulty to observe and measure at the microscale the main challenge remains the identification of the constitutive parameters.

As products become smaller and smaller, accurate prediction of their mechanical behavior requires explicitly modeling of the individual crystals that constitute the material. Crystal plasticity (CP) models, which model dislocation densities instead of discrete dislocations, have been successful applied, e.g., to predict plastic hardening mechanisms. A key challenge of CP models, however, is that their model parameters can only be identified indirectly from their effect on the (microscopic) deformation fields. To this end, a novel integrated digital image correlation (IDIC) approach to identify the material's crystal parameters is introduced, in which the three-dimensional surface deformation fields of a micro-tensile specimen are correlated by optimizing the parameters in a CP simulation.

The lattice structure (e.g., FCC, BCC) is considered to derive the constitutive equations for single crystals. The present study aims at coupling experimental and numerical results and provides a compromise between a reasonable computation time and a sufficiently small scale to achieve the observation of the micromechanical behavior in a material with real engineering applications. Digital Image Correlation enables full displacement and strain fields to be measured and provides insight into the micromechanics of solids. Imaging systems capable of higher magnifications allow the heterogeneity of the micromechanical response to be evaluated.

The objective of this study is to perform an investigation at the microscale and to identify the material parameters of a crystal plasticity model with Integrated Digital Image Correlation (IDIC) [1–6]. Figure 8.1 shows the designed identification procedure. Initially, the crystallographic features, i.e., phase, grain (size, number and orientation) and the geometry of the studied volume are assessed and lead to the design of a representative 3D numerical model. Secondly, the out-of-plane displacement holds essential information regarding the active slip systems. Therefore an experimental method is introduced that utilizes confocal microscopy combined with a 3D surface global DIC formulation to quantify full three-dimensional

---

J.P.M. Hoefnagels (✉) • C. Du
Department of Mechanical Engineering, Eindhoven University of Technology, Eindhoven, The Netherlands
e-mail: j.p.m.hoefnagels@tue.nl

M. Bertin • F. Hild
LMT, ENS Cachan, CNRS, Université, Paris-Saclay, France

A. Baldi et al. (eds.), *Residual Stress, Thermomechanics & Infrared Imaging, Hybrid Techniques and Inverse Problems, Volume 8*,
Conference Proceedings of the Society for Experimental Mechanics Series, DOI 10.1007/978-3-319-62899-8_8

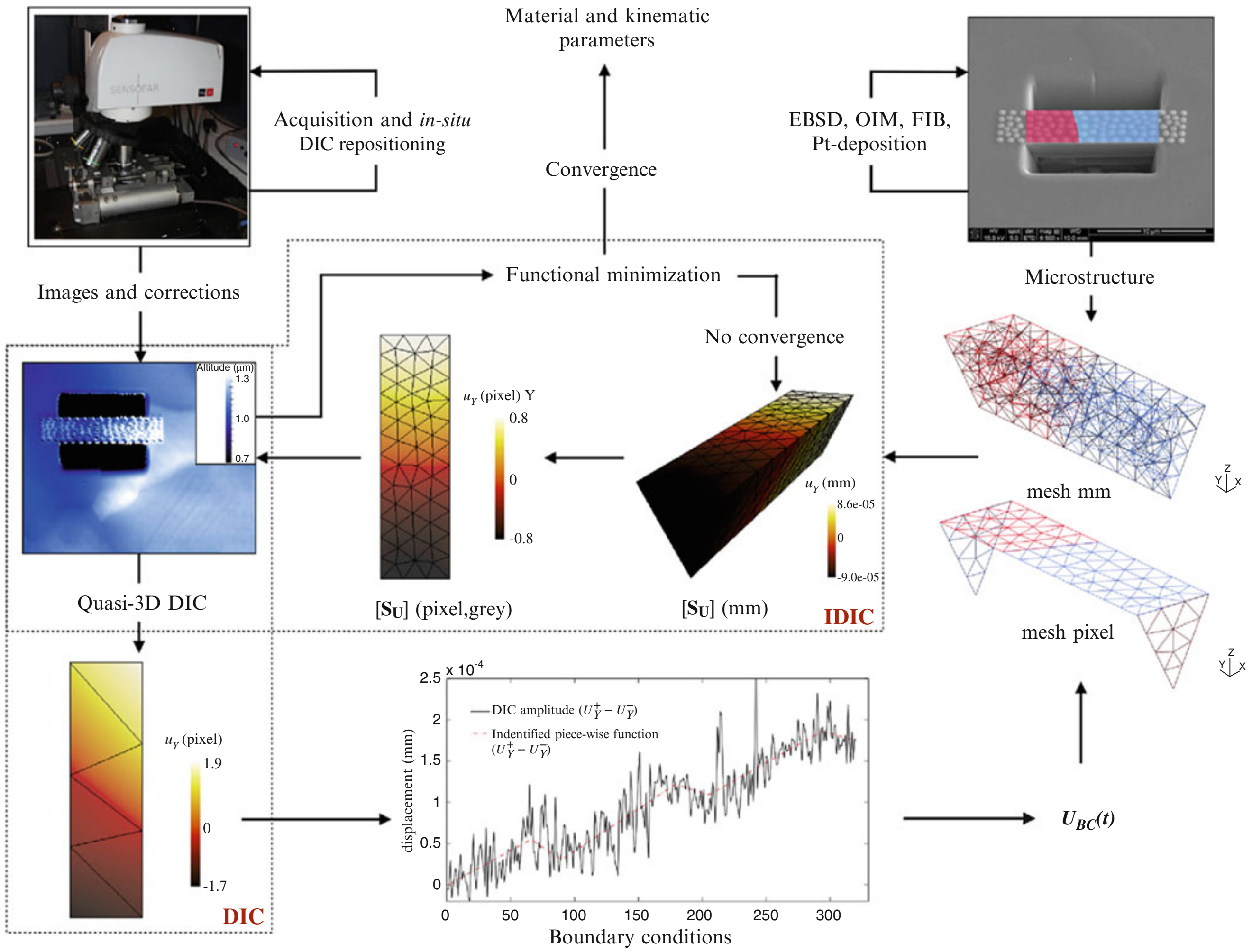

Fig. 8.1 Schematic view of the methods used herein to extract boundary conditions and crystal plasticity parameters [7]

displacement fields of the specimen surface and use these 3D data to extract boundary conditions and identify crystal plasticity parameters [7]. Because of the relatively high noise level computations are run with stabilized boundary conditions. Finally, the sought parameters are identified with integrated-DIC that combines all experimental data, i.e., the surface height profiles, constitutive model, and crystallographic features.

8.2 Results and Conclusion

The IDIC approach works directly on the height profiles. It includes: (i) micro-fabrication, by means of careful FIB milling, of a $12.0 \times 4.0 \times 3.5\ \mu\text{m}^3$ triangular specimen containing two crystals, thus only 1 grain boundary, (ii) loading in an in-situ micro-tensile stage under simultaneous optical microscopy to measure surface height profiles, (iii) global DIC measurement of the 3D boundary displacements conditions of the CP simulation, and (iv) IDIC correlation of the surface topographies using simulated CP deformation fields. It is demonstrated that with this methodology the identification of the boundary conditions and crystal plasticity parameters is successfully achieved [7]. The concept proposed herein is very general and can be applied to any micromechanical experiment aiming to characterize a constitutive law describing a micromechanical behavior. The technique gives new insights into the micro-mechanical behavior with the combination of images and loads based on a methodology that can cope with high noise levels.

References

1. Neggers, J., Hoefnagels, J.P.M., Geers, M.G.D., Hild, F., Roux, S.: Time-resolved integrated digital image correlation. Int. J. Numer. Methods. Eng. **103**(3), 157–182 (2015)
2. Ruybalid, A.P., Hoefnagels, J.P., Sluis, O., Geers, M.G.: Comparison of the identification performance of conventional FEM updating and integrated DIC. Int. J. Numer. Methods. Eng. **106**(4), 298–320 (2015)
3. Bergers, L.I.J.C., Hoefnagels, J.P.M., Geers, M.G.D.: Characterization of time-dependent anelastic microbeam bending mechanics. J. Phys. D. Appl. Phys. **47**(35), 355306 (2014)
4. Hild, F., Bouterf, A., Chamoin, L., Leclerc, H., Mathieu, F., Neggers, J., Pled, F., Tomičević, Z., Roux, S.: Toward 4D mechanical correlation. Adv. Model. Simul. Eng. Sci. **3**(1), 17 (2016)
5. Kleinendorst, S., Hoefnagels, J.P.M., Geers, M.G.D., 2017: Mechanical Shape Correlation: an integrated image correlation approach (submitted for publication)
6. Blaysat, B., Hoefnagels, J.P., Lubineau, G., Alfano, M., Geers, M.G.: Interface debonding characterization by image correlation integrated with double cantilever beam kinematics. Int. J. Solids. Struct. **55**, 79–91 (2015)
7. Bertin, M., Du, C., Hoefnagels, J.P., Hild, F.: Crystal plasticity parameter identification with 3D measurements and integrated digital image correlation. Acta. Mater. **116**, 321–331 (2016)

Chapter 9
Comparison of Residual Stress Characterization Techniques Using an Interference Fit Sample

Jun-Sang Park, John Okasinski, Jonathan Almer, Paul Shade, and T.J. Turner

Abstract Residual stress in an engineering component induced from processing is pervasive and can impact the component's performance significantly. There are numerous destructive and non-destructive techniques that are available to determine the residual stresses in a component. In this work, an interference fit sample was manufactured from a titanium alloy. The sample was equipped with a set of strain gauges to measure the strains induced by the interference process used for sample assembly. Energy dispersive diffraction experiment using synchrotron radiation was conducted to measure the lattice strains in the interference fit sample. Hole drilling measurements were also conducted on the sample. The non-destructive X-ray result is compared with strain gauge measurements, and found to be in good agreement when appropriately averaged.

Keywords Titanium • Interference fit • Energy dispersive diffraction • Lattice strain • Strain gauge

9.1 Introduction

Engineering components typically undergo complex processing paths. These processes typically impart a complex residual stress field in the workpiece that affect its performance. Sometimes processes are designed to induce a favorable residual stress in the workpiece to enhance its performance. Given the complicated geometries of the components used in modern machines and complex residual stress field in them, numerous residual characterization methods have been developed [1, 2].

The goal of this project is to compare and contrast some of the residual strain measurement/stress characterization techniques that are available. An interference fit sample was designed and manufactured for the investigation. The sample was equipped with a set of strain gauges for benchmark strain data. While three residual strain measurement techniques – energy dispersive diffraction (EDD), angle dispersive diffraction, and hole drilling – are being considered in this project, only the strains measured by EDD are shown in this article. The other strain measurements are being compiled and will be available for publication in the near future.

This article is organized as follows. In Sect. 9.2, the sample geometry is described. In Sect. 9.3, the energy dispersive diffraction setup at the 6-BM-A beamline of the Advanced Photon Source (APS), Argonne National Laboratory is described. The strains are compared and contrasted in Sect. 9.4. Concluding remarks are presented in Sect. 9.5.

9.2 Sample

An interference fit geometry is used to induce a residual stress field in the component. Figures 9.1 and 9.2 show the sample. A 10 mm thick Ti-6Al-4V plate was used to manufacture the disk.[1] The alloy had two constituent phases (hexagonal close-packed α and body-centered cubic β) with nominal grain sizes that are on the order of 10 μm for the α phase. The core was made from a stainless steel keyless bushing [3] and tool steel shaft. A set of linear strain gauges and 0°–90° Rossette strain

---

[1] The prior processing information for the alloy is available upon request.

J.-S. Park (✉) • J. Okasinski • J. Almer
X-ray Science Division, Argonne National Laboratory, 60439, Lemont, IL, USA
e-mail: parkjs@aps.anl.gov; okasinski@aps.anl.gov; almer@aps.anl.gov

P. Shade • T.J. Turner
Materials and Manufacturing Directorate, Air Force Research Laboratory, 45433, Wright-Patterson AFB, OH, USA
e-mail: paul.shade.1@us.af.mil; todd.turner.5@us.af.mil

A. Baldi et al. (eds.), *Residual Stress, Thermomechanics & Infrared Imaging, Hybrid Techniques and Inverse Problems, Volume 8*,
Conference Proceedings of the Society for Experimental Mechanics Series, DOI 10.1007/978-3-319-62899-8_9

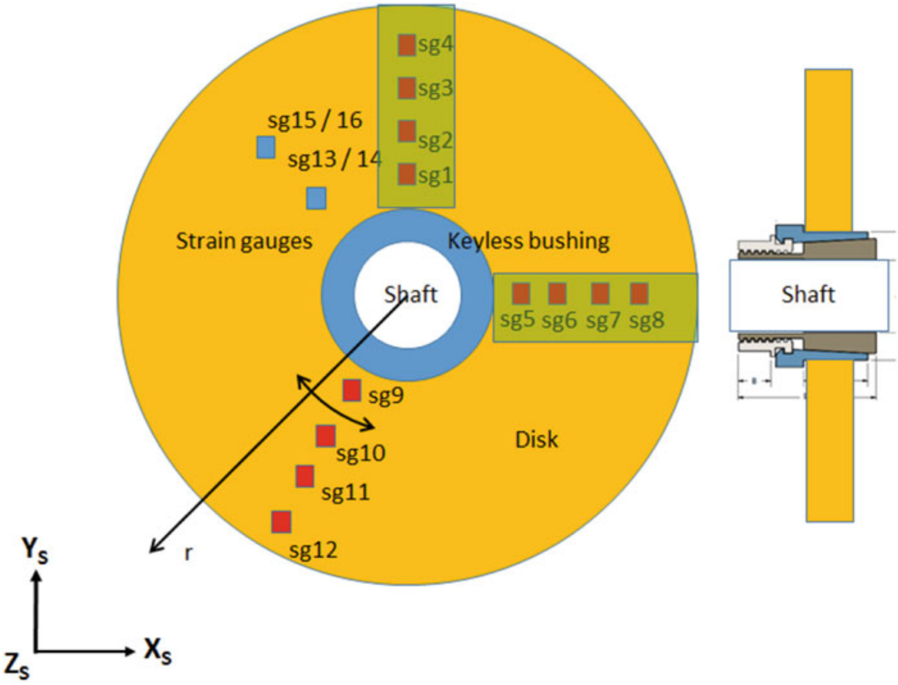

Fig. 9.1 A schematic of the interference fit sample. The linear strain gauges are marked by the *red squares*. The 0°–90° Rossette strain gauges are marked by the *blue squares*. The regions measured by the EDD technique are highlighted in *green*

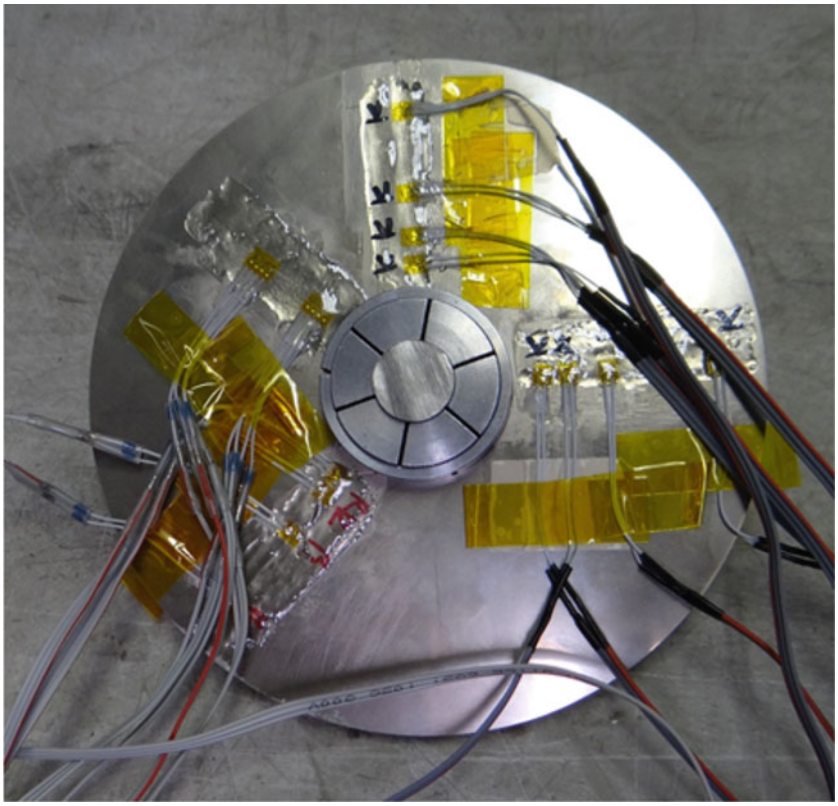

Fig. 9.2 A picture of the sample with strain gauges installed. The diameter of the keyless bushing is 38.1 mm (1.5 inches) and the diameter of the disk is 100 mm

Table 9.1 The strain gauge readings immediately following the sample assembly

Strain gauge ID	Radial distance (mm)	Strain
sg1	5	1.14×10^{-3}
sg2	10	7.80×10^{-4}
sg3	20	4.90×10^{-4}
sg4	40	2.75×10^{-4}
sg5	5	7.17×10^{-4}
sg6	10	5.91×10^{-4}
sg7	20	4.75×10^{-4}
sg8	40	1.66×10^{-4}
sg9	5	1.10×10^{-3}
sg10	10	8.02×10^{-4}
sg11	20	4.55×10^{-4}
sg12	40	2.71×10^{-4}
sg13	5	1.21×10^{-3}
sg14	5	-8.61×10^{-4}
sg15	20	4.84×10^{-4}
sg16	20	-2.72×10^{-4}

gauges were attached to the surface of the disk to monitor the apparent stress applied on the disk. The linear strain gauges were attached such that they measured the hoop component of strain in their respective locations. The Rossette strain gauges were placed such that 0° measured the hoop and the 90° measured the radial component of strain respectively. As torque was applied, the keyless bushing expanded and exerted a stress on the disk. When sufficient levels of strains on the strain gauges below the nominal macroscopic yield were seen, the keyless bushing was set in place with epoxy. Table 9.1 shows the strain data from the strain gauges after the keyless bushing was installed in the disk.

9.3 Energy Dispersive Diffraction

The EDD experiments were conducted at the 6-BM-B beamline of the APS. Figure 9.3 shows a schematic of the setup. In this setup, a series of slits are used to isolate a gauge volume in space located at $\mathrm{O_L}$. A detector is placed in the $\mathbf{Y}_\mathrm{L}$ -$\mathbf{Z}_\mathrm{L}$ plane at an angle of $2\theta_\mathrm{v}$. When a sample is placed at $\mathrm{O_L}$, all families of crystallographic planes that satisfy the Bragg condition diffract and the scattered beam is recorded on the energy discriminating detector (denoted in Fig. 9.3 as Ge detector). Typical data for a particular location in the sample are in terms of intensity vs. energy. For a particular family of crystallographic planes, the deviation of the plane spacing from its reference value due to the existence of residual stress in a workpiece, ϵ_{qq}, is computed using

$$\epsilon_{qq} = \frac{E_0(\mathbf{q})}{E(\mathbf{q})} - 1 \tag{9.1}$$

where $E_0(\mathbf{q})$ and $E(\mathbf{q})$ are the reference and measured energies of the diffracted photon respectively [4]. A three dimensional map of the strain is obtained by translating the sample with respect to the beam. The strain uncertainty is approximately 1×10^{-4}. The spatial resolution along $\mathbf{X}_\mathrm{L}$ and $\mathbf{Y}_\mathrm{L}$ are on the order of 10 µm and the spatial resolution along $\mathbf{Z}_\mathrm{L}$ is on the order of a few mm. The spatial resolutions in $\mathbf{X}_\mathrm{L}$ and $\mathbf{Y}_\mathrm{L}$ depend on the slit settings and the associated translation motions available for sample manipulation. The spatial resolution in $\mathbf{Z}_\mathrm{L}$ depends on the slit settings, $2\theta_\mathrm{v}$, and associated translation motion available for sample manipulation.

For the strain measurement on the interference fit sample, the sample was placed such that $\mathbf{X}_\mathrm{S}$, $\mathbf{Y}_\mathrm{S}$, and $\mathbf{Z}_\mathrm{S}$ were parallel to $\mathbf{X}_\mathrm{L}$, $\mathbf{Y}_\mathrm{L}$, and $\mathbf{Z}_\mathrm{L}$ respectively. Because only one detector was employed, the radial component of strain was measured in the region highlighted by green along $\mathbf{Y}_\mathrm{S}$ in Fig. 9.1; the hoop component of strain was measured for the region highlighted by green along $\mathbf{X}_\mathrm{S}$ in Fig. 9.1. The sample was aligned such that the midsection along the thickness of the disk was measured. The slits were setup to provide 0.2 mm × 0.2 mm beam and $2\theta_\mathrm{v}$ was approximately 5.5°. This yields approximately 3 mm of gauge length thereby avoiding any significant edge effects from partial volume illumination.

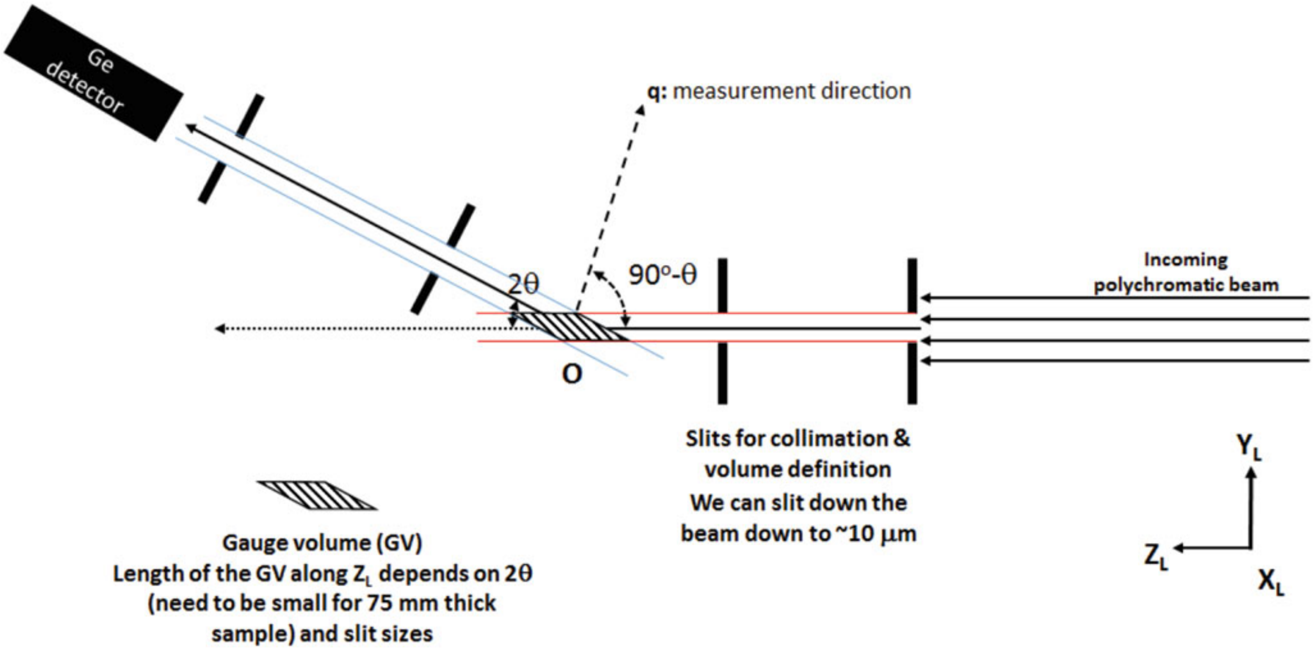

Fig. 9.3 A schematic of gauge volume defined by the slits in the EDD setup

9.4 Results and Discussion

While the alloy used to manufacture the disk is a two phase alloy, the β phase is a minority phase and it was not taken into consideration in the strain measurement. Figure 9.4a, b shows the radial strain and hoop strain maps measured in the green region along $\mathbf{Y}_S$ and $\mathbf{X}_S$ (Fig. 9.1) respectively. As anticipated, the radial component of strain is compressive and the hoop component of strain is tensile. They have the maximum magnitudes at the inner locations of the disk and reduce toward zero at the outer locations of the disk. The magnitudes of the strains are similar to those measured by the strain gauges. However, it is also quite evident that depending on where the strain is measured the strain values can vary significantly. Choosing peaks from other crystallographic planes did not alleviate the significant variation of strain in neighboring diffraction volumes. This scatter in lattice strain is larger than the measurement uncertainty associated with the EDD technique and it is suspected that there is significant scatter in strains at the grain length scale which are superimposed on the continuum length scale strain.

Since the EDD lattice data were taken at higher spatial resolution than the strain gauge data, the EDD data were spatially averaged to match the sample volume probed by the strain gauges. With such averaging, the strains measured by two techniques are remarkably similar. Figure 9.5 shows the spatially-averaged strains from three families of crystallographic planes measured by EDD and corresponding strain gauge readings. While the lattice strains still show some scatter, the trends are much clearer and follow the strain gauge readings well.

9.5 Conclusion and Outlook

In this article, an interference fit sample was manufactured from a titanium alloy with the goal of comparing and contrasting various residual stress characterization techniques that are available. While several non-destructive and destructive techniques are being considered and data are being analyzed, some initial results from energy dispersive diffraction experiments performed at the APS 6-BM-A beamline were compared to the benchmark strain gauge readings from strain gauges attached to the interference fit sample. The initial comparison showed good agreement when appropriately compared. In addition to these measurement, angle dispersive diffraction and hole drilling measurements were performed; these results are being analyzed and compiled and will be available for publication in the near future.

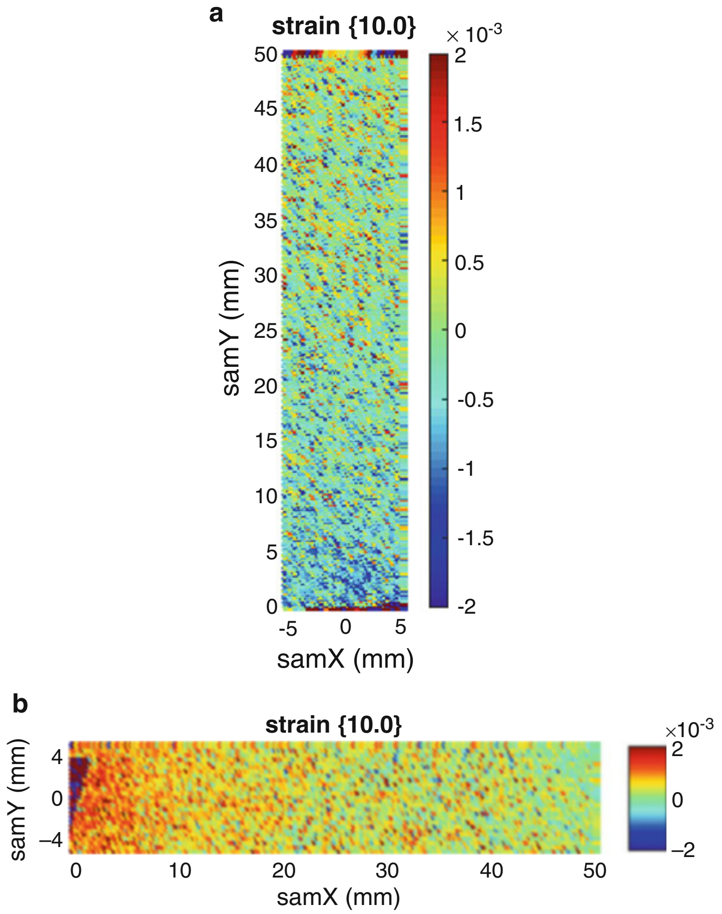

Fig. 9.4 The lattice strain maps measured by EDD technique on the interference fit sample. In these figures, samX and samY denote $\mathbf{X}_S$ and $\mathbf{Y}_S$ respectively. (**a**) The radial component of lattice strain map of the *green region* along $\mathbf{Y}_S$ measured using the {10.0} peak. (**b**) The hoop component of lattice strain map of the *green region* along $\mathbf{X}_S$ measured using the {10.0} peak

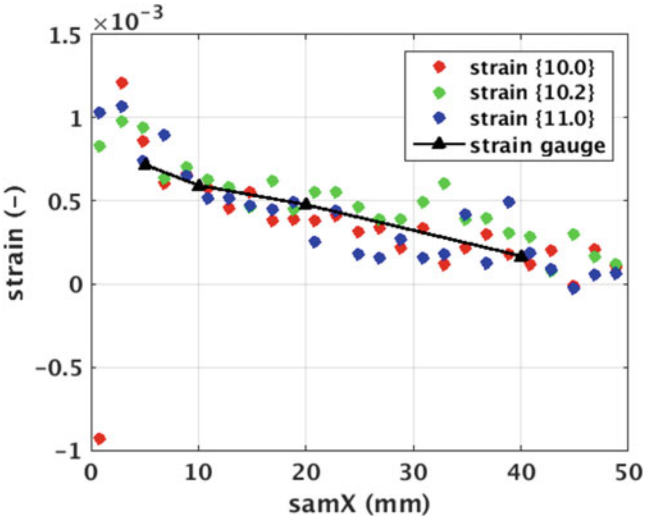

Fig. 9.5 Averaged lattice strain compared to the strains measured by the strain gauges. Here, samX denotes $\mathbf{X}_S$

Acknowledgements This research used resources of the Advanced Photon Source, a U.S. Department of Energy (DOE) Office of Science User Facility operated for the DOE Office of Science by Argonne National Laboratory under Contract No. DE-AC02-06CH11357. Support from the Materials and Manufacturing Directorate of the U.S. Air Force Research Laboratory is acknowledged.

References

1. Noyan, I.C., Cohen, J.B.: Residual Stress: Measurement by Diffraction and Interpretation. Spinger, New York (1987)
2. Schajer, G.S. (ed.): Practical Residual Stress Measurement Methods. John Wiley (2013). 10.1002/9781118402832. http://onlinelibrary.wiley.com/book/10.1002/9781118402832.
3. http://www.fennerdrives.com/trantorque/
4. Croft, M., Zakharchenko, I., Zhong, Z., Gurlak, Y., Hastings, J., Hu, J., Holtz, R., da Silva, M., Tsakalakos, T.: Strain field and scattered intensity profiling with energy dispersive x-ray scattering. J. Appl. Phys. **92**(1), 578 (2002). 10.1063/1.1483373. http://dx.doi.org/10.1063/1.1483373.

Chapter 10
Influence of Thermographic Image Filtering on Hybrid TSA

W. A. Samad and X. Balandraud

Abstract Hybrid thermoelastic stress analysis (Hybrid-TSA) is an experimental thermographic method that has been successfully applied to plenty of structures and loading situations. The main objective is the separation of the TSA stresses, namely the sum of the two principal in-plane stresses. While Hybrid-TSA yields a general better understanding of a component's elastic response, it is mostly useful for structural integrity analysis in terms of stress variation due to fatigue or cracking for instance. In practice, TSA stress separation is accomplished using an Airy stress function, which is derived from compatibility and equilibrium conditions, and is frequently represented in the form of a finite series of coefficients. To date, the analyses mostly focused on determining the appropriate number of coefficients for a given noisy TSA image, excluding the filtering of the TSA raw data. The present study deals with the influence of filtering operations on the results of the method. Synthetic TSA stress fields corrupted by added noise are considered. Gaussian filters are then applied to reduce the difference between theoretical and reconstructed TSA stresses using a reduced number of points on the structure. The influence of the noise level is discussed. The study provides information for a better separation of stresses at an optimal computational cost.

Keywords TSA • Filtering • Noise • Hybrid • Thermography

Nomenclatures

DIC	Digital image correlation
$E_{\%}$	Straight forward local percentage error at pixel
E_{filter}	Weighted *rms* error of filtered image with respect to exact solution
E_{no_filter}	Weighted *rms* error of un-filtered noisy image with respect to exact solution
k	Number of Airy coefficients
K	TSA calibration coefficient
m	Number of TSA data points
m'	Number of total TSA data points selected for Hybrid-TSA
PSA	Photoelastic stress analysis
r & θ	Polar coordinates
R	Disk radius
rms	Root mean square
S	Calibrated TSA image $\sigma_1+\sigma_2$
S^*	Raw TSA image proportional to
S_{exact}	Synthetic TSA image based on exact analytical solution
$S_{filtered}$	S_{noisy} after it undergoes Gaussian filteration
S_{hybrid_filter}	Reconstructed image after = combining $S_{filtered}$ with Airy stress function
$S_{hybrid\_no\_filter}$	Reconstructed image after = combining S_{noisy} with Airy stress function
S_{noisy}	S_{exact} with white noise introduced to it
S_{origin}	Synthetic TSA image evaluated at the center of the compressed disk
t	Disk thickness
TSA	Thermoelastic stress analysis
x & y	Cartesian coordinates

W.A. Samad (✉)
Rochester Institute of Technology, Rochester, NY, USA
e-mail: wascad@rit.edu

X. Balandraud
Université Clermont-Auvergne, Clermont-Ferrand, France

A. Baldi et al. (eds.), *Residual Stress, Thermomechanics & Infrared Imaging, Hybrid Techniques and Inverse Problems, Volume 8*,
Conference Proceedings of the Society for Experimental Mechanics Series, DOI 10.1007/978-3-319-62899-8_10

10.1 Background

Hybrid-experimental approaches facilitate the determination of fundamentally important separate stresses through coupling full-field experimental data with an analytical expression. Full-field experimental methods such as thermoelastic stress analysis (TSA), photoelastic stress analysis (PSA), digital image correlation (DIC), moiré, etc., result in data that are discrete and whose resolution depends on the experimental setup (sensor resolution, lens used, focal distance, grid analyzer, etc.). Moreover, data near geometric singularities such as near holes, notches, and edges are in general unreliable due to different edge effects specific to the experimental approach. Most importantly, raw data often offer one piece of information, e.g. isopachic stresses for TSA, isochromatic stresses for PSA, and displacements for DIC, as opposed to individual separate stress information in the case of analytical solutions and finite element methods. The present study focuses on TSA, where output data are proportional to the summation of the first two principal stresses when considering a two-dimensional plane-stress loading situation as described in Eq. 10.1:

$$S^{*} = K\Delta S = K\Delta\left(\sigma_1 + \sigma_2\right) \tag{10.1}$$

where $S*$ is the measured TSA image, S the calibrated TSA image, and K the calibration coefficient related to the relevant physical properties of the material of interest, surface condition and TSA system parameters [1], often obtained from a test on a separate uniform coupon. A typical TSA test setup is shown in Fig. 10.1. With failure analysis being essential in engineering design, the separation of TSA coupled stresses becomes necessary – and this has been the topic of interest for many research efforts to date. The first determination of individual thermoelastic stresses was presented in [2] by taking into account the boundary conditions and the expected form of the stress distribution. More work was done in the following decade with the focus on performing such separation on structures with various discontinuities: structure with a circular hole [3], beneath concentrated loads [4], elliptical cutout [5], irregularly-shaped discontinuities [6], pinned structures [7] and more recently on unsymmetrical loading condition often encountered in real life structures [8]. A good review of hybrid thermoelastic stress analysis (Hybrid-TSA) approaches and their different timeline of events are presented in [9] in a special issue of the Journal of Experimental Mechanics on Infrared Imaging and Thermomechanics.

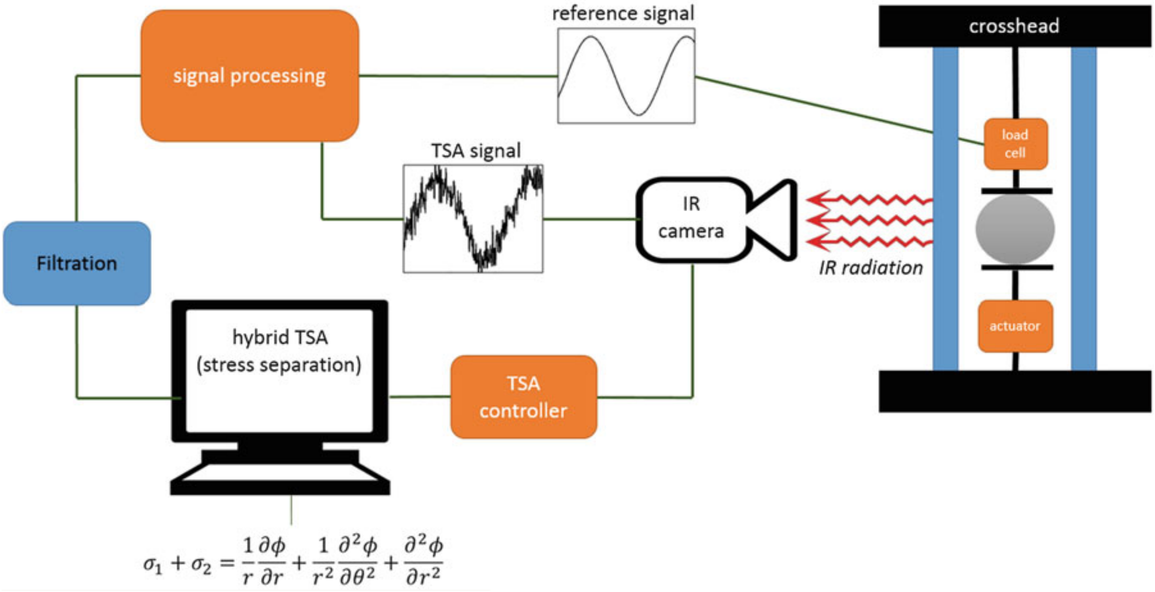

Fig. 10.1 Hybrid-TSA test setup

10.2 Analytical Component

Individual stress components can be determined by combining TSA thermal data of Eq. 10.1. with relevant analytical information. Many such schemes process the recorded thermal information with equations based on an *Airy* stress function. For plane-stress isotropy [10], the *Airy* stress function satisfying conditions of equilibrium and compatibility is given by Eq. 10.2 below:

$$\begin{aligned}\phi = {} & a_0 + b_0 \ln r + c_0 r^2 + d_0 r^2 \ln r + \left(A_0 + B_0 \ln r + C_0 r^2 + D_0 r^2 \ln r\right)\theta + \left(a_1 r + b_1 r \ln r + \tfrac{c_1}{r} + d_1 r^3\right)\sin\theta \\ & + \left(a_1' r + b_1' r \ln r + \tfrac{c_1'}{r} + d_1' r^3\right)\cos\theta + \left(A_1 r + B_1 r \ln r\right)\theta \sin\theta + \left(A_1' r + B_1' r \ln r\right)\theta\cos\theta + \textstyle\sum_{n=2}^{\infty}\left(a_n r^n + b_n r^{n+2}\right. \\ & \left. + \ln r + c_n r^{-n} + d_n r^{2-n}\right)\sin n\theta + \textstyle\sum_{n=2}^{\infty}\left(a_n' r^n + b_n' r^{n+2} + c_n' r^{-n} + d_n' r^{2-n}\right)\cos n\theta\end{aligned} \tag{10.2}$$

where S in Eq. 10.2 can be expressed in terms of the *Airy* stress function coefficients since

$$\sigma_1 + \sigma_2 = \frac{1}{r}\frac{\partial \phi}{\partial r} + \frac{1}{r^2}\frac{\partial^2 \phi}{\partial \theta^2} + \frac{\partial^2 \phi}{\partial r^2} \tag{10.3}$$

To date, some work has been done aiming at determining the effects of: the number of *Airy* coefficients, the number of TSA data points, and the level of noise on the overall accuracy of Hybrid-TSA; but without exploring the potential of filtration of TSA images. While TSA data acquisition software (e.g. DeltaTherm by StressPhotonics [11]) does offer different types of filter, the work presented here is focused on the effectiveness of TSA image filtration in the context of Hybrid-TSA.

10.3 Reconstructing TSA Image

The study here is performed on an isotropic disk that is compressed along its diameter as shown in Fig. 10.1. The isopachic stress expression was simulated using the exact analytical solution given in [12] as shown in Eq. 10.4:

$$S_{exact} = \sigma_1 + \sigma_2 = \frac{-2P}{\pi t}\left[\frac{(R-y)^3 + (R-y)\,x^2}{\left(x^2 + (R-y)^2\right)^2} + \frac{(R+y)^3 + (R+y)\,x^2}{\left(x^2 + (R+y)^2\right)^2} - \frac{1}{R}\right] \tag{10.4}$$

The analytical expression, Eq. 10.4, was used to simulate experimental parameters such as number of data points and more importantly, introduce multiple noise levels. Due to symmetry, only the first quadrant was examined: see Cartesian and polar coordinate systems in Fig. 10.2. The *Airy* expression of S in Eq. 10.3 was reduced to Eq. 10.5 below for the symmetry and location of the origin:

$$S_{Airy} = 4c_0 + \sum_{n=2,4,\ldots}^{\infty}\left[4b_n'\,(n+1)\,r^n \cos n\theta\right] \tag{10.5}$$

The solution to the Hybrid-TSA involves solving an over-determined linear-least squares problem where S_{Airy} is equated to S_{TSA}, given in Eq. 10.6:

$$\left\{S_{Airy}\right\}_{m\times 1} = [A]_{m\times k}\,\{\text{coef}\}_{k\times 1} = \{S_{TSA}\}_{m\times 1} \tag{10.6}$$

where: m is the number of TSA data points used, k the number of coefficients, and $[A]$ the *Airy* matrix. The latter quantity is composed of m 1st stress invariant expressions of the form of Eq. 10.5 in terms of r and θ associated with the m TSA data points used. Upon solving for the coefficients in Eq. 10.6, those are then substituted back into Eq. 10.5 such that the TSA stress field can be reconstructed using Eq. 10.7.The reconstructed image is referred to as S_{hybrid} and is the result of this Hybrid-TSA method.

$$\left\{S_{hybrid}\right\}_{m\times 1} = [A]_{m\times k}\;\left\{[A]_{m\times k}\backslash\{S_{TSA}\}_{m\times 1}\right\} \tag{10.7}$$

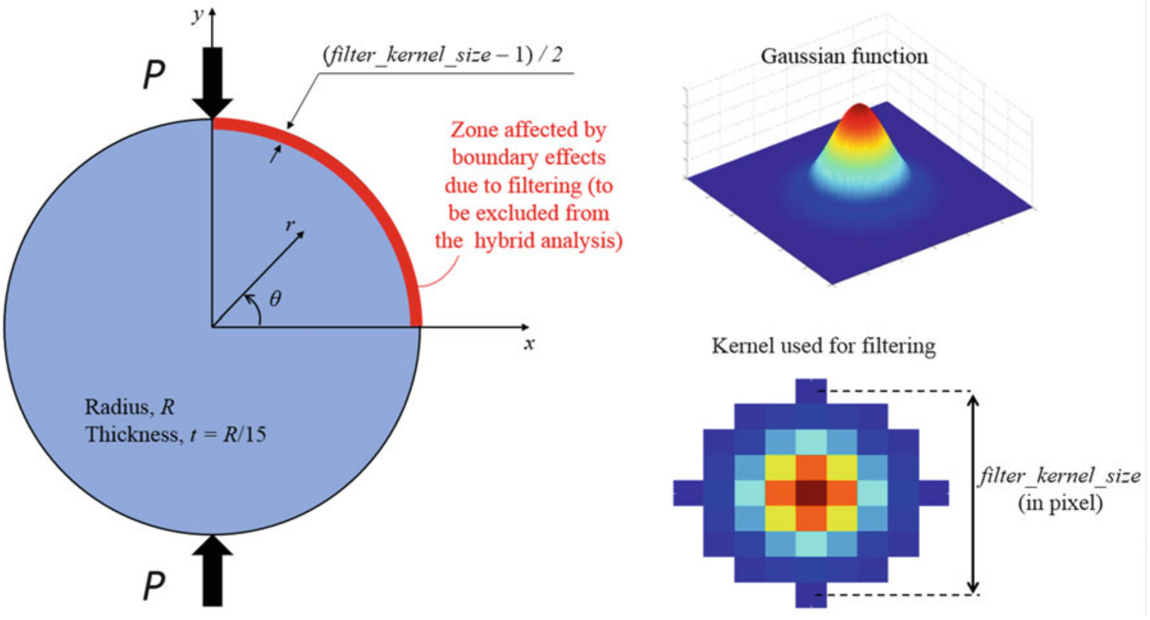

Fig. 10.2 Diametrically loaded disk

10.4 Simulated Experiments

10.4.1 Methodology

For each test case, a single synthetic S_{exact} image is constructed from Eq. 10.4 as an initial step. Second step, 50 white noise images are masked onto the original one for a given white noise level (expressed in percentage being a study parameter). Numerous noisy images are indeed necessary to extract a global trend about the influence of the filter. Step three, filtration is applied to each of the 50 noisy images with the filter kernel size (in pixel being a processing parameter). Step four, all the 50 S_{noisy} and 50 $S_{filtered}$ are pushed into the Hybrid-TSA approach where they are combined with S_{Airy} of Eq. 10.5, and ultimately reconstructed using Eq. 10.7. For every reconstructed image, the error indicators in Eqs. 10.8 and 10.9 below have been used as a metric for the improvement, or in some cases the lack of improvement, experienced from the image filtration.

$$\mathrm{E}_{filter} = \sum \left[\frac{\left| \frac{S_{exact}}{S_{max}} \right| \times \left(S_{hybridfilter} - S_{exact} \right)^2}{N} \right] \tag{10.8}$$

$$\mathrm{E}_{nofilter} = \sum \left[\frac{\left| \frac{S_{exact}}{S_{max}} \right| \times \left(S_{hybridnofilter} - S_{exact} \right)^2}{N} \right] \tag{10.9}$$

where N is the number of pixels used. In addition, a local error at a pixel located at (x, y) can be defined as follows:

$$\mathrm{E}_{\%}(x, y) = \frac{\boldsymbol{S_{hybrid}}\ (\boldsymbol{x}, \boldsymbol{y}) - \boldsymbol{S_{exact}}\ (\boldsymbol{x}, \boldsymbol{y})}{\boldsymbol{S_{exact}}\ (\boldsymbol{x}, \boldsymbol{y})} \times 100\% \tag{10.10}$$

Note that E_{filter} and E_{no_filter} have no unit, and can be thought of as “normalized” global error indicators. Indeed, they take into account the magnitude S_{exact} of each pixel relative to the maximum magnitude S_{max} over the disk (excluding the zone affected by boundary effects, see Sect. 4.3) in computing the root mean square, as opposed to $\mathrm{E}_{\%}$ of Eq. 10.10 which is a “straight forward” local percentage error. As calculation is performed for 50 copies of noise, it is then possible to do a statistical analysis on the output data (E_{filter}, E_{no_filter} and $\mathrm{E}_{\%}$).

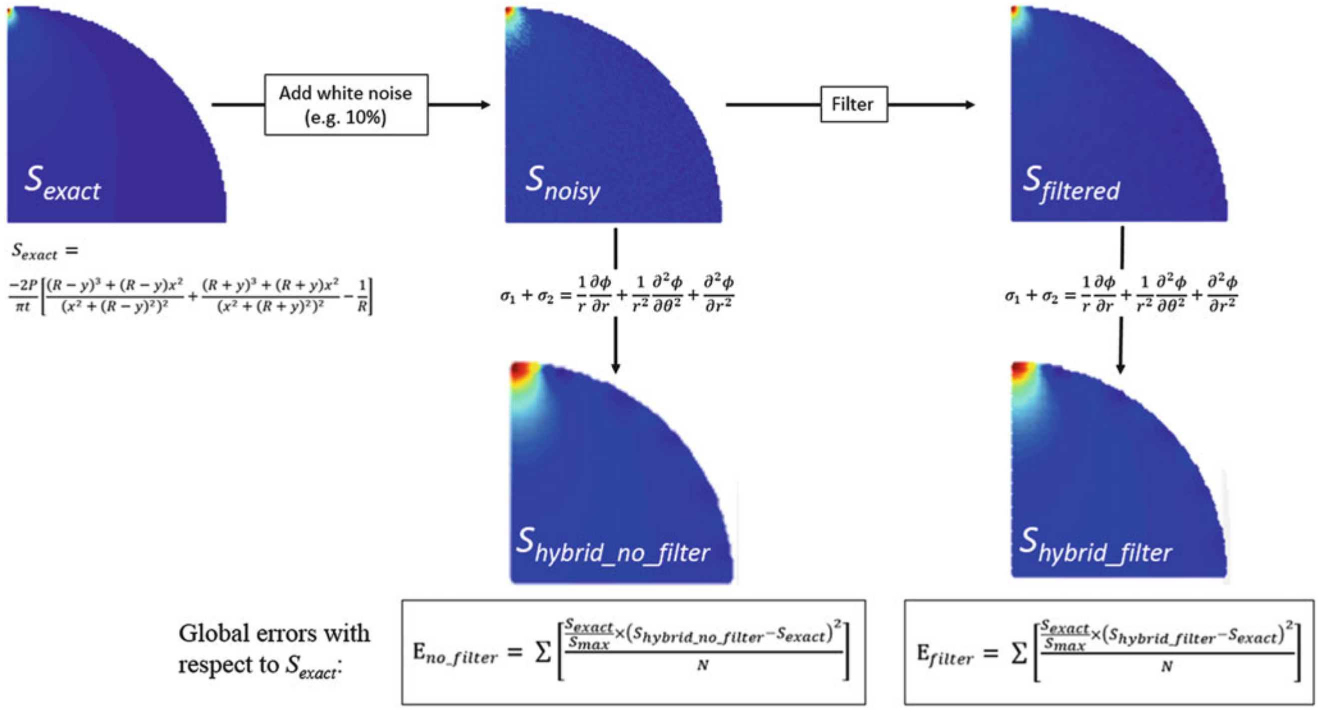

Fig. 10.3 Numerical experiment flow chart

Figure 10.3 describes the flow of the simulated experiment described above. Note that the color bars of the stress contour plots are not shown here as this is for illustration purposes only. The level of white noise in that figure is set here to 10 % such that the differences between S_{exact}, S_{noisy} and $S_{filtered}$ is visually obvious. One immediate observation from the flow chart of Fig. 10.3 is the fact that the hybrid approach itself provides what can be thought of as an "*implicit*" filter to the noisy image, as the reconstructed fields are built from (analytical) continuous functions. This is evident when comparing the reconstructed image $S_{hybrid\_no\_filter}$ and the noisy image S_{noisy} in Fig. 10.3. All S results can be then normalized with respect to S_{origin}, which is the value at $x = y = 0$, see Eq. 10.4:

$$S_{origin} = \frac{-2P}{\pi t}\left[\frac{1}{R}\right] \tag{10.11}$$

10.4.2 Filtration Approach

A Gaussian filtering is applied to each of the 50 noisy images S_{noisy}. In practice, it is performed by convolution of a Gaussian kernel: see Fig. 10.2. A circular kernel is considered with a diameter equal to six times the standard deviation of the Gaussian function, enabling us to capture the main part of the Gaussian (note however that a normalization of the kernel values is required in order to keep a sum of the kernel values equal to one [13]). As a consequence, the filter can be governed by only one parameter: the diameter of the kernel, which is here expressed in pixel (see parameter *filter_kernel_size* in Fig. 10.2). An uneven number is required for *filter_kernel_size* to keep the symmetry of the kernel.

10.4.3 Boundary Effects

Pixels outside the disk are not usable. Different strategies are available to define the filtered values near the boundaries. For the present study, it was chosen to simply exclude the zone affected by boundary effects. In practice, a layer equal to half the kernel diameter is removed from the analysis: see Fig. 10.2. This clearance distance is thus linked to the filter kernel size chosen. Note that the values of the synthetic TSA data S_{exact} near to the very top and bottom (location of point compressive loads) tends to infinity. The clearance zone enables us to exclude also these two stress concentration zones. This is done prior to combining the S_{exact} from Eq. 10.4 with S_{Airy} from Eq. 10.5, such that the linear least square operation of Eq. 10.7 is accomplished without any numerical issues. Still, this simulated test does mimic a real experimental one as it is not uncommon to remove experimental TSA data near edges of cutouts and discontinuities. This is mainly due to the boundary temperature effects as well as boundary vibration effects when the specimen is cyclically loaded while the data is recorded. More information on boundary effects and ways to amend them are discussed in [14].

10.4.4 Results

In a previous study, it was shown that the number of points *m* has an important impact on the quality of the Hybrid-TSA results. In fact, and contrary to what may seem obvious, the greater the number of TSA points used does not render the hybrid-reconstructed results better (regardless of the Airy coefficients used). Moreover, it was revealed that the level of white noise had no influence on the optimal number *k* of Airy stress function coefficients to use [15].

10.4.4.1 Effect of Noise Level

In this numerical test, the number *m* of data points is fixed to 30,000 points, a typical number to use when using a 256 × 256 TSA sensor camera, and the number of Airy stress function coefficients is fixed here to $k = 11$. Moreover, the kernel filter size is fixed to *filter kernel size* $= 7$, and thus the only variable in this numerical experimental is the white noise level. Figure 10.4 below displays both errors E_{filter} and E_{no_filter} with respect to various noise levels varying from 1 % to 10 %. The statistical bar chart reveals that an improvement is achieved by employing the filter prior to the image reconstruction

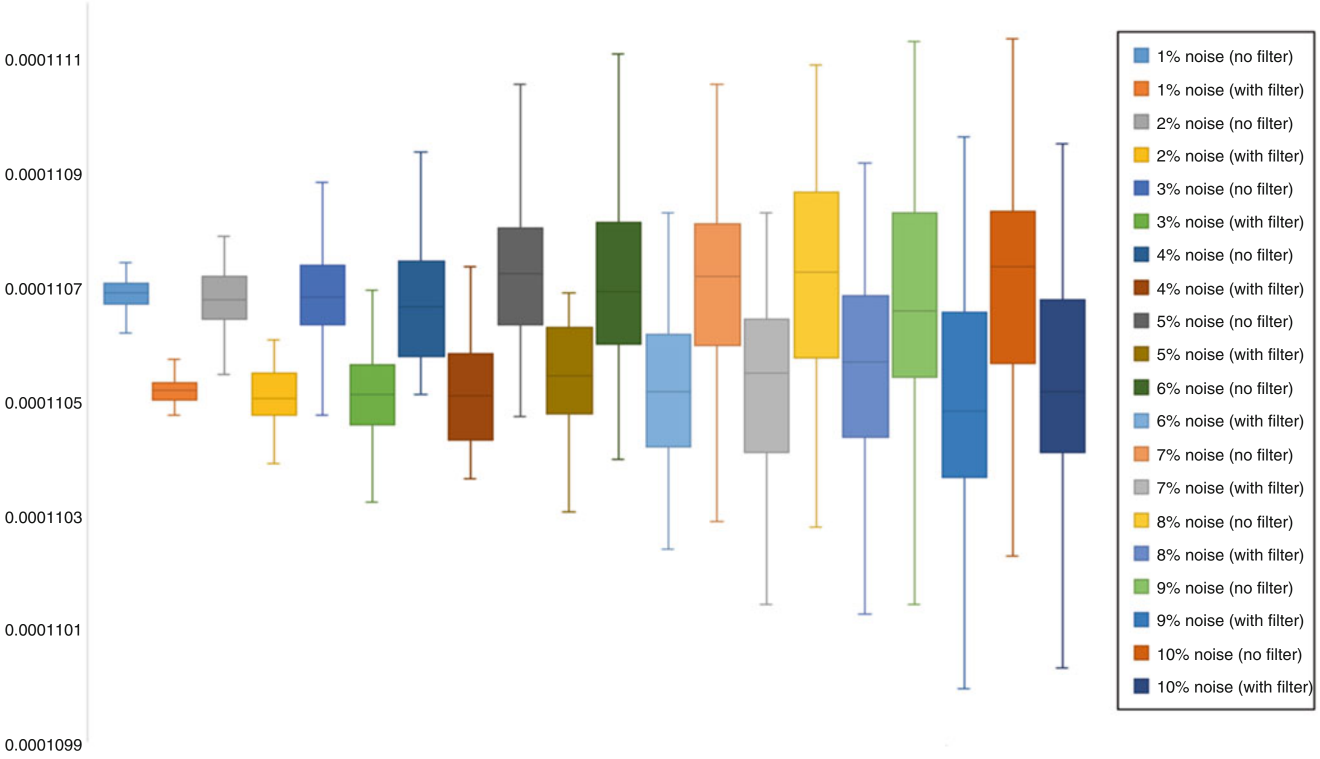

Fig. 10.4 Error bar comparing results pre- VS post- filtration for different white noise levels

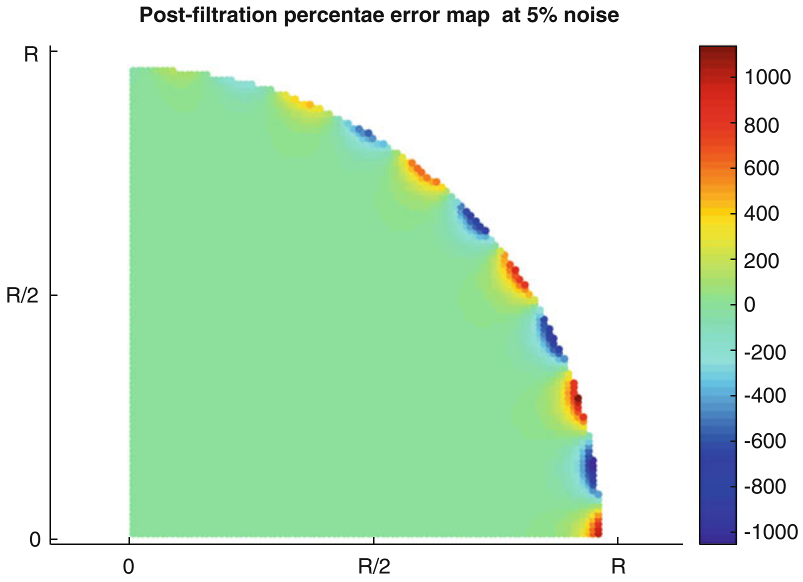

Fig. 10.5 Map of local $\boldsymbol{E}_{\%}(\boldsymbol{x},\boldsymbol{y})$ post-filtration with 5 % noise

for all noise levels. As mentioned earlier, each test configuration (e.g. noise level = 5 %, $m = 30{,}000$, $k = 11$, *filter kernel size* = 7) is performed on 50 synthetic noisy TSA images. That being said, Fig. 10.4 also reveals that the standard deviation of both errors E_{filter} and E_{no_filter} increases with higher noise levels. The stress function effect is quite substantial such that the reconstructed hybrid results are almost independent on the level of the noise. This explains why raw image filtering was never applied for Hybrid-TSA approaches.

Figure 10.5 is a map of the local error $E_{\%}(x, y)$, Eq. 10.10, for a given test scenario with noise level = 5 %. Note that the very high percentage error magnitudes at the edges are at locations of low stress magnitude, where a small change would reflect a high error. This is the main reason why Eqs. 10.8 and 10.9 with weighted *rms* error is more meaningful and representative in these numerical experiments. Also note the fluctuating sinusoidal trend in the error which is a reflection of the stress function expression of Eq. 10.4.

10.4.4.2 Effect of Kernel Size

With the effect of the filtration being small compared to the natural filter due to the stress reconstructing approach based on analytical expression; a few other parameters have been varied, such as the *filter kernel size* parameter and the number of points selected out of the total field to be used in the hybrid approach, denoted m' in the following. Figure 10.6 below is one set of numerical experiments for which the white noise was fixed to 10 %, number of stress function coefficients, k, set to 11, while the filter kernel size is varied for different number of points used, m'. Contrary to what was expected, even for a fairly few number of noisy data points, the stress function had an enough influence to steer the reconstructed image to its correct exact one with the filter kernel size having a minimal effect when looking at the magnitudes of the unitless errors E_{filter} and E_{no_filter} on the y-axis of Fig. 10.6. Similar to the previous numerical experiments, a set of 50 noisy images were used for each test configuration with their corresponding average error being the one plotted in Fig. 10.6.

The study thus far has shown a small influence of a Gaussian filtering to processing of TSA data in the context of Hybrid-TSA, as a consequence of the *implicit* filtration that the stress function introduces to the hybrid result. Other filters are available for the processing of thermal-based data [16] and will be considered in further work as well as the effects of the point location.

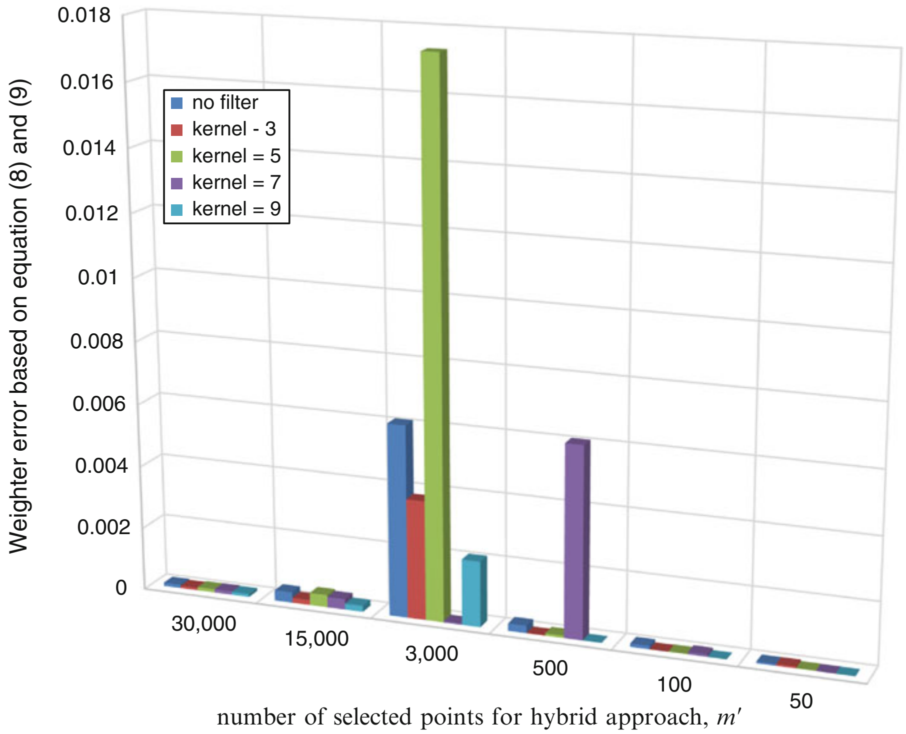

Fig. 10.6 Effects of filter kernel size for different m'

References

1. Stanley, P., Chan, W.: Assessment and deleopment of the thermoelasic technique for engineering application: four years of progress in stress analysis by thermoelasic techniques, vol. 731. SPEI, London (1987)
2. Ryall, A.W.T.G.: Determining stress components from the thermoelastic data: a theoretical study. Mech. Mater. **7**(3), 205–214 (1988)
3. Lin, S.J., Matthys, D.R., R. R. E.: Separating stresses thermoelastically in a central circularly perforated plate using an airy stress function. Strain. **45**(6), 516–526 (2009)
4. Lin, S.J., Quinn, S., Matthys, D.R., New, A.M., Kincaid, I.M., Boyce, B.R.K.A.A., Rowlands, R.E.: Thermoelastic determination of individual stresses in vicinity of a near-edge hole beneath a concentrated load. J. Exp. Mech. **51**(6), 797–814 (2010)
5. Khaja, A., Rowlands, R.E.: Experimentally determined stresses associated with elliptical holes using polar coordinates. Strain. **49**(2), 116–124 (2013)
6. Samad, W.A., Rowlands, R.E.: Full-field thermoelastic stress analysis of a finite structure containing an irregularly-shaped hole. J. Exp. Mech. **54**(3), 457–469 (2014)
7. Samad, W.A., Khaja, A.A., Kaliyanda, A.R., Rowlands, R.E.: Hybrid thermoelastic stress analysis of a pinned joint. J. Exp. Mech. **54**(4), 515–525 (2014)
8. Samad, W.A., Rowlands, R.E.: Individual stress determination in irregular perforated un symmetrically-loaded structures from temperature data. J. Aerosp. Sci. Technol. **63**, 99–91 (2017)
9. Lin, S.J., Samad, W.A., Khaja, A.A., Rowlands, R.E.: Hybrid thermoelastic stress analysis. J. Exp. Mech.: Spec. Issue Infrared Imaging Thermomechanics. **55**(4), 653–665 (2014)
10. Little, R.W.: Elasticity. Dover Publications, New York (1998)
11. StressPhotonics. [Online]. Available: http://www.stressphotonics.com/Product_Pages/Framed_Pages/TSA_DeltaTherm.html.
12. Frocht, M.M.: Photoelasticity. Wiley, New York (1948)
13. Delpueyo, D., Balandraud, X., Grédiac, M.: Heat source reconstruction from noisy temperature fields using an optimised derivative Gaussian filter. Infrared Phys. Technol. **60**, 312–322 (2013)
14. Samad, W.A., Rowlands, R.E.: On improving Thermoelastic stress analysis data near edges of discontinuities. Exp. Appl. Mech. **6**, 157–162 (2014)
15. Samad, W.A., Considine, J.M.: Sensitivity analysis of hybrid thermoelastic techniques. Residual Stress Thermomechanics Infrared Imaging Hybrid. Tech. Inverse. Probl. **9**, 29–36 (2016)
16. Beitone, C., Balandraud, X., Delpueyo, D., Grédiac, M.: Heat source reconstruction from noisy temperature fields using a gradient anisotropic diffusion filter. Infrared Phys. Technol. **80**, 27–37 (2017)

Chapter 11
Optical Analysis of Residual Stress with Minimum Invasion

Sanichiro Yoshida, Fumiya Miura, Tomohiro Sasaki, Daniel Didie, and Shahab Rouhi

Abstract Electronic Speckle-Pattern Interferometry (ESPI) has been applied to analyze welding-induced residual stresses. A tensile load is applied to a butt-welded aluminum alloy specimen (tungsten arc bead-on-plate welding on a 100 × 20 mm plate of 5 mm thick) at loading levels up to 20 % of the yield stress, and the acceleration field is evaluated from subtraction of the displacement fields taken in two consecutive time steps. Based on our previously proposed algorithm, the residual stress is estimated from the acceleration field. The resultant residual stress data are compared with experimental results for the same welded specimen based on acoustoelasticity and X-ray diffractometry. Numerical analysis based on Finite Element Modeling has also been conducted. The residual stress data resulting from all the four methods agree with one another, commonly exhibiting the generally accepted concepts that thermal expansion causes tensile residual stress along the weld line and that the effect is greater at the ending side of butt-welding than starting side. The maximum tensile residual stress along the weld line is estimated to be 76.9 ± 12.8 MPa.

Keywords Residual stress • Butt-welding • Electronic Speckle-Pattern Interferometry • X-ray diffractometry

11.1 Introduction

Residual stress induced by welding is complicated. Its analysis, in particular nondestructive analysis, is not easy. The fundamental difficulty is twofold. First, as a stress locked inside the material, residual stress is hidden from outside and passive analysis is essentially impossible. A certain force must be applied to the material nondestructively and the material's responses must be observed. In doing so, the applied force must be low enough not to affect the state of stress. Second, the effect of welding on the material itself is complicated. The thermal flow through the material depends on a number of parameters such as the phase of the material, ambient temperature along with other factors that affect the cooling rate, fixation of the work, etc. In the cooling phase, permanent deformation occurring at various locations can form tensile or compressive residual stresses alternatively. Our previous experimental study [1] on residual stress induced by butt-welding on dissimilar thin metal plates indicates that the tensile and compressive residual stresses alternate over the specimen with high spatial frequency. This result indicates that if we use a destructive technique, it is necessary to evaluate the residual stress with a small increment, which could weaken the welded work. Application of a nondestructive method is important.

X-ray Diffractometry (XRD) [2] and Acoustoelasticity [3, 4] are probably the most prevailing nondestructive techniques for residual stress analysis. They are well established techniques but have issues as well. XRD is able to analyze only a subsurface region of the specimen, typically within a few atomic layers from the surface. Our previous study [5] indicates that a weld-induced residual stress can be 10–20 μm deep from the surface. XRD will not have sensitivity for this depth. It is also heavily dependent on the crystallographic grain size. Acoutoelasticity requires the knowledge of the third-order elastic coefficient [6], and the result of analysis heavily depends on the accuracy of the coefficient. The acoustic wave inside the specimen often has a number of modes and handling these modes is not straightforward.

S. Yoshida (✉) • D. Didie • S. Rouhi
Department of Chemistry and Physics, Southeastern Louisiana University, Hammond, LA 70402, USA
e-mail: syoshida@selu.edu

F. Miura
Department of Chemistry and Physics, Southeastern Louisiana University, Hammond, LA 70402, USA

Department of Engineering, Niigata University, Ikarashininocho 8050, Nishi-ku, Niigata-shi, Niigata 950-2181, Japan

T. Sasaki
Department of Engineering, Niigata University, Ikarashininocho 8050, Nishi-ku, Niigata-shi, Niigata 950-2181, Japan

A. Baldi et al. (eds.), *Residual Stress, Thermomechanics & Infrared Imaging, Hybrid Techniques and Inverse Problems, Volume 8*,
Conference Proceedings of the Society for Experimental Mechanics Series, DOI 10.1007/978-3-319-62899-8_11

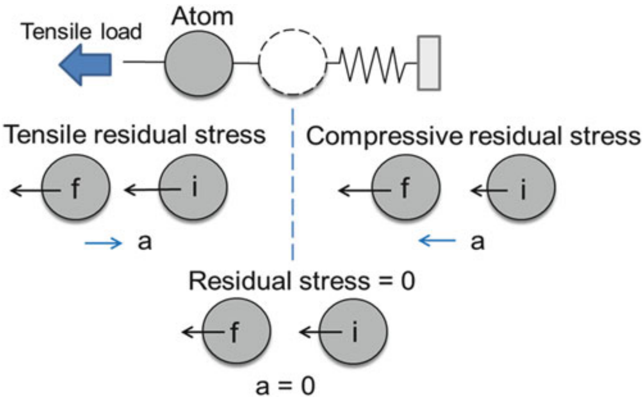

Fig. 11.1 Spring-mass model of residual stress "*i*" and "*f*" stand for "initial" and "final" states

Considering these situations, we previously proposed to use a combination of an optical interferometric technique known as the Electronic Speckle-Pattern Interferometry (ESPI) and acoustoelasticity [1, 5]. We applied the combined technique to butt-welded specimens of dissimilar material and confirmed the feasibility. Sasaki et al. [7] also have confirmed the feasibility of this method in their analysis of fatigue induced residual stresses. In the present study, we used XRD in addition to ESPI and Acoustoelasticity to analyze a butt-welded aluminum alloy specimen. We also conducted Finite Element Modeling to simulate the thermal effect of the welding to the specimen used for the experiment. Results of all four methods show good qualitative agreement with one another in (a) the residual stress along the weld line tends to be tensile and (b) the tendency is greater at the side when the welding is completed than it is started. The aim of this paper is to report on these experimental studies and discuss the experimental results along with the numerical results.

11.2 Principle of Operation of ESPI Method

Compressive and tensile residual stresses create situations where the material is pushed toward and pulled from the equilibrium, respectively. Hence, they can be modeled by a mass connected to a compressed or stretched spring. Consider in Fig. 11.1 two time-steps when an external force continuously pulls the mass connected to a spring. If the spring is initially (at the first time-step) compressed, the external force pulls the mass toward the equilibrium. Consequently, the velocity of the mass in the final state (the second time-step) is greater than the initial state. In other words, the acceleration is in the same direction as the external force. Conversely, if the spring is initially stretched, the external force pulls the mass further away from the equilibrium. Consequently, the spring resists the external force and the velocity of the mass at the final state is lower than the initial state; the acceleration is opposite to the direction of the external force.

In-plane sensitive Electronic Speckle-Pattern Interferometry (ESPI) is capable of taking displacement data of an object under deformation on a continuous basis with a preset interval. This capability allows us to record displacement of a specimen being pulled at a constant rate at given time steps as a full-field data. By setting the interval between neighboring time steps constant and making the interval small as compared with the pulling rate, we can evaluate the velocity at each time step by dividing the displacement recorded at each time step by the constant interval. Further, by subtracting these velocity data obtained by a given time step from that in the preceding time step, we can obtain the acceleration as a full-field data at each time step. More details about the procedure to record acceleration are discussed under Sect. 11.3 (Fig. 11.2).

11.3 Experiments

11.3.1 Specimen

A bead-on-plate specimen of aluminum alloy 5,083 processed by gas tungsten arc welding is used for the present study. Figure 11.3 shows the dimension and microscopic images of the specimen. Three horizontal lines and 11 vertical lines indicated in Fig. 11.3a bottom defines the coordinate points used to measure the acoustic velocity with an ultrasonic

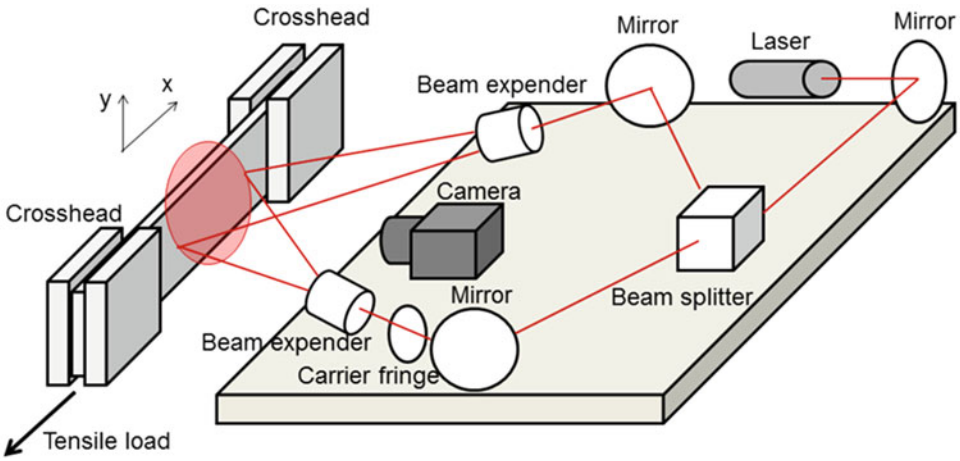

Fig. 11.2 ESPI setup

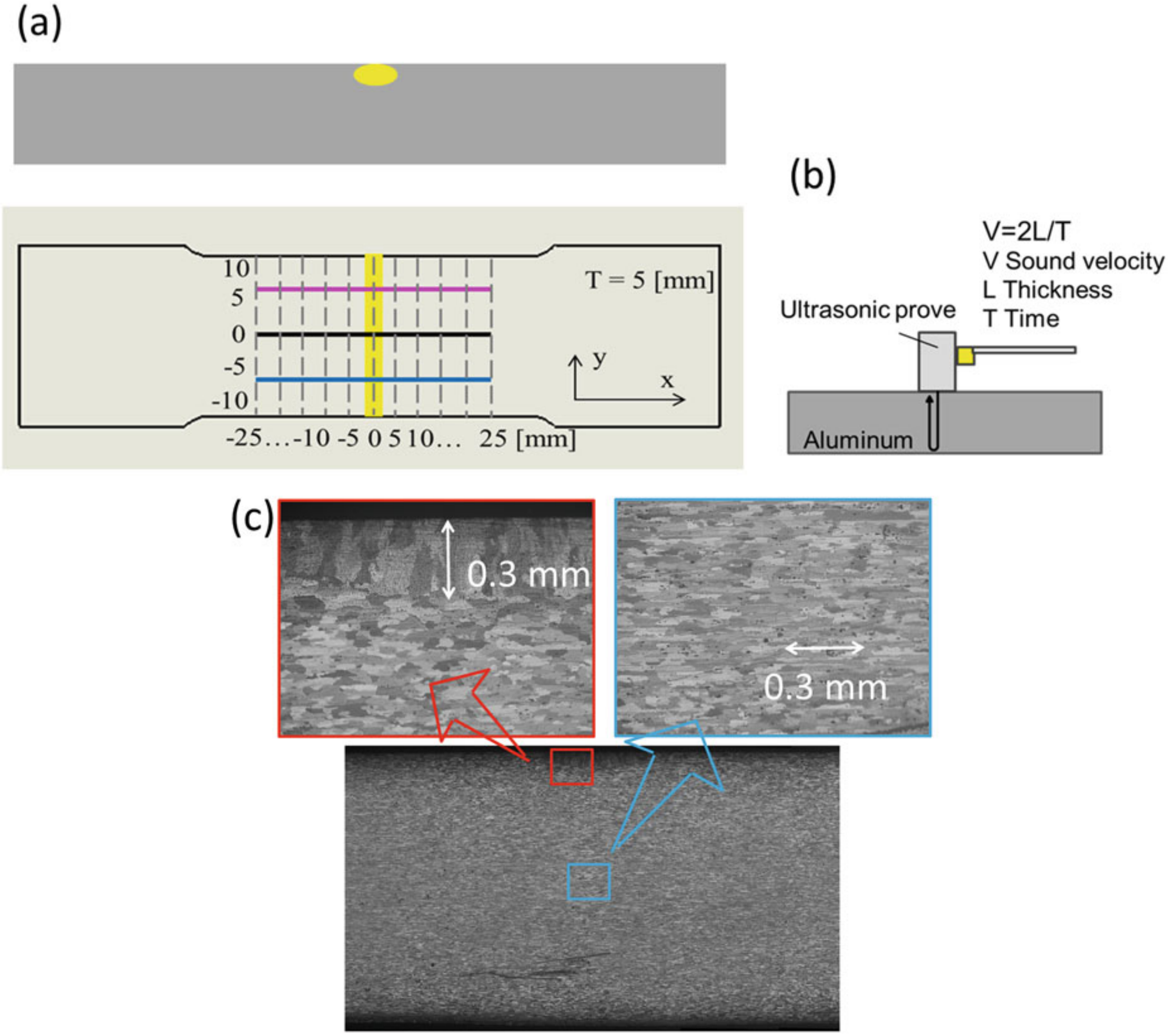

Fig. 11.3 (**a**) Dimension of the specimen; (**b**) acoustic transducer; (**c**) microscopic image of the specimen

Table 11.1 Welding conditions

Welding speed	Welding current	Welding voltage	Shielding gas	Cooling
5.0 mm/s	100 A	200 V	Argon (10 l/min)	Ambient air cooled

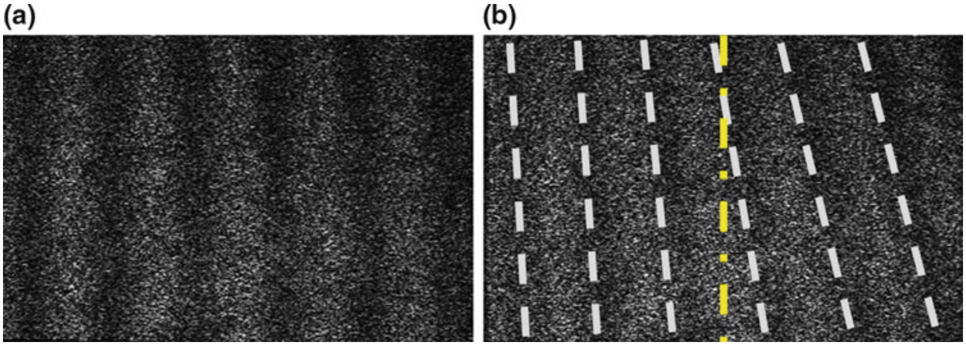

Fig. 11.4 (**a**) Carrier fringes; (**b**) Typical fringes due to deformation *vertical line* in the *middle* indicates the weld line

contact transducer as shown in Fig. 11.3b. The top drawing in Fig. 11.3a illustrates the depth of the bead-on-plate welding schematically. The microscopic image in Fig. 11.3c indicates that the depth of the welding is 0.3 mm, or less than 10 % of the thickness. The plate was placed on a copper table without any fixture to restrain its thermally induced deformation. Table 11.1 summarizes the welding conditions.

11.3.2 Electronic Speckle-Pattern Interferometry (ESPI)

Pulling the specimen with a constant rate of 10 μm/s, we continuously recorded interferometric image of it with a digital camera (Fig. 11.2) at a frame rate of 30 frame/s. By changing the incident angle of the left laser beam of the interferometer, we introduced a known amount of relative phase (a carrier fringe system) every 10 N of tensile load increment. Subtraction of interferometric images yields fringe patterns as shown in Fig. 11.4. Here Fig. 11.4a shows carrier fringes and (b) shows fringes due to deformation on top of the phase represented by the carrier fringes. Note that the fringes in (b) are slant and the fringe interval is higher near the bottom side than the top side. This indicates that the specimen undergoes more horizontal stretch towards the top side than the bottom.

11.3.3 Acoustic Transducer

The acoustic transducer shown in Fig. 11.3b can be operated in three modes; shear wave modes traveling in the x and y directions, and the longitudinal mode in the z direction. The xyz-coordinate system is shown in Fig. 11.3a. In all modes, the acoustic wave reflects off the rear surface and received on the front surface. Therefore, the measured wave velocity represents the elastic property of the specimen averaged over the thickness.

11.3.4 X-Ray Diffractometry (XRD)

We used a standard X-ray diffractometer for this study. The residual stress was determined from the slope of the $2\theta - \sin^2\psi$ plot. Here θ is the angle of diffraction, ψ is the angle between the specimen surface and the crystallographic plane, and the residual stress is compressive/tensile if the slope is positive/negative [2]. The margin of error for the present XRD was approximately 10 %.

11.4 Results and Discussion

11.4.1 Acceleration Measurement with ESPI

Figure 11.5 shows the acceleration field that we generated using ESPI with the above-mentioned method. Here, (a) is the result for the welded specimen and (b) is for a non-welded specimen of the same material and dimension that we used as a control. Both data were generated when a tensile load was increased from 2,000 to 2,010 N. As explained by Fig. 11.1 and the related explanation, when residual stress is compressive the corresponding acceleration is in the same direction as the external tensile load, and when residual stress is tensile the acceleration is opposite to the tensile load. In the present case, since the applied tensile load is leftward, and according to the coordinate system shown in Fig. 11.3a the leftward direction is negative, negative acceleration represents compressive residual stress; conversely, positive acceleration represents tensile residual stress.

Figure 11.5 indicates the following tendency. (1) The non-welded specimen exhibits a flatter profile near the weld line ($x = 0$ mm) as compared with the welded specimen. (2) The welded specimen indicates that along the weld line the residual stress tends to be tensile. On both size of the weld line, the residual stress is more compressive for all three lines perpendicular to the weld line (three lines at $y = -5$, 0 and 5 mm) in common. (3) Along the weld line, the residual stress is most tensile-like at $y = 0$ mm followed by at $y = 5$ mm, and it is compressive-like at $y = -5$ mm.

From (1) and (2) we can say that the near weld-line feature of the profile observed in Fig. 11.5b represents the effect of welding. Tendency (2) is consistent with the following generally accepted concept; “During the heating phase a butt-welded region undergoes thermal expansion and this induces permanent compressive deformation in the surrounding regions. During the cooling phase, the thermally expanded material at the welded region tries to shrink but the shrinkage is hindered by the permanently compressed surrounding regions. Hence, the residual stress of a butt-welded region tends to be tensile.” Tendency (3) is consistent with another generally accepted concept that “this effect (that a butt-welded region tends to be residually tensile) is greater near the ending side of the welding than the starting side because the heat is more diffusive at the beginning of welding when the entire work is lower in the temperature.”

11.4.2 Acoustic Velocity Measurement

Figure 11.6 shows acoustic wave velocity in the x-direction that we measured with the contact acoustic transducer (Fig. 11.3b) for (a) the welded specimen, (b) the non-welded specimen and (c) the ratio of the velocity measured in the welded specimen to the non-welded specimen. We made these measurements prior to the ESPI experiment. Similar to the ESPI measurement case in Fig. 11.5, the non-welded specimen shows a less feature in the profile. According to acoustoelasticity [3], the sound velocity increases when the residual stress is compressive and decreases if it is tensile. The vertical axis of three plots in Fig. 11.6 is reversed so that upward direction corresponds to tensile residual stress, as Fig. 11.5.

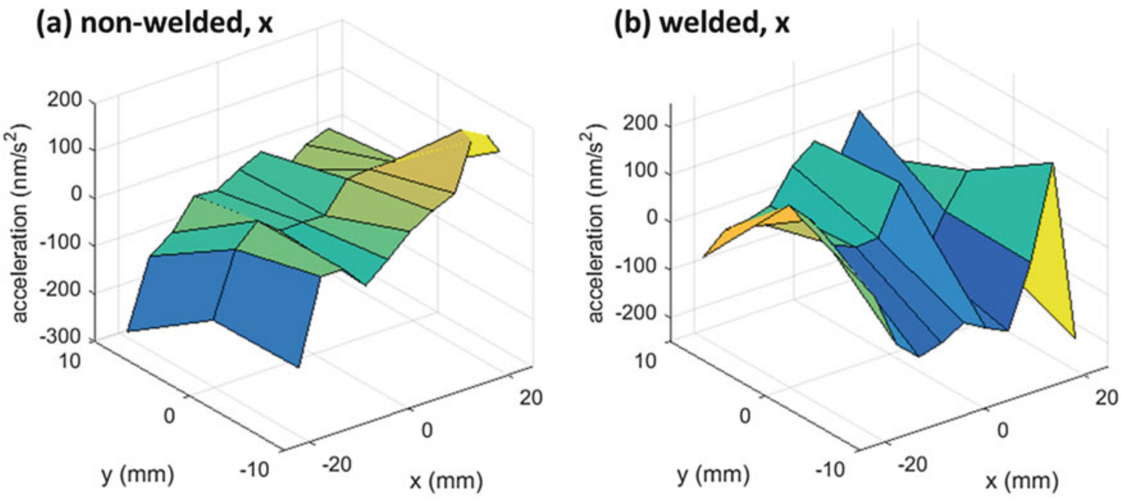

Fig. 11.5 Acceleration field of (**a**) non-welded and (**b**) welded specimens

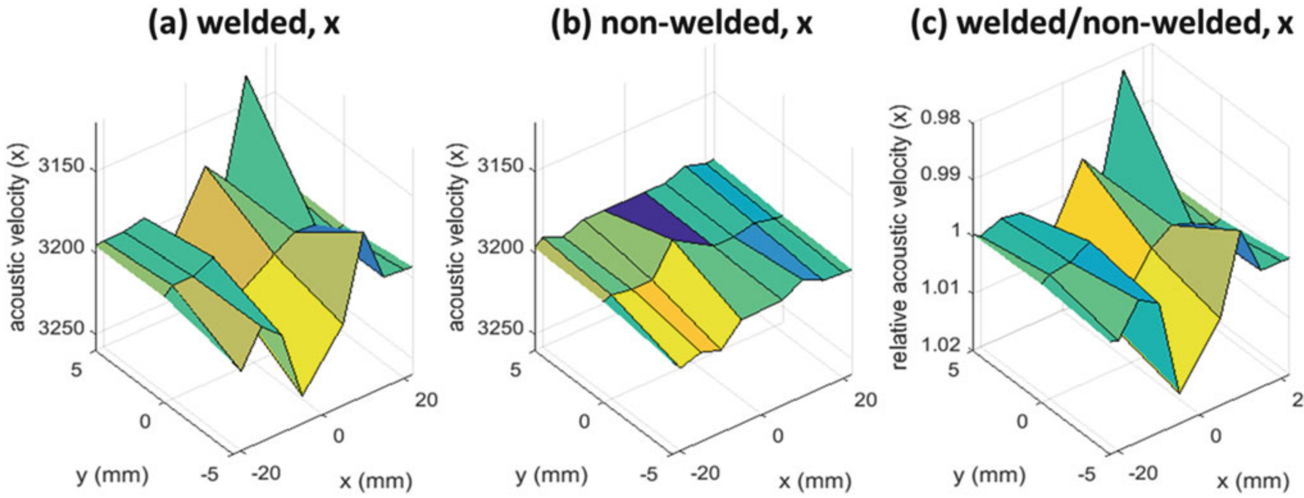

Fig. 11.6 Acoustic velocities measured in (**a**) welded specimen, (**b**) non-welded specimen, and (**c**)the ratio

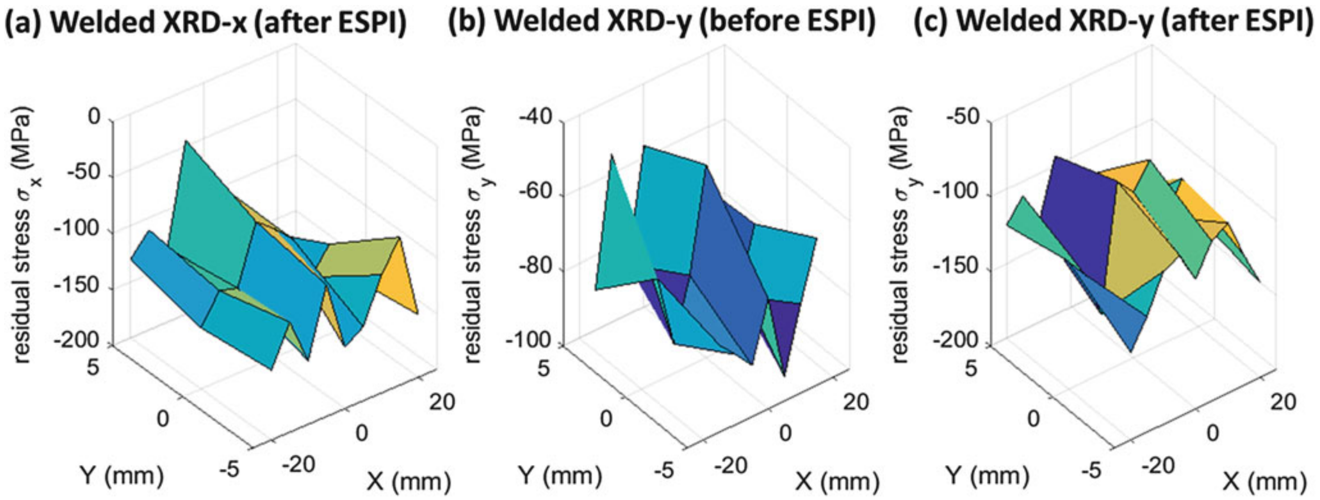

Fig. 11.7 Residual stress by XRD (**a**) σ_x after ESPI, (**b**) σ_y before ESPI, and (**c**) σ_y after ESPI measurement

11.4.3 Residual Stress Measurement with XRD

Figure 11.7 are residual stress components in the x and y directions evaluated with the X-ray diffractometer. Figure 11.7a is the x-component evaluated after the above-discussed acceleration measurement with ESPI; (b) and (c) are the y-component measured before and after the acceleration measurement, respectively. The sign convention of the residual stress is that tensile stress is positive and compressive stress is negative. All cases in Fig. 11.7 indicate that the residual stress is compressive. The non-welded specimen measured by the same X-ray diffractometer with the exact same procedure also showed compressive residual stress at all points of measurement; the average stress measured at five representative points was -121.6 ± 12.8 MPa. We repeated the measurement after annealing the non-welded specimen and found the same level of compressive residual stress (the average at the same representative points was -127.4 ± 13.4 MPa). The reason for the compressive residual stress is unknown at this time. However, this indicates that residual stress data for the welded-specimen are shifted toward the compressive side as much as -121.6 ± 12.8 MPa (call the offset compressive residual stress).

Figure 11.7a indicates that along the weld line the residual stress is more tensile like. Moreover, it clearly shows that the positive y side, the side where the welding ended, is more tensile-like than the negative y side. This feature is consistent with the acceleration data shown in Fig. 11.5b. In Fig. 11.7a, the peak stresses along the line of $x = -5$ mm in at $y = \pm 5$ mm are -44.6 MPa and -81.9 MPa, respectively. If the above-argued offset compressive residual stress is taken into account, the peak stress values at these two points become 76.9 ± 12.8 MPa and 39.6 ± 12.8 MPa, respectively. In other words, along the line of $x = -5$ mm, the residual stress is tensile.

Comparison of Figs. 11.7b and 11.7c provides us the effect of the tensile load applied to the specimen for the acceleration measurement. It is seen that the profile (shape) of the residual stress is unchanged and as a whole the residual stress tends to be more compressive after the acceleration measurement. The latter is understood as representing the Poisson's effect associated with the tensile loading for the acceleration measurement; as the specimen is pulled along the x-axis, it undergoes compressive deformation along the y-axis.

11.4.4 Finite Element Modeling and Overall Assessment

We conducted Finite Element Modeling (FEM) of the welded specimen to simulate the thermal effect induced by the butt-welding. The specimen used for the simulation was the same as the one used in the experiment discussed above. In accordance with the above-mentioned concept that the thermal expansion that the welded region undergoes during the heating phase causes compressive permanent deformation in the surrounding regions, our FEM model restrained any part of the material from further deformation once the stress of the part reached the compressive yield point.

The copper table that the specimen was placed during the welding should act as the heat sink on the rear surface. It is considered that the cooling rate from the rear surface is significantly higher than the top surface where the welding torch heats the plate. To simulate this effect, we used a higher convection rate for the rear surface. The heat source had a Gaussian profile (1.2 cm Full Width at Half Maximum) with the electric input power of 20 kW and a coupling coefficient to the specimen of 0.9 % in heat was used [8].

The residual stress was evaluated at 500 s after the welding torch reached the top side. We carefully analyzed the temporal change in the stress behavior from the moment when the welding was completed and found that there was no visible change at 500 s. The x-component of the residual stress resulting from the FEM is discussed in the next section.

11.4.5 Comparison of Results from All Methods

Figure 11.8 compares the residual stresses (the x-component) resulting from all the methods used in this study. The following observations can be made

1. Results from all four methods indicate peak tensile-like residual stress (more) parallel to the weld line near the weld. Here the word "tensile-like" is used to mean that the residual stress is greater in the positive direction. The XRD result shown in Fig. 11.8c is obtained by removing the offset stress of -121.6 MPa (the average compressive residual stress measured in non-welded and non-annealed specimen) from the raw XRD result shown in Fig. 11.7a.
2. The XRD result after the offset removal indicates the peak residual stress along the weld line is tensile from the starting to the ending side of the welding. The decrease in the residual stress from the horizontal center ($y = 0$ mm) to the starting side of the weld ($y = -5$ mm) appears to be less than the ESPI or FEM result and comparable to the acoustic case. The reason for these difference and similarity is unclear at this time.
3. ESPI, FEM and XRD results show the tendency that the ending side of welding is more tensile like than the starting side. Since the FEM uses only thermal expansion and permanent compressive deformation, this observation indicates that this tendency is explained by thermal expansion and permanent compressive deformation.
4. ESPI and FEM results show sharp decrease in residual stress (towards compressive) from the horizontal center to the starting side of the welding and relatively gradual change between the horizontal center and the ending side of the welding. Our FEM study indicates this tendency is related to the relative cooling efficiency between the top and bottom surfaces. When the same cooling rate is used for the top and bottom surfaces, there is a sharp increase towards tensile stress from the ending side of welding to the horizontal center.

11.5 Summary

The present study confirms the accepted concept that the residual stress tends to be tensile along the weld line and the effect is greater near the ending side of the weld than the starting side. The FEM assumes only thermal expansion and permanent compressive deformation. The agreement with the experimental results indicates that this effect dominates, at least under the welding and material conditions used in this study. The qualitative agreement in the residual stress profile with the

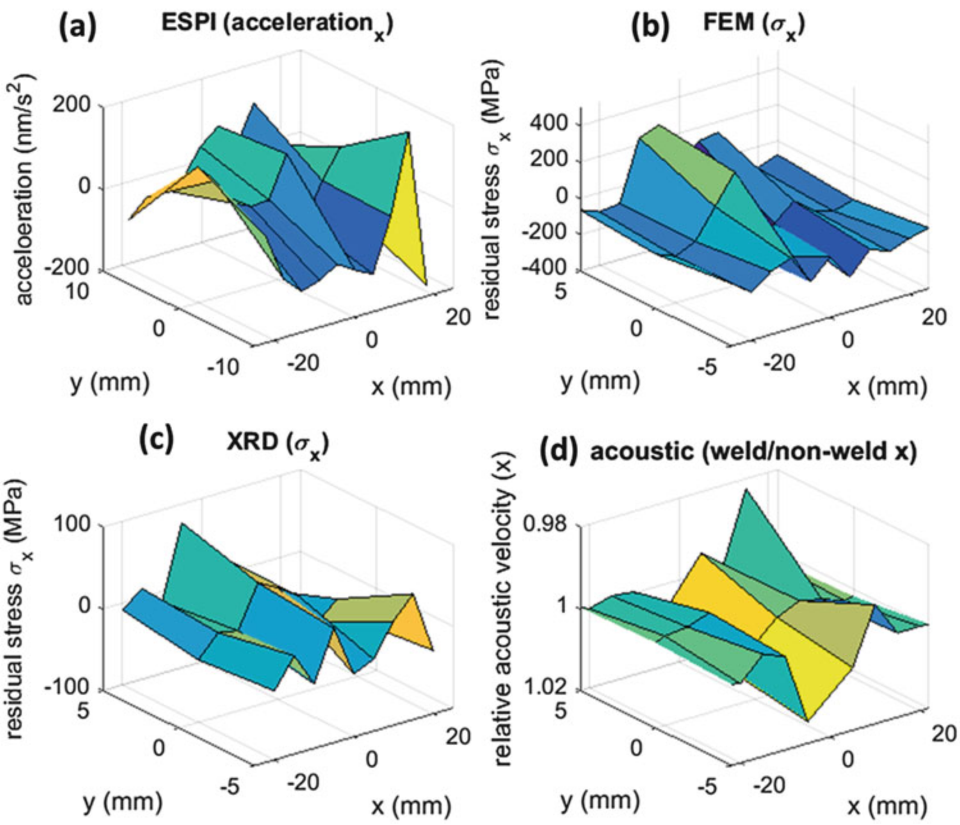

Fig. 11.8 Comparison of residual stress x-component from **a** ESPI, **b** FEM, **c** XRD and **d** Acoustoelasticit

XRD, FEM and Acoustoelasticic results validates the operation principle of the residual stress measurement based on the acceleration measurement with ESPI. This opens up the possibility of nondestructive, full-field residual stress analysis.

Acknowledgement The present research is in part supported by the Louisiana Board of Regents Pilot-fund grant LEQSF(2016-17)-RD-C-13 and Southeastern Louisiana University STAR grant.

References

1. Yoshida, S., Sasaki, T., Craft, S., Usui, M., Haase, J., Becker, T., Park, I.K.: Stress analysis on welded specimen with multiple methods. In: Jin, H., Sciammarella, C., Yoshida, S., Lamberti, L. (eds.) Advancement of Optical Methods in Experimental Mechanics, pp. 143–152. Springer, New York (2014)
2. Fitzpatrick, M.E., Fry, A.T., Holdway, P., Kandil, F.A., Shackleton, J., Suominen, L.: Determination of Residual Stresses by X-Ray Diffraction—Issue 2 Measurement Good Practice Guide No. 52. National Physical Laboratory, Teddington (2005)
3. Hughes, D.S., Kelly, J.L.: Second-order elastic deformation of solids. Phys. Rev. **92**, 1145–1149 (1953)
4. Dorfi, H.R., Busby, H.R., Janssen, M.: Ultrasonic stress measurements based on the generalized acoustic ratio technique. Int. J. Solids Struct. **33**, 1157–1174 (1996)
5. Yoshida, S., Sasaki, T., Usui, M., Sakamoto, S., Gurney, D., Park, I.K.: Residual stress analysis based on acoustic and optical method. Materials. **9**, (2016). doi:10.3390/ma9020112
6. Muir, D.D.: One-sided ultrasonic determination of third order elastic constants using angle-beam acoustoelasticity measurements. Ph.D. Thesis, Georgia Institute of Technology, Atlanta, GA, USA (2009)
7. Sasaki, T., Ono, H., Yoshida, S., Sakamoto, S.: Fatigue analysis of 7075 aluminum alloy by optoacoustic method. Presented at Society of Experimental Mechanics 2017 annual meeting. (n.d.)
8. Bonifaz, E.A.: Finite element analysis of heat flow in single-pass arc welds, Weld. Res. Suppl. **2000**, 121-s–125-s (n.d.) Available online: https://app.aws.org/wj/supplement/WJ_2000_05_s121.pdf. Accessed 28 Aug 2016

Chapter 12
Determination of Constitutive Properties in Inverse Problem Using Airy Stress Function

A. Alshaya, John M. Considine, and R. Rowlands

Abstract A new inverse problem formulation is developed using the Airy stress function. Inverse methods are used to determine the constitutive properties of a graphite/epoxy laminated composite loaded vertically by processing measured values of *v*-displacement component with an Airy stress function in complex variables. Displacements are recorded using digital image correlation. The traction-free conditions on the symmetrically located sided notches are satisfied analytically using conformal mappings and analytic continuation. The traction-free on the vertical free edge and a symmetrical condition on horizontal line of symmetry are imposed discretely. The primary advantage of this new formulation is the direct use of displacement data, eliminating the need for numerical differentiation when strain data is required. The inverse method algorithm determined the constitutive properties with errors range from 2% to 10%. Selection of Airy coefficients, test geometry configuration and comparison with other inverse methods will be addressed.

Keywords Composites • Airy stress function • Inverse problems • Digital image correlation • Complex variables

12.1 Introduction

The Airy stress function in complex variables was used extensively in determining stresses from measured displacements [1–4]. The Airy stress function can be processed with other measured data using thermoelasticity [5–7], photoelasticity [8], digital image correlation [2], moiré [9] or strain gages [10]. These hybrid methods do not necessitate knowing the applied loads, smooths the measured data and determines individual stresses throughout, including on the edge of the hole. All of the prior applications of the mapping technique evaluated the stresses by using the constitutive properties found experimentally from standard tensile tests whereas the present approach only evaluated these properties using the measured displacement from Digital Image Correlation.

One method of evaluating constitutive properties of orthotropic materials is the use of inverse methods (IM). Avril and Pierron [11] reviewed several IM approaches and showed their general equivalency. IM can be generally described as the iterative adjustments of parameters (constitutive properties) in a numerical model (Airy stress function scheme) to minimize the difference between an experimentally measured quantity (displacement) and the numerically calculated quantity.

By comparing FEM calculated out-of-plane displacement with those measured by shadow moiré, Le Magorou et al. [12] determined bending/torsion rigidities in composite wood panels by the resolution of IM. Molimard et al. [13] evaluated constitutive properties of a composite material by minimizing the difference between moiré-measured displacements and those predicted by FEM in a perforated tensile plate. Similarly, Genovese et al. [14] used IM procedures to evaluate a truss system and a composite plate. Considine [15] determined material properties in heterogeneous materials from full-field simulated displacement data using IM. Each of these references incorporated a specific type of IM entitled FEMU-U (finite element method updating – displacement). The root mean square of displacement differences, also called a cost function, between the measured values and those predicted by FEM are minimized by iteratively changing constitutive properties in

---

A. Alshaya (✉)
Kuwait University, Kuwait, Kuwait
e-mail: alshaya@wisc.edu

J.M. Considine
Materials Research Engineer, U.S. Forest Service, Forest Products Laboratory, One Gifford Pinchot Drive, Madison, WI 53726, USA
e-mail: jconsidine@wisc.edu

R. Rowlands
University of Wisconsin-Madison, Madison, WI, USA

A. Baldi et al. (eds.), *Residual Stress, Thermomechanics & Infrared Imaging, Hybrid Techniques and Inverse Problems, Volume 8*,
Conference Proceedings of the Society for Experimental Mechanics Series, DOI 10.1007/978-3-319-62899-8_12

the FEM model. FEMU-U is attractive because displacements are first-order outputs of high-resolution full-field techniques of DIC and ESPI where strain is a second-order output and has greater noise associated with numerical differentiation.

In 2-D models, the degree of freedom is $(\text{number of nodes}) \times 2 - (\text{number of constitutive parameters}) - 1$. For homogeneous, isotropic materials, the number of constitutive properties is two (E, v); for homogeneous, orthotropic materials, the number of constitutive parameters are four (E_{11}, E_{22}, G_{12}, v_{12}). For either case, the number of degrees of freedom is large and the problem is solved by minimizing least squares of the chosen cost function. The goal of this work is to evaluate the constitutive properties of a composite plate containing symmetrically-located sided-notches and vertically loaded in the strongest/stiffest material direction using IM and Airy stress function scheme. The authors are unaware of prior utilization of mapping and complex variables to experimentally determine the constitutive properties in notched composites from displacement data.

12.2 Relevant Equations

For plane problems having rectilinear orthotropy and no body forces, the Airy stress function, F, can be expressed as a summation of two arbitrary analytical functions, $F_1\,(z_1)$ and $F_2\,(z_2)$, of the complex variables, z_1 and z_2, as [13]

$$\mathcal{F} = 2Re\left[F_1\left(z_1\right) + F_2\left(z_2\right)\right] \tag{12.1}$$

such that $z_j = x + \mu_j y$ for $j = 1\,, 2$ and Re denotes the ‘real part’ of a complex number. The complex material properties μ_1 and μ_2 depend on the constitutive properties. The displacements in rectangular coordinates (x, y) of the physical $z(=x + iy)$ plane can be expressed in terms of the stress functions. By introducing the new stress functions

$$\Phi\left(z_1\right) = \frac{dF_1\left(z_1\right)}{dz_1}, \quad \text{and } \Psi\left(z_2\right) = \frac{dF_2\left(z_2\right)}{dz_2} \tag{12.2}$$

one can write the displacements as

$$u = 2Re\left[p_1\Phi\left(z_1\right) + p_2\Psi\left(z_2\right)\right] - w_o y + u_o \tag{12.3}$$

$$v = 2Re\left[q_1\Phi\left(z_1\right) + q_2\Psi\left(z_2\right)\right] + w_o y + v_o \tag{12.4}$$

where w_o , u_{o}, and v_{o} are constants of integration and characterize any rigid body translations (u_{o} and v_{o}) and rotation (w_o). The other quantities, which depend on material properties, are

$$p_1 = \frac{\mu_1^2}{E_{11}} - \frac{v_{12}}{E_{11}}, \quad p_2 = \frac{\mu_2^2}{E_{11}} - \frac{v_{12}}{E_{11}}, \quad q_1 = -\frac{v_{12}}{E_{11}}\mu_1 + \frac{1}{E_{22}\mu_1}, \quad q_2 = -\frac{v_{12}}{E_{11}}\mu_2 + \frac{1}{E_{22}\mu_2} \tag{12.5}$$

When the plate is loaded physically in a testing machine, the rigid body motions, u_o , v_o , and w_o are zero. Plane problems of elasticity classically involve determining the stress functions, $\Phi(z_1)$and $\Psi(z_2)$, throughout a component and subject to the boundary conditions around its entire edge. For a region of a component adjacent to a traction free-edge, $\Phi(z_1)$ and $\Psi(z_2)$ can be related to each other by the conformal mapping and analytic continuation techniques. The displacements can then be expressed in terms of the single stress function, $\Phi(z_1)$. Moreover, $\Phi(z_1)$ will be represented by a truncated power-series expansion whose unknown complex coefficients are determined experimentally. Once $\Phi(z_1)$ and $\Psi(z_2)$ are fully evaluated, the individual displacements are known from Eqs. 12.3 through 12.4. For a significantly large region of interest in a finite structure, it may also be necessary to satisfy other boundary conditions at discrete locations.

Conformal mapping is introduced to simplify the plane problem by mapping the region R_z of a complicated physical $z = x + iy$ plane of a loaded component into a region R_ζ of a simpler shape in the $\zeta = \xi + i\eta$ plane, the latter being a unit circle if one represents the stress function as a Laurent series, Fig. 12.1 [13–21]. The new coordinate system (and resulting geometry) is usually chosen to aid in solving the equations and the obtained solution from this simplified domain can then be mapped back to the original physical geometry for a valid solution.

Assume that a mapping function of the form $z = \omega(\zeta)$ exists and which maps R_ζ of the simpler plane into R_z of the more complicated physical plane. For orthotropy, auxiliary planes and their induced mapping functions are defined in terms of $\zeta_j = \xi + \mu_j\eta$, therefore $z_j = \omega_{\text{j}}(\zeta_j)$, for $j = 1\,, 2$. The induced conformal mapping functions are one-to-one and invertible. The

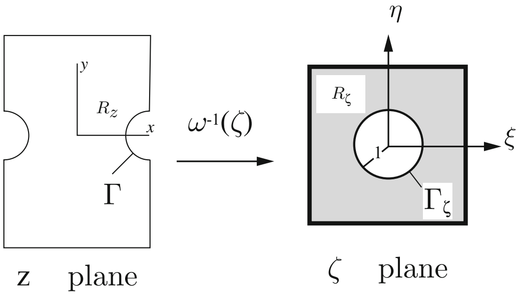

Fig. 12.1 Mapping circular cutout in the physical z-plane into exterior region of a unit circle in $\zeta -$ plane

stress functions $\Phi(z_1)$ and $\Psi(z_2)$ can be expressed as the following analytic functions of ζ_1 and ζ_2. Derivatives of the stress functions with respect to their argument are

$$\Phi'(z_1) = \Phi'(\zeta_1)\frac{d\zeta_1}{dz_1} = \frac{\Phi'(\zeta_1)}{\omega_1'(\zeta_1)}, \quad \Psi'(z_2) = \frac{\Psi'(\zeta_2)}{\omega_2'(\zeta_2)} \tag{12.6}$$

The analyticity of the mapping functions satisfies the equilibrium and compatibility throughout region R_z of the physical plane.

12.2.1 *Traction-Free Boundaries*

Using the concept of analytic continuation, the individual stress functions for a region R_ζ adjacent to a traction-free boundary of the unit circle of an orthotropic material are related by [23, 24]

$$\Psi(\zeta_2) = B\overline{\Phi\left(1/\bar{\zeta}_2\right)} + C\Phi(\zeta_2) \tag{12.7}$$

where B and C are

$$B = \frac{\bar{\mu}_2 - \bar{\mu}_1}{\mu_2 - \bar{\mu}_2}, \quad C = \frac{\bar{\mu}_2 - \mu_1}{\mu_2 - \bar{\mu}_2} \tag{12.8}$$

Equation (12.7) enable the displacements of the structure to be expressed in terms of a single stress function, $\Phi(\zeta_1)$, the latter which can be represented by a Laurent series expansion. Equation (12.7) assumes ability to map the physical boundary of interest into the unit circle in the mapped plane. Reference [25] contains a simple, clear derivation of Eq. (12.7).

12.2.2 *Mapping Formulation*

For a region adjacent the circular notch of radius R, the following function [19]

$$z_j = \omega_{\mathrm{j}}(\zeta_j) = \frac{R}{2}\left[\left(1 - i\mu_j\right)\zeta_j + \frac{1 + i\mu_j}{\zeta_j}\right], \quad j = 1, 2 \tag{12.9}$$

maps the region of the exterior of a unit circle, R_ζ, of the $\zeta -$ plane into the region R_z of the z-physical plane, Fig. 12.2. The inverse of the induced mapping function is

$$\zeta_j = \omega_j^{-1}(z_{\mathrm{j}}) = \frac{z_j \pm \sqrt{z_j^2 - R^2\left(1 + \mu_j^2\right)}}{R\left(1 - i\mu_j\right)}, \quad j = 1, 2 \tag{12.10}$$

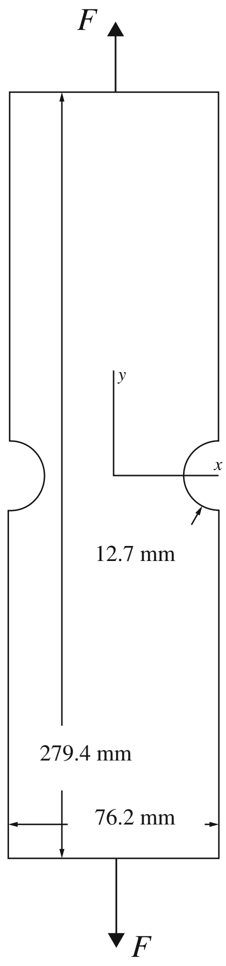

Fig. 12.2 Vertically-loaded finite Gr/E $[0_{13}/90_5/0_{13}]$ composite plate with circular side notches

The branch of the square root in Eq. (12.10) is chosen such that $|\zeta_j| \geq 1$ for $j = 1, 2$.

12.2.3 *Mapping Collocation and Displacements*

The single stress function can be expresses as the following finite Laurent series [17]

$$\Phi\left(\zeta_1\right) = \sum_{\substack{j=-N \\ j\neq 0}}^{N} A_j \zeta_1^j \tag{12.11}$$

where $A_j = a_j + ib_j$ are the unknown complex coefficients (a_j and b_j are both real numbers). The $j = 0$ term contributes to rigid-body motion and can be omitted. Substituting Eq. (12.11) into (12.7) yields

$$\Psi\left(\zeta_2\right) = \sum_{\substack{j=-N \\ j\neq 0}}^{N} \left(\overline{A}_j B \zeta_2^{-j} + A_j C \zeta_2^j\right) \tag{12.12}$$

where $\overline{A}_j$ is the complex conjugate of A_j. At least for a finite, simply connected region R_ζ , $\Phi(\zeta_1)$ is a single-valued analytic function. Orthotropic composite whose complex parameters are purely imaginary when the directions of material symmetry are parallel and perpendicular to the applied load require that only odd terms be retained in the Laurent expansions. From Eqs. (12.3) and (12.4), the displacements can be written as

$$u = 2 \sum_{\substack{j=-N,-N+2,\ldots \\ j\neq 0}}^{N} \operatorname{Re}\left\{\left[p_1\zeta_1{}^j + p_2C\zeta_2{}^j\right]A_j + p_2B\zeta_2{}^{-j}\overline{A}_j\right\} \tag{12.13}$$

$$v = 2 \sum_{\substack{j=-N,-N+2 \\ j\neq 0}}^{N} \operatorname{Re}\left\{\left[q_1\zeta_1{}^j + q_2C\zeta_2{}^j\right]A_j + q_2B\zeta_2{}^{-j}\overline{A}_j\right\} \tag{12.14}$$

The only unknowns in these expressions for the displacements are the complex coefficients $A_j = a_j + ib_j$, the other quantities involve geometry (location) or material properties. Because the summation in Eqs. (12.13) through (12.14) involves only the odd values of N, the number of complex coefficients, A_j, is $N + 1$ and the number of real coefficients, a_j and b_j, is $2(N + 1)$. These coefficients can be determined from measured displacement data. It should be noted that by using conformal mapping and analytic continuation techniques, Eqs. (12.13) through (12.14) imply that the induced stresses satisfy equilibrium and traction-free conditions in the adjacent portion of the entire boundary. However, unlike a classical boundary-value problem where one would typically evaluate the unknown coefficients, A_j, by satisfying the boundary and loading conditions around the entire shape, one can use a combination of the measured stresses and/or displacements from within region R_z to determine these unknown complex coefficients, A_j. Additional known boundary conditions may also be imposed at discrete locations. The concept of collecting measured data in a region R^* adjacent to an edge Γ, mapping R_z into R_ζ such that Γ of the physical z-plane is mapped into the unit circle in the $\zeta-$plane whereby the traction-free conditions on Γ are satisfied continuously, relating the two complex stress functions to each other, plus satisfying other loading conditions discretely on the boundary of the component beyond Γ will be referred to as the mapping-collocation technique.

The interior displacement data v^* at m different locations within region R^* and q known stress conditions (in terms of σ_{xy}) at discrete points along the free outer surface and line of symmetry ($y = 0$) are employed. A system of simultaneous linear equations $[V]_{(m+q)\times 2(N+1)}\{c\}_{2(N+1)\times 1} = \{V^*\}_{(m+q)\times 1}$, is formed whose matrix $[V]$ consists of analytical expressions of displacement component v^*, Eq. (12.14), and the expressions of the known stress conditions, vector $\{c\} = \{a_{-N}, b_{-N}, a_{-N+2}, b_{-N+2}, \ \ldots\ , a_{N-2}, b_{N-2}, a_N, b_N\}$ has $2(N + 1)$ unknown real coefficients, and vector $\{V^*\}$ includes the m measured displacement values of v^* and q discretely imposed stress conditions such that $m + q \gg N + 1$. The best values of the coefficients A_j, in a least-squares numerical sense, can then be determined. The variables $\zeta_j = \xi + \mu_j\eta$ are related to the physical locations $z = x + iy$ through the inverse mapping function $z_j = \omega_j(\zeta_j)$ of Eqs. (12.9) through (12.10).

12.2.4 Inverse Method Procedure

The particular inverse method used here is combining displacement produced from Airy stress function scheme with displacements measured using DIC. Through an iterative process that determines new constitutive parameters, the displacement difference between measured DIC and produced from Airy stress function is minimized. The function to be minimized is

$$f\left(\widehat{v}_{Airy}, P\right) = \|r\|, \quad \text{where } r = \widehat{v}_{DIC} - \widehat{v}_{Airy} \tag{12.15}$$

where $\widehat{v}_{Airy}$ and $\widehat{v}_{DIC}$ are vector containing nodal v-displacements determined by Airy stress function scheme and DIC, respectively. P is a vector containing the constitutive parameters, E_1, E_2, ν_{12}, G_{12} and $\|r\|$ is the norm of r. Because Eq. (12.15) is nonlinear with respect to P, iterative procedures are appropriate methods for minimizing of $f\left(\widehat{v}_{Airy}, P\right)$ and determination of P. LMA (Levenberg-Marquardt Algorithm) is commonly used because it combines the benefits of Steepest Descent Method and Gauss-Newton Method. The LMA has the form [15]

$$P_{i+1} = P_i - \left(J^T J + \lambda \cdot \text{diag}\left(J^T J\right)\right)^{-1} J^T r \tag{12.16}$$

where i is iteration number, J and J^T are Jacobian and Jacobian transpose, determined by backward difference, $J_{m,n} = \frac{\partial r_m}{\partial P_n}$; m is number of nodal displacements and n is number of constitutive parameters (4 in this work), and λ is non-negative damping factor, adjusted each iteration step, adjusts between Steepest Descent Method and Gauss-Newton Method.

The primary disadvantage of LMA is the need for matrix inversion during each iteration. In most applications, reduced iterations compensate for the matrix inversion.

After calculating a new P_{i+1}, the constitutive parameters are checked for validity, i.e., a positive-definite stiffness matrix, and are adjusted if not valid. The validated P_{i+1} are inputs to a new analysis and the resulting nodal displacements are used to determine f_{i+1}. If $f_{i+1} < f_i$, the constitutive parameters are updated, $P_{i+1} \rightarrow P_i$, λ is reduced by a factor of 10, and the next iterations begins. If $f_{i+1} > f_i$, then λ is increased by a factor of 10 and P_i is not updated. As $\lambda \rightarrow 0$, LMA becomes exactly the Gauss-Newton Method.

12.3 Experimental Details

The developed inverse hybrid-DIC approach is utilized to analyze a finite-width tensile [$0_{13}/90_5/0_{13}$] graphite/epoxy orthotropic plate (from Kinetic Composites, Inc., Oceanside, CA; $E_1 = 104$ GPa, $E_2 = 28$ GPa, $G_{12} = 2.9$ GPA, $v_{12} = 0.16$ [1]) with side notches of radius $R = 12.7$ mm was loaded in the strongest/stiffest material direction (1-, y-direction), Fig. 12.2. Over-all laminate dimensions are 279.4 mm long, 76.2 mm wide and 5.28 mm thick. The side notches were machined with a water jet. The coordinate origin is at the center of the plate and the response is symmetric about x- and y-axes. The laminate elastic properties were obtained from conducting uniaxial tensile tests in the strong/stiff (y-direction), weak/compliant (x-direction) and 45-degree orientations [1].

12.3.1 Digital Image Correlation

Digital Image Correlation (DIC) is a full-field computer-based image analysis technique for the non-contact measurement of displacements of a surface equipped with a speckle pattern. The method tracks the motion of the speckles by comparing the gray scale value at a point (subset) in a deformed and undeformed configuration. Two sets of images are recorded; the first image typically being at zero load and the second image under load. Vic-Snap software (by Correlated Solutions, Inc., Columbia, SC, USA) was used to record the images of the plate in its loaded and unloaded conditions and to evaluate the displacements for post-processing. When utilizing two cameras, a separate calibration grid (provided by Correlated Solution with the DIC package) was used to evaluate the displacement data in physical units rather than in pixels. Quality displacement information at and near the edge of the notch and at (near) the longitudinal edge of the specimen is unavailable because the DIC software's correlation algorithm is unable to track a group of pixels (subset) which lack neighboring pixels. To perform the tracking, the subset is shifted until the pattern in the deformed image closely matches that of the reference image.

The measured DIC data were digitalized in matrix form and combined with the Airy stress function to determine the constitutive properties. Recognizing one has fewer complex coefficients to evaluate than amount of data from which to evaluate them, the coefficients were determined using least squares. Although the recorded displacement data at, and adjacent to, an edge are unreliable and raw displacement information in composites is inherently noisy, the present technique overcomes these challenges by avoiding the use of recorded data on and near edges and by processing the measured interior data with a stress function, mapping and analytic continuation.

12.3.2 Plate Preparation and Data Recording and Processing

A random speckle pattern of white dots on a black background was applied to the composite's surface. The plate was statically loaded in the hydraulic grips of a 20 kips capacity MTS hydraulic testing machine from 0 N to 7,117 N in 890 N load increments. Displacement data were recorded and processed at each load increment. Before conducting the quantitative analysis, two cameras were used to capture the three displacement components by which to verify there was no out-of-plane

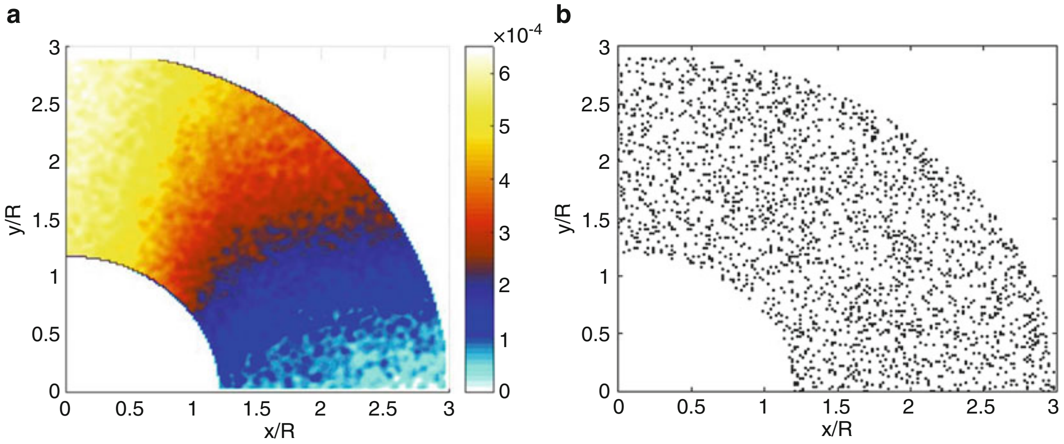

Fig. 12.3 (**a**) Averaged recorded v-displacement data from Vic-snap from all four quadrants; (**b**) Source locations of $m = 2{,}200$ DIC values

bending [1]. The recorded v-displacement information was exported to MATLAB (Mathworks, Inc. 2015) to convert each pixel into a data point, i.e., points. Since DIC data typically are unreliable on and near an edge, no recorded displacements were used within at least 2.95 mm = 0.12 in. of the boundary of the notch.

The DIC correlated solution software provided approximately 102,200 values of v when the analysis was carried out for 17 subsets in five steps. The plate is geometrically and mechanically symmetrical about the vertical y-axes. Since the top end of the physically tested plate was fixed stationary while the bottom end moved vertically downward, the zero vertical displacement was shifted to be at the horizontal middle of the plate to represent the case of the plate being extended at both top and bottom ends. The measured v-displacement data were subsequently averaged about all quadrants to cancel any asymmetry and the resulting averaged measured of values of 17,666 v-displacement data are plotted in the second quadrant as shown in Fig. 12.3a. For the subsequently used mathematical mapping, the coordinate origin was also transferred to the center of the left notch. Due to the previously mentioned unreliability, recorded data on and near the edge of the notch were not employed. Only 2,200 of the available 17,666 v-displacements were selected randomly and used. Their source locations are shown in Fig. 12.3b. The region of Fig. 12.3b is denoted as region R^*. Like most experimental data, the measured data incorporate some noise which necessitate collecting more measured input values than the number of unknown coefficients of a stress function. In addition to the selected v-displacements associated with Fig. 12.3b, $\sigma_{xy} = 0$ was imposed at each of 12 equally-spaced discrete locations along the left vertical traction-free edge of the plate and along the horizontal line of symmetry, $y = 0$. The total number of equations (side conditions), $m + q$, where $m = 2{,}200$ and $q = 24$, exceeds the number of real coefficients, $2(N + 1)$, producing an overdetermined system which can be solved using a least-squares. The system was solved in MATLAB using the backslash '\' operator.

12.3.3 *Evaluating Number of Coefficients to Employ*

The coefficients, $A_j = a_j + ib_j$, were evaluated using Eqs. (12.9) through (12.10) to map the physical plane into the unit circle in the ζ-plane. The unreliable v-displacement values on and near the boundary of the side notch motivated using only v-displacements originating at locations shown in Fig. 12.3b. The magnitude of the complex coefficients, A_j, were determined from Eq. (12.14) using the measured v-displacement data located inside the region R^*, Fig. 12.3b, and imposing zero shear stress discretely along the outer left vertical free surface and the line of symmetry, $y = 0$. The number of real coefficients, $2(N + 1)$, to retain was selected to be 6 complex (12 real) coefficients [1].

12.4 Results

Table 12.1 shows the calculated values of constitutive parameters using Airy stress function scheme and DIC displacement data. LMA requires two initial estimates of P in order to calculate J and begin iterations. Genovese et al. [14] evaluated the

Table 12.1 Calculated values of constitutive properties using inverse method and airy stress function scheme

Parameters	First initial guess	% error	Second initial guess	% error	Calculated values	Final % error
E_1 (GPa)	181	80.0%	110	10.0%	103	2.9%
E_2 (GPa)	39.8	60.0%	22.4	20.0%	22.3	10.4%
G_{12} (GPa)	4.61	60%	2.59	20.0%	2.58	10.4%
ν_{12}	0.167	10%	0.122	20.0%	0.140	7.9%

Target values of elastic constants are $\boldsymbol{E_1} = 101$ GPa, $\boldsymbol{E_2} = 24.9$ GPa, $\boldsymbol{G_{12}} = 2.88$ GPa, $\boldsymbol{\nu_{12}} = 0.152$ [1]

effect of initial estimates on the number of iterations using FEMU-U in an overdetermined system and found that poor initial estimates increased the iterations required for minimization, but minimization was eventually achieved. Although evaluation of initial estimates is beyond the scope of this investigation, an informal analysis showed lack of convergence for poor initial estimates, primarily because the rate of convergence was different of each constitutive parameters.

12.5 Summary, Discussion and Conclusions

A new inverse problem formulation is developed using the Airy stress function, Levenberg-Marquardt Algorithm, and DIC measured displacement to determine the constitutive properties of a graphite/epoxy laminated composite loaded vertically. The primary advantage of this new formulation is the direct use of displacement data, eliminating the need for numerical differentiation when strain data is required. The inverse method algorithm determined the constitutive properties with errors range from 2% to 10%.

References

1. Alshaya, A.A.: Experimental, analytical and numerical analyses of orthotropic materials and biomechanics application. PhD thesis, University of Wisconsin-Madison (2017)
2. Alshaya, A., Rowlands, R.: Experimental stress analysis of a notched finite composite tensile plate. Compos. Sci. Technol. **144**, 89–99 (2017.) ISSN 0266-3538, http://dx.doi.org/10.1016/j.compscitech.2017.03.007. (http://www.sciencedirect.com/science/article/pii/S0266353816312143)
3. Ju, S.H., Rowlands, R.E.: Thermoelastic determination of KI and KII in an orthotropic graphite–epoxy composite. J. Compos. Mater. **37**(22), 2011–2025 (2003)
4. Ju, S.H., Rowlands, R.E.: Mixed-mode thermoelastic fracture analysis of orthtropic composites. Int. J. Fract. **120**(4), 601–621 (2003)
5. Lin, S.T., Rowlands, R.E.: Thermoelastic stress analysis of orthotropic composites. Exp. Mech. **35**(3), 257–265 (1995)
6. Alshaya, A., Shuai, X., Rowlands, R.: Thermoelastic stress analysis of a finite orthotropic composite containing an elliptical hole. Exp. Mech. **56**(8), 1373–1384 (2016)
7. Rhee, J., Rowlands, R.E.: Thermoelastic-numerical hybrid analysis of holes and cracks in composites. Exp. Mech. **39**(4), 349–355 (1999)
8. Hawong, J.S., Lin, C.H., Lin, S.T., Rhee, J., Rowlands, R.E.: A hybrid method to determine individual stresses in orthotropic composites using only measured isochromatic data. J. Compos. Mater. **29**(18), 2366–2387 (1995)
9. Baek, T.H., Rowlands, R.E.: Experimental determination of stress concentrations in orthotropic composites. J. Strain Anal. Eng. Des. **34**(2), 69–81 (1999)
10. Baek, T., Rowlands, R.: Hybrid stress analysis of perforated composites using strain gages. Exp. Mech. **41**(2), 195–203 (2001)
11. Avril, S., Pierron, F.: General framework for the identification of constitutive parameters from full-field measurements in linear elasticity. Int. J. Solids Struct. **44**(14–15), 4978–5002 (2007)
12. Le Magorou, L., Bos, F., Rouger, F.: Identification of constitutive laws for wood-based panels by means of an inverse method. Compos. Sci. Technol. **62**(4), 591–596 (2002)
13. Molimard, J., Le Riche, R., Vautrin, A., Lee, J.-R.: Identification of the four orthotropic plate stiffnesses using a single open-hole tensile test. Exp. Mech. **45**(5), 404–411 (2005)
14. Genovese, K., Lamberti, L., Pappalettere, C.: Improved global–local simulated annealing formulation for solving non-smooth engineering optimization problems. Int. J. Solids Struct. **42**(1), 203–237 (2005)
15. Considine, J.M., Vahey, D.W., Matthys, D., Rowlands, R.E., Turner, K.T.: An inverse method for analyzing defects in heterogeneous materials. In: Proulx, T. (ed.) Application of Imaging Techniques to Mechanics of Materials and Structures, Volume 4: Proceedings of the 2010 Annual Conference on Experimental and Applied Mechanics, pp. 339–346. Springer New York, New York (2013)
16. Lekhnitskii, S.G.: Anisotropic Plates. Gordon & Breach Scientific Publishers, New York (1968)
17. Bisshopp, F.: Numerical conformal mapping and analytic continuation. Q. Appl. Math. **41**, 125–142 (1983)
18. Challis, N.V., Burley, D.M.: A numerical method for conformal mapping. IMA J. Numer. Anal. **2**(2), 169–181 (1982)
19. Lekhnitskii, S.G.: Theory of Elasticity of an Anisotropic Elastic Body. Holden-Day, San Francisco (1963)

20. Lin, S.T., Rowlands, R.E.: Hybrid stress analysis. Opt. Lasers Eng. **32**(3), 257–298 (1999)
21. Muskhelishvili, N.: Some Basic Problems of the Mathematical Theory of Elasticity. Springer, Leyden (1977)
22. Savin, G.N.: Stress Concentration Around Holes. Pergamon Press 1961
23. Bowie, O.L., Freese, C.E.: Central crack in plane orthotropic rectangular sheet. Int. J. Fract. Mech. **8**(1), 49–57 (1972)
24. Gerhardt, T.D.: A hybrid/finite element approach for stress analysis of notched anisotropic materials. J. Appl. Mech. **51**(4), 804–810 (1984)
25. Huang, Y.-M.: Determination of individual stresses from thermoelastically measured trace of stress tensor. PhD thesis, University of Wisconsin-Madison

Chapter 13
High-Speed Infrared Imaging for Material Characterization in Experimental Mechanic Experiments

Marc-André Gagnon, Frédérick Marcotte, Philippe Lagueux, and Vince Morton

Abstract Heat transfers are involved in many phenomena such as friction, tensile stress, shear stress and material rupture. Among the challenges encountered during the characterization of such thermal patterns is the need for both high spatial and temporal resolution. Infrared imaging provides information about surface temperature that can be attributed to the stress response of the material and breaking of chemical bounds. In order to illustrate this concept, high-speed infrared sequences were recorded during tensile and shear testing experiments carried out on steel and aluminum samples. Results from split-Hopkinson experiments carried out on a polymer material at high strain-rate are also presented. The results illustrate how high-speed and high-definition infrared imaging in the midwave infrared (MWIR, 3–5 μm) spectral range can provide detailed information about the thermal properties of materials undergoing mechanical testing.

Keywords Infrared • Imaging • Hopkinson • Tensile • Heat

13.1 Introduction

Characterization of mechanical properties such as Young's modulus, shear strain, viscosity and fracture toughness is very important in the development process of new materials. Researchers must typically carry out many different measurements like tensile displacement tests, compression tests and fatigue tests in order to determine these parameters. One of the most common way of characterizing materials consist in establishing a stress-strain curve. The stress-strain curve reflects the behaviour of the overall sample at the macroscopic level. It does not contain any information at the microscopic level on how the sample deforms or breaks locally during testing. For example, materials typically release heat as they undergo alterations because of elastic or plastic deformations (i.e., work). It is well known that thermal energy is released during the breaking of chemical bounds. Therefore, being able to monitor heat profiles across the sample during testing may provide complementary information about its mechanical properties. Depending on the extent of the applied constrains and the sample's properties, the material can switch from one regime to another (e.g., from elastic to plastic) very quickly. Therefore, measurement techniques with high temporal and/or spatial resolution are usually required for proper investigation. In this work, high-speed infrared imaging was carried out during tensile and shear stress tests on steel and aluminum respectively. In addition, results from a split-Hopkinson experiment carried out on a polymer material at high strain rate (>100 strain/s) are presented. This strain-rate regime is relevant for situations like impact and automotive crashes. The data collected in such experiments are used for validating finite element simulations for determining accurate material models. The results illustrate how infrared imaging can bring some additional insights for material characterization in experimental mechanics research.

13.2 Experimental

All samples were coated using a high-emissivity paint prior to testing. Consequently, the temperature values measured by infrared thermography are considered close to their actual surface thermodynamic temperature. A high-elongation extensometer from MTS was used for all experiments. A 12.5-mm gauge steel sample was pulled at 10 strain/s (125 mm/s).

M.-A. Gagnon (✉) • F. Marcotte • P. Lagueux • V. Morton
Telops, 100-2600 Saint-Jean Baptiste, Québec City, QC, Canada
e-mail: marc-andre.gagnon@telops.com

A. Baldi et al. (eds.), *Residual Stress, Thermomechanics & Infrared Imaging, Hybrid Techniques and Inverse Problems, Volume 8*,
Conference Proceedings of the Society for Experimental Mechanics Series, DOI 10.1007/978-3-319-62899-8_13

The aluminum sample was pulled under adiabatic shear conditions. The woven carbon fibre epoxy-polymer matrix sample was pulled at 2 mm/min. The Telops FAST M2K is a cooled high-performance infrared camera featuring a 320 × 256-pixel indium antimonide (InSb) focal plane array (FPA) detector covering the 3–5.5 μm spectral range. A 50-mm Janos lens was used along with a 0.25-inch extender ring for tensile and shear tests. For the tensile stress test carried out on the steel sample, a 128 × 256-pixel sub-portion of the FPA detector was used for imaging at 4350 frames per second. For the shear stress test carried out on the aluminum sample, a 192 × 192-pixel sub-portion of the FPA detector was used for imaging at 3350 frames per second. For the split-Hopkinson test carried out on a polymer (PVC-like) sample at about 100 strain/s. A 64 × 64-pixel sub-portion of the FPA detector was used for imaging at 12480 frames per second.

13.3 Results and Discussion

A tensile test was first carried out on a steel sample. Selected images recorded during the experiment, corresponding to different stages of a typical stress-strain curve are shown in Fig. 13.1. In the first three frames (Fig. 13.1a–c), the sample is still in the elastic deformation regime. The measured temperatures are slightly higher than room temperature (initial temperature of the sample prior to testing) and temperature increases are homogeneously distributed all across the sample. The infrared frames collected at a later stage (Fig. 13.1d–f) correspond to the necking stage, where localized deformations and important temperature increases occur. In the plastic deformation regime, the temperature rises locally and more rapidly than thermal exchanges (adiabatic conditions). Temperature rises on the order of +115 °C were measured, which is in good agreement with prior work on similar samples [1]. Finally, frames collected just before (g), during (h) and after (i) the fracture point are shown in Fig. 13.1. Beyond the fracture point, heat conduction through the sample and rapid cooling near the fracture area can be monitored (data not shown). The time labels in Fig. 13.1 illustrate how fast the sample switches from one regime to another and highlight the need for high temporal resolution in this kind of experimental testing.

Fig. 13.1 Selected infrared images recorded during a tensile stress test carried out on a steel sample

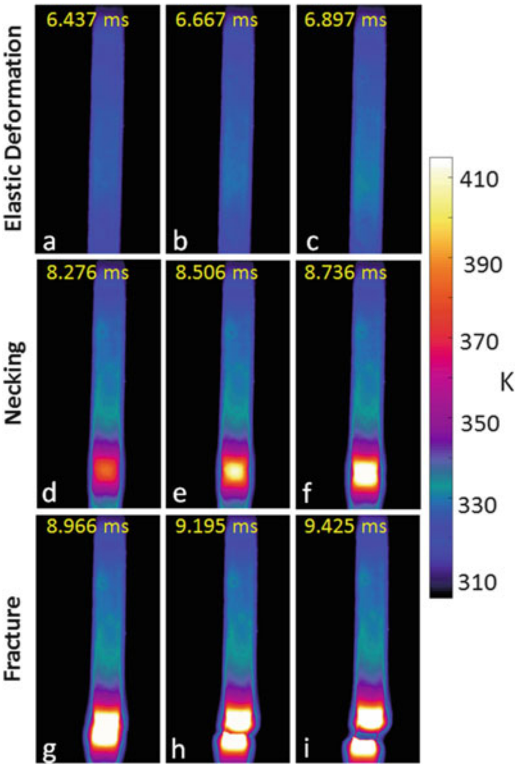

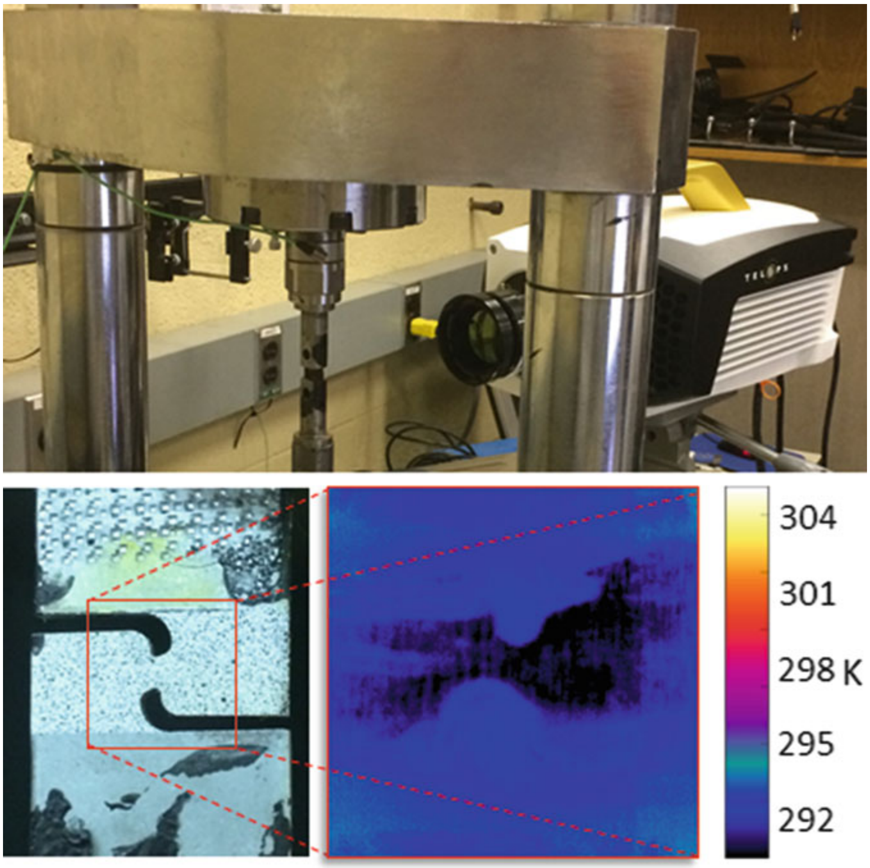

Fig. 13.2 A typical sample (before being painted) used for this test (*bottom left*) as well as a representative infrared image of the shear area (*bottom right*)

In order to demonstrate the versatility of high-speed infrared imaging, a shear test was carried out on an aluminum sample, as shown in Fig. 13.2. In shear conditions, the constraint must be applied in a perpendicular plane. In order to perform such measurements with a high-elongation extensometer, a special cut-out was made in the sample, as shown in Fig. 13.2. This special shape also strongly dictates where the fracture will likely happen.

For this reason, this area was targeted for infrared imaging, as shown in Fig. 13.3. Selected frames recorded during the shear stress experiment are presented in Fig. 13.3a. In the early stage, the temperature rises rapidly within the area of the (eventual) fracture. Once again, the experimental conditions ensure that adiabatic shear conditions prevail and that thermal equilibrium is not reached. Under such conditions, the sample mostly undergoes localized heating and softening. This favors stress release as the sample is being pulled. Therefore, moderate heat release occurs in the course of the fracture (approximately +30 °C). Successive frames recorded during the material's rupture are shown in Fig. 13.3b. Once again, it can be seen that high-speed infrared imaging is needed in order to provide enough details to characterize the fracture's onset.

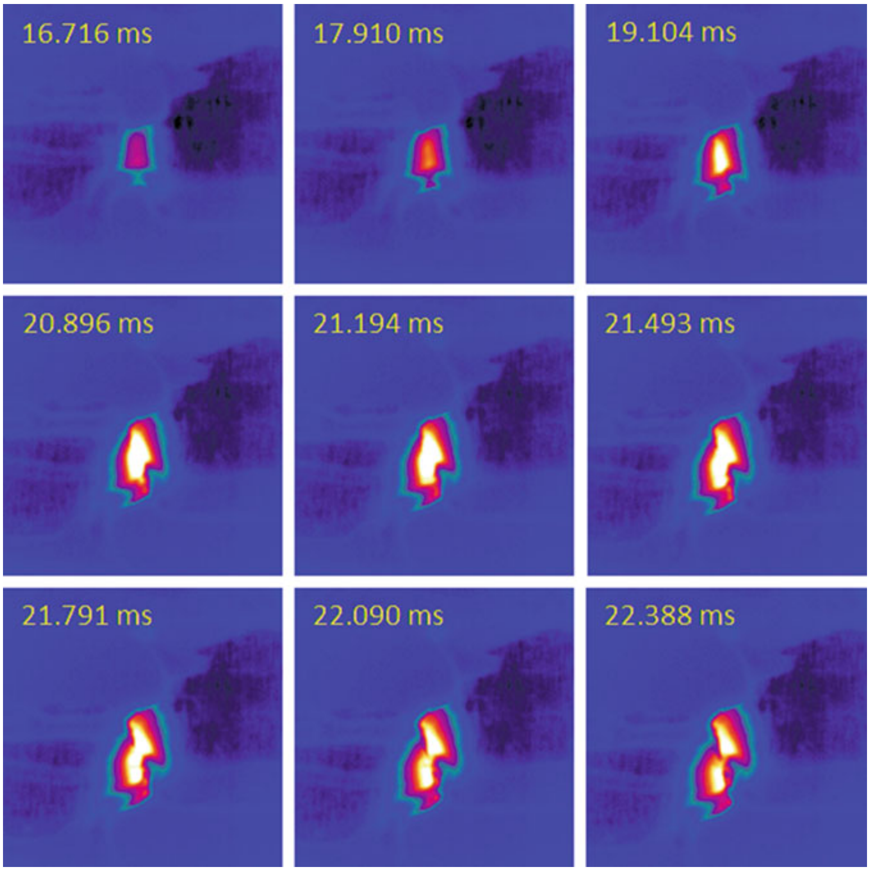

Fig. 13.3 Selected infrared images representing different stages of the shear experiment on aluminum

Split-Hopkinson experiments were carried out at high strain-rate on PVC-like polymer material. Selected infrared images recorded during the experiment are shown in Fig. 13.4. In the early stage after the incident bar strikes the material, the sample heats homogeneously, which is consistent with the elastic deformation regime. As the material switches to a plastic deformation regime, localized heating on both sides of the sample takes place. The sample keeps heating as the sample deforms. At some stage, the maximum stress point is reached and stress hardening occur [2]. No mechanical alteration of the sample occurs beyond this point. The sample axial length (L) relative to its initial length (L_i) was estimated from the image sequence and plotted against time, as shown in Fig. 13.5. As expected, plastic deformation occurs as soon as the incident bar hits the sample. The sample axial length gradually decreases as a function of time until then stops.

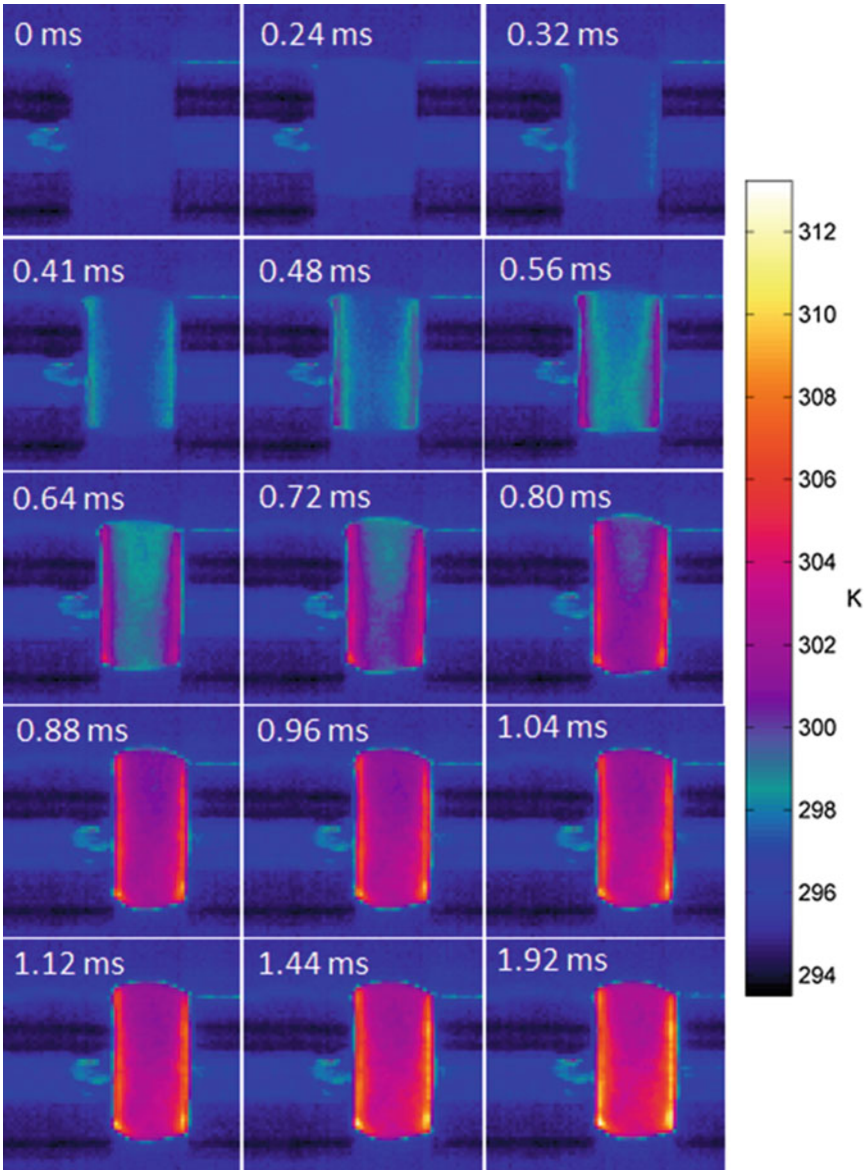

Fig. 13.4 Selected infrared images representing different stages of the split-Hopkinson experiment on a polymer sample

Mechanical process and heat transfer take place on very different timescales. In order to visualize these very different phenomena, a 3D view of the net temperature increase at various stages of the experiment is shown in Fig. 13.6. The thermal gradient gradually progresses from the sides toward the center of the sample. Significant temperature increase occurs after there is no more mechanical. Being able to track and measure these phenomena is important in order to calculate an accurate energy budget (thermal + work).

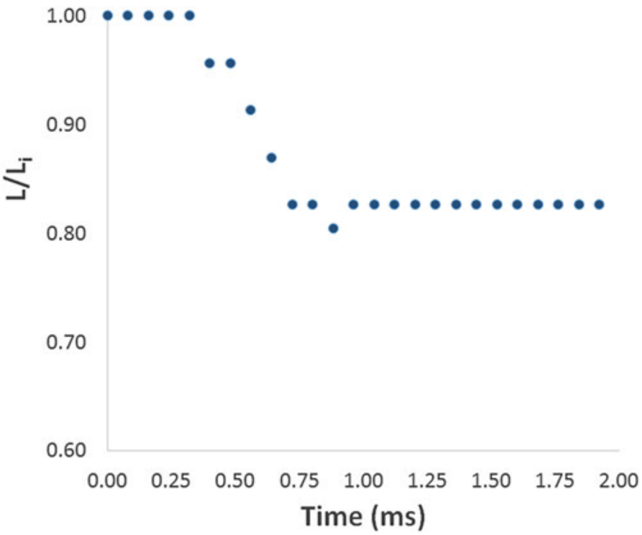

Fig. 13.5 Sample compression as a function of time

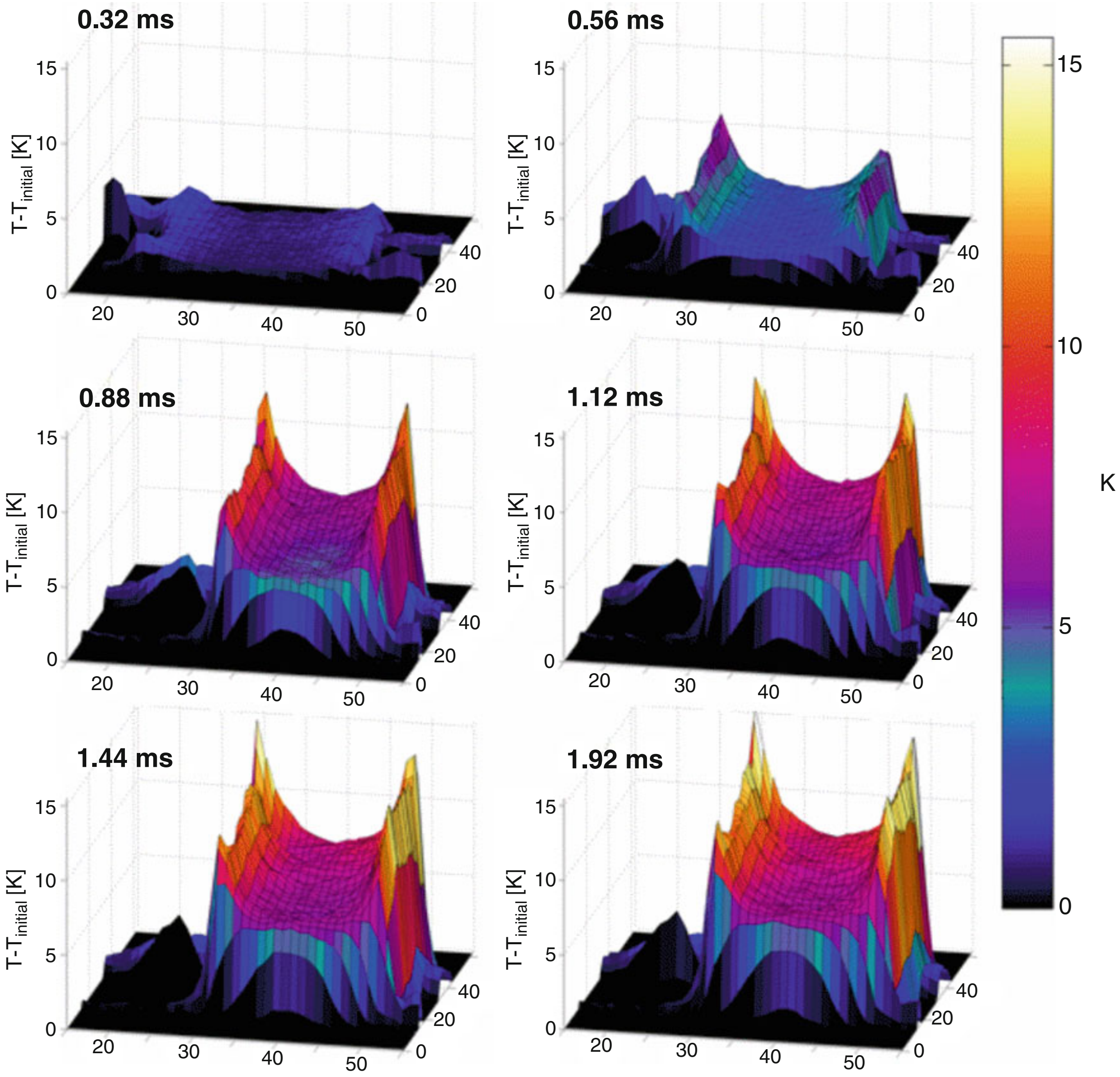

Fig. 13.6 3D–views of the net temperature increase at different times

13.4 Conclusions

Heat release associated with tensile and shear testing can be successfully monitored using high-speed infrared imaging. Heat spots resulting from energy release in the course of the breaking of chemical bonds can be monitored with high-resolution infrared imaging. Infrared imaging was shown to be a useful tool for monitoring temperature profiles and an important asset for obtaining the most out of each experiment, especially in the case of sample-destructive testing experiments. Experiments at high strain-rate require very fast frame rates as the whole sequence of events takes place in less than a millisecond. Under these conditions, spatial and temporal resolution are both important assets for computing an energy budget and improve material models.

Acknowledgments Telops would like to acknowledge the support of Clifford Butcher, Giovanni Montesano and Michael Worswick from the Mechanical Engineering laboratory of the University of Waterloo (Canada) as well as Arild Holm Clausen and Trond Auestad from the Structural Impact Laboratory (SIMLab) of the Norwegian University of Science and Technology in this work.

References

1. Haneef, T., et al.: Study of the tensile behavior of AISI type 316 stainless steel using acoustic emission and infrared thermography techniques. J. Mat. Res. Technol. **4**, 241–253 (2014)
2. Ognedal, A.S., et al.: Void nucleation and growth in mineral-filled PVC – an experimental and numerical study. Int. J. Solids Struct. **51**, 1494–1506 (2014)

Chapter 14
A Spatio-Temporal Approach for iDIC-Residual Stress Measurement

Antonio Baldi

Abstract Recently, the Integrated-Digital Image Correlation (iDIC) has been proposed as a simple and effective approach for residual stress measurement. iDIC is a variant of the classical Digital Image Correlation where the "standard" displacement functions are replaced by problem-specific ones. By this simple modification, stress components become the unknowns of the problem, thus allowing a single-pass analysis. However, implementation of the Integral Method for estimation of depth-dependent Residual Stress components is difficult. In particular, the Least Squares approach is not possible.

This work suggests a two-pass approach: in the former the direct solution of the triangular linear system is solved. In the latter, the previous estimates are used as starting point for a global minimization involving all the acquired images.

Keywords Integrated digital image correlation • Residual stress • Integral method • Reverse methods

14.1 Introduction

Most technological processes induce (as side effect) self balanced stress fields, known as *residual stresses*, in mechanical components. Residual stresses are particularly critical because they add to load-induced stress fields, thus potentially inducing failure at load levels significantly lower than expected. The most used residual stress measurement technique is the *hole drilling* [1], a semi-destructive technique consisting in drilling a small hole in the surface, to successively compute stress components from the strain/displacement field observed on surface. Strains are usually measured using a strain gauge rosette, but various alternative techniques have been proposed. In particular, the Integrated Digital Image Correlation (iDIC) has been recently proposed as an effective approach for residual stress analysis both for isotropic [2] and orthotropic [3] materials. This technique is a direct derivative of Digital Image Correlation [4] and uses the same basic principle: given a pair of images acquired before and after the event of interest (respectively f and g), the intensity of each pixel remains the same irrespectively of the motion of the object under study. From the theoretical viewpoint, this statement can be written as

$$f(x, y) = g(x + u,\ y + v) \tag{14.1}$$

where u and v are the components of the displacement vector $\mathbf{u}$. The expansion in Taylor series truncated to the first or second term of the right side part of Eq. 14.1 gives, after some easy algebraic manipulation, the well known *optical flow* equation

$$\frac{\partial f}{\partial x}\dot{u} + \frac{\partial f}{\partial y}\dot{v} + \frac{\partial f}{\partial t} = 0 \tag{14.2}$$

Looking at Eq. 14.2, it is apparent that its solutions is challenging, because it contains two unknowns, i.e. the problem is ill-conditioned. The standard approach to the solution of (14.2) is due to Lukas-Kanade [5]: they assumed that the displacement field around a point can be described by simple shape functions—usually constant or bilinear polynomials—thus, reducing the number of unknowns from two times the number of pixels involved in the local area, to the number of controlling parameters of the shape functions. The unknowns are identified by a Least Squares approach minimizing a local functional involving the intensities of the reference and target image:

A. Baldi (✉)
Department of Mechanical Engineering, Chemical and Materials Engineering, University of Cagliari, Via Marengo 2, 09123, Cagliari, Italy
e-mail: antonio.baldi@dimcm.unica.it

A. Baldi et al. (eds.), *Residual Stress, Thermomechanics & Infrared Imaging, Hybrid Techniques and Inverse Problems, Volume 8*,
Conference Proceedings of the Society for Experimental Mechanics Series, DOI 10.1007/978-3-319-62899-8_14

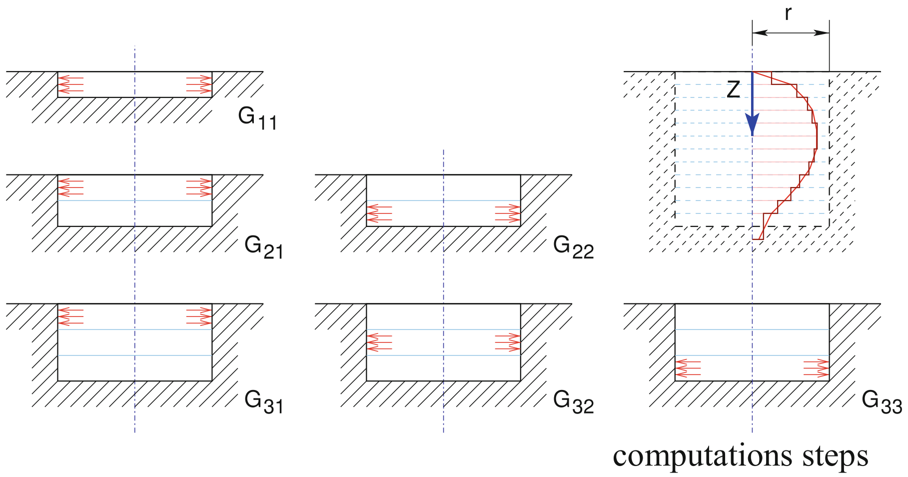

Fig. 14.1 Schematic representation of the computations steps involved in the integral method

$$\chi^2 = \sum_k \sum_l [f(k,l) - g(k+u, l+v)]^2 \tag{14.3}$$

where the summations extend over the pixel of the local area (subset). The computation of derivatives of (14.3) with respect to the parameters of the shape functions (i.e. of the u and v functions) leads to a linear system which apparently solve the problem. Actually this is not the case, because the numerical values of the derivatives depend on the point of evaluation, i.e. on the unknowns, thus an iterative solution algorithm is required. To obtain field data, the above sketched computation has to be repeated to sample the active area on a regular grid.

Digital Image Correlation is not a particularly good technique for residual stress measurement. Indeed, its sensitivity is relatively low; moreover, the measurement is particularly difficult near the hole, i.e. in the most interesting region, thus researchers had to cope with artifacts [6]. iDIC completely overcome all these problems by integrating problem-specific displacement functions inside the DIC algorithm. The advantages are significant: because the shape functions are able to describe the experiment globally, there is no need to partition the domain and a single, huge set of pixel is used. This ensures high reliability and robustness against local perturbations. Moreover, the parameters controlling the displacement functions are the stress components, thus, the result of the iDIC analysis are the residual stress components (the standard process requires a two step analysis, the measurement of the displacement/strain data and successively the computation of stress components).

Even though the single-step processing of iDIC is elegant and grants a robust and accurate solution (because a single reverse process is used instead of two), it becomes a problem when the residual stress varies with depth. The standard approach to this problem is the integral method [7]: the stress distribution, a smooth function of depth, is approximated with a stepwise function (Fig. 14.1). For each step, a hole increment is performed and the strain/displacement field on the surface is acquired. To correlate the acquired displacements with stresses one has to consider that for each hole increment, the observed deformation depends on the newly released stress components and on all the previous ones. This leads to the linear system

$$\mathbf{G}\,\overrightarrow{\sigma} = \overrightarrow{f} \tag{14.4}$$

where $\overrightarrow{\sigma}$ is the vector of stress components, $\overrightarrow{f}$ the vector of the observed strain/displacements and **G** is the influence matrix. The element G_{ij} of **G** is the deformation/displacement observed on surface after hole increment i caused by a unitary load at depth j. Because no influence is assumed on stress below the bottom of the hole, **G** is a lower triangular matrix. G_{ij} is a number when strain gauge are used and a block sub-matrix when optical methods are involved, because at each step, the displacement of all points imaged on the surface are estimated. The linear system (14.4) can be easily solved either using a standard algorithm or—in the case of optical methods, when the system is overdetermined—by a least squares approach, i.e. solving

$$\mathbf{G}^T\mathbf{G}\,\overrightarrow{\sigma} = \mathbf{G}^T\overrightarrow{f} \tag{14.5}$$

In principle, Eq. 14.4 applies to iDIC with small modifications: indeed, the unknowns are still the stress components; however, while in (14.4) the known terms are the measured displacements, in the iDIC equivalent the known terms are the summation of intensity differences between the undrilled and drilled image, i.e. a dynamic quantity depending on the displacement vector which, by itself depends on the stress components. In short, iDIC requires an iterative approach and the problem is nonlinear. Thus, to ensure convergence, a suitable starting point, near enough to the sought solution, is required.

The identification of a tentative solution is relatively easy: remembering that for each pixel k on the surface, a G_{ij} exists (thus, G_{ijk} is G_{ij} related to pixel k), it is possible to use a "standard" iDIC code (related to a single step) where the error functional at step i has been corrected by subtracting from the known terms the contributions of stress components for the increments $1 \ldots i$-1, i.e. $\sum_{k=1}^{N} \sum_{l=1}^{i-1} G_{ilk}\sigma_l$ where N is the number of active pixels. Thus, the tentative solution can be obtained by performing a series of iDIC analyses, each involving data from a single step.

It is worth to note that the above proposed algorithm strictly mimics the solution procedure for lower triangular linear matrices, but with a noteworthy difference: at each step a reverse process is performed. Thus, significant errors may appear in the estimated stress values. Moreover, an erroneous estimate affects all the successive steps, thus making the solution progressively noisier.

Summarizing, we propose a three steps approach: in the first one, the residual stress components are computed using the above sketched algorithm. Once the $\sigma_x(z)$ ($\sigma_y(z)$, $\tau_{xy}(z)$) are known, it is possible to perform a global minimization in space and in time: the unknowns of the problem are the rigid body translation components and the stress components at each level; thus, the error function involves all the acquired images.

References

1. ASTM E837-08e1: Standard test method for determining residual stresses by the hole-drilling strain-gage method. Am. Soc.Test. Mat. West Conshohocken. PA. (2008). doi:10.1520/E0837-08E01
2. Baldi, A.: Residual stress measurement using hole drilling and integrated digital image correlation techniques. Exp. Mech. **54**(3), 379–391 (2014). doi:10.1007/s11340-013-9814-6
3. Baldi, A.: Residual stress analysis of orthotropic materials using integrated digital image correlation. Exp. Mech. **54**(7), 1279–1292 (2014). doi:10.1007/s11340-014-9859-1
4. Sutton, M.A., Orteu, J.J., Schreier, H.: Image correlation for shape, motion and deformation measurements: basic concepts, theory and applications. Springer (2009) doi:10.1007/978-0-387-78747-3
5. Lucas B.D., Kanade T.: An iterative image registration technique with an application to stereo vision. In: Proceedings of Imaging Understanding Workshop, **130**:121–130 (1981)
6. Schajer, G.S., Winiarski, B., Withers, P.: Hole-drilling residual stress measurement with artifact correction using full-field DIC. Exp. Mech. **53**(2), 255–265 (2013). doi:10.1007/s11340-012-9626-0
7. Schajer, G.S.: Measurement of non-uniform residual stresses using the hole-drilling method. J. Eng. Mat. Technol. **110**(4: Part I), 338–343 (1988.) Part II: pp. 344–349

Chapter 15
Detection of Early Stage Material Damage Using Thermophysical Properties

Mulugeta A. Haile, Natasha C. Bradly, Michael D. Coatney, and Asha J. Hall

Abstract This paper presents a preliminary study on the effects of fatigue induced microstructural damage on the thermophysical properties of carbon fiber polymer composites commonly used for aerospace applications. The goal is to identify thermal properties that may serve as viable indicators of early stage material damage during structural health monitoring (SHM). A series of fatigue tests were conducted on multilayer composite specimens with peak stress $\sigma_{\max} = 0.55\sigma_{\mathrm{u}}$ (the static strength) and stress ratio $R = 0.1$. The cyclic load was paused periodically at predefined cycle intervals starting from 100 cycles through end of test at 150 k cycles. At each pause, the front side of the specimen is instantaneously heated with a high intensity flash followed by temperature measurements by two thermocouples attached at the front and back sides the rectangular specimen. Simultaneously, IR images are recorded using high speed camera. Changes in thermophysical properties including heat transfer rate (Q), thermal conductivity (k), heat capacity (c) were computed as functions of fatigue cycles. Preliminary data shows that the time-temperature (T-t) evolution is correlated to the number of fatigue cycles or consumed fatigue life of the specimens.

Keywords Thermography • Early stage composite damage • Fatigue • Structural health monitoring • Microcrack

15.1 Introduction

Until most recently, composite materials were considered as fatigue insensitive and less prone to fatigue damage. One of the reasons implied behind this statement was that the conventional loading levels applied to composite systems were far too low to initiate any local damage that could induce failure under repeated loading [1, 2]. As such, the requirement for no growth of defects has always been assumed to be sufficient for the design of composite airframes. However, with the continuous improvement of composite manufacturing methods during the last decades and the requirements on structural weight reduction for future air platforms means that composite structures are subjected to loads increasingly closer to their ultimate static strength [3]. Such increase in operational loads by reducing the capacity margin down to a minimum is likely to lead to situations where series fatigue damage develop. To date, there are no theoretical predictive or simulation models to reliable describe the mechanics of cumulative fatigue damage in composites [4, 5]. Hence structural state awareness, diagnostics, and life predictions are primarily data-driven, carried out using structural health monitoring (SHM) sensors such as ultrasonic pitch-catch, pulse-echo, optical FBG, strain gages, and acoustic emission sensors. Existing structural health monitoring sensors however are only reliable for detecting large or macroscale damages (such as large crack, delamination or debond). For critical airframe structures, information on macroscale damage will not provide sufficient warning time for corrective actions. Hence there is a continued search for reliable early stage damage detection techniques in composite airframe structures and systems.

Thermophysical properties of solids, such as thermal conductivity, transmittance, diffusivity and the kinetics of interaction and energy exchange among the principal carriers are based on microscopic (or atomic) level material configuration and interaction. Changes in microscopic material state (or configuration) due to stress concentration, shear localization, adiabatic shear bands, crazing, and dislocation, that typically appear in the early stage of fatigue damage, may be correlated to changes in the thermophysical properties. A thorough investigation into the correlation of thermophysical properties of composite with progressive fatigue damage in terms of microscopic states (crazes, dislocation), however, has not been performed yet. There is evidence, nonetheless, that thermal discontinuities occur due to microscopic defects induced by cyclic loading. Figure 15.1 shows the connection between early stage fatigue damage and its effect on the thermal properties of the

---

M.A. Haile • N.C. Bradly (✉) • M.D. Coatney • A.J. Hall
US Army Research Laboratory, Vehicle Technology Directorate, Aberdeen Proving Ground, Aberdeen, MD, USA
e-mail: natasha.c.epps-bradley.civ@mail.mil

A. Baldi et al. (eds.), *Residual Stress, Thermomechanics & Infrared Imaging, Hybrid Techniques and Inverse Problems, Volume 8*,
Conference Proceedings of the Society for Experimental Mechanics Series, DOI 10.1007/978-3-319-62899-8_15

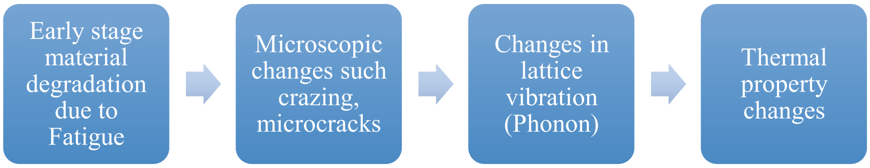

Fig. 15.1 Changes in microscopic material state (or configuration) due to stress concentration, shear localization, adiabatic shear bands, crazing, dislocation that typically appear in the early stage of fatigue damage, may be correlated to changes in the thermophysical properties

constituent materials. Hence the focus of this study is to investigate the relations between early stage fatigue damage, the ensuing internal microscopic degradation, and the changes thermal properties of composite materials. The main emphasis is on the relationship between variations in the heat transfer rate and fatigue cycles N.

15.2 Theory

The material property of a composite depends on properties of the fiber and matrix, the volume fraction, and the interfacial property. The fibers impart most of the strength and stiffness to the composite while the matrix transfers the external load to the fiber through interfacial bonding. The reliability of a composite structure as a whole depends primarily on the integrity of the interfacial bonding between the matrix and fibers and how well the load is being transferred. Almost always early stage fatigue damage starts at the interface and precedes all other modes of failure. It doesn't result in the final failure of the composite, but does contribute to strength/stiffness degradation in the laminate. Once an interfacial damage appears it gradually spreads through the entire width of the laminate.

Much like the mechanical strength and/or stiffness, the quality of the interface also affects the heat transfer property of the composite mainly in the transverse direction (perpendicular to fibers). Since carbon fibers have excellent longitudinal (axial) conductivity the interface is not critical to longitudinal heat transfer. In the transverse direction, however heat flux must cross the fiber-matrix interface repeatedly. Therefore, any change in the interfacial integrity will have a major effect on the transverse thermal properties such as thermal conductivity, transmittance and heat transfer rate.

Heat-transfer effects include thermal conduction, radiation, and convection in which the heat passes through the material to make the temperature uniform in the specimen. Temperature distribution in general carries useful information about the structural material property. Studies have shown that the thermal conductivity, k, may be used for measuring the degree of anisotropy in load bearing structures [6]. Variations in thermal conductivity may arise as a result of local inhomogeneity or flaws in the material [7]. In general, the thermal behavior of a solid is governed not only by its thermal conductivity but also by its heat capacity, c. The ratio of these two properties is termed as the thermal diffusivity, $\alpha = k/c$, which is often the governing parameter for unsteady state heat transfer. A high value of the thermal diffusivity implies a capability for rapid and considerable changes in temperature.

As stated earlier, the focus of this study is to investigate the correlation of thermal properties of composites to early stage fatigue damage. Since the fiber-matrix interface is the weakest part of a laminate [8], any change in the observed thermal property is typically assumed to be due adverse changes (degradation) in the integrity of the interface.

15.3 Experimental Setup

The experimental phase of the study presented here uses pulsed thermography shown in Fig. 15.2 to monitor the temperature-time (T-t) evolution and the heat transfer rate through the carbon epoxy test specimen. In pulsed thermography, the surface of a specimen is heated with a brief (typically, a few milliseconds), spatially uniform pulse of light from a xenon flash lamp source. An IR camera interfaced to a PC monitors the time dependent response of the specimen surface temperature to the thermal impulse. Typically in areas of the specimen surface closest to a thermal discontinuity (e.g. a wall, layer boundary or delamination, debond), the transient flow of heat from the surface into the sample bulk is wholly or partially obstructed, thus causing a transient, local temperature increase at the surface. In the test performed here, simultaneous to the IR imaging, the front and back temperatures of the specimen few millimeters away from the tip of the center hole (which is the region of maximum stress concentration) are measured using two thermocouples. The arrangement of various systems used in the test are shown in Fig. 15.2.

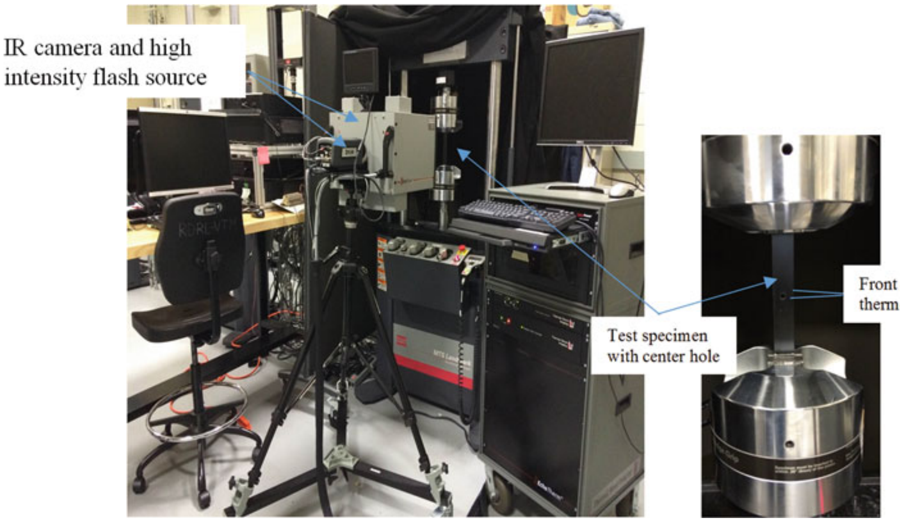

Fig. 15.2 Experimental setup showing the pulsed thermography. The test sample is a rectangular carbon-epoxy laminate with a centre (fastener) hole. Two thermocouples are attached at the front and back near the centre hole in the mode-I direction. Surface temperatures are measured after the application of the high intensity flash at the front of the specimen

The fatigue test specimen is loaded on a hydraulic servo controlled uniaxial test frame and is subjected to a tension-tension sinusoid at a frequency of 5 Hz and load ratio $\sigma_{min}/\sigma_{max} = 0.1$. The test specimen is $[(\pm 45^o)_2/0^o]s$ symmetric laminate with a thickens of 0.128 in (3.25 mm). The peak load of the sinusoid $P_{max} = 20$ kN.

During data acquisition, the cyclic load is paused periodically at predefined cycle intervals starting from 100 cycles through end of test at 150 k cycles. At each pause, the specimen is allowed to cool down to room temperature so as to bring the specimen to the same initial energy state during each successive pause while allowing for the dissipation of viscoelastic heating before probing the thermal properties. After the specimen is cooled to room temperature (22 °C), the front side is instantaneously heated with a high intensity flash followed by temperature measurements by two thermocouples attached at the front and back sides the rectangular specimen and IR imaging.

15.4 Results and Discussions

Figure 15.3 shows the readings of the front and back thermocouples at after the application of a high intensity flash at the given fatigue cycle. Each curve denotes the evolution of (T-t) at specific number fatigue cycles.

The plots are color mapped from blue (low cycle count) to red (high cycle count). Fig. 15.3a shows the temperature decay at the front of the specimen, Fig. 15.3b shows the transient temperature increase at the back of the specimen while Fig. 15.3c shows the relative changes in the surface temperature at the back and front of the specimen.

Immediately after the application of flash, the temperature of the front surface increase by about 4-°F. After a brief delay the temperature of at the back increases as the heat conducts through the thickness. The data shows that the (T-t) evolution is well correlated to the number of fatigue load cycles that the specimen has absorbed at any given time. Notice the clear trend of the color mapped lines with blue (low cycle) lines clearly separated from the red (high cycle) lines. As N increases, the specimen appears to lose the input energy, i.e. the external heat imparted by the flash, rather very quickly. The data from the back thermocouple shows that, the peak recorded temperature at the back of the specimen drops sharply as the fatigue cycles continue to increase. A possible explanation for this observation is as follows: the process of accumulation and development of fatigue damage is associated with crazing and microcracking, which is determined by the processes of initiation, motion, generation, and merging of point defects. The density of microcracks grows with increase of the loading cycles N. High density microcrack leads to loosening of material, primarily around the interface and in/around regions of high stress concentration in the matrix. This creates higher thermal resistance in the transverse direction where the heat is supposed to flow. The high transverse thermal resistance (created by the microcraks and loose material) forces the heat transfer possibly along the fiber direction (high thermal conductivity). A comprehensive explanation of the observed heat flux phenomena, however, is yet to be established.

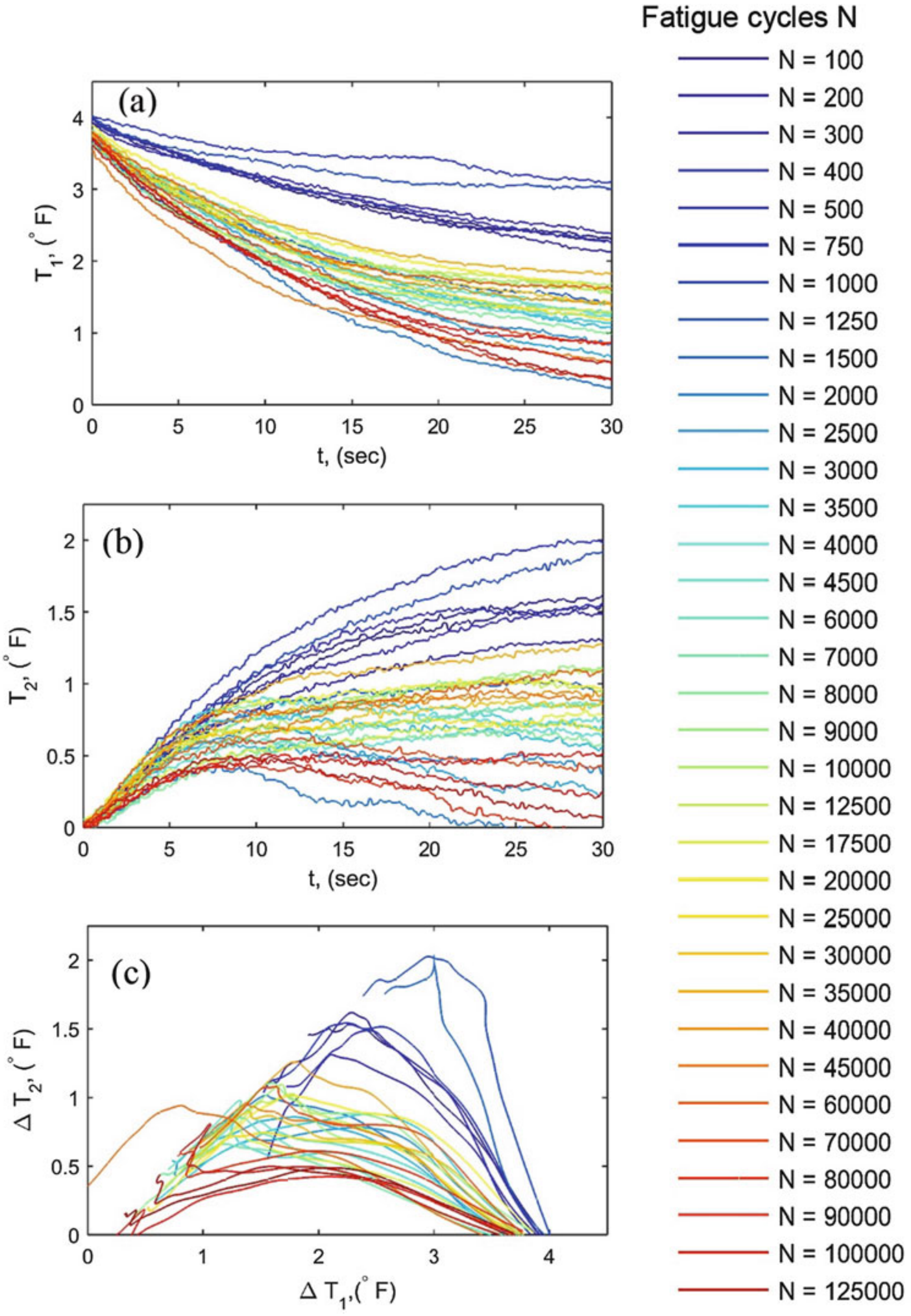

Fig. 15.3 Readings of the front (T_1) and back (T_2) thermocouples at various cycle count N at the tip of a center hole on a carbon-epoxy laminate. The plots are color mapped from *blue* (low cycle count) to *red* (high cycle count). The data shows that the heat capacity of the specimen, as well its thermal conductivity change with the number of applied fatigue cyclic. The change in thermal property may be attributed to increase in microcrack density and the loosening of material around fiber-matrix interface. (**a**) Temperature of the front surface T_1 as a function of time, (**b**) Temperature of the back surface T_2 as a function of time, (**c**) Temperature of the front surface as a function of the back surface

15.5 Conclusions

This study is primarily intended to investigate the feasibility of detecting early stage structural damage in carbon-epoxy systems, such as crazes and microcracks using changes in themophysical properties of the material. Several published work is available on the subject area of thermography for the detection of large scale damage events such as delamination, debonding or large cracks in structures. However, the work presented here, is among the first attempts to detect early stage damage in composite structure well before the appearance of large damage. The central hypothesis of the paper is that changes in microscopic material state resulting from stress concentration, shear localization, adiabatic shear bands, crazing, microcracks that typically appear in the early stage of fatigue damage, are correlated to changes in the thermophysical properties. To test the hypothesis a carbon epoxy specimen is subjected to increasing cyclic loading. The cyclic load was paused periodically at predefined cycle intervals starting from 100 cycles through end of test at 150 k cycles. At each pause, the front side of the specimen is instantaneously heated with a high intensity flash followed by temperature recordings by two thermocouples attached at the front and back sides the rectangular specimen. The data shows that the (T-t) evolution is well correlated to the number of fatigue load cycles that the specimen has absorbed (aka usage). The trending of (T-t) may be explained in terms of change in microcrack density (damage) and the ensuing change in the transverse thermal resistance and heat flow patterns. Additional tests are required to further validate the observed phenomena and verify the hypothesis. If such can be done successfully, thermal measurements may be used as a new structural health monitoring technique to estimate the extent of internal damage in the early stage of the life cycle of a components as well as provide a reliable prediction of remaining useful life of airframe components.

References

1. Haile, M.A., Chen, T.K., Sediles, F., et al.: Estimating crack growth in rotorcraft structures subjected to mission load spectrum. Int. J. Fatigue. **43**, 142–149 (2012)
2. Haile, M.A., Chen, T.-K., Shiao, M., Le, D.: Crack growth behavior in preloaded metallic nested-angle plates under flight load spectrum. Exp. Appl. Mech. **6**, 3–11
3. Haile, M.A., Hall, A.J., Yoo, J.H., et al.: Detection of damage precursors with embedded magnetostrictive particles. J. Intell. Mater. Syst. Struct. **27**, 1567–1576 (2015)
4. Haile, M.A., Riddick, J.C., Assefa, A.H.: Robust particle filters for fatigue crack growth estimation in rotorcraft structures. IEEE Trans. Reliab. **65**, 1438–1448 (2016)
5. Haile, M., Ghoshal, A.: Application of compressed sensing in full-field structural health monitoring, in Proc. SPIE 8346, Smart Sensor Phenomena, Technology, Networks, and Systems Integration., San Diego, CA, USA, pp. 46–53 (2012)
6. Pathak S.V.: Enhanced heat transfer in composite materials (Master's Thesis). Ohio University, Athens (2013)
7. Benveniste, Y.: Effective thermal conductivity of composites with a thermal contact resistance between the constituents: Nondilute case. J. Appl. Phys. **61**(8), 2840 (1987)
8. Campbell, F.C.: Structural composite materials. Materials Park, ASM International (2010)

Chapter 16
Repeatability of Contour Method Residual Stress Measurements for a Range of Material, Process, and Geometry

Mitchell D. Olson, Adrian T. DeWald, and Michael R. Hill

Abstract This paper examines precision of the contour method using five residual stress measurement repeatability studies. The test specimens evaluated include: an aluminum T-section, a stainless steel plate with a dissimilar metal slot-filled weld, a stainless steel forging, a titanium plate with an electron beam slot-filled weld, and a nickel disk forging. These specimens were selected to encompass a range of typical materials and residual stress distributions. Each repeatability study included contour method measurements on five to ten similar specimens. Following completion of the residual stress measurements an analysis was performed to determine the repeatability standard deviation of each population. In general, the results of the various repeatability studies are similar. The repeatability standard deviation tends to be relatively small throughout the part interior and there are localized regions of higher repeatability along the part perimeter. The repeatability standard deviations over most of the cross-section range from 5 MPa, for the aluminum T-section, to 35 MPa, for the stainless steel forging. These results provide expected precision data for the contour method over a broad range of specimen geometries, materials, and stress profiles.

Keywords Repeatability • Repeatability standard deviation • Measurement repeatability • Precision • Contour method • Residual stress

16.1 Introduction

Precision is an important parameter to consider when selecting a measurement technique since it provides the expected measurement variability for a given test method. The definition of precision is the closeness of agreement between independent test results obtained under stipulated conditions. Precision is closely related to measurement repeatability. Repeatability is the precision where the stipulated conditions require the same test method applied to identical test specimens, in the same laboratory, by the same operator, over a short interval of time [1]. Repeatability is quantified by the repeatability standard deviation, which is simply the standard deviation of test results from a repeatability study.

The repeatability of the contour method has been determined in prior publications in a quenched aluminum bar [2] and a stainless steel plate with a stainless steel slot-filled weld [3]. The repeatability study in the quenched aluminum bar found a stress field that had large magnitude compressive stress along the bar periphery (around −175 MPa) and tensile stress at the center of the bar (around 175 MPa). The repeatability standard was between 5 and 10 MPa over most of the cross-section, with localized regions and the periphery having larger repeatability standard deviations (maximum as large as 20 MPa). The repeatability study in the stainless steel plate found repeatability standard deviations under 20 MPa at most locations with localized regions up to 30 MPa.

The primary objective of the present study is to build on the prior studies [2, 3] and determine contour method repeatability under a representative set of conditions. The set of conditions includes alloys of iron, aluminum, titanium, and nickel, reflecting key industrial alloys. The set of conditions also includes a range of geometry, including plate, disk, and tee-section.

Submitted for presentation at SEM 2017 Annual Conference and Exposition on Experimental and Applied Mechanics, Indianapolis, IN, June 12–15, 2017

M.D. Olson (✉) • A.T. DeWald
Hill Engineering, LLC, 3083 Gold Canal Drive, Rancho Cordova, CA, USA
e-mail: molson@hill-engineering.com

M.R. Hill
University of California, Davis, Department of Mechanical and Aerospace Engineering, One Shields Avenue, Davis, CA, USA

A. Baldi et al. (eds.), *Residual Stress, Thermomechanics & Infrared Imaging, Hybrid Techniques and Inverse Problems, Volume 8*,
Conference Proceedings of the Society for Experimental Mechanics Series, DOI 10.1007/978-3-319-62899-8_16

16.2 Methods

16.2.1 Overview

Contour method repeatability was assessed in five different configurations: an aluminum T-section, a stainless steel plate with a dissimilar metal (DM) slot-filled weld, a stainless steel forging, a titanium plate with an electron beam (EB) slot-filled weld, and a nickel alloy disk. Each repeatability assessment included contour method measurements on sets of replicate specimen and statistical analysis to determine the repeatability standard deviation for each set. Since the contour method is a destructive measurement technique that requires physically cutting the specimen in half (details below), it is impossible to repeatedly measure the same specimen. Thus, a set of specimen was prepared for each configuration and care was taken to obtain specimens with consistent residual stress distributions. The following is a brief description of each specimen type.

16.2.2 Geometry and Material

16.2.2.1 Aluminum T-Section

Aluminum T-section specimens were fabricated from bars cut from 79.38 mm (3.125 in) thick 7050-T7451 aluminum plate that had been stress relieved by stretching. The bars had a length of 762 mm (30.0 in), a height of 79.38 mm (3.125 in), and a width of 82.55 mm (3.25 in). The bars were heat treated, including a quench, to induce high residual stress indicative of the -T74 temper. The heat treatment used the recipe described in [4] that consists of heating the specimens to 477 °C (890 °F) for 3 h, quenching in room temperature water, artificial aging at 121 °C (250 °F) for 8 h followed by additional aging at 177 °C (350 °F) for 8 h. T-sections were then machined from the bars to represent an airframe structural member. Each T-section had a length of 254 mm (10.0 in), a height of 50.8 mm (2.0 in), a width of 82.55 mm (3.25 in), and a leg thicknesses of 6.35 mm (0.25 in), as shown in Fig. 16.1.

16.2.2.2 Stainless Steel DM Welded Plate

Stainless steel dissimilar metal (DM) weld specimens were fabricated from one long plate made of high-strength 316 L stainless steel. The plate had a 25.4 mm (1.0 in) by 152.4 mm (6.0 in) cross-section and a length of 1.22 m (48.0 in). A slot was machined along the entire length of the plate with a depth of 9.53 mm (0.375 in), a width of 19.05 mm (0.75 in), and a 70° root angle. The slot and plate cross-section can be seen in Fig. 16.2. Prior to filling the slot with weld material, the plate was constrained by welding the plate to an additional support plate. The weld joining the plate to the support plate was a continuous 7.94 mm (0.313 in) fillet weld that was applied along both 1.22 m edges of the plate. The slot weld was made using eight passes, each continuous along the entire length of the plate using an automated welder of 0.89 mm (0.035 in) diameter A52M (ERNiCrFe-7A) wire. Welding was gas tungsten arc welding (GTAW) with 250 A current, 10.5 V voltage, and 101.6 mm/min (4 in/min) travel speed.

Following welding, the fillet welds were machined away to release the DM welded plate from the support plate and the ends of the DM welded plate were removed to eliminate the inconsistent weld bead geometry at the start and stop of the weld (139.7 mm (5.5 in) of material was removed from the weld start and 63.5 mm (2.5 in) was removed from the weld stop). The remaining section was 1.02 m (40.0 in) long.

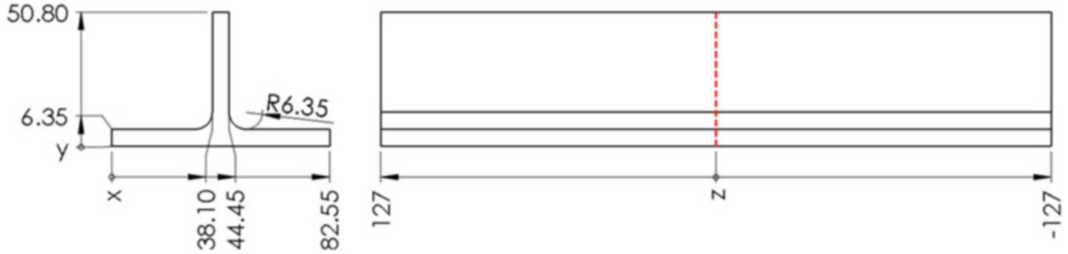

Fig. 16.1 Aluminum T-section dimensions and measurement location (dimensions in mm)

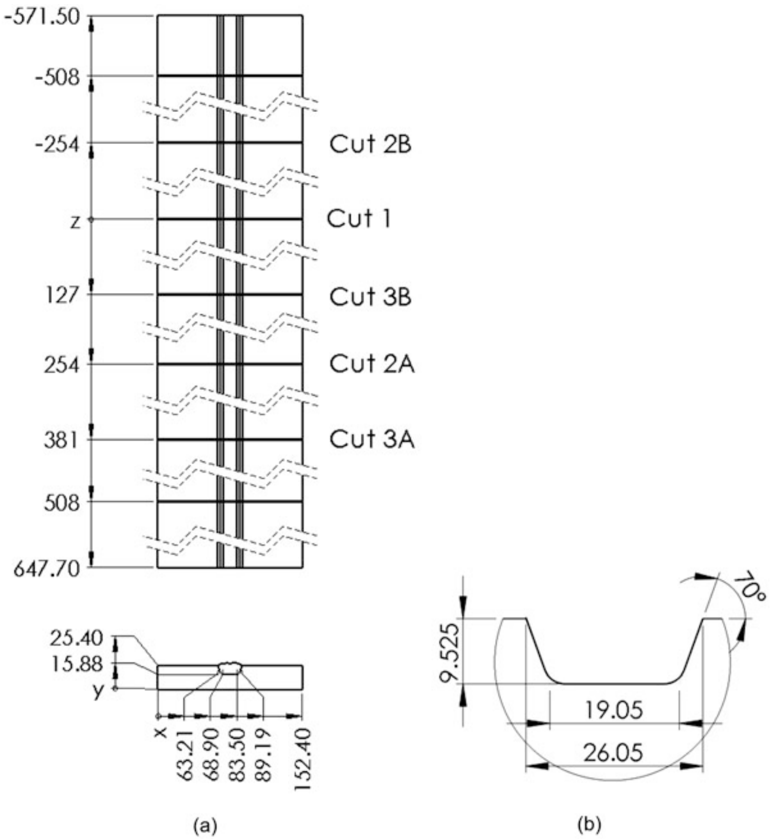

Fig. 16.2 Stainless steel dissimilar metal (**a**) dimensions and measurement locations and (**b**) slot details (dimensions in mm)

16.2.2.3 Titanium Electron Beam Welded Plate

Titanium alloy electron beam (EB) welded plate specimens were fabricated using one long Ti-6Al-4 V plate, with similar geometry to the stainless steel DM welded plate (same cross-section and slot dimensions). The weld process is a typical additive manufacturing process, but service parts would typically be subjected to thermal stress relief. The groove was filled along the entire length of the plate with 8-passes of 3.18 mm (0.125 in) diameter Ti-6Al-4 V wire. After completion of the weld, the plate was sectioned into 101.6 mm (4.0 in) long pieces, as shown in Fig. 16.3.

16.2.2.4 Stainless Steel Forging

Stainless steel forging specimens in 304 L are roughly hemi-spherical with an outer diameter of 73.7 mm (2.9 in). They include a forged internal cavity with inner diameter of 30.5 mm (1.2 in), and a height of 50.8 mm (2.0 in) (Fig. 16.4). The specimens were produced using a multi-stage forging process. The specimen billets were heated to 980 °C (1800 °F) for 60 min, die pressed to 75% of their original height in a hydraulic press, cooled to room temperature, heated to 1750 °F for 60 min, and subjected to a high-energy rate forging operation. Next, the specimens were cooled to room temperature, annealed at 955 °C (1750 °F) for 30 min, and then water quenched. The final processing steps consisted of reheating the specimens to 845 °C (1550 °F) for 60 min, a final high-energy rate forging operation, followed by a final water quench.

16.2.2.5 Nickel Alloy Disk

Nickel alloy (Udimet-720Li) disk specimens had a diameter of 151.20 mm (5.95 in) and a maximum height of 70.41 mm (2.77 in), as is shown in Fig. 16.5. The specimens were forged and heat treated, including a quench, to achieve desired mechanical properties. The heat treatment consisted of pre-heating the specimens to 1080 °C (1975 °F), forging to the

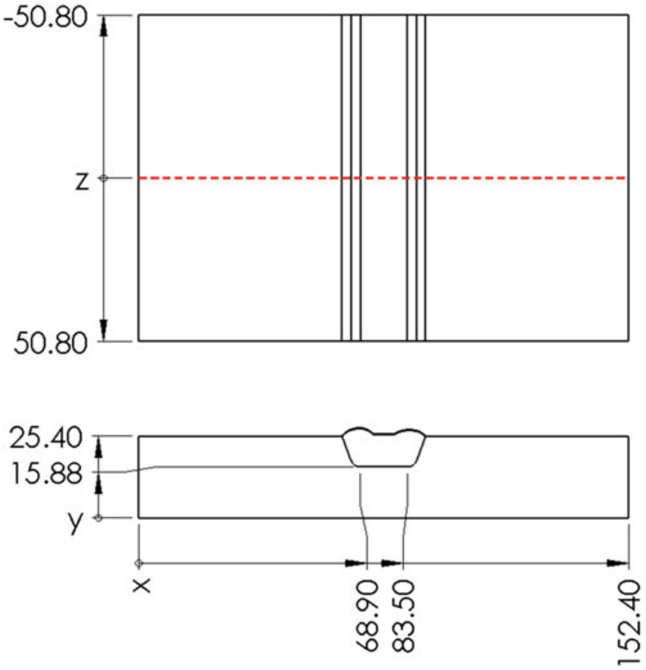

Fig. 16.3 Titanium electron beam welded plate dimensions and measurement location (dimensions in mm)

nominally finished shape, solution heat treating at 1105 °C (2020 °F), and oil quenching. The specimens were then stabilized at 760 °C (1400 °F) for 8 h, air cooled, aged at 650 °C (1200 °F) for 24 h and then air cooled to room temperature. Since the amount of available material was limited, three disks were sectioned in half to give six nominally identically half disk specimens.

16.2.3 Contour Method

The contour method is a residual stress measurement technique whose theoretical basis was established by Prime [5]. A contour method measurement will cut a part along a given measurement plane and deformation of the cut surfaces will occur as a direct result of residual stress release and redistribution. The resulting deformed cut surface profiles can be measured and when the negative of the measured surface profiles are applied as a displacement boundary condition in a finite element model of the half part, the residual stress released normal to the cutting plane can be determined. Detailed experimental steps for the contour method have been provided by Prime and DeWald [6].

The contour method measurements for each repeatability study followed nominally the same procedure with a summary given here. For each contour method measurement, the specimen was cut in two using a wire electric discharge machine (EDM) while the specimen was rigidly clamped to the EDM frame. Following cutting, the profile of each of the two opposing cut faces was measured with a laser scanning profilometer to determine the surface height normal to the cut plane as a function of in-plane position. Surface height data were taken on a grid of points with spacing between 100 and 200 μm in each direction. The two cut surface profiles were then aligned, averaged on a common grid, and the average was fit to a smooth bivariate analytical function. The residual stress release on each measurement plane was found by applying the negative of the smoothed surface profile as a boundary condition on the cut face of a linear elastic finite element model of the cut part. Each model used the corresponding set of elastic material properties given in Table 16.1.

16.2.4 Repeatability Experiments

For each of the five specimen types described above, a contour method repeatability experiment was performed. The repeatability studies involved performing a single contour method measurement on a set of similar test specimens. Each

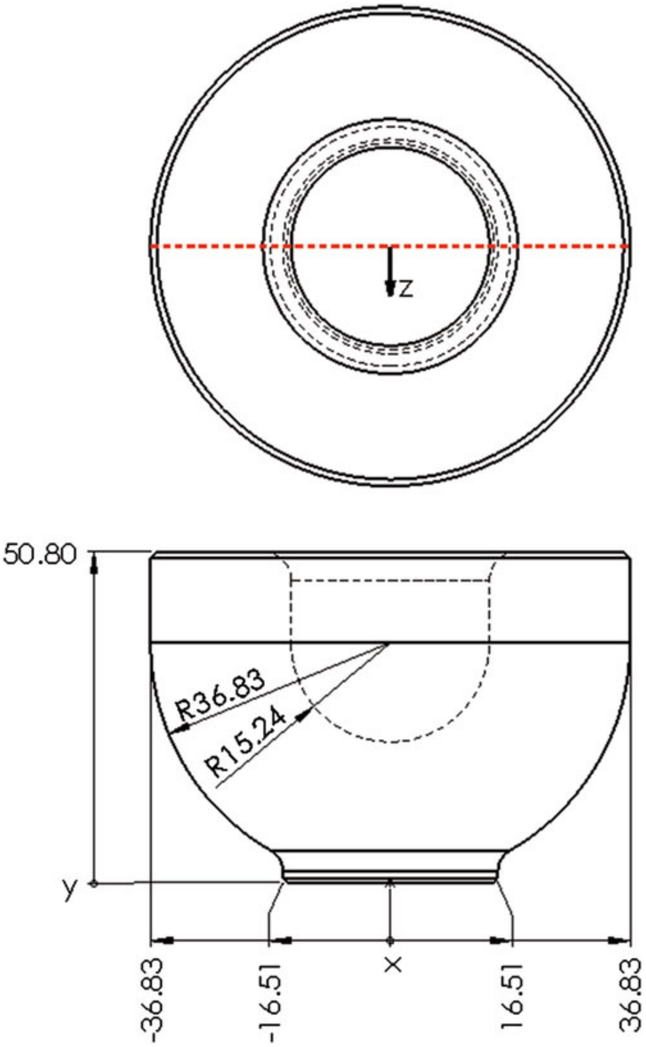

Fig. 16.4 Stainless steel forging dimensions and measurement location (dimensions in mm)

measurement provided a 2D map of residual stress. All measurements were performed in a consistent manner to assess measurement repeatability. The following is a brief description of the measurements performed on each set of specimens.

For the aluminum T-section specimens, contour method measurements were performed at the mid-length of ten specimens (127 mm (5 in) from each end, as shown in Fig. 16.1). Six titanium welded specimens were measured at the plate mid-length, as shown in Fig. 16.3. The contour method measurements on the stainless steel forgings were performed at the specimen mid-width (shown in Fig. 16.4) for six specimens. For the six nickel alloy (half) disk specimens, contour method measurements were performed at the specimen mid-width (shown in Fig. 16.5). Stress release from sectioning the disks in half was found using a supplemental stress analysis in conjunction with the strain change recorded before and after sectioning (using strain gages at multiple locations). The total hoop stress, including the effect of sectioning, is reported for the disk specimens.

The stainless steel DM weld repeatability study consisted of measurements at different positions along the length of the plate, rather than making measurements in nominally identical specimens removed from the long plate. This was done to preserve the original residual stress field present in the plate, which is more representative of a highly constrained weld employed at pressurized water reactor (PWR) nuclear power plants. The repeatability experiment consisted of five contour method measurements, where each measurement repeatedly cut the plate in half. Figure 16.2 show that the first measurement (Cut 1) cut the plate in half; the second (Cut 2A) and third measurements (Cut 2B) cut each of the half plates in half; and the fourth (Cut 3A) and fifth measurements (Cut 3B) cut two of the quarter plates in half. Corrections were made to account for the small changes in residual stress as the specimen size was reduced by previous contour measurements. The corrections used the data from prior contour method measurements at the subsequence measurement plane was as done in [7].

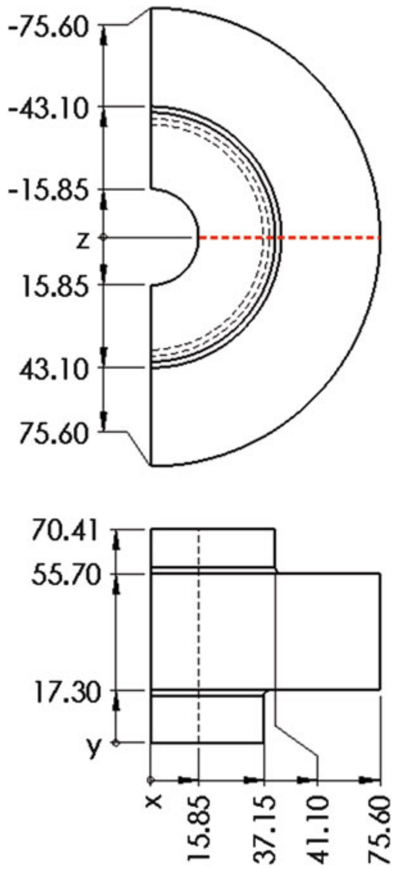

Fig. 16.5 Nickel disk dimensions and measurement location (dimensions in mm)

Table 16.1 Material properties for each of the specimens used in the repeatability studies

Specimen	Elastic modulus (GPa)	Poisson's ratio	Yield strength (MPa)
Aluminum T-section (7085-T74)	71	0.33	460
Titanium EB welded plate (Ti-6Al-4V)	110	0.31	960
Nickel disk (Udimet-720Li)	200	0.31	300–500
Stainless steel forging (304 L)	200	0.249	210
Stainless steel DM welded plate (316 L plate)	203	0.3	440
Stainless steel DM welded plate (A52 weld)	211	0.289	345–482

Following completion of the contour method measurements the mean and repeatability standard deviation were calculated for each repeatability experiment using standard formulae. This provides a mean 2D stress map and a 2D map of the repeatability standard deviation.

16.3 Results

Residual stress 2D maps of mean and repeatability standard deviation for all configurations are shown in Figs. 16.6, 16.7, 16.8, 16.9, 16.10, 16.11, 16.12, 16.13, 16.14, and 16.15. The median, mean, 75th percentile, 95th percentile, and maximum value of the repeatability standard deviation for all configurations is tabulated in Table 16.2.

The mean longitudinal residual stress in the aluminum T-section has compressive stress at the left and right edges of the bottom flange (minimum value of approximately −240 MPa) and at the top of the center flange (minimum value of approximately −70 MPa) with tensile stress at the intersection of the bottom and center flanges (peak value of approximately 100 MPa) (Fig. 16.6a). The measured residual stress is similar between the ten measurements as is indicated by the repeatability standard deviation (Fig. 16.6b) and the line plots (Fig. 16.7). The repeatability standard deviation is low at most

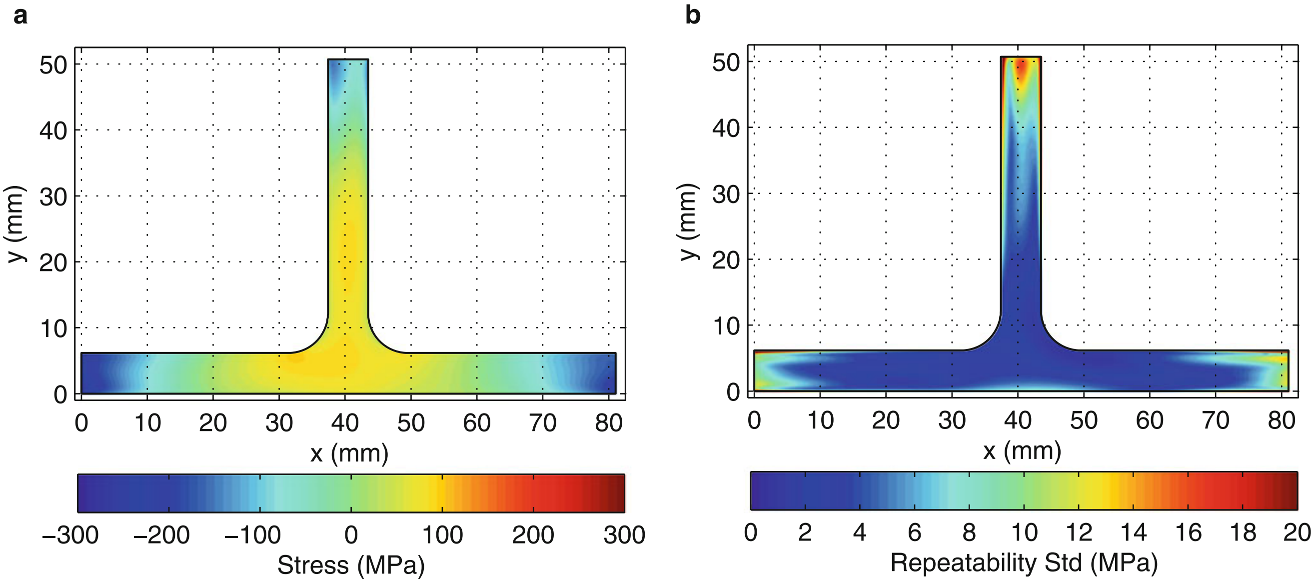

Fig. 16.6 (**a**) Mean and (**b**) repeatability standard deviation for the aluminum T-section specimens

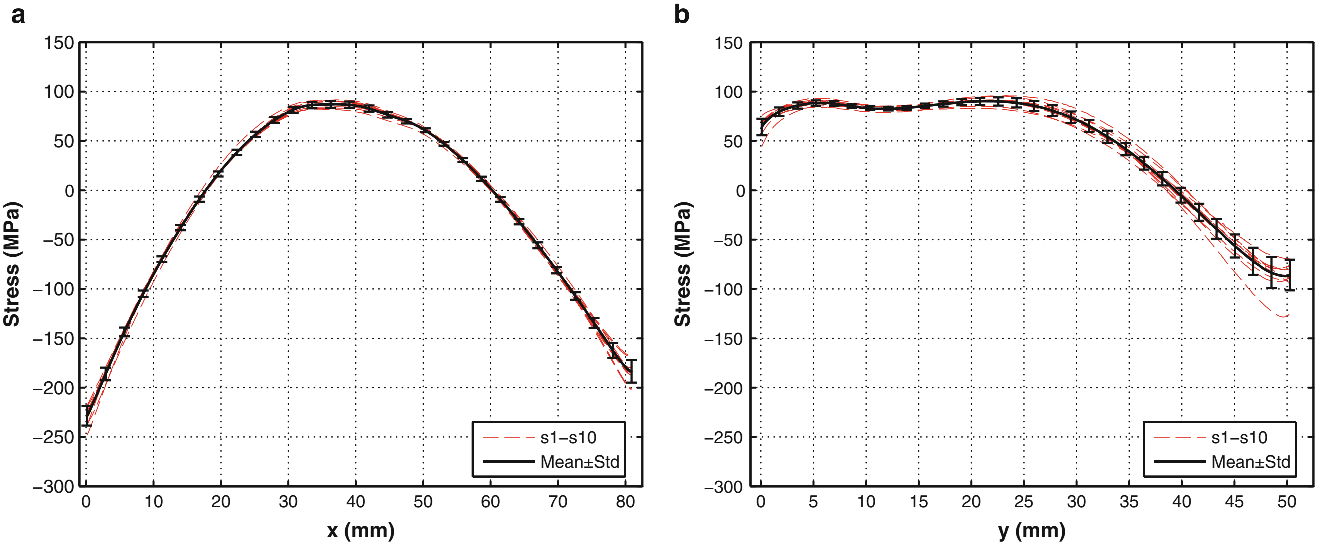

Fig. 16.7 *Line* plots of individual measurements (*dashed*) and the mean and repeatability standard (*solid black*) for the aluminum T-section samples along the (**a**) x-direction at y = 3.18 mm and (**b**) along the y-direction at x = 40.52 mm

points (average of 5 MPa), but with localized regions at the edges of the bottom and center flanges where the repeatability standard deviations is larger (95th percentile at 13 MPa).

The mean longitudinal residual stress in the stainless steel DM welded plate has tensile stress in the weld area and heat-affected zone (maximum value of approximately 380 MPa) and near the left and right edges of the plate where the plate was welded to the support fixture (maximum value of approximately 400 MPa) (Fig. 16.8a). There is compensating compressive stress toward the top of the plate at the left and right edges (minimum value of approximately −260 MPa). The stress line plots for each individual measurement and the mean (Fig. 16.9) show that the stress in nominally consistent between specimen, with modest differences at the top and bottom of the plate. Most points had low repeatability standard deviations (average of 17 MPa), but there are localized regions near the part boundary where the repeatability standard deviation is larger (95th percentile at 36 MPa), as shown in Fig. 16.8b.

The mean longitudinal stress in the titanium EB welded plate has tensile stress in the weld area (maximum value of approximately 350 MPa) and compensating compressive stress in the heat-affected zone (minimum value of approximately −200 MPa) (Fig. 16.10a). The line plots in Fig. 16.11 show that the stress is very consistent between each specimen. Most

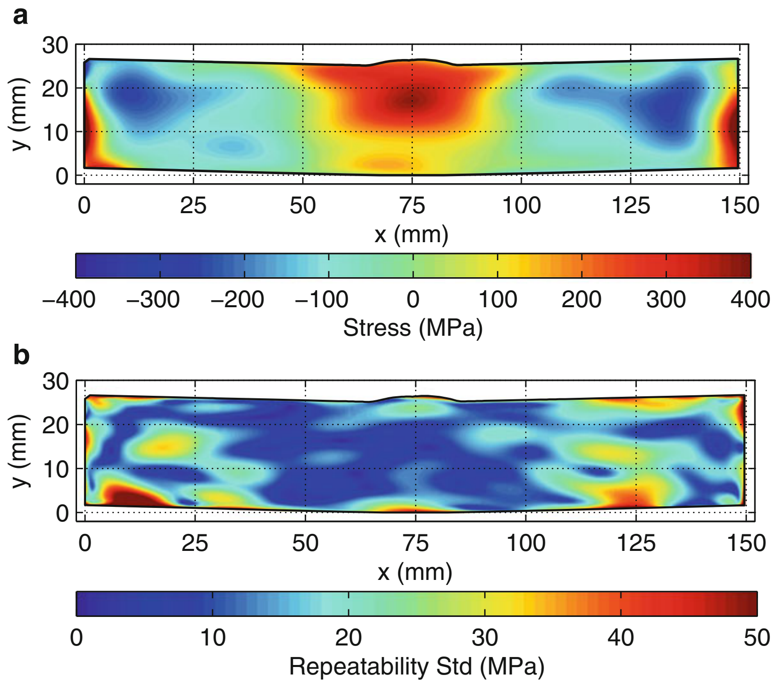

Fig. 16.8 (**a**) Mean and (**b**) repeatability standard deviation for the stainless steel DM welded specimens

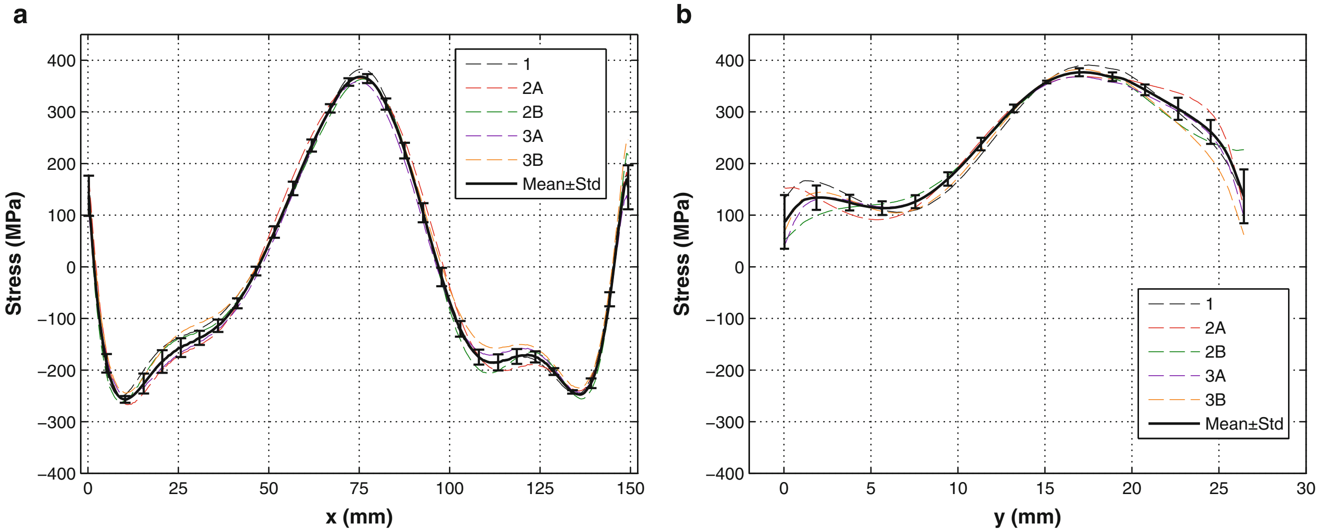

Fig. 16.9 *Line* plots of individual measurements (*dashed*) and the mean and repeatability standard (*solid black*) for the stainless steel DM welded samples along the (**a**) x-direction at y = 19.05 mm and (**b**) along the y-direction at x = 76.2 mm

points had a low repeatability standard deviation (average of 8 MPa), with localized regions near the part boundary having higher repeatability standard deviations (95th percentile at 17 MPa), as shown in Fig. 16.10b. In this case, the repeatability standard deviation appears to be more spatially uniform over the cross-section than was found in other cases.

The mean hoop stress in the stainless steel forging has tensile stress adjacent to the internal cavity (maximum value of approximately 340 MPa) and compensating compressive stress near the outer surfaces of the forging (minimum value of approximately −260 MPa) (Fig. 16.12a). Five of the six measurements were nominally consistent, with one being a significant outlier (maximum tensile stress was approximately 100 MPa larger than all the other measurements) as is shown in Fig. 16.13. To further illustrate the outlying measurement, line plots of the stress measured in all six specimens are shown in Fig. 16.14. The repeatability standard deviation reported in Fig. 16.12b, which omits the outlier measurement, has a low repeatability standard deviation (mean at 24 MPa) with localized regions having higher repeatability standard deviations

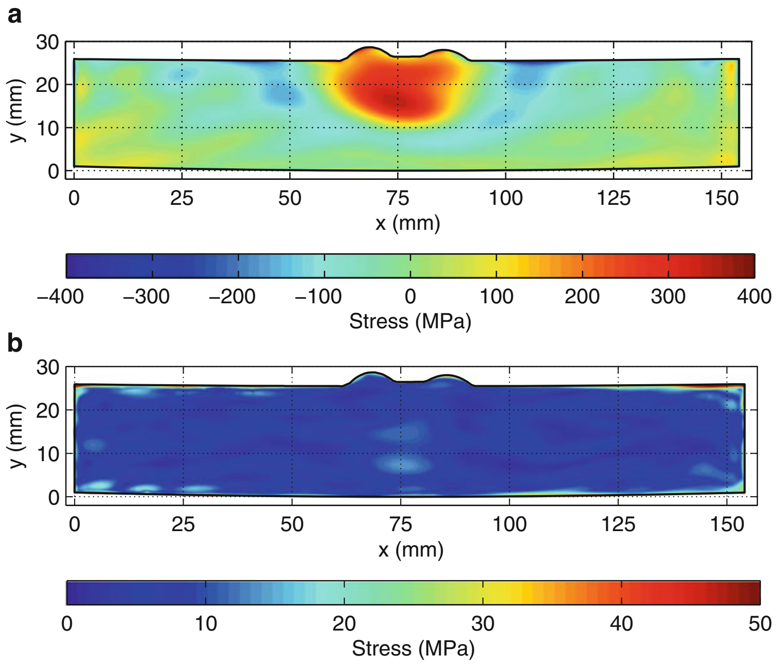

Fig. 16.10 (**a**) Mean and (**b**) repeatability standard deviation for the titanium EB welded plate specimens

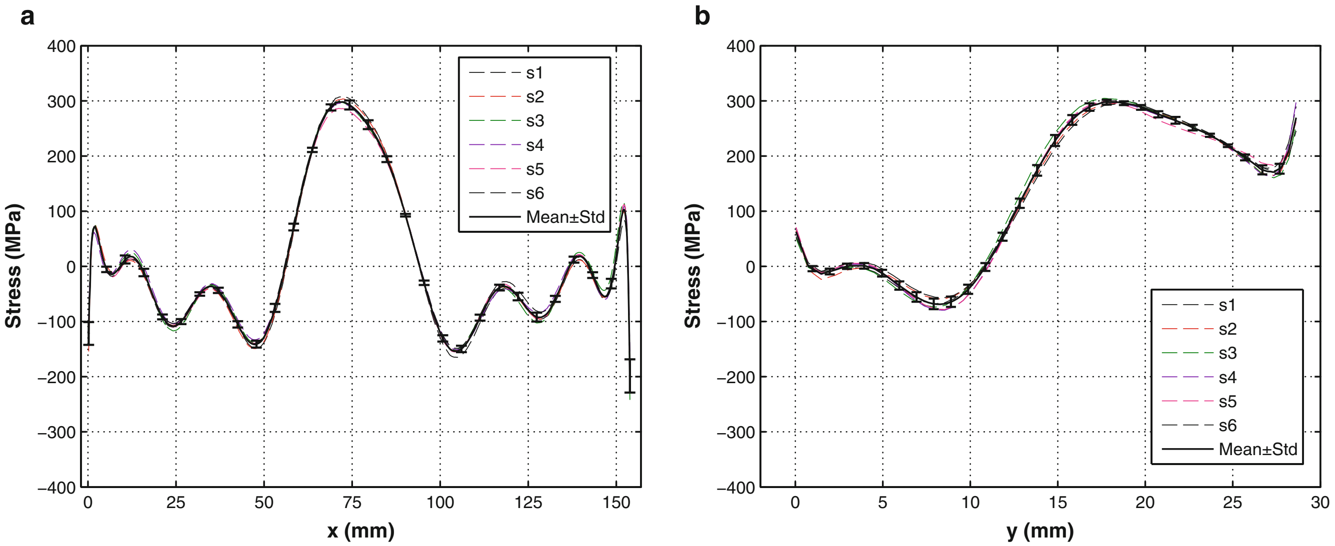

Fig. 16.11 *Line* plots of individual measurements (*dashed*) and the mean and repeatability standard (*solid black*) for the titanium EB welded plate samples along the (**a**) x-direction at y = 20.32 mm and (**b**) along the y-direction at x = 68.15 mm

(95th percentile at 52 MPa). (The repeatability standard deviation including the outlier measurement us larger, with values up to 135 MPa near the forging cavity).

The mean hoop stress in the nickel disk has tensile stress towards the disk inner diameter at mid-thickness (maximum value of approximately 450 MPa) and compensating compressive stress toward the disk periphery (minimum value of approximately −580 MPa) (Fig. 16.15a). Line plots (Fig. 16.16) show that the measurements are consistent relative to magnitude of stresses being measured. The repeatability standard deviation distribution is consistent with those from the other configurations, but with more spatial variation over the cross-section. Most points have a modest repeatability standard deviation (average of 25 MPa) and localized regions of high repeatability standard deviation (95th percentile at 52 MPa) particularly near the top and bottom of the disk (Fig. 16.15b).

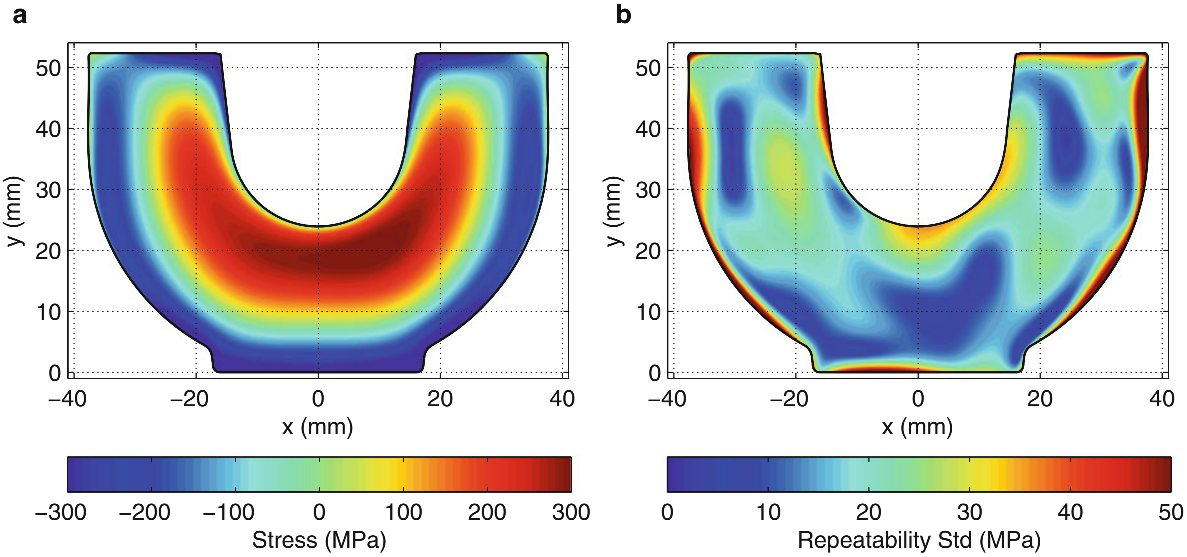

Fig. 16.12 (**a**) Mean and (**b**) repeatability standard deviation for the stainless steel forging specimens

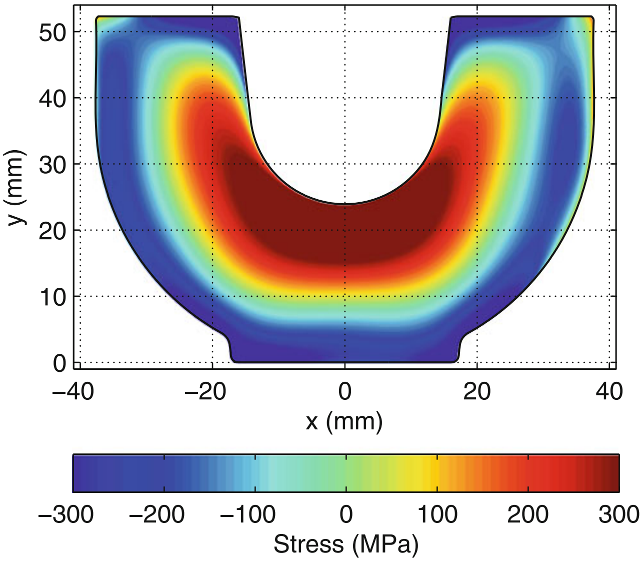

Fig. 16.13 Outling stainless steel forging measurements (S2)

16.4 Discussion

The present repeatability experiments provide similar results to those reported in earlier work [2, 3]. In the study using aluminum bars [2], both the measured stress and the repeatability standard deviation was very similar to the results found in the present aluminum T-section. The repeatability standard deviation was below 10 MPa at most points with maximum values near the part perimeter at 20 MPa for both parts. Similarly, in a study using a stainless steel plate with a stainless steel slot-filled weld [3], the repeatability standard deviation was below 20 MPa at most points, which is very close to the values found in the stainless steel DM welded plate reported here.

The repeatability standard deviation trend found among the five configurations is consistent. There tends to be relatively stable and low magnitude repeatability standard deviation over most of the specimen interior and localized regions of higher variability along the part perimeter. The magnitude of the repeatability standard deviation increases with elastic modulus of the material, as shown in Fig. 16.17a. The materials with the largest elastic moduli also have the largest repeatability standard deviation and alternatively materials with lower elastic moduli have smaller repeatability standard deviations. To better interpret the results, the mean, median, 75th percentile, and 95th percentile of the repeatability standard deviation for

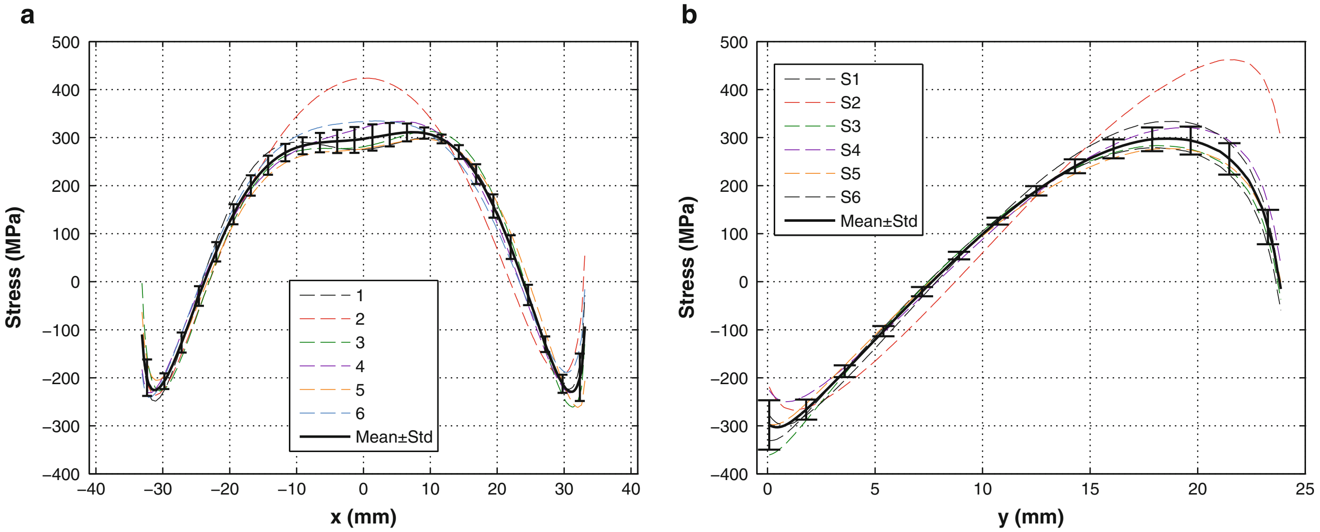

Fig. 16.14 *Line* plots of individual measurements (*dashed*) and the mean and repeatability standard (*solid black*) for the stainless steel forging samples along the (**a**) x-direction at y = 19.05 mm and (**b**) along the y-direction at x = 0

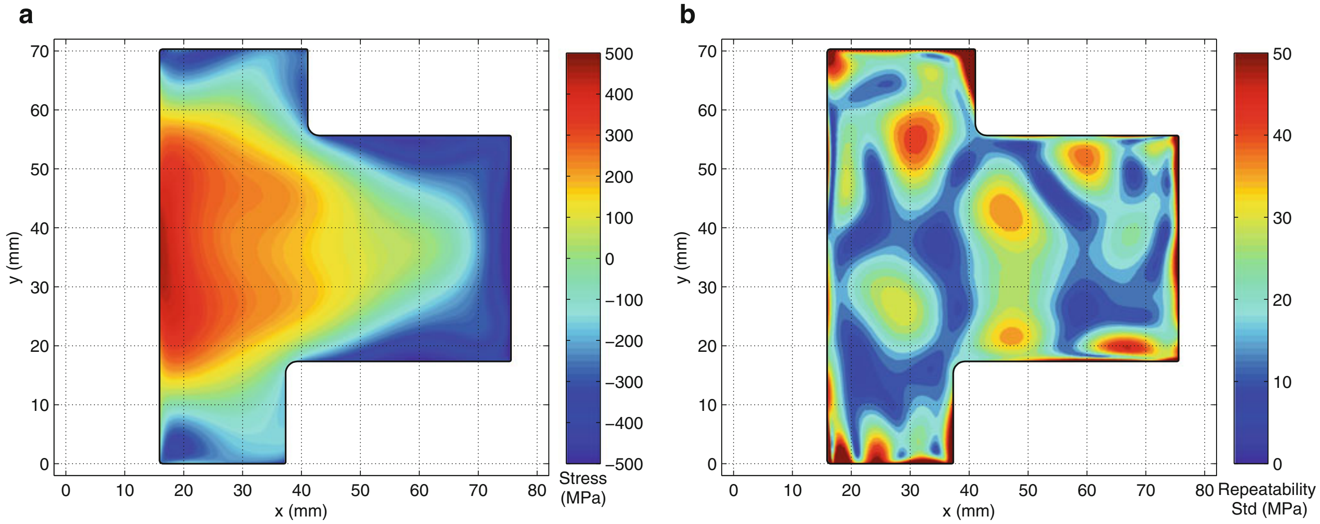

Fig. 16.15 (**a**) Mean and (**b**) repeatability standard deviation for the nickel disk specimens

Table 16.2 Repeatability standard deviation statistical values

Specimen	Median (MPa)	Mean (MPa)	75th percentile (MPa)	95th percentile (MPa)
Aluminum T-section (7085-T74)	3.7	5.1	6.2	12.6
Titanium EB welded plate (Ti-6Al-4V)	5.9	7.7	8.3	17.3
Nickel disk (Udimet-720Li)	21.5	24.9	29.7	51.7
Stainless steel forging (304 L)	20.3	23.8	27.6	52.3
Stainless steel DM welded plate	14.9	17.3	21.6	36.3

each specimen was calculated and is shown in Fig. 16.17. The median is lower than the mean, which suggests the distribution of repeatability standard deviation is skewed toward larger values. The trend is consistent across cross-sectional shapes and underlying processes (quenching, forging, welding).

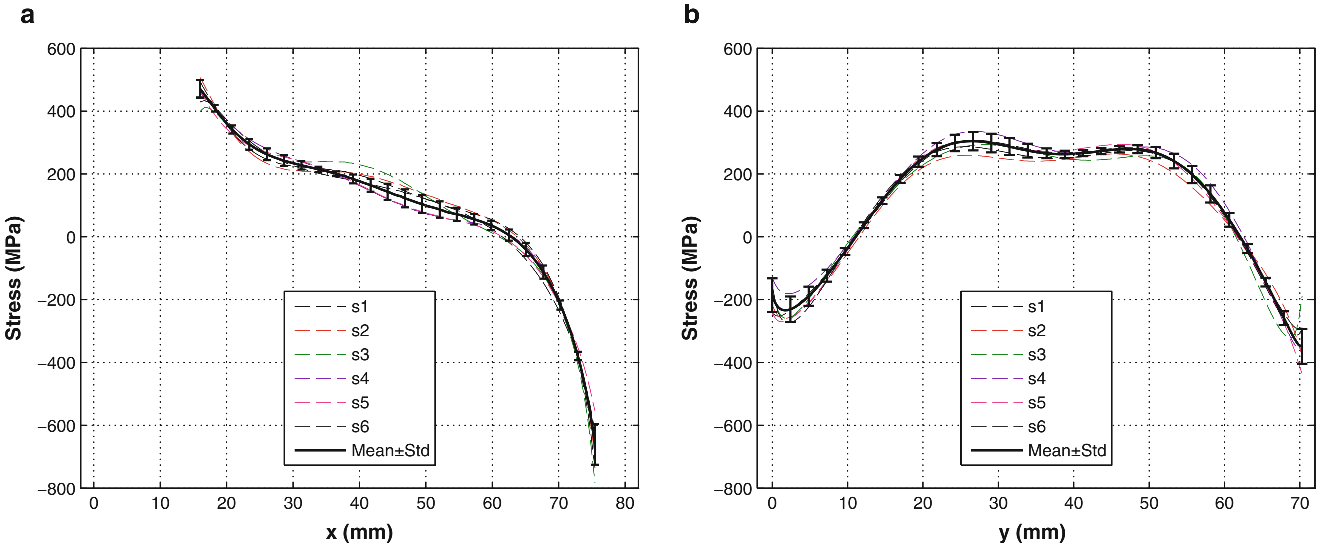

Fig. 16.16 *Line* plots of individual measurements (*dashed*) and the mean and repeatability standard (*solid black*) for the nickel disk samples along the (**a**) x-direction at y = 3.18 mm and (**b**) along the y-direction at x = 40.52 mm

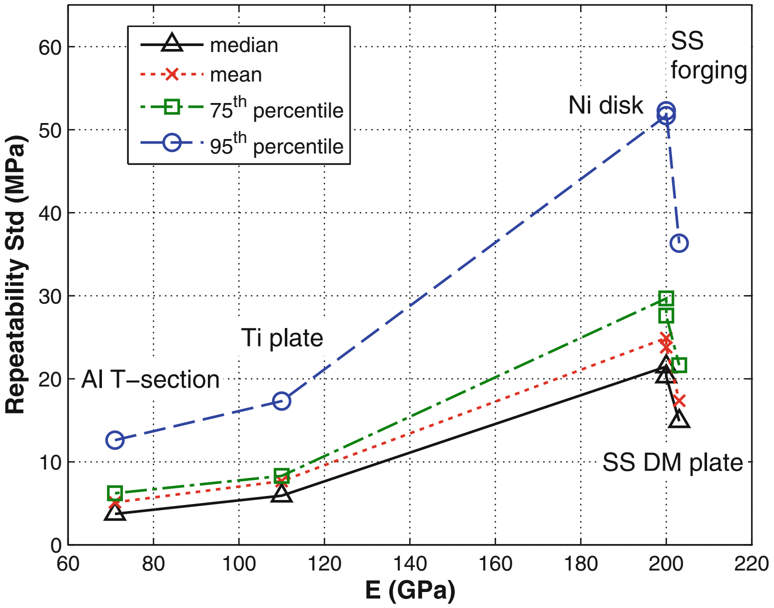

Fig. 16.17 Repeatability standard deviation versus elastic modulus (E)

16.5 Summary/Conclusions

Five repeatability studies were performed using an aluminum T-section, a stainless steel plate with a dissimilar metal slot-filled weld, a stainless steel forging, a titanium plate with an electron beam slot-filled weld, and a nickel disk forging. Each repeatability study included five to ten contour method measurements and determined the repeatability standard deviation. The results of the repeatability studies show consistent levels of repeatability over most of the specimen interior and localized regions of higher variability (typically along the part perimeter). The mean repeatability standard deviation ranged from 5 MPa for the aluminum T-section to 35 MPa for the stainless steel forging, which represent the minimum and maximum values of the population. Similarly, the value of the 95th percentile repeatability standard deviation ranged from 15 MPa for the aluminum T-section to 85 MPa for the stainless steel forging.

Acknowledgements The authors acknowledge, with gratitude, the U.S. Air Force for providing financial support for this work (contract FA8650-14-C-5026). We would also like to acknowledge Steve McCracken from the Electric Power Research Institute for supplying and fabricating the stainless steel plate with a dissimilar metal slot-filled weld, Thomas Reynolds from Sandia National Laboratory for providing the stainless steel forgings, and Brian Streich from Honeywell for providing the nickel disk forgings.

References

1. E11 Committee: Practice for use of the terms precision and bias in ASTM test methods. ASTM International, West Conshohocken (2010)
2. Hill, M.R., Olson, M.D.: Repeatability of the contour method for residual stress measurement. Exp. Mech. **54**(7), 1269–1277 (2014)
3. Olson, M.D., Hill, M.R., Willis, E, Peterson, A.G., Patel, V.I., Muránsky, O.: Assessment of weld residual stress measurement precision: Mock-up design and results for the contour method. J. Nucl. Eng. Radiat. Sci. (2015)
4. SAE Aerospace: Aerospace material specification 4342: Aluminum alloy extrusions: Solution heat treated, stress relieved, s, and overaged. (2006)
5. Prime, M.B.: Cross-sectional mapping of residual stresses by measuring the surface contour after a cut. J. Eng. Mater. Technol. **123**(2), 162–168 (2001)
6. Prime, M.B., DeWald, A.T.: The contour method. In: Schajer, G.S. (ed.) Practical Residual Stress Measurement Methods, Ch 5, pp. 109–138. Wiley, West Sussex (2013)
7. Wong, W., Hill, M.R.: Superposition and destructive residual stress measurements. Exp. Mech. **53**(3), 339–344 (2013)

Chapter 17
System Identification of Structures with Modal Interference

Chang-Sheng Lin

Abstract Previous studies show that when a system has repeated modes in frequency domain, the multiple-input and multiple-output (MIMO) concept can be applied to effectively identify the modal parameters. In this study, the MIMO concept is extended to the time domain for system identification of systems with modal interference. When performing a modal analysis of a structural system with close modes or high damping, the results of identification may be poor due to modal interference, and the estimation of system order is important to the effectiveness of modal identification. By introducing the concept of the singular value decomposition (SVD) in Eigensystem Realization Algorithm (ERA), and simplifying the identification process of ERA, the system order will be estimated effectively even for a system having close (even repeated) modes. In addition, the correlation matrix is also used to perform SVD, and then directly identify modal parameters, i.e., omitting the additional process of constructing the generalized Hankel matrix, which provides a more efficient method of identification of modal parameter. Also, in this paper, the SVD algorithm is introduced to the identification process of Ibrahim Time-Domain Method. The order of system matrix is efficiently determined, and the modal identification of a system with close modes through the ITD method can then be well implemented.

Keywords Singular value decomposition (SVD) • Eigensystem realization algorithm (ERA) • Ibrahim time-domain method (ITD)

17.1 Introduction

Modal estimation techniques have been extensively developed in the past, including the frequency-domain methods and the time-domain methods. The time-domain methods manipulate signals in time domain and sometimes work under the consideration that only output response is available, so that we can usually take advantage of time-domain methods in performing modal estimation form practical response data. The frequency-domain methods often require evaluation of the frequency response functions (FRFs) from the measured input and output data, and then estimate modal parameters of a system [1]. Based on the Prony's theory, Brown et al. developed the least square complex exponential algorithm (LSCE) [2] using a squared output matrix constructed by multichannel impulse response functions, which is a well-known technique in conventional modal analysis yielding global estimates of residues and poles. In 1982, Vold and Rocklin further proposed poly reference complex exponent method (PRCE) [3] to perform modal identification for the case that one of the modes may not be present in the response data. In 1985, Juang and Pappa [4] proposed the Eigensystem Realization Algorithm (ERA) using the impulse response or the free vibration response of the system to construct the Hankel matrix, which is an augmented matrix containing Markov parameters, for reducing the effect of noise, and making the parameters estimation more accurate. Subsequently, they also proposed a modification of ERA, generally known as ERA/DC (Eigensystem Realization Algorithm with Data Correlation) [5, 6]. ERA/DC uses data correlations to reduce the noise effect in the process of modal-parameter identification. In addition, when performing a modal analysis of a structural system, the results of identification may be poor due to modal interference, which might even introduce the problem of identifiability. Modal interference refers to the phenomenon that vibration energy of each mode of a system may overlap with other modes within certain frequency range. This phenomenon usually results in the difficulty of identification of modal parameters, especially when the identification is performed in the frequency domain. The causes of modal interference may include closely spaced modal frequencies, high damping ratios, and large damping non-proportionality [7]. The influences of modal interference to each cause are difference, and the well-identified modal parameters of a system may not be obtained due to each cause.

C.-S. Lin (✉)
Department of Vehicle Engineering, National Pingtung University of Science and Technology, Neipu, Taiwan
e-mail: changsheng@mail.npust.edu.tw

A. Baldi et al. (eds.), *Residual Stress, Thermomechanics & Infrared Imaging, Hybrid Techniques and Inverse Problems, Volume 8*,
Conference Proceedings of the Society for Experimental Mechanics Series, DOI 10.1007/978-3-319-62899-8_17

In this paper, to effectively estimate the modal parameters of a system with close modes, by introducing the concept of the singular value decomposition (SVD) in the process of conventional ERA algorithm and Ibrahim time-domain method (ITD), we could determine the order, as well as the number of modes to be identified, of the system by examining the distribution of the singular values associated with the responses of the system. Once the system order, i.e., the number of modes to be identified is determined, and the modal identification through the ERA or ITD method can then be well implemented.

17.2 Simplification of Eigensystem Realization Algorithm with Data Correlation

In the conventional Eigensystem Realization Algorithm (ERA) [4], by introducing the correlation technique, the distortion led by measurement noise in the parametric estimation can be reduced, and improve the effectiveness of modal identification. In practice, we construct a data correlation-function matrix $R(k)$ of the impulse responses, which are composed of measured response from every channel with different time-delayed signals. This modification of ERA is generally known as Eigensystem Realization Algorithm with Data Correlation (ERA/DC) [5, 6]. It should be mentioned that, in this paper however, we directly use the correlation matrix for modal identification, and avoid the additional construction of generalized Hankel matrix in conventional ERA or ERA/DC, described as follows.

In the ERA/DC, the definition and factorization of a data correlation-function matrix can be expressed as

$$R(k) = H(k)H(0)^T = P_\alpha A^k \vartheta_\alpha \tag{17.1}$$

where $H(k) \approx \frac{1}{l}\left[Y_{k+\tau} Y_k^T\right]_{p\times p}$ For the condition of $k = 0$, $R(0)$ can be written as follows

$$R(0) = P_\alpha \vartheta_\alpha \tag{17.2}$$

To estimate the P_α and ϑ_α, the singular value decomposition (SVD) of $R(0)$ will be performed, and the correlation matrix can then be factorized as the product of two matrixes. From Eq. 17.1, the following equation when $k = 1$ can be derived as

$$R(1) = P_\alpha A \vartheta_\alpha \tag{17.3}$$

The state matrix A of a system can be determined by solving Eqs. 17.2 and 17.3, and the modal parameters could be estimated through the eigenvalue analysis for state matrix A.

17.3 Singular Value Decomposition for Ibrahim Time-Domain Method

When performing the modal identification through Ibrahim Time-domain method (ITD), the system matrix **[A]** in ITD can be estimated by using least-squares method as follows

$$[\mathbf{A}] = [\mathbf{Y}]\,[\mathbf{X}]^{\mathrm{T}}\Big([\mathbf{X}]\,[\mathbf{X}]^{\mathrm{T}}\Big)^{-1} \tag{17.4}$$

Introducing the Singular Value Decomposition, the Eq. 17.4 can be rewritten as

$$[\mathbf{A}] = [\mathbf{Y}]\,[\mathbf{X}]^{\mathrm{T}}\Big([\mathbf{U}]\,[\Sigma]\,[\mathbf{V}]^{\mathrm{T}}\Big)^{-1} \tag{17.5}$$

where **[U]** and **[V]** are both unitary matrices. Due to that **[U]** and **[V]** are the matrices with orthonormal property, (i.e., $[\mathbf{U}]^{-1} = [\mathbf{U}]^{\mathrm{T}},\ \ [\mathbf{V}]^{-1} = [\mathbf{V}]^{\mathrm{T}}$), Eq. 17.5 can then be derived as

$$[\mathbf{A}] = [\mathbf{Y}]\,[\mathbf{X}]^{\mathrm{T}}\,[\mathbf{V}]\,[\mathbf{\Sigma}]^{-1}[\mathbf{U}]^{\mathrm{T}} \tag{17.6}$$

It should be mentioned that, by examining the numbers of the non-zero singular values of $[\mathbf{\Sigma}]$ associated with the responses of the system, we could determine the order, as well as the number of modes to be identified, of a system, and also further confirm if the phenomenon of omitted modes exists. In addition, by performing the singular value decomposition

(SVD) algorithm of $[\mathbf{X}][\mathbf{X}]^{\mathrm{T}}$, we could directly determine the order of a system without the procedures of examining the Fourier spectrum associated each of the response channels to roughly find the important modes of the system under consideration, and also significantly reduce relatively much calculations required in the conventional channel-expansion technique.

17.4 Numerical Simulations

To demonstrate the effectiveness of the present method, we consider 6-dof chain-model system. The mass matrix ***M***, stiffness matrix ***K***, and the proportional damping matrix ***C*** of the system are given as follows:

$$\mathbf{M}=\begin{bmatrix}1&0&0&0&0&0\\0&1&0&0&0&0\\0&0&2&0&0&0\\0&0&0&2&0&0\\0&0&0&0&1&0\\0&0&0&0&0&1\end{bmatrix} N\cdot \sec^2/m \qquad \mathbf{K}=600\times\begin{bmatrix}2&-1&0&0&0&0\\-1&2&-1&0&0&0\\0&-1&2&-1&0&0\\0&0&-1&2&-1&0\\0&0&0&-1&2&-1\\0&0&0&0&-1&2\end{bmatrix} N/m$$

$$\mathbf{C}=0.01\mathbf{M}+0.002\mathbf{K}+0.5\begin{bmatrix}1&\cdots&1\\\vdots&\ddots&\vdots\\1&\cdots&1\end{bmatrix} N\cdot\sec/m$$

Note that the system has non-proportional damping, because the damping matrix C cannot be expressed as a linear combination of ***M*** and ***K***. The simulated impulse function serves as the excitation input acting on the each mass point of the system. The sampling interval is chosen as, $\Delta t = 0.01\mathrm{s}$ and the sampling period is $T = N_t \cdot \Delta t = 120.00\mathrm{s}$. The displacement responses of the system were obtained using Newmark's method. To examine the robustness of the proposed identification approach under noisy conditions, 5% noise is added to the simulated displacement response data. Due to the poor performance of damping ratio identification obtained from the responses contaminated with noise through ERA in the previous studies, we introduce the correlation technique to theory of modal identification to improve effectiveness of parametric estimation. Once the data-correlation matrix $R(k)$ of the impulse responses Y_k could be constructed, the state matrix ***A*** can thus be estimated through the SVD analysis, and modal estimation can be performed by solving the eigenvalue problem associated with the state matrix ***A***. The data-correlation matrix $R(k)$ is written as follows

$$R(k)=H(k)H(0)^T=\begin{bmatrix}\sum_{i=1}^{10000}Y_{k+i}Y_i & \sum_{i=1}^{10000}Y_{k+i}Y_{i+1} & \cdots & \sum_{i=1}^{10000}Y_{k+i}Y_{i+11}\\ \sum_{i=1}^{10000}Y_{k+i+1}Y_i & \sum_{i=1}^{10000}Y_{k+i+1}Y_{i+1} & \cdots & \sum_{i=1}^{10000}Y_{k+i+1}Y_{i+11}\\ \vdots & \vdots & \ddots & \vdots\\ \sum_{i=1}^{10000}Y_{k+i+11}Y_i & \sum_{i=1}^{10000}Y_{k+i+11}Y_{i+1} & \cdots & \sum_{i=1}^{10000}Y_{k+i+11}Y_{i+11}\end{bmatrix}_{72\times 72}$$

To determine the system order, we implement the SVD for $R(k)$. The estimated number of singular values is the order of a system. By examining the distribution of the singular values associated with the responses of the system, we could determine the order, as well as the number of modes to be identified, of the system. The result is shown in Fig. 17.1, from which the order of the system model was determined to be 12. The results of modal identification are summarized in Table 17.1, which shows that in general, the errors in natural frequencies are less than 2% and the error in damping ratios are less than 5%. It should be mentioned that the results of damping ratio identification is better through the ERA/DC algorithm.

In addition, ITD method is employed to perform modal identification from the previous response data, and SVD analysis is used to determine the number of modes to be identified. Through the channel-expansion technique, when the number of channels of a system has been expanded sufficiently, $[\mathbf{X}][\mathbf{X}]^{\mathrm{T}}$can be evaluated and performed SVD analysis. The distribution of the singular values of the data-expansion matrices $[\mathbf{X}][\mathbf{X}]^{\mathrm{T}}$ shows a clear drop around the 12th singular value, as shown in Fig. 17.2, from which the order of the system model, i.e., the number of modes to be identified, is determined to be 12. The results of modal estimation obtained from the simulated impulse response data contaminated with 5% noise are summarized in Table 17.2, which shows that the both errors in natural frequencies and damping ratios are well-identified.

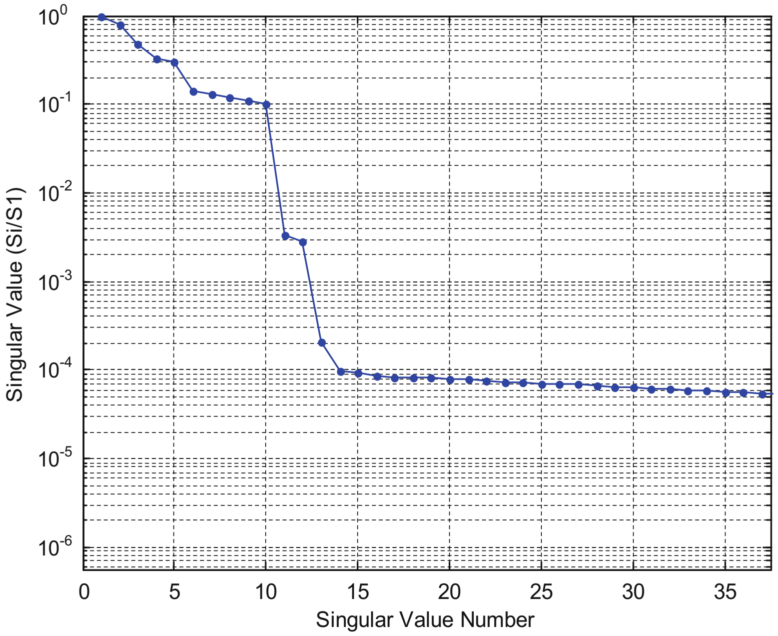

Fig. 17.1 Singular values associated with the responses (contaminated with 5% noise) corresponding to impulse force

Table 17.1 Results of modal identification of a 6-DOF system with close modes (ERA)

	Natural frequency (Hz)			Damping ratio (%)		
Mode	Exact	ERA	Error (%)	Exact	ERA	Error (%)
1	1.39	1.39	0.06	10.65	10.66	0.01
2	3.17	3.16	0.33	2.01	2.00	0.60
3	4.39	4.37	0.62	4.23	4.19	0.92
4	5.05	5.01	0.83	3.19	3.15	1.36
5	6.86	6.77	1.35	4.33	4.06	6.28
6	6.93	6.83	1.53	4.37	4.30	1.59

17.5 Conclusions

Modal interference often degrades the accuracy of identification results and even causes problems of identifiability in the process of modal identification. The accurate estimation of the order of system matrix is important when performing the ERA algorithm and ITD method. By introducing the singular value decomposition in conjunction with least-squares analysis to solve the system matrix, the order of the system can be determined to avoid the phenomenon of omitted modes, and also significantly reduce relatively much calculations required in the conventional channel-expansion technique. Through numerical simulations, the proposed method has been confirmed the validity for modal identification of a system with modal interference.

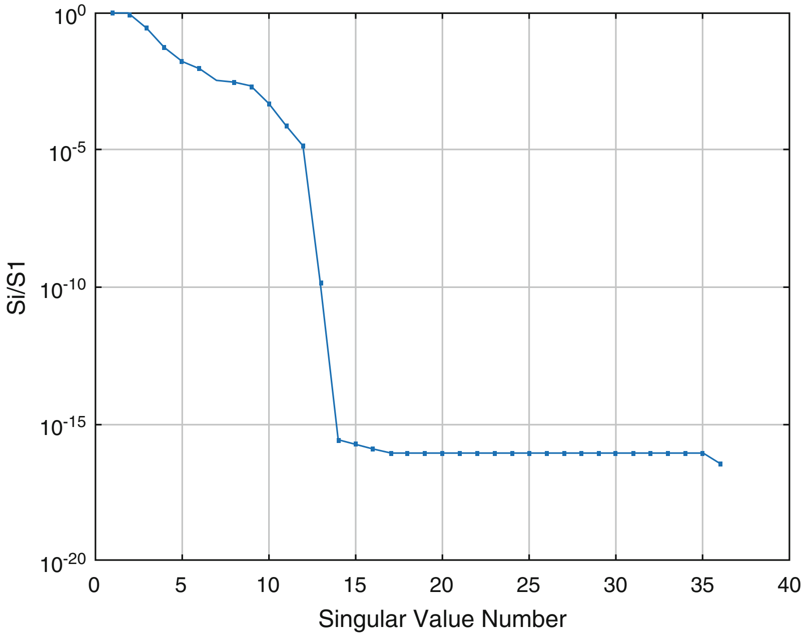

Fig. 17.2 Singular values associated with the data-expansion matrix **[X][X]**^{T} of the free decay responses (contaminated with 5% noise) corresponding to an impulse input

Table 17.2 Results of modal identification of a 6-DOF system with close modes (ITD)

	Natural frequency (Hz)			Damping ratio (%)		
Mode	Exact	ITD	Error (%)	Exact	ITD	Error (%)
1	1.39	1.37	1.39	10.65	9.36	13.78
2	3.17	3.16	0.07	2.01	1.71	17.57
3	4.39	4.20	4.67	4.23	3.92	7.80
4	5.05	4.80	5.15	3.19	2.89	10.39
5	6.86	6.84	0.42	4.33	4.20	3.11
6	6.93	6.92	0.20	4.37	4.22	3.57

References

1. Hougen, J.O., Walsh, R.A.: Pulse testing method. Chem. Eng. Prog. **57**(3), 69–79 (1961)
2. Brown, D.L., Allemang, R.L., Zimmerman, R.D., Mergeay, M.: Parameter estimation techniques for modal analysis. SAE Tech. Pap. 790221 (1979)
3. Vold, H., Rocklin, G. T.: The numerical implementation of a multi-input modal estimation method for mini-computers. Proceedings of 1st International Modal Analysis Conference, pp. 542–548 (1982)
4. Juang, J.N., Pappa, R.S.: An eigensystem realization algorithm for modal parameter identification and modal reduction. J. Guid. Control. Dyn. AIAA. **8**(5), 620–627 (1985)
5. Juang, J.N., Pappa, R.S.: Effects of noise on modal parameter identification by the eigensystem realization algorithm. J. Guid. Control. Dyn. AIAA. **9**(3), 294–303 (1986)
6. Juang, J.N., Cooper, J.E., Wright, J.R.: An eigensystem realization algorithm using data correlations (ERA/DC) for modal parameter identification. Control.Theory. Adv. Technol. **4**(1), 5–14 (1988)
7. Rayleigh, L: The Theory of Sound, **1, 2**, 2nd ed. Dover Publications, 1897 (re-issue 1945)

Chapter 18
Influence of Printing Constraints on Residual Stresses of FDM Parts

C. Casavola, A. Cazzato, V. Moramarco, and G. Pappalettera

Abstract The Fused Deposition Modelling (FDM) is nowadays one of the most widespread and employed processes to build complex 3D prototypes directly from a STL model. In this technique, the part is built as a layer-by-layer deposition of a feedstock wire. This typology of deposition has many advantages but produces rapid heating and cooling cycles of the feedstock material that introduces residual stresses in the part during the build-up. Consequently, warping, de-layering and distortion of the part during the print process are common issues in FDM parts and are related to residual stresses. The common techniques employed to obtain parts of correct shape and dimensions, such as depositing glue on the bed, have the aim to constrain the object on the printing bed, though this increases the residual stresses in the parts. The aim of the present work is to measure the residual stresses in several points of printed parts, both on top and bottom, in order to verify if the constrain conditions used during the printing produce substantial variation from a point to another. The residual stresses have been measured in ABS parts employing the hole-drilling method. In order to avoid the local reinforcement of the strain gage, an optical technique, i.e. ESPI (electronic speckle pattern interferometry), is employed to measure the displacement of the surface due to the stress relaxation and, consequently, calculate the residual stresses.

Keywords 3D printing • Residual stress • Fused deposition modelling • Hole drilling • ESPI

18.1 Introduction

The Fused Deposition Modelling (FDM), invented in the early 1990s by Stratasys, is one of the most employed 3D printing techniques in both consumer and enterprise business. This process has been employed to build complex 3D prototypes directly from a computerized solid model in many fields such as aerospace, medical, construction, and cultural [1, 2] but, nowadays, there are many other potential fields where it can be employed. Moreover, the diffusion of the low-cost desktop 3D printers such as RepRap, Ultimaker, Maker-Bot, Cube, etc., has made this technology widely accessible even at home and office. In this process, as for many others 3D printing technologies [3], the model is built as a layer-by-layer deposition of a feedstock material. Initially, the raw material is in the form of a filament that is partially melted, extruded and deposited by a numerically controlled heated nozzle onto the previously built model [1]. After the deposition, the material cools, solidifies and sticks with the surrounding material. Due to the layer-by-layer construction and the orientation of the material deposition, once the entire model has been deposited, the FDM part shows orthotropic material properties with a behaviour similar to a laminate orthotropic structure [4]. Initially, the FDM printers have been able to build parts only in acrylonitrile-butadiene-styrene (ABS) and polylactic acid (PLA). However, nowadays, many others materials have been employed and developed, e.g., metal [5], ceramics [6], bioresorbable polymer (PCL) [7], metal/polymers mixture materials [8], and short fibre composites [9]. The PLA, compared to ABS, have a stronger mechanical resistance and a lower coefficient of thermal expansion. The last property improves the printability of the material because reduces the de-layering problems and the warp effect during the printing phase. This distortion effect of the part during the print is one of the most important issues in the FDM process, because it could seriously affect the shape and the final dimensions of the parts or it could prevent the finalization of the objects due to unsticking of the object from the bed. The distortions are due to the continuous rapid heating and cooling cycles of the deposited material [10, 11]. A common technique in order to reduce this problem is to employ a heated bed with some type of adhesive on the surface. Although, such procedures help to reduce distortions, they can increase the residual stresses of the final part.

C. Casavola • A. Cazzato • V. Moramarco (✉) • G. Pappalettera
Dipartimento di Meccanica, Matematica e Management (DMMM), Politecnico di Bari, Viale Japigia 182, 70126, Bari, Italy
e-mail: vincenzo.moramarco@poliba.it

A. Baldi et al. (eds.), *Residual Stress, Thermomechanics & Infrared Imaging, Hybrid Techniques and Inverse Problems, Volume 8*,
Conference Proceedings of the Society for Experimental Mechanics Series, DOI 10.1007/978-3-319-62899-8_18

Some papers have dealt with experimental measurements of residual stress distribution in plastic parts [12–14] but few works in FDM parts [11, 15]. Turnbull et al. [12] carried out a comparison among several techniques to measure residual stresses in ABS, Polycarbonate, and Nylon. They concluded that the hole drilling can be employed as a valid measurement method to measure residual stresses in plastic materials. Nau et al. [13] highlighted that the process parameters and procedures applied for stress analysis in metallic materials cannot be employed in polymers. They pointed out that the surface preparation of specimens, the strain gauge bonding, and the drilling speed are critical issues in order to obtain a correct measure. However, both Turnbull et al. [12] and Nau et al. [13] did not consider the local reinforcement effect that the installation of a rosette produces in materials that have a low Young's modulus. Indeed, Magnier et al. [14] studied the influence of material viscoelasticity, room temperature and local reinforcement of the strain gauge on the measure of deformation by HDM of plastic materials. They highlighted that the use of strain gauge to measure the deformation on plastic materials can produce a difference up to 30% between the results recorded by strain gauge and DIC. Casavola et al. [11, 16–17] studied the effect on residual stresses of the raster orientation in FDM parts. They found that the stacking sequence +45°/−45° shows the lowest values of residual stresses. Moreover, they highlighted that there is not a clear difference between the bottom and the top of the printed specimens. Only one paper has tried to deal with the residual stress issues in FDM part by numerical simulation. Zhang and Chou [18], using simplified material properties and boundary conditions, have simulated different deposition patterns and have demonstrated the feasibility of using the element activation function to reproduce the filament deposition. They found that there was a modification of the residual stress distributions changing the tool-path pattern. However, they did not validate their model using residual stress measurements but only by comparing the distortion of the printed part and the numerical prediction.

The aim of the present work is to measure the residual stresses in several points of printed parts, both on top and bottom, in order to verify if the constrain conditions employed during the printing produce a substantial variation from a point to another. The residual stresses have been measured in ABS parts employing the hole-drilling method. In order to avoid the local reinforcement of the strain gage, an optical technique, i.e. ESPI (electronic speckle pattern interferometry), is employed to measure the displacement of the surface due to the stress relaxation and, consequently, to calculate the residual stresses.

18.2 Materials and Methods

A RepRap Prusa i3 equipped with a marlin firmware and a nozzle with a diameter of 0.4 mm has been employed to produce the specimens. These have a rectangular shape and the dimensions of $80 \times 40 \times 7$ mm. Four stacking sequences have been studied, i.e., the raster angles are ±30°, ±45°, 0°/90° and 0° only. A layer with a 0° raster angle has the deposited beads parallel to the major side of the specimen. Moreover, the samples have been manufactured with the minimum dimension of the part perpendicular to the build platform. The Fig. 18.1 shows the coordinate system for the deposition and for the residual stresses.

The parameters reported in Table 18.1, such as the layer thickness or the number of contour lines, have been kept constant for every specimen.

In Table 18.1, the air gap is the distance between two, adjacently deposited, beads of the same layer; the layer thickness and the bead width are respectively the height and the width of a deposited filament. The number of contours represents how many edges have been deposited before filling the inner part by inclined beads. The bed temperature has been set to 90 °C and some glue on the bed has been employed to reduce the warping effect. The solid model, created using a 3D CAD, has been sliced using the open source software Slic3r.

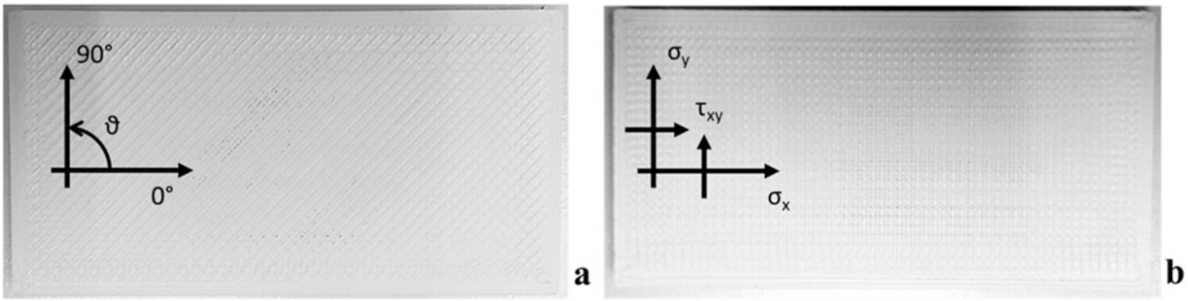

Fig. 18.1 Specimen examples with ±45° (**a**) and 0°/90° (**b**) stacking sequence

Table 18.1 Fixed printer parameters

Parameter	Value
Air gap [mm]	0
Layer thickness [mm]	0.2
Bead width [mm]	0.67
Number of contour lines	3
Bed temperature [°C]	90
Nozzle temperature [°C]	215

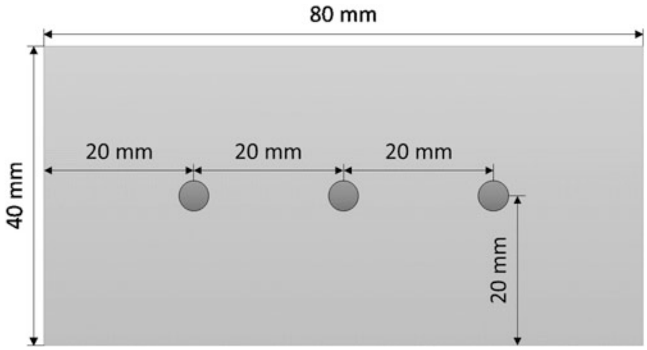

Fig. 18.2 Holes position on the *top* and the *bottom* of the specimens

In this work, the ESPI technique has been employed to measure the displacement around a hole drilled inside the material. Due to the orthotropic behaviour of FDM parts, the isotropic model usually implemented in commercial hole drilling software cannot be used. Thus, an orthotropic FEM model has been developed to calculate the displacements due to some known stress cases. The combination between the experimental displacement data and the FE model allows calculating the residual stress in the parts [17].

The measure of the residual stresses has been carried out on three different samples for each stacking sequence and in order to calculate the mean values. Moreover, three holes have been drilled on the top of each specimen, i.e. starting from the last layer deposited, and three on the bottom, i.e. starting from the first layer deposited (Fig. 18.2). Finally, an average value of the two side holes has been calculated and compared to the values of the central hole.

The holes were drilled by means of a high-speed turbine which is mounted on a precision travel stage. Turbine rotation speed was set to 5,000 rpm after some preliminary tests that indicated that this speed allows obtaining good quality holes [11]. The cutter is made by tungsten coated by TiN and it has a nominal diameter $d = 1.59$ mm. Compressed air was activated during the test to clean the surface of the sample by the formation of drilling chips. The holes were drilled to a depth of 0.6 mm through 30 drill increments to contain the temperature during the drilling phase on lower values. In order to reduce the computational time, the residual stress calculation has been done on 15 drill increments.

A diode pumped solid-state laser source ($\lambda = 532$ nm) was used to shine the sample and to generate the speckle pattern. The laser beam is divided in two parts by a beamsplitter and delivered by two optical fibres. The beam emerging out from the first fibre is collimated and then directed towards the sample at a given angle ($\alpha = 54°$). The beam emerging from the second fibre, instead, is directed towards the CCD matrix of the camera and it acts as a reference beam. The CCD camera (640×480 pixel) itself is placed at a given angle with respect to the normal to the sample ($\beta = 34°$). Light diffused by the sample interferes on the CCD matrix with the reference beam. Four-step temporal phase shifting algorithm was adopted in order to obtain the phase [19, 20]. This means that four reference images are taken initially having a $\pi/2$ phase difference among each other. Another set of four images is, analogously taken for each drill increment. These intensity patterns were subtracted from the reference intensity patterns recorded on the sample before starting the drilling procedure. This operation allows obtaining fringe patterns encoding the information about the displacement experienced by the sample along the sensitivity vector.

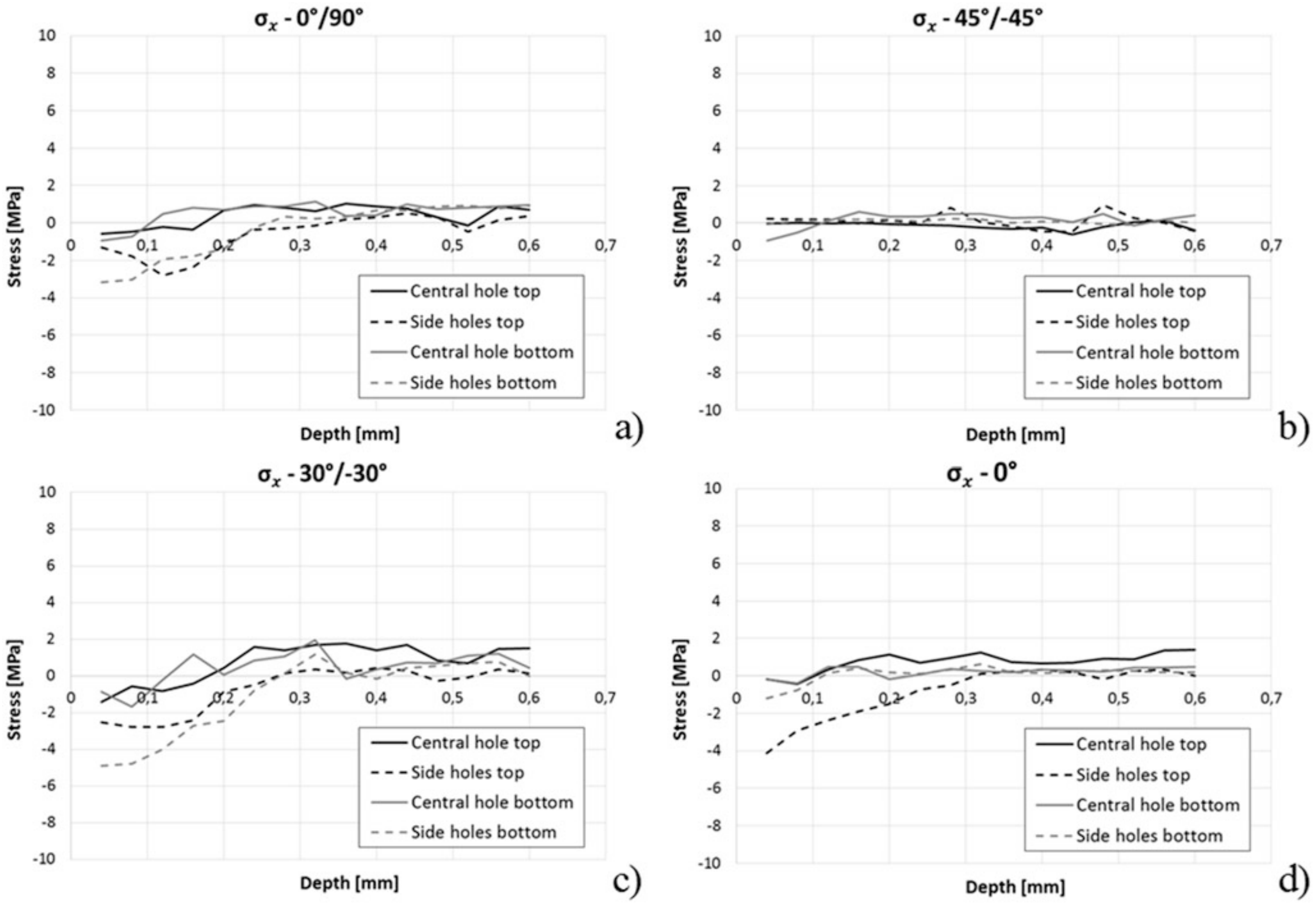

Fig. 18.3 Residual stresses in x direction for 0°/90° (**a**), 45°/−45° (**b**), 30°/−30° (**c**) and 0° (**d**) raster orientations

18.3 Results and Discussions

The σ_x, σ_y, and τ_{xy} residual stresses trends for the four stacking sequences and for the top and the bottom of the specimens have been shown in Figs. 18.3, 18.4 and 18.5. Moreover, it has been reported the comparison between the side holes and the central hole residual stresses values. As pointed out also by Casavola et al. [15], there are some differences among the studied configurations for σ_x and σ_y residual stresses. These differences are remarkable near the surface of the specimens, i.e. until 0.2 mm, while no clear differences can be identified in depth for all the stacking sequences. The ±30° configuration shows (Figs. 18.3c and 18.4c) the higher absolute values of residual stress both on the top and on the bottom of the specimens. Moreover, this stacking sequence shows the highest value of residual stress recorded during this experimental campaign (Fig. 18.4c).

The lowest residual stresses have been measured in ±45° in the specimens. Both in the σ_x and τ_{xy} are near the zero both on the top and on the bottom of the specimens (Figs. 18.3b and 18.5b), while the σ_y, although is not null, shows values lower in comparison with the other configurations (Fig. 18.4b).

The comparison between the residual stresses in side and central positions shows that, generally, the σ_x is higher in the side positions. The difference is remarkable near the surface and beyond 0.2 mm, while, in depth, the residual stresses tend to a value near zero. On the other hand, for the σ_y stress, the difference between the side and central holes is not clear and the trends are almost overlapped. The difference between side and central hole in the x-direction is probably the result of the constraint using the glue of the sample warpage during the printing phase. As in the x-direction, i.e. the major side of the specimen, the warpage is much more important than the y-direction, this could explain the difference between the residual stresses in x and y directions.

For the τ_{xy} (Fig. 18.5) it cannot be observed any significant difference among the stacking sequences, the side of the specimens, and the central and side holes. Indeed, the values of residual stress are roughly between −1 and +1 MPa in all configurations.

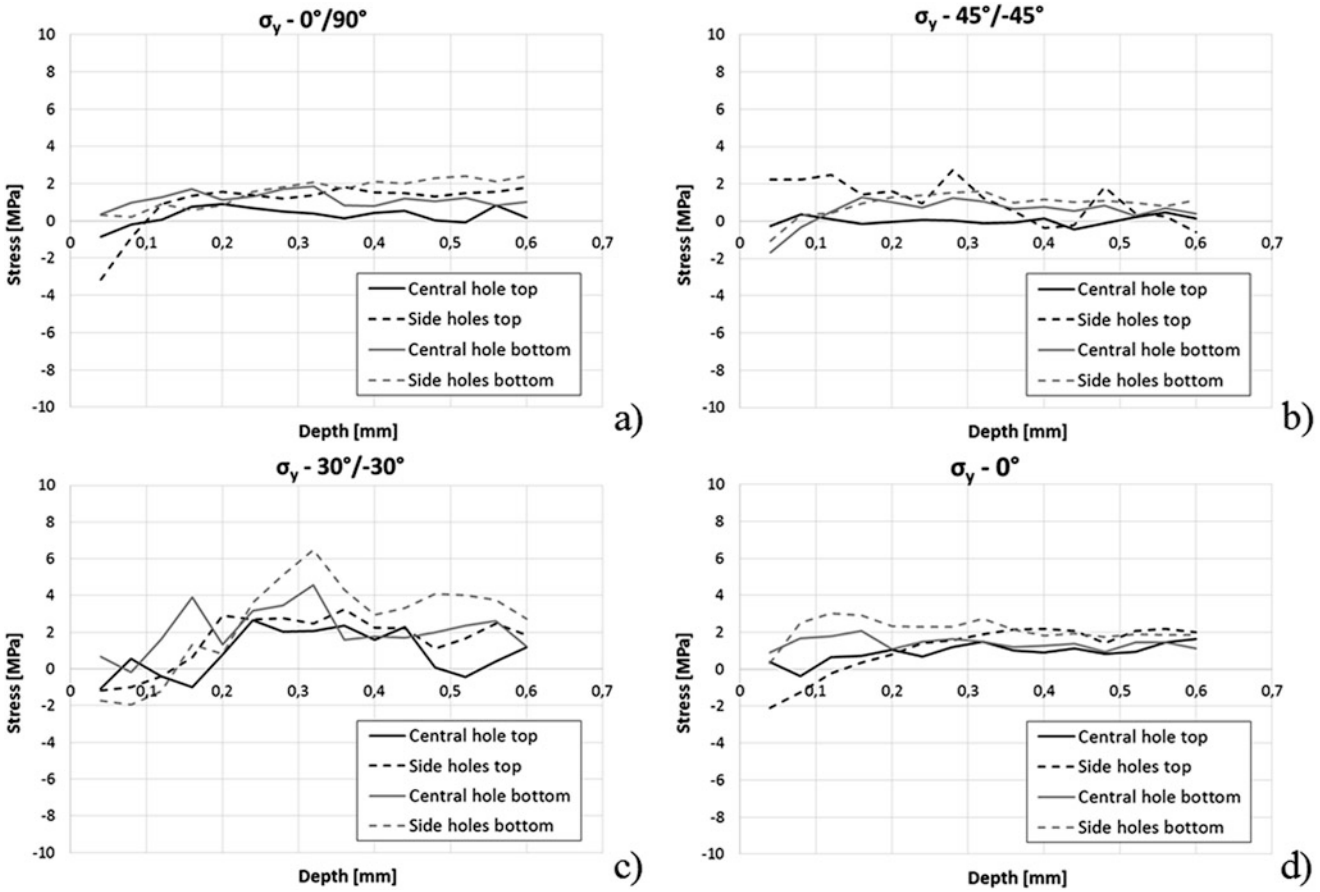

Fig. 18.4 Residual stresses in y direction for 0°/90° (**a**), 45°/−45° (**b**), 30°/−30° (**c**) and 0° (**d**) raster orientations

18.4 Conclusions

In this paper, the measure of the residual stresses in FDM printed parts has been carried out by the hole-drilling method. In order to avoid the local reinforcement of the strain gage, an optical technique, i.e. ESPI (electronic speckle pattern interferometry), is employed to measure the displacement of the surface due to the stress relaxation and, consequently, calculate the residual stresses. The aim of the work was to measure the residual stresses in several points of 3D printed parts, both on top and bottom, to verify if the constrain conditions employed during the printing produce substantial variation from a point to another. This comparison has been carried out among four stacking sequences, i.e. ±30°, ±45°, 0°/90° and 0° only. The specimens have been made of ABS and they have the dimensions of 80 × 40 × 7 mm.

The results show that, whereas for σ_x and σ_y there are some differences, for τ_{xy} it cannot be observed any difference among the stacking sequences, the sides of the specimens, and the comparison between central and side holes. For σ_x and σ_y, the differences are remarkable near the surface of the specimens, i.e. until 0.2 mm, but below this depth, there are no clear differences among the studied configurations. Whereas the ±30° configuration is the worst stacking sequence because it shows the highest values of residual stresses, the ±45° should be the best configuration to have low residual stresses in the specimens.

The comparison between the residual stresses in side and central positions shows that, for the σ_x stress, the side positions has higher, in absolute value, residual stresses. On the other hand, for the σ_y stress, this difference is not clear and the different trends are almost overlapped. The difference between side and central hole is probably the result of the constrain using the glue of the sample warpage during the printing phase. As in the x-direction, i.e. the major side of the specimen, the warpage is much more important than the y-direction, this could explain the difference between the residual stresses in x and y directions. These results confirm that residual stress management in FDM part is an important problem that must be properly addressed and they show, in a clear way, that constrain the specimens avoiding the warpage increases the residual stresses in the finished part.

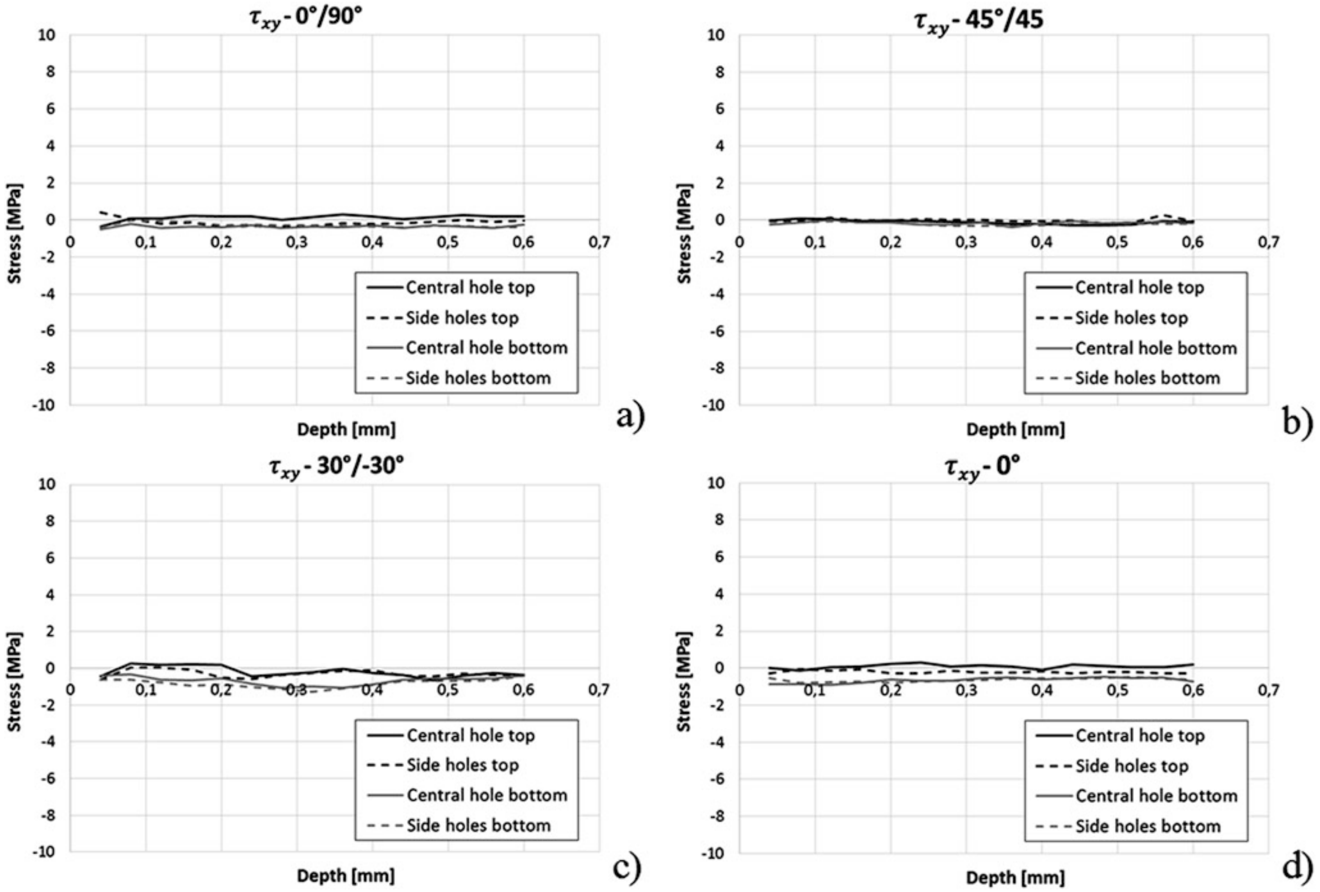

Fig. 18.5 Residual stresses in xy direction for 0°/90° (**a**), 45°/−45° (**b**), 30°/−30° (**c**) and 0° (**d**) raster orientations

Acknowledgment This research was co-funded by Fondo di Sviluppo e Coesione 2007-2013 – APQ Ricerca Regione Puglia “Regional program for Smart Specialization and Social and Environmental sustainability”– FutureInResearch.

References

1. Yan, X., Gu, P.: A review of rapid prototyping technologies and systems. Comput. Aided Des. **28**(4), 307–318 (1996)
2. Petzold, R., Zeilhofer, H.F., Kalender, W.A.: Rapid prototyping technology in medicine—basics and applications. Comput. Med. Imaging Graph. **23**(5), 277–284 (1999)
3. Chua, C.K., Chou, S.M., Wong, T.S.: A study of the state-of-the-art rapid prototyping technologies. Int. J. Adv. Manuf. Technol. **14**(2), 146–152 (1998)
4. Casavola, C., et al.: Orthotropic mechanical properties of fused deposition modelling parts described by classical laminate theory. Mater. Des. **90**, 453–458 (2016)
5. Mireles, J., et al.: Development of a fused deposition modeling system for low melting temperature metal alloys. J. Electron. Packag. **135**(1), 011008–011008 (2013)
6. Allahverdi, M., et al.: Processing of advanced electroceramic components by fused deposition technique. J. Eur. Ceram. Soc. **21**(10–11), 1485–1490 (2001)
7. Zein, I., et al.: Fused deposition modeling of novel scaffold architectures for tissue engineering applications. Biomaterials. **23**(4), 1169–1185 (2002)
8. Masood, S.H., Song, W.Q.: Development of new metal/polymer materials for rapid tooling using Fused deposition modelling. Mater. Des. **25**(7), 587–594 (2004)
9. Zhong, W., et al.: Short fiber reinforced composites for fused deposition modeling. Mater. Sci. Eng. A. **301**(2), 125–130 (2001)
10. Kantaros, A., Karalekas, D.: Fiber Bragg grating based investigation of residual strains in ABS parts fabricated by fused deposition modeling process. Mater. Des. **50**, 44–50 (2013)
11. Casavola, C., et al.: Preliminary study on residual stress in FDM parts. In: Residual Stress, Thermomechanics & Infrared Imaging, Hybrid Techniques and Inverse Problems, vol. 9, pp. 91–96. Springer International Publishing, Cham, Switzerland (2017)

12. Turnbull, A., Maxwell, A.S., Pillai, S.: Residual stress in polymers – evaluation of measurement techniques. J. Mater. Sci. **34**(3), 451–459 (1999)
13. Nau, A., et al.: Application of the hole drilling method for residual stress analyses in components made of polycarbonate. Z. Kunststofftechnik/J. Plast. Technol. **3**, 66–85 (2011)
14. Magnier, A., Nau, A., Scholtes, B.: Some aspects of the application of the hole drilling method on plastic materials. In: Conference Proceedings of the Society for Experimental Mechanics Series. (2016)
15. Casavola, C., et al.: Residual stress measurement in Fused Deposition Modelling parts. Polym. Test. **58**, 249–255 (2017)
16. Casavola, C., Campanelli, S.L., Pappalettere, C.: Preliminary investigation on distribution of residual stress generated by the selective laser melting process. J. Strain Anal. Eng. Des. **44**(1), 93–104 (2009)
17. Casavola, C., Campanelli, S.L., Pappalettere, C.: Experimental analysis of residual stresses in the selective laser melting process. Society for Experimental Mechanics – 11th International Congress and Exhibition on Experimental and Applied Mechanics 2008, 3, pp. 1479–1486, 2008
18. Zhang, Y., Chou, Y.: Three-dimensional finite element analysis simulations of the fused deposition modelling process. Proc. Inst. Mech. Eng. B J. Eng. Manuf. **220**(10), 1663–1671 (2006)
19. Kujawinska, M.: Use of phase-stepping automatic fringe analysis in moire interferometry. Appl. Opt. **26**(22), 4712–4714 (1987)
20. Ghiglia, D.C., Pritt, M.D.: Two-dimensional phase unwrapping: Theory, algorithms, and software, vol. 4. Wiley, New York (1998)